



University  
of Glasgow

Laing, Andrew Brian. (2010) *Optimisation of detectors for the golden channel at a neutrino factory*. PhD thesis.

<http://theses.gla.ac.uk/2216/>

Copyright and moral rights for this thesis are retained by the author

A copy can be downloaded for personal non-commercial research or study, without prior permission or charge

This thesis cannot be reproduced or quoted extensively from without first obtaining permission in writing from the Author

The content must not be changed in any way or sold commercially in any format or medium without the formal permission of the Author

When referring to this work, full bibliographic details including the author, title, awarding institution and date of the thesis must be given

# Optimisation of Detectors for the Golden Channel at a Neutrino Factory

Andrew Brian Laing



University  
*of*  
Glasgow

*School of Physics & Astronomy*

October 2010

A thesis submitted for the degree of Doctor of Philosophy  
at the University of Glasgow

© A. Laing 2010

# Optimisation of Detectors for the Golden Channel at a Neutrino Factory

## Abstract

That neutrinos have mass and mix is now well established experimentally. Measurements of the properties of neutrinos from both natural and man-made sources have measured the large mixing angles and mass squared differences. In order to fully understand the nature of the neutrino, and ultimately the lepton sector, a number of measurements remain to be made. The Neutrino Factory would produce an intense beam of  $\nu_\mu$  ( $\bar{\nu}_\mu$ ) and  $\bar{\nu}_e$  ( $\nu_e$ ) from the decay of muons creating an intense flux of neutrinos. Such a facility would be capable of constraining the already measured mixing parameters to unprecedented accuracy while achieving sensitivity to the measurement of the third mixing angle and leptonic CP violating phase unrivaled by other facilities. The golden channel is characterised by the observation of a primary muon of the opposite charge to that decaying at the source, however, since this signal is subdominant the large data sample of correct sign muons have the potential to produce backgrounds to the desired signal channel and as such understanding the cross-sections to high accuracy enables a far better understanding of the response of the detector. Making these measurements requires the optimisation of all aspects of the detectors used for the measurement of the interaction properties as well as those which search for the appearance of neutrino flavours not present at the source.

Pixellated silicon detectors are capable of high resolution three dimensional track reconstruction and vertexing. In studying active pixel sensors (APS) it was sought to understand the feasibility of commercially available technology to perform vertexing at a detector positioned within 1 km of the neutrino factory source. Using such technology at this near detector would improve significantly the ability of the experiment to constrain the cross-sections of neutrinos. These measurements would be particularly important in understanding neutrino induced charm production since the decays, in particular of  $D^{+/-}$ , can produce penetrating muons with the potential to confuse the extraction of the appearance of  $\nu_\mu$  ( $\bar{\nu}_\mu$ ). The capability to observe the impact parameter of the decaying meson significantly improves the accuracy of any measurement of the charm production cross-section.

A Magnetised Iron Neutrino Detector (MIND) of large mass (50-100 ktonne) has been studied as the far detector where high suppression of the beam inherent backgrounds can be achieved due to the powerful suppression of hadronic particles in iron. Particular focus has been given to the introduction of a realistic reconstruction of the signal and analysis which optimises the signal efficiency below 5 GeV which has been identified by theoretical

studies as key to the accurate measurement of the oscillation parameters down to low values. Studies of this detector have led to the extraction of the expected response of the detector to both golden channel signals and demonstration of the power of such an analysis to the measurement of the remaining oscillation parameters.

Using minimal assumptions in the digitization of the simulated signal, the reconstruction and analysis of a large data-set of neutrino interactions, including deep-inelastic scattering (DIS), quasi-elastic scattering (QEL) and resonant pion production (RES), in MIND has led to the extraction of response matrices predicting signal efficiency for both  $\nu_\mu$  and  $\bar{\nu}_\mu$  appearance with thresholds between 2-3 GeV while suppressing key beam inherent backgrounds to at or below the  $10^{-4}$  level. Such a response has been shown to open the possibility of sensitivity to the measurement of leptonic CP violation through the measurement of the mixing complex phase  $\delta_{CP}$  down to  $\theta_{13} \simeq 0.2^\circ$  for maximal violation and to most possible values from  $\theta_{13} \sim 1^\circ$ . Sensitivity to the measurement of  $\theta_{13}$  and to the determination of the true mass hierarchy is maintained down to  $\theta_{13} \simeq 0.25^\circ$ .

*to those who have an opinion  
and those who have put up with mine...*

## Acknowledgements

There are many people who I'd like to thank, for various reasons but we'll stick to stuff relevant to the last few years. Firstly, as tradition dictates, thank you to Paul Soler who has guided me through the four years of my PhD, forcing me to go such terrible places as Japan, Spain and India (to name but a few). It continually impresses me how quickly you understand something that has caused me days of confusion and invariably threats to take a sledge hammer to my computer. Thank you, also, for being the only person but for myself and, I hope, the examiners to have read (and this, I imagine, will remain true for ever more) the document cover to cover.

I now come to my various other supervisors (official and otherwise) who have had the dubious pleasure of listening to me when both I think I understand or am convinced of my ignorance. Val O'Shea, who I think remembers now that he is associated to me somehow, has given me numerous pieces of advice spanning a variety of subjects. Lars Eklund and Andy Blue for great help in the lab, patience with my stupidity when but a newbie and various forays into music and sports. The indomitable Dr. Dimska has affected my course through the last few years greatly. Whether working together in the lab, forgetting to tell me he 'tidied up' our analysis code or demanding booze, you have helped me to enjoy my time as a PhD student. Thanks to Dan for all those early ROOT lessons, the KarmaROOTra lives on. Everyone else from the motley lunch crew: Kenny, Aaron, Richie, Graeme, Juan Pablo etc., from the lab Fiona, John and Fred and from the Atlas offices: Chris, Cristina etc. ta very much.

Chief among my secret bosses has been Anselmo Cervera. Though I'm not convinced that you understood a word I was saying for the first few months, you managed to get me working and the majority of the work that I present here I owe to you. Gracias por invitarme a Valencia y ayudarme tanto en todo el trabajo de MIND. A Anselmo y los demás de Valencia os debo mucho. Los meses que pasé allí fueron los más interesantes y divertidos del doctorado. Desde el día que llegué, cuando no hablaba ni una palabra de ningún idioma que entendíais, me tratabais como un amigo. Gracias a Justo por ayudarme con el código y por ser tan polémico, a Francesc por enseñar el baile del mal y unas Fallas y semanas Santas de puta madre, gracias también a Laura, Raphaël, Joan, Luis, Lorena, Pau, María y Ana, la liáis mucho pero como mola! Fuera del despacho de los guays en sus despachos tranquilos también quiero agradarme a Michel, ya me entiendes, verdad? Markus, danke schön dafür, immer ein freund zu sein und mit mir die whiskies zu trinken. Christian, I'll learn how to run eventually, cheers for the salsa lessons, the runs (or attempts) and for being more guiri than me! Gracias Jordi, sin ti no habría entendido los fits. Gracias Paola, la italiana más rápida de Valencia y una fuente de conocimiento, pasamos unos días divertidos por la ciudad, tengo

ganas de caminar otra vez por las fallas comiendome buñuelos. Cheers Martin, for teaching me rum and for being a great friend. Terminando el paso por Valencia ya salgo del IFIC y voy caminando (a veces) a la piscina de Burjassot. Primero, gracias a Juanjo, te debo más que la piscina pero pasábamos la mayoría del tiempo juntos allí, cuantos cienes de crol y cuanta alegría conocer a un profesor a quien le interesa pasar horas con los 'plebs'. Gracias a todo el equipo de natación: Miguelín, Miguelo, Pilar, Raphaël y Francesc otra vez y todos los demás que intentaban seguirnos, nunca en la vida había sido el más rápido en la piscina, pero me vais a ganar nadando así! Ya voy a Campanar, *el barrio*, muchas gracias Sonia, te debo de la 'a' a 'todopoderosa'. Gracias por todo: las fiestas, el arroz al horno y mucho más. Cheers Ralph and Jenna, gracias \*para hablar el español guiri con \*yo. A los que no aparecen aquí gracias también, claro que me olvido de alguien.

Last, but by all means not least, I come to those who escape association to anything physics related. I owe existence to my mum and dad so cheers for that! Thank you so much for everything, I don't think I could cover half of the thanks your due in all the pages of this bit of paper but know I'm grateful. Thanks Steven, good luck in California, remember that regular skype home not only keep mum happy but go some way to stopping you from getting a terrible accent. Cheers Nick, Chris and Gareth for gid booze, gid chat and healthy dolops of cynicism. For joining me so many times for the now institutional (or institutionalised) liz Christmas eves thanks to all the rest of the Woodmill crowd. Cheers to all the flatmates I've had over the years, Amanda, Neil and Vava particularly. Now I come to those who swim, play waterpolo or like me, try. I truly hated uni when I first came, without you lot I would have left after my first degree and probably had no good memories of Glasgow. Thank you particularly to Helen "Bobbin's Burd" Fullerton, Stewart "W@k" Carlile, Odeeps (you have no other name!), Kirsty "Rampant Rabbit" McDonald, Kenny "Walnuts" Walaron, Trina "Funbags" Hewitt and Gordon "Bobbin" Hewitt and so many more. Do I really remember being able to \_rink all that?

## **Declaration**

The research results presented in this thesis are the product of my own work. Appropriate references are provided when results of third parties are mentioned. The research presented here was not submitted for another degree in any other department or university.

**Andrew Brian Laing**

# Contents

<b>1</b>	<b>An introduction to neutrino physics</b>	<b>1</b>
1.1	Discovery of the neutrino . . . . .	1
1.1.1	Parity violation and the standard model neutrino . . . . .	1
1.2	Neutrino mixing . . . . .	2
1.2.1	Oscillations in Vacuum . . . . .	3
1.2.2	Generalisation to Matter oscillations . . . . .	5
1.3	Neutrino Mass . . . . .	8
1.4	Neutrino Oscillation Phenomenology . . . . .	10
1.4.1	The Neutrino Factory golden channel . . . . .	10
1.4.1.1	The intrinsic degeneracy . . . . .	11
1.4.1.2	The $\Delta m_{13}^2$ sign degeneracy . . . . .	12
1.4.1.3	The octant degeneracy . . . . .	13
1.4.1.4	The magic baseline . . . . .	13
1.5	Conclusion . . . . .	14
<b>2</b>	<b>Neutrino oscillation experimental status</b>	<b>15</b>
2.1	Introduction . . . . .	15
2.2	Experiments using natural sources of neutrinos . . . . .	15
2.2.1	Solar Neutrinos . . . . .	15
2.2.2	Atmospheric Neutrinos . . . . .	20
2.3	Reactor experiments . . . . .	22
2.4	Accelerator experiments . . . . .	23
2.4.1	Conventional and Super beams . . . . .	23
2.4.2	New accelerator concepts . . . . .	27
2.5	Conclusion . . . . .	27
<b>3</b>	<b>The Neutrino Factory</b>	<b>29</b>
3.1	Introduction . . . . .	29

3.2	Muon production . . . . .	29
3.2.1	Proton driver . . . . .	29
3.2.2	Target, capture and decay . . . . .	30
3.2.2.1	Pion capture . . . . .	31
3.3	Muon Phase Rotation and Cooling . . . . .	31
3.3.1	MICE . . . . .	32
3.4	Re-acceleration and storage . . . . .	33
3.5	Detector Concepts . . . . .	34
3.5.1	Near detectors . . . . .	34
3.5.2	Far detectors . . . . .	34
3.6	Physics at a neutrino factory . . . . .	35
3.7	Conclusion . . . . .	41
<b>4</b>	<b>Active Pixel Sensors for vertex detection at the Near Detector</b>	<b>42</b>
4.1	Introduction . . . . .	42
4.2	Physics at the near detector . . . . .	42
4.2.1	Charm production background . . . . .	43
4.2.2	A silicon vertex detector at the near detector . . . . .	44
4.3	APS technology . . . . .	45
4.4	The Vanilla detector . . . . .	46
4.4.1	Gain determination using photon transfer curve method . . . . .	47
4.4.2	Device Linearity . . . . .	49
4.5	HEPAPS4 . . . . .	49
4.5.1	Sensitivity of HEPAPS4 to electron passage . . . . .	50
4.5.2	Exposure to 6 GeV electrons at DESY . . . . .	51
4.5.3	Exposure to $^{90}\text{Sr}$ $\beta$ source . . . . .	53
4.6	Discussion . . . . .	55
4.7	Conclusions . . . . .	55
<b>5</b>	<b>Development of reconstruction and analysis software for a Magnetised Iron Neutrino Detector</b>	<b>57</b>
5.1	Introduction . . . . .	57
5.2	MIND parameterisation and expected event yields . . . . .	58
5.3	Reconstruction tools . . . . .	59
5.3.1	Muon candidate extraction . . . . .	59
5.3.1.1	Kalman Filter candidate extraction . . . . .	60
5.3.1.2	Cellular Automaton candidate extraction . . . . .	60

5.3.2	Candidate fitting . . . . .	61
5.3.3	Hadronic reconstruction . . . . .	62
5.4	Analysis tools and cuts . . . . .	63
5.4.1	Muon candidate quality cuts . . . . .	63
5.4.2	$\nu_\mu$ CC selection cuts . . . . .	64
5.4.3	Fiducial cuts . . . . .	68
5.4.4	Kinematic cuts . . . . .	68
5.4.5	Summary of analysis cuts . . . . .	68
5.5	Analysis Results . . . . .	68
5.5.1	$\bar{\nu}_\mu$ charge current interactions . . . . .	70
5.5.1.1	Incorrect charge assignment . . . . .	70
5.5.1.2	Wrong sign muons from hadron decays . . . . .	70
5.5.1.3	Inclusive $\bar{\nu}_\mu$ background with fiducial and kinematic cuts . . . . .	71
5.5.2	Neutral current interactions . . . . .	72
5.5.3	$\nu_e$ charge current interactions . . . . .	72
5.5.4	Summary . . . . .	74
5.6	Conclusions . . . . .	74

## **6 The Golden Channel oscillation signal with a Magnetised Iron Neutrino Detector 78**

6.1	Introduction . . . . .	78
6.2	Neutrino event generation . . . . .	78
6.3	Simulation of MIND using Geant4 . . . . .	81
6.4	Digitization . . . . .	83
6.5	Reconstruction and analysis of Geant4 MIND . . . . .	84
6.5.1	Event reconstruction . . . . .	86
6.5.1.1	Hadron shower reconstruction . . . . .	91
6.5.2	Analysis of potential signal and background . . . . .	91
6.5.2.1	q/p relative error . . . . .	92
6.5.2.2	Neutral current rejection . . . . .	92
6.5.2.3	Kinematic cuts . . . . .	93
6.5.2.4	Additional cuts . . . . .	95
6.5.2.5	Cut summary . . . . .	99
6.6	MIND response to the Golden Channel . . . . .	99
6.6.1	Analysis efficiency . . . . .	100
6.6.2	Inelasticity and the difference in efficiencies . . . . .	104

6.6.3	Systematic study . . . . .	106
6.7	Summary and future work . . . . .	109
6.7.1	Development of the analysis . . . . .	111
6.7.1.1	Energy deposit likelihood analysis . . . . .	111
6.7.1.2	$\mu$ momentum measurement by range . . . . .	114
6.7.1.3	Hadronic reconstruction . . . . .	114
6.7.2	Unaccounted backgrounds . . . . .	114
6.8	Conclusions . . . . .	115
<b>7</b>	<b>Sensitivity of MIND to the Neutrino Factory golden channel oscillation</b>	<b>117</b>
7.1	Introduction . . . . .	117
7.2	The NuTS framework . . . . .	118
7.3	Fitting for $\theta_{13}$ and $\delta_{CP}$ simultaneously . . . . .	118
7.4	Sensitivity to $\theta_{13}$ . . . . .	120
7.5	Sensitivity to $\delta_{CP}$ . . . . .	121
7.6	Sensitivity to the mass hierarchy . . . . .	121
7.7	Influence of near detector data . . . . .	122
7.7.1	Flux measurement . . . . .	123
7.8	Flux projection for non-oscillation prediction . . . . .	123
7.9	Comparison of near detector projection to standard fit method . . . . .	126
7.10	Conclusions . . . . .	129
<b>8</b>	<b>Conclusions</b>	<b>131</b>
	<b>Bibliography</b>	<b>133</b>
<b>A</b>	<b>Response Matrices for chapter 5 analysis</b>	<b>143</b>
<b>B</b>	<b>Response Matrices for chapter 6 analysis</b>	<b>146</b>

# List of Tables

2.1	<i>Calculated neutrino fluxes from the SNO salt phase and SSM predicted <math>^8B</math> flux.</i>	19
4.1	<i>Summary of measured gains for each reset type and read noise level.</i>	48
4.2	<i>Summary of key characteristics of the HEPAPS4 chip.</i>	50
5.1	<i>Expected absolute number of interactions in a 51 ktonne MIND at a distance of 4000 km from <math>10^{21} \mu^+</math> decays at 25 GeV in a NF storage ring.</i>	59
5.2	<i>Summary of analysis cuts.</i>	70
5.3	<i>Summary of expected fractional signal and background with true neutrino energy.</i>	74
6.1	<i>Summary of cuts applied to select the golden channel appearance signals. The level of absolute efficiency and the background level which would contribute the highest absolute number of background events (assuming the parameter values of table 5.1-row 1) after each cut are also shown.</i>	99
A.1	<i>Signal Efficiency response matrix; All values <math>\times 10^{-2}</math></i>	143
A.2	<i><math>\bar{\nu}_\mu</math> CC background response matrix; All values <math>\times 10^{-3}</math></i>	144
A.3	<i>Neutral current background response matrix; All values <math>\times 10^{-3}</math></i>	144
A.4	<i><math>\nu_e</math> CC background response matrix; All values <math>\times 10^{-3}</math></i>	145
B.1	<i><math>\nu_\mu</math> appearance detection efficiency. All values <math>\times 10^{-4}</math></i>	146
B.2	<i><math>\bar{\nu}_\mu</math> CC background. All values <math>\times 10^{-4}</math>.</i>	147
B.3	<i><math>\nu_e</math> CC background. All values <math>\times 10^{-4}</math>.</i>	147
B.4	<i>NC background. All values <math>\times 10^{-4}</math>.</i>	148
B.5	<i><math>\bar{\nu}_\mu</math> appearance detection efficiency. All values <math>\times 10^{-4}</math></i>	149
B.6	<i><math>\bar{\nu}_\mu</math> CC background. All values <math>\times 10^{-4}</math>.</i>	149
B.7	<i><math>\bar{\nu}_e</math> CC background. All values <math>\times 10^{-4}</math>.</i>	150
B.8	<i>NC background. All values <math>\times 10^{-4}</math>.</i>	150

# List of Figures

1.1	<i>Neutrino oscillation in vacuum</i> (figure taken from [1]). . . . .	4
1.2	<i>The three neutrino (mass)<sup>2</sup> spectrum</i> (figure taken from [2]). . . . .	6
1.3	<i>The W exchange process which augments the mass splittings in matter</i> (taken from [1]). . . . .	7
1.4	<i>Tritium <math>\beta</math> decay spectrum endpoint showing deviation caused by a 1 eV <math>\nu_e</math> effective mass</i> (taken from [3]) . . . . .	9
1.5	<i>Feynman diagram for neutrinoless double beta decay.</i> . . . . .	9
1.6	<i>Continuous spectrum of solutions for one polarity and baseline (left), Remaining intrinsic solutions using two polarities (right)</i> (taken from [4]) . .	12
1.7	<i>Solving the degeneracy with multiple baselines (left) and with multiple channels (right)</i> (taken from [4]) . . . . .	13
2.1	<i>Expected solar neutrino spectra</i> (taken from [5]). . . . .	16
2.2	<i>Solar PP cycle reaction chain with branching fractions</i> . . . . .	17
2.3	<i>SuperKamiokande solar angle correlation</i> (from [6]) . . . . .	19
2.4	<i>Global fits to solar neutrino data post SNO. (left) All data. (right) Influence of SNO and SK data.</i> (taken from [7]) . . . . .	20
2.5	<i>Zenith angle distributions for fully contained events with Monte Carlo zero oscillation prediction (blue) and data points (black circles), (left) electron-like, (right) muon-like in the Super-Kamiokande detector</i> (taken from [8]). .	21
2.6	<i>Contours of three family oscillation analysis of SK data</i> (taken from [8]). . .	22
2.7	<i>KamLAND results showing the allowed parameter region and comparison to solar neutrino data (left) and the oscillatory form of L/E data for the ratio of observed to no oscillation prediction</i> (taken from [9]). . . . .	23
2.8	<i>K2K measurement of atmospheric oscillation parameters</i> (taken from [10]).	25
2.9	<i>Confidence Interval contours in the fit of the MINOS Far Detector antineutrino data (red) to the hypothesis of two-flavor oscillations</i> (taken from [11]).	26

2.10	<i>Observed <math>\nu_e</math> spectrum in MINIBoONE with expected background and comparison to LSND (left) and exclusion plot based on MINIBoONE observation (right) (taken from [12]).</i>	26
2.11	<i>Schematic of Beta Beam facility to accelerate and store <math>{}^6\text{He}</math> and <math>{}^{18}\text{Ne}</math> (or <math>{}^8\text{Li}</math> and <math>{}^{18}\text{B}</math>) ions.</i>	28
3.1	<i>The neutrino factory facility.</i>	30
3.2	<i>Schematic of expected momentum rotation due to an ionization cooling channel (taken from [13]).</i>	32
3.3	<i>Planned staged evolution of the MICE experiment.</i>	33
3.4	<i>Expected fluxes at source from stored <math>\nu_\mu</math> (left) and stored <math>\bar{\nu}_\mu</math> (right) at 25 GeV.</i>	36
3.5	<i>Variation of golden channel oscillation probability (<math>\bar{\nu}_\mu</math> app. (left) <math>\nu_\mu</math> app. (right)) with distance for fixed <math>E_\nu = 17</math> GeV and (top) fixed <math>\delta_{CP} = 45^\circ</math>, (bottom) fixed <math>\theta_{13} = 8^\circ</math>.</i>	36
3.6	<i>Variation of golden channel oscillation probability (<math>\bar{\nu}_\mu</math> app. (left) <math>\nu_\mu</math> app. (right)) with energy for fixed <math>L = 4000</math> km and (top) fixed <math>\delta_{CP} = 45^\circ</math>, (bottom) fixed <math>\theta_{13} = 8^\circ</math>.</i>	37
3.7	<i>Variation of <math>\nu_\mu</math> appearance flux (<math>\bar{\nu}_\mu</math> app. (left) <math>\nu_\mu</math> app. (right)) with energy for fixed <math>L = 4000</math> km and (top) fixed <math>\delta_{CP} = 45^\circ</math>, (bottom) fixed <math>\theta_{13} = 8^\circ</math>.</i>	38
3.8	<i>Sensitivity to <math>\sin^2 2\theta_{13}</math> at <math>5\sigma</math> relative to optimal (white) successively taking into account statistics, systematics, correlations and degeneracies. The diamond marks the optimal combination in each case (taken from [14]).</i>	39
3.9	<i>Sensitivity to maximal CP-violation (<math>\delta_{CP} = \pi/2</math> or <math>\delta_{CP} = 3\pi/2</math>) for true mass hierarchy normal (taken from [14]).</i>	39
3.10	<i>Sensitivity to normal hierarchy for different values of <math>\delta_{CP}</math> (taken from [14]).</i>	40
3.11	<i>Sensitivity to <math>\delta_{CP}</math> for different detector threshold energies (taken from [14]).</i>	40
4.1	<i>Feynman diagram for DIS charm production (figure taken from [15]).</i>	43
4.2	<i>Possible backgrounds to a wrong sign muon search from charm meson decays.</i>	44
4.3	<i>An APS pixel. Basic pixel structure common to Vanilla and HEPAPS4 within dotted line; additional electronics for Vanilla flushed reset outside.</i>	46
4.4	<i>Examples of PTC curves for three reset modes.</i>	48
4.5	<i>Distribution of calculated pixel gains for Vanilla working in Digital readout mode for the three possible reset modes.</i>	49
4.6	<i>Response versus irradiance for Vanilla with the three reset modes (left) and variance from a linear fit to the non-saturation region as % of the measured range (right).</i>	50

4.7	<i>Pedestal and Noise for each pixel in one region of interest.</i>	51
4.8	<i>Distribution of accepted seeds in one ROI. Center of beam indicated from row 150.</i>	52
4.9	<i>Cluster analysis results for DESY testbeam. Left: Signal distribution in ADC. Right: Signal distribution in number of pixels.</i>	52
4.10	<i>Source testing setup.</i>	53
4.11	<i>Noise distribution calculated from 1800 dark frames.</i>	54
4.12	<i>Source cluster analysis results. Left: Cluster signal distribution, Right: Cluster size distribution.</i>	54
5.1	<i>Muon candidate purity as a function of true muon momentum for i) the Kalman filter extraction method and ii) the Cellular Automaton method.</i>	60
5.2	<i>Momentum resolution for as a function of <math>\mu</math> momentum.</i>	62
5.3	<i>i) <math>\frac{\sigma_{q/p}}{q/p}</math> likelihood for signal and background from <math>\bar{\nu}_\mu</math> CC for all energies considered, and ii) <math>\frac{\sigma_{q/p}}{q/p} \log</math> likelihood ratio (<math>\mathcal{L}_{q/p}</math>).</i>	64
5.4	<i>PDFs of the three parameters used for NC/CC likelihood separation. i) Number of hits in candidate <math>l_{hit}</math>, ii) Fraction of visible energy in candidate <math>l_{frac}</math> and iii) Variance of energy deposit in candidate <math>l_{var}</math>.</i>	66
5.5	<i>Log likelihood discriminator distributions for energy fraction <math>&lt; 0.999</math>, i) <math>\mathcal{L}_1</math>, defined in Eq. 5.7, ii) <math>\mathcal{L}_2</math>, defined in Eq. 5.8 and iii) for energy fraction <math>\geq 0.999</math>, <math>\mathcal{L}_3</math>, defined in Eq. 5.9.</i>	67
5.6	<i>Distributions of kinematic variables: Reconstructed muon momentum (left) and <math>Q_t</math> variable in GeV/c units (right) versus reconstructed neutrino energy, for (top→bottom) signal, <math>\bar{\nu}_\mu</math> CC backgrounds, NC background and <math>\nu_e</math> CC background. All events reconstructed with energy <math>&gt; 30</math> GeV are shown in an overflow bin.</i>	69
5.7	<i>Charge mis-assignment and hadron to muon mis-identification background i) with track quality cuts only and ii) including <math>\nu_\mu</math> CC selection cuts.</i>	71
5.8	<i>Wrong sign muon decay background with track quality and <math>\nu_\mu</math> CC selection cuts.</i>	71
5.9	<i>Expected background from <math>\bar{\nu}_\mu</math> CC interactions when events are randomly generated in the entire detector: i) after track quality, <math>\nu_\mu</math> CC selection and fiducial cuts, and ii) including kinematic cuts.</i>	72
5.10	<i>Expected background from <math>\bar{\nu}_\mu</math> NC interactions, i) with track quality cuts (Eq. 5.5) only, ii) including <math>\nu_\mu</math> CC selection cuts, iii) substituting track quality cuts of Eq. 5.5 by those of Eq. 5.6 and iv) including kinematic cuts.</i>	73

5.11	$\nu_e$ CC background to golden channel signal, i) with track quality and $\nu_\mu$ CC selection cuts, and ii) including kinematic cuts. . . . .	73
5.12	Expected signal identification efficiency: i) after track quality and $\nu_\mu$ CC selection cuts, ii) including fiducial cuts, and iii) including kinematic cuts. .	75
5.13	Response matrix in true/reconstructed neutrino energy for signal and backgrounds: i) signal efficiency, ii) backgrounds from $\nu_\mu$ CC, iii) NC and iv) $\nu_e$ CC. The area of the rectangles is proportional to the relative size of the response matrix element. . . . .	76
6.1	Experimentally measured cross-sections for Quasi-elastic, single pion and deep inelastic $\nu_\mu$ CC interactions with the predictions made by Nuance [16].	79
6.2	Proportion of total number of interactions of different $\nu$ interaction processes for events generated using Nuance and passed to the G4mind simulation. (top) $\bar{\nu}_\mu$ (left) and $\nu_e$ CC (right), (middle) $\nu_\mu$ (left) and $\bar{\nu}_e$ CC (right) and (bottom) NC from antineutrinos (left) and neutrinos (right). . . . .	80
6.3	Exclusive cross-section parameterisation for $\nu_\mu$ CC (left) and $\bar{\nu}_\mu$ CC interactions (right). . . . .	81
6.4	Voxel raw energy deposit showing a peak at $\sim 4$ MeV above a noise background.	83
6.5	Difference of voxel position and contained deposit positions. . . . .	84
6.6	The digitization and voxel clustering of an example event: (top left) bending plane view, (top right) non bending plane, (bottom) an individual scintillator plane. The individual hits are small dots (in red), the blue squares are the voxels and the black asterisks represent the centroid positions of the clusters.	85
6.7	Difference between calculated cluster position and weighted sum of raw deposits included for 1 voxel (top left), 2 voxels (top right) and 3 voxels (bottom).	87
6.8	Muon candidate hit purity for $\nu_\mu$ CC (top) and $\bar{\nu}_\mu$ CC (bottom) interactions extracted using (left) Kalman filter method and (right) Cellular automaton method. . . . .	89
6.9	Pulls on the five Kalman filter vector parameters and the measured momentum resolution: (top) X (left) and Y (right) position, (middle) X (left) and Y (right) slopes and (bottom) momentum pull (left) and momentum resolution (right). . . . .	90
6.10	Distribution of $\frac{\sigma_{q/p}}{q/p}$ for signal and background processes. . . . .	92
6.11	PDF of $\frac{\sigma_{q/p}}{q/p}$ (left) and the resulting log likelihood distribution ( $\mathcal{L}_{q/p}$ ) for a test statistic (right). . . . .	93

6.12	<i>Likelihood distributions for the NC rejection parameters. (top left) Clusters in candidate, (top right) fraction of visible energy in candidate and (bottom) candidate mean deposit per plane. CC in black and NC in red. . . . .</i>	94
6.13	<i>Distribution of log likelihood <math>\mathcal{L}_1</math>. . . . .</i>	94
6.14	<i>Distributions of kinematic variables: (left) Reconstructed muon momentum with reconstructed neutrino energy for (top→bottom) <math>\nu_\mu</math> (<math>\bar{\nu}_\mu</math>) signal, <math>\nu_\mu</math> (<math>\bar{\nu}_\mu</math>) CC background, NC background, <math>\nu_e</math> (<math>\bar{\nu}_e</math>) CC background and (right) <math>Q_t</math> variable (in the same order). . . . .</i>	96
6.15	<i>Distribution of the proportion of clusters fitted in the trajectory. . . . .</i>	97
6.16	<i>Distributions of momentum and displacement with cut levels: (top left) relative displacement in the bending plane to the <math>z</math> direction against candidate hits for signal events, (top right) reconstructed momentum against displacement in <math>z</math> for signal events and (bottom) as top for <math>\nu_\mu</math> (<math>\bar{\nu}_\mu</math>) CC backgrounds. . . . .</i>	97
6.17	<i>Distribution of the <math>qp_{par}</math> variable with the region where the parameter is <math>&lt; 0</math> representing those candidates fitted with charge opposite to the initial Kalman filter (region of highest occupancy shown). . . . .</i>	98
6.18	<i>Background from mis-identification of <math>\nu_\mu</math> (<math>\bar{\nu}_\mu</math>) CC interactions as the opposite polarity. (left) <math>\bar{\nu}_\mu</math> CC reconstructed as <math>\nu_\mu</math> CC, (right) <math>\nu_\mu</math> CC reconstructed as <math>\bar{\nu}_\mu</math> CC. (top) As a function of true energy, (bottom) response matrices in the true/reconstructed energy plane. Box sizes represent relative proportions with numeric values available in appendix B. . . . .</i>	100
6.19	<i>Background from mis-identification of NC interactions as <math>\nu_\mu</math> (<math>\bar{\nu}_\mu</math>) CC interactions. (left) NC reconstructed as <math>\nu_\mu</math> CC, (right) NC reconstructed as <math>\bar{\nu}_\mu</math> CC. (top) As a function of true energy, (bottom) response matrices in the true/reconstructed energy plane. Box sizes represent relative proportions with numeric values available in appendix B. . . . .</i>	101
6.20	<i>Background from mis-identification of <math>\nu_e</math> (<math>\bar{\nu}_e</math>) CC interactions as <math>\nu_\mu</math> (<math>\bar{\nu}_\mu</math>) CC interactions. (left) <math>\nu_e</math> CC reconstructed as <math>\nu_\mu</math> CC, (right) <math>\bar{\nu}_e</math> CC reconstructed as <math>\bar{\nu}_\mu</math> CC. (top) As a function of true energy, (bottom) response matrices in the true/reconstructed energy plane. Box sizes represent relative proportions with numeric values available in appendix B. . . . .</i>	102
6.21	<i>Efficiency of reconstruction of <math>\nu_\mu</math> (<math>\bar{\nu}_\mu</math>) CC interactions. (left) <math>\nu_\mu</math> CC efficiency, (right) <math>\bar{\nu}_\mu</math> CC efficiency. (top) As a function of true energy, (bottom) response matrices in the true/reconstructed energy plane. Box sizes represent relative proportions with numeric values available in appendix B. . . . .</i>	103

6.22	<i>Evolution of the MIND <math>\bar{\nu}_\mu</math> CC detection efficiency. For 2000 analysis see [17], for 2005 see [18] and for 2007 see [19] . . . . .</i>	104
6.23	<i><math>\nu_\mu</math> CC and <math>\bar{\nu}_\mu</math> CC signal detection efficiency as a function of <math>y</math> (top left) and the normalised distribution of all events considered in each polarity as a function of <math>y</math> (top right). (bottom) Normalised distributions for <math>\nu_\mu</math> CC (left) and <math>\bar{\nu}_\mu</math> CC events in the <math>y</math>, true energy plane. . . . .</i>	105
6.24	<i>Variation of signal efficiency (top) and NC backgrounds (bottom) due to a 6% variation in the hadron shower energy and direction resolution and a more pessimistic 50% reduction in angular resolution (focussed on region of greatest variation). . . . .</i>	107
6.25	<i>Efficiencies for a pure DIS sample compared to the nominal case. (top) Signal efficiency, (second line) <math>\nu_\mu</math> (<math>\bar{\nu}_\mu</math>) CC background, (third line) NC background and (bottom) <math>\nu_e</math> (<math>\bar{\nu}_e</math>) CC background. <math>\nu_\mu</math> appearance on the left and <math>\bar{\nu}_\mu</math> appearance on the right. . . . .</i>	108
6.26	<i>Calculated error on signal efficiencies on increasing (top) and decreasing (bottom) the proportion of non-DIS interactions in the dataset. (left) Errors on true energy <math>\nu_\mu</math> CC efficiency and (right) errors on true energy <math>\bar{\nu}_\mu</math> CC efficiency . . . . .</i>	110
6.27	<i>Log likelihood distributions for the four possible scenarios. (top left) <math>\mathcal{L}_1</math>, (top right) <math>\mathcal{L}_2</math>, (bottom left) <math>\mathcal{L}_3</math> and (bottom right) <math>\mathcal{L}_4</math> . . . . .</i>	112
6.28	<i>Comparison of signal efficiency (left) and <math>\nu_\mu</math> CC background (right) for analysis with cluster pdf only (black) and using the likelihood parameters of equations 6.15- 6.18. . . . .</i>	113
6.29	<i>Two dimensional likelihoods for the fraction of visible energy in the candidate and its number of clusters for (left) signal and (right) NC interactions. . . . .</i>	113
7.1	<i>Examples of fits to simulated data for the standard IDS neutrino factory with normal mass hierarchy (left) and with a fit using the incorrect mass hierarchy (right). . . . .</i>	119
7.2	<i>Sensitivity to <math>\theta_{13}</math> for true normal hierarchy (left) and true inverted hierarchy (right). . . . .</i>	120
7.3	<i>Sensitivity to <math>\delta_{CP}</math> for true normal hierarchy (left) and true inverted hierarchy (right). . . . .</i>	121
7.4	<i>Sensitivity to the true mass hierarchy for true normal hierarchy (left) and true inverted hierarchy (right). . . . .</i>	122

7.5	<i>Difference in expected fluxes at near and far sites: (top) <math>\nu_e</math> flux through a 1 m radius detector 100 m and 1 km from a 600 m decay straight (left) and at a 7 m radius detector 4000 km from the Neutrino factory; (bottom) <math>\nu_\mu</math> flux for the same detectors (using unpolarised muon expectation).</i> . . . . .	124
7.6	<i>Comparison of predicted to true flux through the ND for stored <math>\mu^+</math> (left) and stored <math>\mu^-</math> (right). (top) Actual spectra and (bottom) fractional residuals.</i> . . . . .	127
7.7	<i>Fits to simulated data using the near-far prediction (left) and compared to equivalent fits performed using the standard method (right). All fits assume normal hierarchy.</i> . . . . .	128
7.8	<i>Projection of the minimum <math>\chi^2</math> onto (left) the <math>\theta_{13}</math> axis and (right) the <math>\delta_{CP}</math> axis.</i>	128
7.9	<i>Quality of fit to <math>\theta_{13}</math> (left) and <math>\delta_{CP}</math> (right) for a range of values. Using the projection method (top) and the standard method (bottom).</i> . . . . .	129

# Chapter 1

## An introduction to neutrino physics

### 1.1 Discovery of the neutrino

Upon measuring the beta spectrum of various radioactive ions physicists were left with a dilemma. The observed continuous spectrum was inconsistent with the two body process expected. In order to solve the problem a third particle was required to take part in the decay. The proposal of a neutral particle of not more than 1% of the proton mass by Pauli [20] meant that the theory of conservation of energy could be saved, however, as no experimental discovery of such a particle had been made the proposal was tentative at best. The discovery of the neutron, which was, however, too massive to be the proposed particle, led one of Pauli's contemporaries, Enrico Fermi, to a more complete description of the beta decay as the decay of the neutron into a proton, electron and another spin 1/2 particle of very low mass which he re-named "neutrino":  $n \rightarrow p + e^- + \bar{\nu}_e$ . This decay would be mediated by the newly discovered weak interaction the strength of which could be understood via the coupling constant  $G_F$ .

The neutrino was finally discovered by the Savannah river reactor experiment in 1956 [21], more than twenty years later. The discovery was awarded with a Nobel prize.

#### 1.1.1 Parity violation and the standard model neutrino

In observing an asymmetry in the angular distribution of beta electrons from polarised cobalt-60 nuclei [22] the parity violating nature of the weak interaction was confirmed. However, the implications of this result for the understanding of the neutrino were not fully understood until the publication of another important result. By studying the polarisation of  $\gamma$ s emitted promptly by the daughter products of  $\beta^+$  and  $\beta^-$  isotopes *Golhaber et al.* concluded that neutrinos can only exist in the left handed chiral state where momentum and spin are op-

positely aligned and that antineutrinos exist only in the right handed state [23]. These two results led to the vector - axial vector theory of the weak interaction (V-A) in the standard model where without a right handed doublet the Yukawa couplings which give mass to the fermions leave the neutrino massless [24].

As will be demonstrated in the following sections and in chapter 2 the phenomenon of neutrino oscillations requires that at least one of the neutrinos have non-zero mass and as such physically significant discoveries of such processes require the extension of the model and strongly indicate the existence of new physics. The simplest way in which neutrino masses and mixing can be introduced to the standard model requires the introduction of  $m$  ‘sterile’ neutrinos which do not have any couplings in the existing standard model and results in a Lagrangian describing the  $W$  couplings of

$$\mathcal{L}_W = -\frac{g}{\sqrt{2}} \sum_{\substack{\alpha=e,\mu,\tau \\ i=1,2,3}} (\overline{\ell_{L\alpha}} \gamma^\lambda U_{\alpha i} \nu_{Li} W_\lambda^- + \overline{\nu_{Li}} \gamma^\lambda U_{\alpha i}^* \ell_{L\alpha} W_\lambda^+). \quad (1.1)$$

There is as yet no confirmed discovery of the existence of these sterile states though it is implied by all of the competing theoretical explanations of neutrino mass and mixing.

## 1.2 Neutrino mixing

Using data from the LEP accelerator studies of the  $Z^0$  resonance the number of neutrinos which take part in the weak interaction with a mass less than half the  $Z^0$  mass can be measured to be:  $2.92 \pm 0.05$  [25], independent of model. This number is consistent with the 3 weak eigenstates observed coupling to the  $W$  bosons in charged current interactions,  $\nu_e$ ,  $\nu_\mu$  and  $\nu_\tau$ . Considering these weak eigenstates  $\nu_\alpha$  as separate to the mass eigenstates  $\nu_i$  it can be seen that they must be related by a  $3 \times 3$  matrix as shown in equation 1.2. This matrix would be diagonal in the case that the weak eigenstates were the same as the corresponding mass state. In the minimal extension to the standard model required to allow a non-diagonal mixing matrix,  $U$  must be unitary and is generally parameterised as shown in equation 1.3 as the Pontecorvo-Maki-Nagawa-Sakata (PMNS) matrix [26, 27].

$$\begin{pmatrix} \nu_e \\ \nu_\mu \\ \nu_\tau \end{pmatrix} = U \begin{pmatrix} \nu_1 \\ \nu_2 \\ \nu_3 \end{pmatrix} \quad (1.2)$$

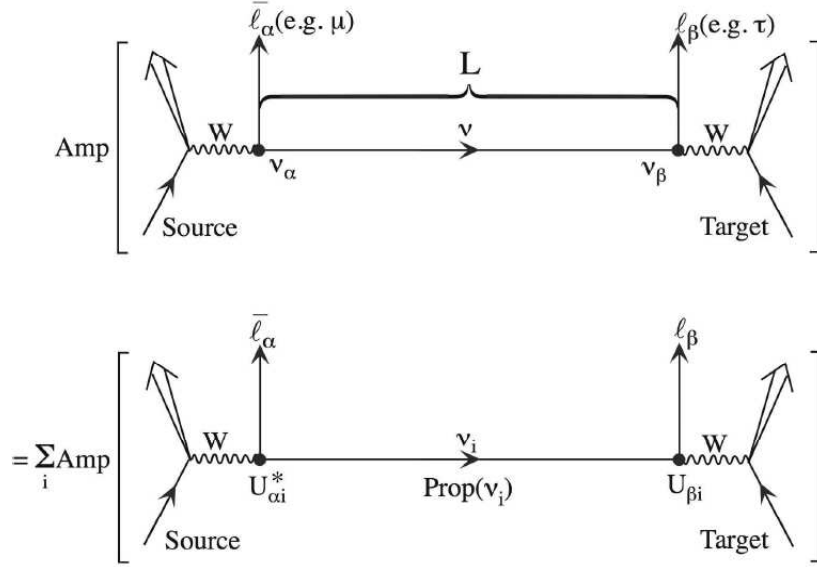
$$U_{PMNS} = \begin{pmatrix} c_{12} & s_{12} & 0 \\ -s_{12} & c_{12} & 0 \\ 0 & 0 & 1 \end{pmatrix} \begin{pmatrix} 1 & 0 & 0 \\ 0 & c_{23} & s_{23} \\ 0 & -s_{23} & c_{23} \end{pmatrix} \begin{pmatrix} c_{13} & 0 & s_{13}e^{i\delta_{CP}} \\ 0 & 1 & 0 \\ -s_{13}e^{-i\delta_{CP}} & 0 & c_{13} \end{pmatrix} \\
 \times \begin{pmatrix} 1 & 0 & 0 \\ 0 & e^{i\phi_2} & 0 \\ 0 & 0 & e^{i\phi_3} \end{pmatrix} \tag{1.3}$$

Here  $s_{ij} \equiv \sin \theta_{ij}$  and  $c_{ij} \equiv \cos \theta_{ij}$  with  $\theta_{ij}$  the three mixing angles and  $\delta_{CP}$ ,  $\phi_2$  and  $\phi_3$  complex phases – the parameters  $\phi_2$  and  $\phi_3$  only enter if neutrinos are their own antiparticles (see section 1.3).

### 1.2.1 Oscillations in Vacuum

It can be seen from equation 1.3 that any flavour eigenstate  $|\nu_\alpha\rangle$  can be considered as a linear combination of the mass eigenstates such that  $|\nu_\alpha\rangle = \sum_i U_{\alpha i} |\nu_i\rangle$  and conversely the mass eigenstate can be considered as  $|\nu_i\rangle = \sum_\alpha U_{\alpha i}^* |\nu_\alpha\rangle$ . This relation implies a non-zero probability that a neutrino created in the flavour state  $\nu_\alpha$  via  $W$  exchange with the charged lepton  $\bar{\ell}_\alpha$  can interact after propagating some distance  $L$  as the flavour eigenstate  $\nu_\beta$ . Since the neutrino will propagate in one of the mass states (as illustrated by Fig. 1.1) the amplitude of this process can be described by  $\text{Amp}(\nu_\alpha \rightarrow \nu_\beta) = \sum_i U_{\alpha i}^* e^{-im_i \tau_i} U_{\beta i}$  where  $\tau_i$  is the proper time in the neutrino rest frame. Considering Lorentz invariance and that the probability for such a process should be described by  $|\text{Amp}(\nu_\alpha \rightarrow \nu_\beta)|^2$ , where only the relative propagation phases of the mass states are physically significant, it can be shown (illustrated in equation 1.4 for the relative phase between the first two mass states  $\delta\phi(12)$ ) that the propagator for a mass state  $i$  can be written as  $\text{Prop}(\nu_i) = e^{-im_i^2 L/2E}$  and the probability of oscillation between two weak states is unambiguously described by equation 1.5.

$$\begin{aligned}
 \delta\phi(12) &= (E_2 t - p_2 L) - (E_1 t - p_1 L) \\
 &= (p_1 - p_2)L - (E_1 - E_2)t \\
 &\quad \text{and since } t = L/\bar{v} \text{ where } \bar{v} \equiv \frac{p_1 + p_2}{E_1 + E_2} \\
 \delta\phi(12) &\cong \frac{p_1^2 + p_2^2}{p_1 + p_2} L - \frac{E_1^2 - E_2^2}{p_1 + p_2} L \\
 &= (m_2^2 - m_1^2) \frac{L}{p_1 + p_2} \cong (m_2^2 - m_1^2) \frac{L}{2E}
 \end{aligned} \tag{1.4}$$


 Figure 1.1: *Neutrino oscillation in vacuum* (figure taken from [1]).

$$\begin{aligned}
 P(\nu_\alpha \rightarrow \nu_\beta) &= |Amp(\nu_\alpha \rightarrow \nu_\beta)|^2 \\
 &= \delta_{\alpha\beta} - 4 \sum_{i>j} \Re(U_{\alpha i}^* U_{\beta i} U_{\alpha j} U_{\beta j}^*) \sin^2 \left( \frac{\Delta m_{ij}^2 L}{2E} \right) \\
 &\quad + 2 \sum_{i>j} \Im(U_{\alpha i}^* U_{\beta i} U_{\alpha j} U_{\beta j}^*) \sin \left( \frac{\Delta m_{ij}^2 L}{2E} \right),
 \end{aligned} \tag{1.5}$$

where  $\Delta m_{ij}^2 = m_j^2 - m_i^2$ .

If conservation of the  $CPT$  symmetry is assumed it must be true that  $P(\bar{\nu}_\alpha \rightarrow \bar{\nu}_\beta) = P(\nu_\beta \rightarrow \nu_\alpha)$  which implies that the the same oscillation probability for  $CP$  partners must be equal except for the the mixing matrix being replaced by its complex conjugate,  $P(\bar{\nu}_\alpha \rightarrow \bar{\nu}_\beta; U) = P(\nu_\alpha \rightarrow \nu_\beta; U^*)$ . Therefore, a difference in the probabilities of oscillation for neutrinos and antineutrinos is possible if the mixing matrix is complex but only for oscillation between two differing weak states as  $CPT$  conservation implies that  $\Delta_{\alpha\beta} \equiv P(\nu_\alpha \rightarrow \nu_\beta) - P(\bar{\nu}_\alpha \rightarrow \bar{\nu}_\beta) = 0$  for  $\alpha = \beta$ . The distinct nature of the charged leptons which accompany a neutrino and antineutrino CC interaction mean that this difference is possible regardless of whether a neutrino is its own antiparticle [1].

If only the first two generations are considered, in analogy to the situation where the third mixing angle  $\theta_{13} = 0$ , it can be demonstrated that the mixing matrix is described by a rotation in space:

$$U_{2D} = \begin{pmatrix} \cos\theta & \sin\theta \\ -\sin\theta & \cos\theta \end{pmatrix}. \tag{1.6}$$

Considering the two weak states involved in such mixing as  $|\nu_e\rangle$  and  $|\nu_\mu\rangle$  the oscillation probabilities for appearance and disappearance are those described by equations 1.7 where oscillation for neutrinos and antineutrinos are exactly equivalent.

$$\begin{aligned} P(\nu_e \rightarrow \nu_\mu) &= P(\nu_\mu \rightarrow \nu_e) = \sin^2 2\theta \sin^2 \left( \frac{\Delta m_{ij}^2 L}{4E} \right) \\ P(\bar{\nu}_e \rightarrow \bar{\nu}_\mu) &= P(\bar{\nu}_\mu \rightarrow \bar{\nu}_e) = 1 - \sin^2 2\theta \sin^2 \left( \frac{\Delta m_{ij}^2 L}{4E} \right) \end{aligned} \quad (1.7)$$

It is known that there are three neutrino weak eigenstates which couple to the  $W$  boson, corresponding to  $\nu_e$ ,  $\nu_\mu$  and  $\nu_\tau$  and as such there are at least three neutrino states which must be considered in the extraction of oscillation probabilities. The full three flavour oscillation probabilities require some assumptions to be extracted. As can be seen from Fig. 1.2, the mass squared splitting corresponding to the solar parameters (see chapter 2 for evidence of neutrino oscillations),  $\Delta m_{sol}^2 = \Delta m_{12}^2$ , is significantly smaller than that which drives atmospheric oscillations,  $\Delta m_{atm}^2$  which describes either  $\Delta m_{23}^2$  or  $\Delta m_{13}^2$ . For an experiment chosen with an appropriate  $L/E$  the smaller mass splitting cannot be seen by the experiment and the oscillation probabilities can be approximated by those shown in equation 1.8 [1], assuming  $|\Delta m_{12}^2| \ll |\Delta m_{23}^2|$ , with neutrino and anti neutrino oscillation equivalent.

$$\begin{aligned} P(\nu_\alpha \rightarrow \nu_\beta) &\cong 4|U_{\alpha 3}U_{\beta 3}|^2 \sin^2 \left( \frac{\Delta m_{23}^2 L}{4E} \right) \\ P(\nu_\alpha \rightarrow \nu_\alpha) &\cong 1 - |U_{\alpha 3}|^2(1 - |U_{\alpha 3}|^2) \sin^2 \left( \frac{\Delta m_{23}^2 L}{4E} \right) \end{aligned} \quad (1.8)$$

However, in high intensity experiments the effect of the solar splitting cannot be ignored and a better approximation is achieved by expanding in the small parameters  $\theta_{13}$ ,  $\frac{\Delta_{12}}{\Delta_{13}}$  and  $\Delta_{12}L$  with  $\Delta_{ij} = \frac{\Delta m_{ij}^2}{2E}$  – shown in equation 1.9 [17] for the  $\nu_e \rightarrow \nu_\mu$  channel.

$$\begin{aligned} P(\nu_e \rightarrow \nu_\mu) &= s_{23}^2 \sin^2 2\theta_{13} \sin^2 \left( \frac{\Delta_{13}L}{2} \right) + c_{23}^2 \sin^2 2\theta_{12} \sin^2 \left( \frac{\Delta_{12}L}{2} \right) \\ &+ \tilde{J} \cos \left( +\delta_{CP} - \frac{\Delta_{13}L}{2} \right) \frac{\Delta_{12}L}{2} \sin \left( \frac{\Delta_{13}L}{2} \right) \\ &\text{with } \tilde{J} \equiv c_{13} \sin 2\theta_{12} \sin 2\theta_{23} \sin 2\theta_{13} \text{ the Jarlskog coefficient} \\ &\text{and } P(\bar{\nu}_e \rightarrow \bar{\nu}_\mu) \text{ equivalent but for the interchange } +\delta_{CP} \rightarrow -\delta_{CP}. \end{aligned} \quad (1.9)$$

## 1.2.2 Generalisation to Matter oscillations

In general, the path of any observed neutrino from its source will intersect some form of matter. For neutrinos described by the minimal extension to the standard model, interactions with matter cannot change the flavour of the neutrino and as such any observed flavour change in a beam implies neutrino mass and mixing. However, the cross-sections for interactions

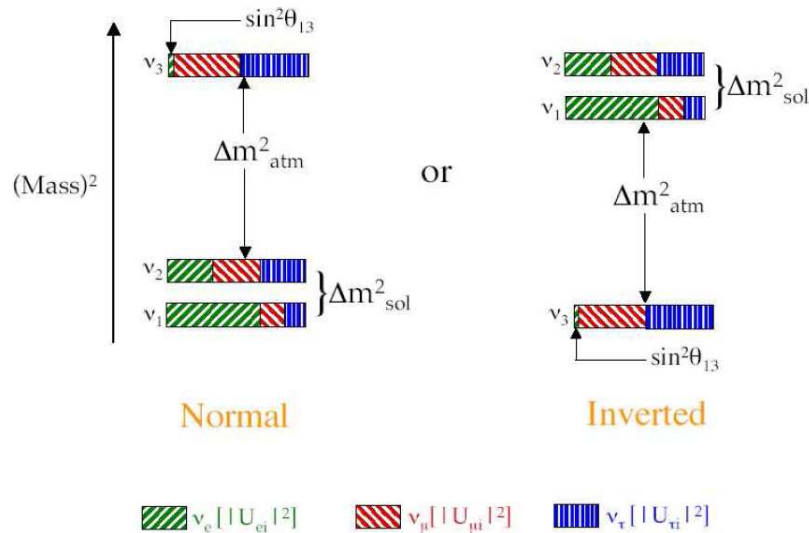


Figure 1.2: *The three neutrino (mass)<sup>2</sup> spectrum*(figure taken from [2]).

between neutrinos and matter differ for the different weak eigenstates and indeed between neutrinos and antineutrinos. One type of interaction of particular interest is coherent scattering from electrons which while not changing the beam content causes an augmentation of the mass splittings. This augmentation is known as the Mikheyev-Smirnov-Wolfenstein (MSW) effect [28, 29].

The passage of neutrinos through matter can be conveniently described using the Schrödinger equation  $i\frac{\partial}{\partial t}\Psi(t) = \mathcal{H}\Psi(t)$ , where  $\Psi(t)$  is the wavefunction and  $\mathcal{H}$  is the Hamiltonian. The Hamiltonian must contain terms concerned with the couplings of the different neutrinos to the  $W$  and  $Z$  bosons. The  $Z$  couplings for all species are equal and as such any change to the Hamiltonian will be proportional to the identity matrix. As described above, only relative phases affect oscillation probabilities and as such neutral current couplings will have no physical effect on the oscillation probabilities. However, as illustrated in Fig. 1.3  $\nu_e$  elastic (forward) scattering can also be mediated by  $W$  bosons while such a process is not possible for other species. This adds an interaction energy term  $V = \sqrt{2}G_F N_e$  to the  $\mathcal{H}_{\nu_e\nu_e}$  entry of the Hamiltonian and  $-V$  to the corresponding antineutrino entry. As such defining  $A \equiv V$  for neutrinos and  $A \equiv -V$  for antineutrinos the Hamiltonian can be shown in the scenario where the solar mass splitting can be neglected to be to be that shown in equation 1.10.

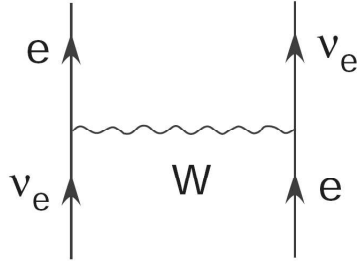


Figure 1.3: *The W exchange process which augments the mass splittings in matter* (taken from [1]).

$$\mathcal{H} = \frac{\Delta_M}{2} \begin{bmatrix} -\cos 2\theta_M & \sin 2\theta_M \\ \sin 2\theta_M & \cos 2\theta_M \end{bmatrix}$$

where:

$$\Delta_M \equiv \sqrt{\Delta_{23}^2 \sin^2 2\theta_{13} + (\Delta_{23} \cos 2\theta_{13} - A)^2} \quad (1.10)$$

and

$$\sin 2\theta_M \equiv \frac{\Delta_{23} \sin 2\theta_{13}}{\Delta_M}$$

where:

$$\Delta_{ij} = \frac{\Delta m_{ij}^2}{2E}.$$

The full analytical formulae for oscillations in matter were derived in [30]. However, in order to understand the physical implications of these relations it is easier to expand in the same small parameters as in the vacuum case plus the parameter  $\frac{\Delta_{12}}{A}$  to achieve equation 1.11 which was shown in [17] to be accurate to within 10% over the parameter space allowed by the current best fits to experimental data (see chapter 2 for more detail on experimental measurements).

$$\begin{aligned} P(\nu_e (\bar{\nu}_e) \rightarrow \nu_\mu (\bar{\nu}_\mu)) = & s_{23}^2 \sin^2 2\theta_{13} \left( \frac{\Delta_{13}}{\tilde{B}_\mp} \right)^2 \sin^2 \left( \frac{\tilde{B}_\mp L}{2} \right) \\ & + c_{23}^2 \sin^2 2\theta_{12} \left( \frac{\Delta_{12}}{A} \right)^2 \sin^2 \left( \frac{AL}{2} \right) \\ & + \tilde{J} \frac{\Delta_{12} \Delta_{13}}{A \tilde{B}_\mp} \sin \left( \frac{AL}{2} \right) \sin \left( \frac{\tilde{B}_\mp L}{2} \right) \cos \left( \pm \delta_{CP} - \frac{\Delta_{13} L}{2} \right) \end{aligned}$$

where:

$$\tilde{B}_\mp \equiv |A \mp \Delta_{13}|. \quad (1.11)$$

Equation 1.11 clearly shows that this oscillation channel is very sensitive to the  $CP$  phase and the  $\theta_{13}$  mixing angle. However, extraction of the value of  $\delta_{CP}$  is complicated by the fact

that even for  $\delta_{CP} = 0$  there remains a difference in the oscillation probabilities caused by matter effects. This ‘fake CP’ violation means that the use of an asymmetry parameter of the form

$$A_{e\mu}^{CP} = \frac{P(\nu_e \rightarrow \nu_\mu) - P(\bar{\nu}_e \rightarrow \bar{\nu}_\mu)}{P(\nu_e \rightarrow \nu_\mu) + P(\bar{\nu}_e \rightarrow \bar{\nu}_\mu)} \quad (1.12)$$

via the interaction spectra is not a viable method for the extraction of the CP phase as uncertainties in the matter parameter mean removal of this additional effect is less robust than considering the energy dependence of the signals [17, 31].

### 1.3 Neutrino Mass

As mentioned above a confirmed measurement of neutrino oscillations requires that at least one neutrino has non-zero mass and that the neutrino mass eigenstates are not degenerate. However, oscillations do not probe the absolute scale of neutrino masses nor indeed the nature of that mass.

There are several ways to directly measure the effective masses of the weak eigenstates, however, at the time of interaction it is not possible to know which of the mass states the neutrino is in and as such the accurate determination of the neutrino mixing parameters is necessary to extract the mass of the individual  $\nu_i$ . The present best bound on the  $\nu_e$  effective mass at  $m_{\nu_e} < 2$  eV comes from tritium decay experiments [25]. Using high resolution spectrometry and calorimetry of the beta electrons emitted from a tritium source it is possible to measure the deviation from the calculated  $m_\nu = 0$  spectrum endpoint which, as illustrated by Fig. 1.4, should be equal to the  $\nu_e$  effective mass. Tritium is chosen due to its low endpoint energy, low Z and short half-life which maximises statistics and the accuracy with which the  $m_\nu = 0$  spectrum can be calculated. Measures of the other weak state masses require more complex experiments which are often statistics limited and as such give looser bounds (for a more complete description of mass measurements see [3]). The KATRIN experiment [32] will begin data taking soon with sensitivity to  $m_{\nu_e}$  below 1 eV.

Determination of the mixing parameters, the mass hierarchy and a direct mass measurement of the  $\nu_e$  effective mass will allow a full understanding of the absolute scale of the neutrino mass states and their mixing, however, another important result remains. There exists the possibility that neutrinos are not Dirac fermions like the other leptons but Majorana particles. Majorana theorised that the neutrino could be a 2-component object [33] and hence be identical to its antiparticle. This implies that total lepton number is not always conserved in contrast to the minimal standard model extension where Dirac neutrino masses require that lepton number is a symmetry. The process of neutrinoless double beta decay ( $0\nu\beta\beta$ ) was first described in [34];  $0\nu\beta\beta$  essentially involves the  $\bar{\nu}_e$  from a standard  $\beta$  decay being

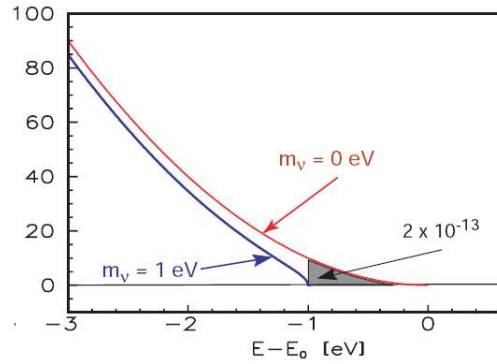


Figure 1.4: Tritium  $\beta$  decay spectrum endpoint showing deviation caused by a 1 eV  $\nu_e$  effective mass (taken from [3])

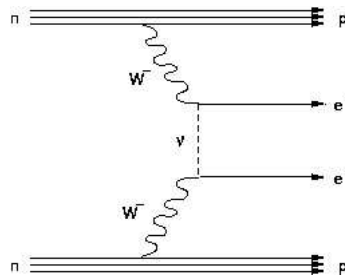


Figure 1.5: Feynman diagram for neutrinoless double beta decay.

absorbed immediately as a  $\nu_e$  by a neutron emitting a second electron (illustrated in Fig. 1.5). This process requires that neutrino and antineutrino be identical and as such any observation of  $0\nu\beta\beta$  would confirm that neutrinos are Majorana particles. If neutrinos are found to be Majorana particles their light masses can be explained via their interaction with massive right handed neutrinos via the mechanism known as the See-Saw model [35]. In this model the mass of these right handed partners is much larger than the electroweak symmetry breaking scale, with smaller active neutrino masses implying greater mass scales for the right handed neutrinos.

A number of neutrinoless double beta decay experiments are currently running or under construction. Using a variety of isotopes with measured standard double beta decay half-lives they seek to discover  $0\nu\beta\beta$  by observing an excess of events with energy equal to the Q-value of the interaction [36].

## 1.4 Neutrino Oscillation Phenomenology

The PMNS matrix itself gives no indication of the sizes of either the mixing angles or the mass splittings. However, a number of parameter groupings were formulated as possible explanations after the first experimental studies indicated a reduction in solar neutrino flux (see section 2.2.1). Due to the high electron density in the sun the correct description is highly sensitive to solar data. The method of the ‘iso-SNU’ (where SNU is a standard neutrino unit and 1 SNU is equivalent to  $10^{-36}$  captures/s/absorber nucleus) was used to define the regions allowed by the data; this involves the overlapping of contours of the combinations of  $\Delta m^2$  and  $\theta$  values which can describe the data from various experiments. Depending on the mass splittings and mixing angles chosen by nature the oscillation can be considered to happen entirely within the sun; the MSW solutions SMA and LMA (Small/Large Mixing Angle) describe this scenario with mass squared splittings  $\sim 10^{-5}$  and either small or large mixing angles. Two other types of solution exist: the long oscillation wave solution (LOW) which would have  $\Delta m^2 \sim 10^{-7}$  and large mixing angles and solutions which have  $\Delta m^2 \sim 10^{-11}$  and as such would not have a resonant transition in the sun but oscillate almost entirely in the vacuum (see Fig. 2.4). As will be described in chapter 2 current experimental evidence strongly favours the oscillation scenario where the mixing angles are large, the mass squared differences small and that matter enhancement takes place (the LMA-MSW model). However, there are still certain situations in which the complexity of the oscillation probabilities can be reduced allowing for a simplified analysis.

The optimisation of an oscillation experiment relies partly on the phenomenology of the oscillation channel which will be studied. Since the phase of the oscillation is proportional to  $L/E$ , in all cases the baseline distance for a particular experiment can be chosen to be at the point where maximum difference is expected from the zero oscillation hypothesis. The baselines of experiments can also be chosen to satisfy conditions where the matter effects are essentially zero or where one ‘part’ of a particular probability formula dominates. For example, the low energy of solar neutrinos means that oscillations can be effectively described by two flavour oscillations considering only the mass splitting  $\Delta m_{12}^2$  and first mixing angle  $\theta_{12}$ .

### 1.4.1 The Neutrino Factory golden channel

The oscillation probability  $P(\nu_e \rightarrow \nu_\mu)[P(\bar{\nu}_e \rightarrow \bar{\nu}_\mu)]$  shown in equation 1.11 can be considered to be made of three parts:  $P_{atm}$ ,  $P_{sol}$  and  $P_{int}$ , shown in 1.13 for units of  $[\Delta m^2] = \text{eV}^2$ ,

$[L] = \text{km}$  and  $[E_\nu] = \text{GeV}$ :

$$\begin{aligned}
 P_{atm} &= s_{23}^2 \sin^2 2\theta_{13} \left( \frac{\Delta_{13}}{B_\mp} \right)^2 \sin \left( 2.54 \tilde{B}_\mp L \right) \\
 P_{sol} &= c_{23}^2 \sin^2 2\theta_{12} \left( \frac{\Delta_{12}}{A} \right)^2 \sin^2 (2.54 AL) \\
 P_{int} &= \tilde{J} \frac{\Delta_{12}}{A} \frac{\Delta_{13}}{B_\mp} \sin (2.54 AL) \sin \left( 2.54 \tilde{B}_\mp L \right) \cos (\pm \delta_{CP} - 2.54 \Delta_{13} L)
 \end{aligned} \tag{1.13}$$

The relative experimental ease with which muons can be reconstructed in a charged current interaction along with its sensitivity to the remaining unknown parameters has identified this oscillation channel as key to future oscillation experiments [17, 31]. For  $\theta_{13} \geq 1^\circ$  the atmospheric and interference terms ( $P_{atm}$  and  $P_{int}$ ) dominate, however, in the case of a neutrino factory where spectral information is of interest (facility described in greater detail in chapter 3) the high luminosity beam means that, particularly for smaller values of  $\theta_{13}$ , the solar term cannot be ignored. There are, however, certain situations where a simplified treatment is possible.

For baselines shorter than  $\sim 3000$  km the matter effects have little impact on the oscillation probabilities and as such the more simple vacuum oscillation formula describes the channel well. While this effectively removes the ‘fake CP’ violation caused by the matter, this relationship simplifies further from equation 1.9 at very short distances resulting in a scenario where neutrinos and antineutrinos act similarly and the different contributions are very difficult to disentangle [17] meaning that simultaneous determination of  $\delta_{CP}$  and  $\theta_{13}$  may not be possible in this scenario.

Optimisation of the golden channel physics sensitivity has led to the definition of baseline distances for the neutrino factory in a number of scenarios. These have not only been derived to allow the detector to see the oscillation maximum but to allow the resolution of certain degenerate solutions that exist in the oscillation channel due to systematic effects.

#### 1.4.1.1 The intrinsic degeneracy

The intrinsic degeneracy describes the existence of some set of values  $(\theta_{13}, \delta_{CP})$  which give the same probability as the values chosen by nature  $(\bar{\theta}_{13}, \bar{\delta}_{CP})$  and was first described in [37]. Measuring only one polarity at one baseline without energy information leads to a continuous spectrum of possible solutions while the introduction of another polarity still leaves another solution as shown in Fig. 1.6. These two sets of solutions are not necessarily both CP conserving or violating and as such not excluding the fake solution could lead to a completely different conclusion about the leptonic sector than that chosen by nature. These solutions can be effectively excluded by using spectral information in fits to the observed signal and by the combination of more than one detector distance as the mirror solutions are strongly

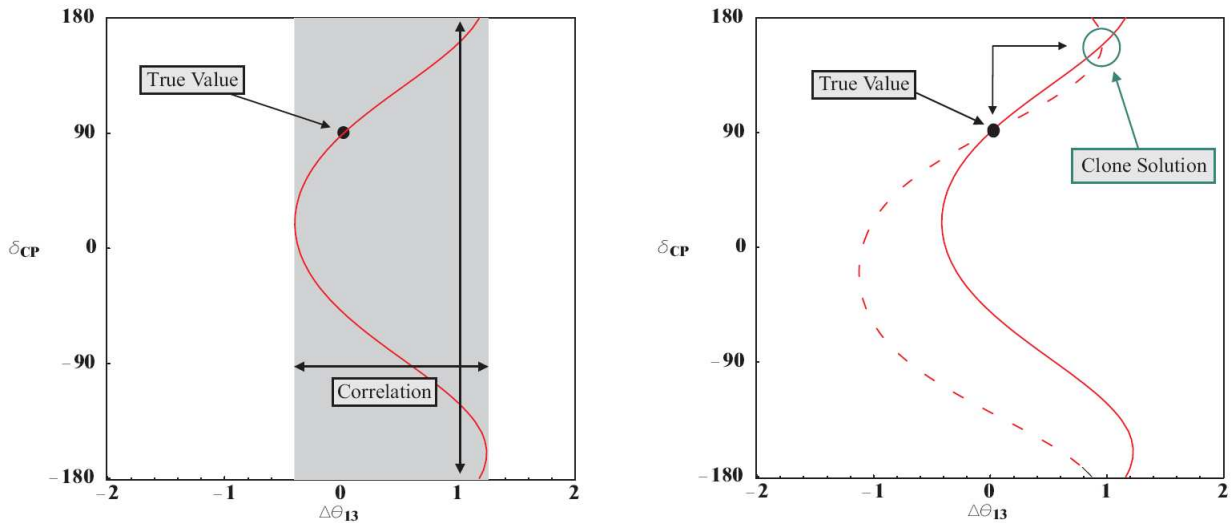


Figure 1.6: *Continuous spectrum of solutions for one polarity and baseline (left), Remaining intrinsic solutions using two polarities (right)* (taken from [4])

dependent on both energy and baseline. Alternatively, one could observe a complementary oscillation channel (both scenarios are illustrated in Fig. 1.7). Equation 1.14 demonstrates this dependency for the case of neutrinos:

$$\theta_{13} = -\frac{Y_+}{2X_+} \cos\left(\delta - \frac{\Delta_{13}L}{2}\right) \pm \left[ \left( \frac{Y_+}{2X_+} \cos\left(\delta - \frac{\Delta_{13}L}{2}\right) \right)^2 + \frac{1}{X_+} (P(\nu_e \rightarrow \nu_\mu)(\bar{\theta}_{13}, \bar{\delta}_{CP}) - P_{sol}) \right]^{\frac{1}{2}}, \quad (1.14)$$

with  $X_+$  and  $Y_+$  representing the parts of  $P_{atm}$  and  $P_{int}$  not dependent on the parameters  $\theta_{13}$  and  $\delta_{CP}$  respectively. The equivalent equal probability curve for antineutrinos is obtained by the interchange  $\delta_{CP} \rightarrow -\delta_{CP}$ ,  $X_+(Y_+) \rightarrow X_-(Y_-)$ .

#### 1.4.1.2 The $\Delta m_{13}^2$ sign degeneracy

If the sign of the large mass splitting is still undetermined in the era of the neutrino factory there is the possibility again of finding degenerate solutions for  $\theta_{13}$  and  $\delta_{CP}$  if the opposite sign to that chosen by nature is assumed in the analysis (as demonstrated in [38]). In order to avoid this ambiguity it is preferable to use a long baseline where matter effects are large enough that the neutrino and antineutrino probabilities are very different regardless of the value of  $\delta_{CP}$ . This scenario allows for the resolution of this degeneracy down to small values of  $\theta_{13}$ .

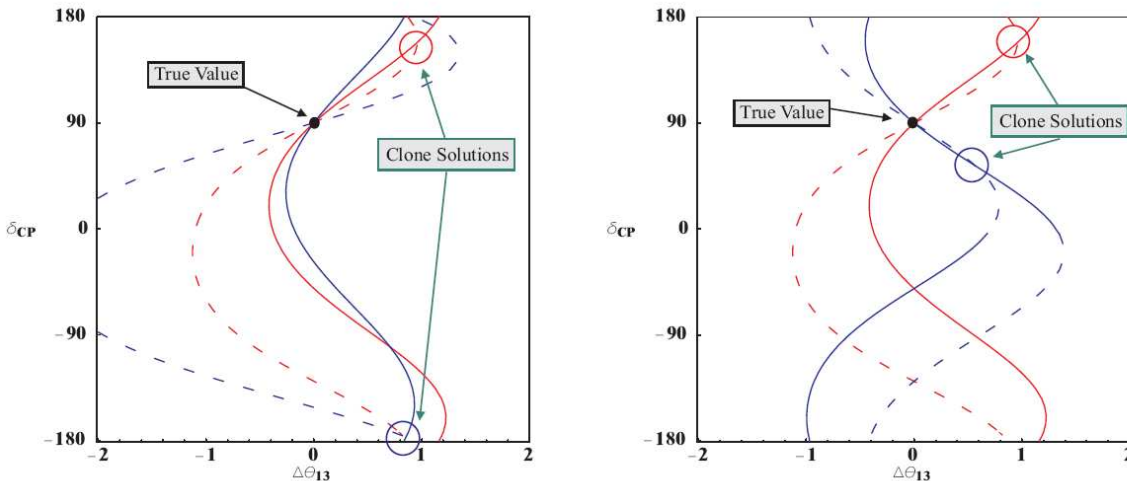


Figure 1.7: *Solving the degeneracy with multiple baselines (left) and with multiple channels (right) (taken from [4])*

### 1.4.1.3 The octant degeneracy

Current measurements have a best fit value for the large mixing angle at  $\theta_{23} = 45^\circ$  ( $\sin^2 2\theta_{23} > 0.92$ ). However, the error on this measurement allows the true value to lie in the region  $36.7^\circ < \theta_{23} < 53.2^\circ$ . Assuming the wrong octant for the mixing angle (the exchange  $\theta_{23} \rightarrow \pi - \theta_{23}$ ) can again lead to degenerate solutions to the probability. Resolution of this ambiguity is aided by the use of two different baselines and by spectral information. However, even if  $\theta_{23}$  is very well measured by disappearance measurements there remains certain scenarios where this ambiguity cannot be completely resolved. Measurement of the  $\nu_e \rightarrow \nu_\tau$  channel could aid this resolution but high efficiency detection of  $\nu_\tau$  interactions is very difficult.

### 1.4.1.4 The magic baseline

The currently favoured experimental scenario involves one of the two experimental detectors being placed at a very distant site to correspond to a baseline of  $\sim 7500$  km, known as the magic baseline. This baseline has been identified as particularly useful in breaking the degeneracies mentioned above [39]. At this distance the terms  $P_{sol}$  and  $P_{int}$  effectively cancel leaving only the atmospheric term. As such at this distance the probability is only dependent on  $\theta_{13}$  and the parameters which have already been measured and the effects of  $\theta_{13}$  and the true mass hierarchy cannot be cancelled by competing terms in the other parts of the oscillation probability. The exact position of maximum “magicness” depends purely on the matter density profile, the error on the knowledge which is as yet unclear, but the improvement in

degeneracy resolution is present for detector baselines within a few hundred kilometres of the optimum position.

## 1.5 Conclusion

The theory of neutrino oscillations has been presented, with discussion of the effect of passage through matter. Additionally, the current theoretical understanding of the nature and size of the neutrino masses has been discussed with the implications for the extension of the standard model mentioned. Through a combination of experiments with intense neutrino beams using detectors at multiple baselines the oscillation sector can be understood fully and without ambiguity. Armed with this understanding, the neutrino sector can be resolved fully with additional measurements of absolute mass and neutrinoless double beta decay.

# Chapter 2

## Neutrino oscillation experimental status

### 2.1 Introduction

Since the discovery of the solar neutrino deficit many experiments using solar, atmospheric and man-made neutrinos as sources have probed the possibility and attempted to measure the parameters of neutrino oscillations. Observation of the flux of  $\nu_e$  expected from the sun using nuclear conversion first indicated the possibility that neutrino oscillation could be a physical process with further confirmation of the observed deficit coming from real time observations of the same source. These results led to the use of atmospheric neutrinos to confirm oscillations for  $\nu_\mu$ , a variety of experiments using antineutrinos created in nuclear reactors and by bombarding targets with accelerator beams to create intense beams, all of which enriched the field further.

### 2.2 Experiments using natural sources of neutrinos

The current best measurements and global accepted values rely heavily on the disappearance measurements of  $\nu_e$  from the sun and  $\nu_\mu$  from the decay of charged pions created by high energy interactions in the atmosphere.

#### 2.2.1 Solar Neutrinos

The Standard Solar Model (SSM) [40] is an extremely successful theory describing the sun as a giant fusion reactor. Fusion of hydrogen and other low Z elements is carried out predominantly via the processes summarised by Fig. 2.2, which produce sufficient photon pressure to maintain hydrostatic balance in the sun and emit an electromagnetic spectrum consistent with that observed. Observation of  $\nu_e$  from the sun offers one of only two methods of

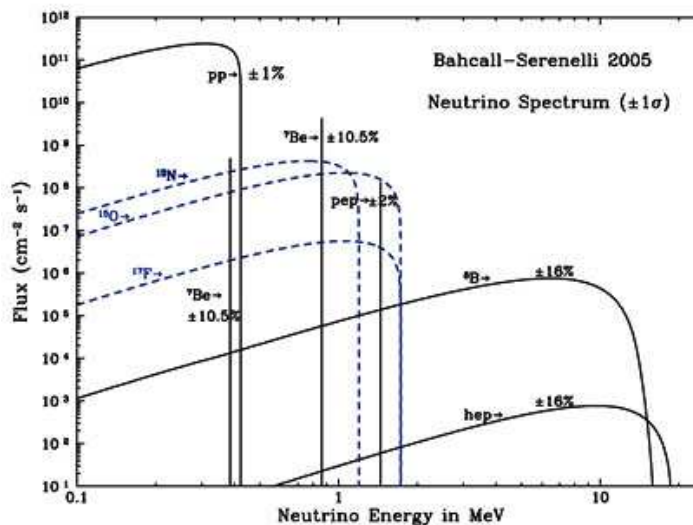
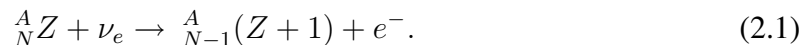


Figure 2.1: *Expected solar neutrino spectra* (taken from [5]).

studying the solar core, the other being helioseismology. The processes predicted to take place in the core of the sun by the SSM indicate the spectrum of neutrinos expected (shown in 2.1), with the observed luminosity allowing for a theoretical prediction of the neutrino abundances. As can be seen in Figures 2.1 and 2.2 a number of different processes contribute to the solar neutrino flux. The  $pp$  cycle is responsible for  $\sim 99.6\%$  of the flux below 0.4 MeV where the contribution of this process ends. Other important processes which have been studied by experiments are those from the  ${}^8B$  process which provides neutrinos with an energy spectrum from sub-MeV energies up to a few 10s of MeVs and the monoenergetic  ${}^7Be$  neutrinos which contribute  $\sim 10\%$  of the flux at an energy of  $\sim 0.9$  MeV.

There have been essentially two types of detector used to observe the solar neutrino flux. Early experiments were of radiochemical type relying on the reaction



The nucleus is chosen so that an unstable daughter nucleus is produced by the  $\nu_e$  capture whose decay can be detected at a later date. Solar neutrinos were first detected by the Homestake experiment [41], *data taken from 1970-1992*, which used 615 tons of common cleaning fluid  $C_2Cl_4$  (tetrachloral ethene) in a radiochemical experiment utilising the reaction:



Each data run lasted 2 months after which the argon atoms could be removed chemically and counted. Data taking continued over 30 years with a final flux calculated to be  $\sim 1/3$  of that predicted by SSM.

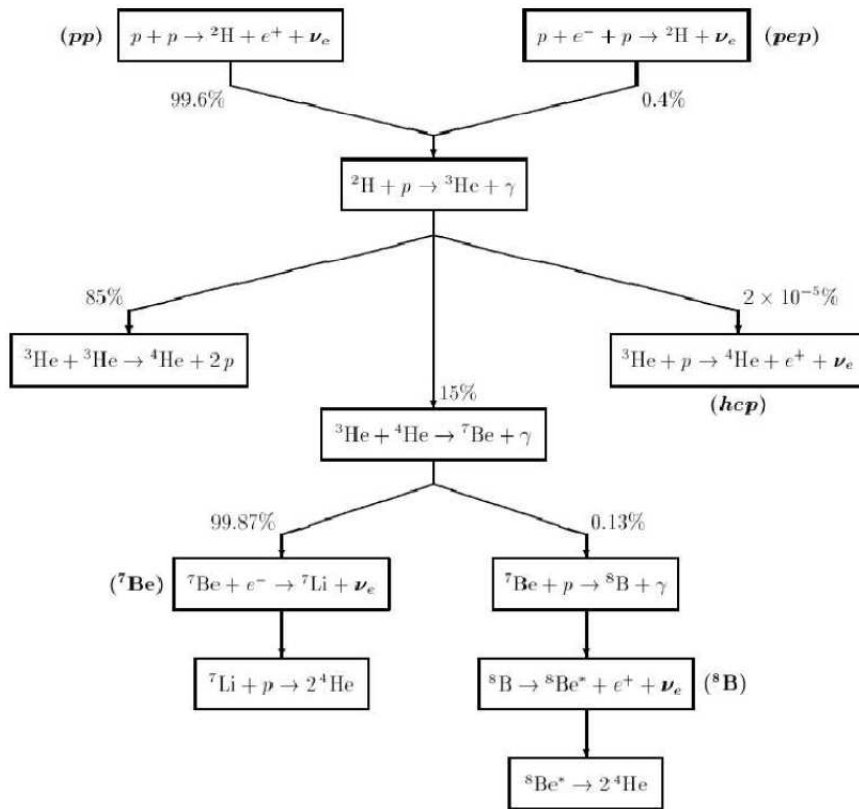


Figure 2.2: Solar PP cycle reaction chain with branching fractions

A further two experiments using the radiochemical approach were built both using the reaction  $\nu_e + {}^{71}\text{Ga} \rightarrow e^- + {}^{71}\text{Ge}$  which has a lower energy threshold and as such allows detection of a greater part of the pp spectrum. The SAGE [42] experiment, 1988-2000, analysed 92 runs over a period of 12 years and reported  $70.8_{-5.2}^{+5.3}(\text{stat})_{-3.2}^{+3.7}(\text{sys})$  SNU where 1 SNU =  $10^{-36}$  captures/s/absorber nucleus. GALLEX [43], 1991-1997, reported  $77.5 \pm 6.2(\text{stat})_{-4.7}^{+4.3}(\text{sys})$  SNU after six years of operation and 65 gallium extractions. Both results should be compared with the SSM prediction of  $128_{-7}^{+9}$  SNU. While one of the possible explanations of this deficit is neutrino oscillations, the lack of any real time or directional information meant that the source of the detected neutrinos was unclear. Moreover, without a measure of the absolute neutrino flux other possible interpretations including neutrino decay and decoherence exist.

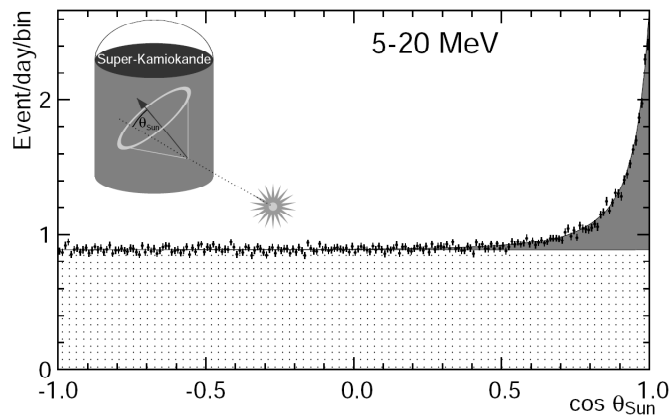
The next generation of experiments were required to remove these ambiguities. Large scale water and heavy water Cherenkov detectors instrumented with photo-detectors were selected as a viable technology due primarily to the possibility to take advantage of the highly directional electron-neutrino elastic scattering interaction  $\nu_e + e^- \rightarrow \nu_e + e^-$  which has an energy threshold of  $\sim 5$  MeV and as such would be sensitive predominantly to  ${}^8\text{B}$  neutrinos (see Fig. 2.1). During the early 1990s the Kamiokande and Super-Kamiokande (SK) water Cherenkov detectors [6] took data using this interaction. The SK detector is a 50 ktonne cylindrical ultra-pure water Cherenkov detector instrumented with 1885 8-inch Photomultiplier tubes (PMTs) on its inner edge and 11146 20-inch PMTs around its 22.5 ktonne fiducial volume. The detected Cherenkov light allows for unprecedented directional resolution as well as energy measurement. A data taking run of 1496 days observing the electron scattering of  $\nu_e$  reconstructed a clear angular correlation of neutrino direction with the sun's position, illustrated in Fig. 2.3. This data run measured interactions of  $\nu_e$  consistent with a flux of  $2.35 \pm 0.02 \pm 0.08 \times 10^6 \text{ cm}^{-2} \text{ s}^{-1}$  which is  $\sim 0.46$  of the flux predicted by the SSM.

The Sudbury Neutrino Observatory (SNO) [44], 1999-2006, used a 1000 tonne target mass of heavy water ( $D_2O$ ) enabling the observation of both CC and NC interactions via the processes described in equation 2.3.

$$\begin{aligned}
 \text{Elastic Scattering (ES)} \quad & \nu_e + e^- \rightarrow \nu_e + e^- \\
 \text{Charge Current (CC)} \quad & \nu_e + d \rightarrow e^- + p + p \\
 \text{Neutral Current (NC)} \quad & \nu_x + d \rightarrow \nu_x + p + n
 \end{aligned} \tag{2.3}$$

where  $\nu_x$  denotes any active neutrino type.

Since the NC cross section is equal for all active neutrino species, such sensitivity enables a measurement of the absolute flux of active neutrinos from the sun. Elastic scattering measurements utilised Cherenkov light as in SK. The charged current interactions of  $\nu_e$  are characterised by the Cherenkov light from an electron and scintillation light from two recoil


 Figure 2.3: *SuperKamiokande solar angle correlation* (from [6])

Interaction	Flux ( $\times 10^6 \text{cm}^2 \text{s}^{-1}$ )
Elastic Scattering	$2.35^{+0.22}_{-0.22}(\text{stat})^{+0.15}_{-0.15}(\text{sys})$
Charged Current	$1.60^{+0.06}_{-0.06}(\text{stat})^{+0.08}_{-0.09}(\text{sys})$
Neutral Current	$4.94^{+0.21}_{-0.21}(\text{stat})^{+0.38}_{-0.34}(\text{sys})$
SSM predicted ${}^8B$	5.69 or 4.51 (depending on metallicity model [40])

 Table 2.1: *Calculated neutrino fluxes from the SNO salt phase and SSM predicted  ${}^8B$  flux.*

protons. NC interactions provoke the dissociation of the deuterium nucleus into a neutron and proton. Such a reaction can be detected by the delayed decay photons emitted when the neutron is captured by a deuterium nucleus in the absence of an electron-like Cherenkov ring. Detection efficiency of neutral currents was significantly improved in the second data run by the addition of 2 tonnes of NaCl due to the larger neutron capture cross-section of the chlorine nucleus.

The NC measurements yielded a calculated flux consistent with that predicted by the SSM, while the CC interactions  $\sim 1/3$  of that expected (results summarised in table 2.1) which is consistent with the observations of SK. The combination of all solar neutrino experimental results up to and including SNO proves a powerful dataset in the determination of the correct model interpretation of oscillations. As can be seen from Fig. 2.4 the SNO and SK data are particularly influential in the fit which strongly favours the LMA-MSW solution. However, particularly when the possibility of sterile neutrinos is included [45], the interpretation becomes somewhat analysis dependent. It is clear that the conclusions of these combined fits would be strengthened by data at lower energies, particularly in the region of 1 MeV where oscillations in several solar scenarios should be peaked.

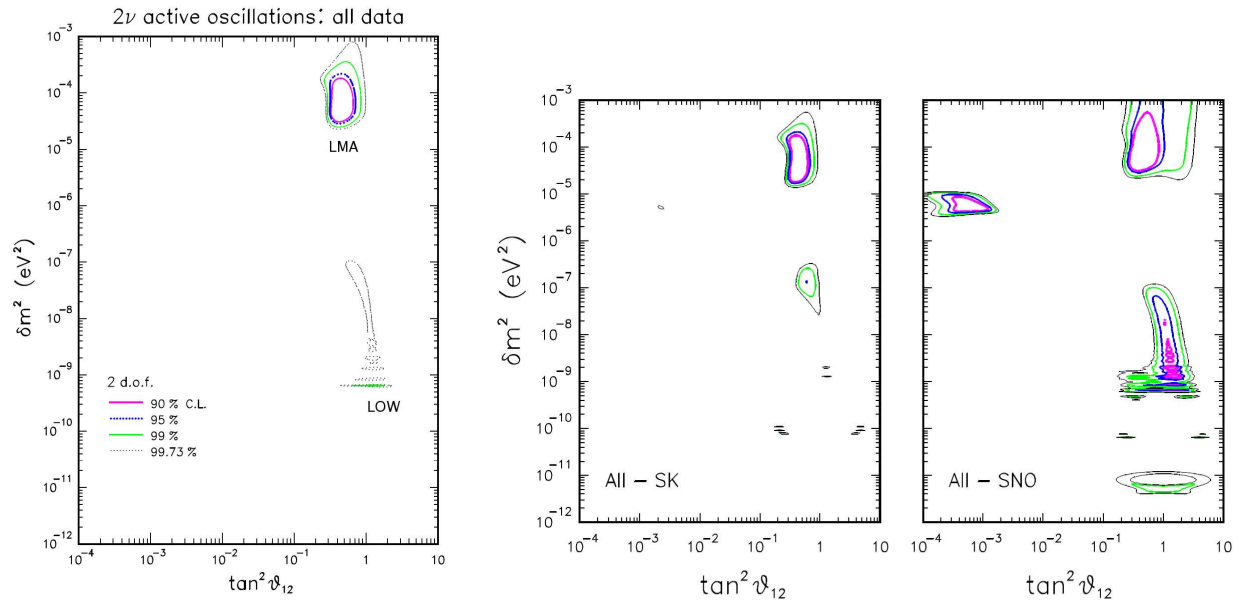


Figure 2.4: *Global fits to solar neutrino data post SNO. (left) All data. (right) Influence of SNO and SK data. (taken from [7])*

Sensitivity to lower energy neutrinos, particularly from the monoenergetic  ${}^7\text{Be}$  process was achieved recently by the Borexino experiment [46], *2007-present*. The high level of radio-purity required to efficiently suppress background processes has been achieved using an active target of pseudocumene (PC, 1,2,4-trimethylbenzene) doped with scintillators and surrounded by two active buffer zones which are separated using nylon and encased in steel. Scintillation light from interactions is detected in PMTs on the detector inner edge. The whole detector is then submerged in an ultra-pure water tank instrumented to detect the Cherenkov light from cosmic muons. The first data run has reported a  ${}^7\text{Be}$  neutrino rate of  $49 \pm 3_{\text{stat}} \pm 4_{\text{syst}}$  counts/(day·100 ton) which is in very good agreement with the LMA-MSW oscillation prediction of  $48 \pm 4$  counts/(day·100 ton).

## 2.2.2 Atmospheric Neutrinos

Neutrinos created by the decay of charged pions and muons from high energy collisions in the upper atmosphere are termed atmospheric neutrinos. An approximately uniform distribution of sources across the atmosphere is expected due to the extra-solar origin of the primary particles. As such, any atmospheric neutrino observatory has essentially two baselines; observing neutrinos from above and those which have traversed the earth's interior. The SK detector has observed the disappearance of atmospheric  $\nu_\mu$  by looking for the distinctive single clear ring of Cherenkov light produced by a muon created via quasi-elastic interactions.

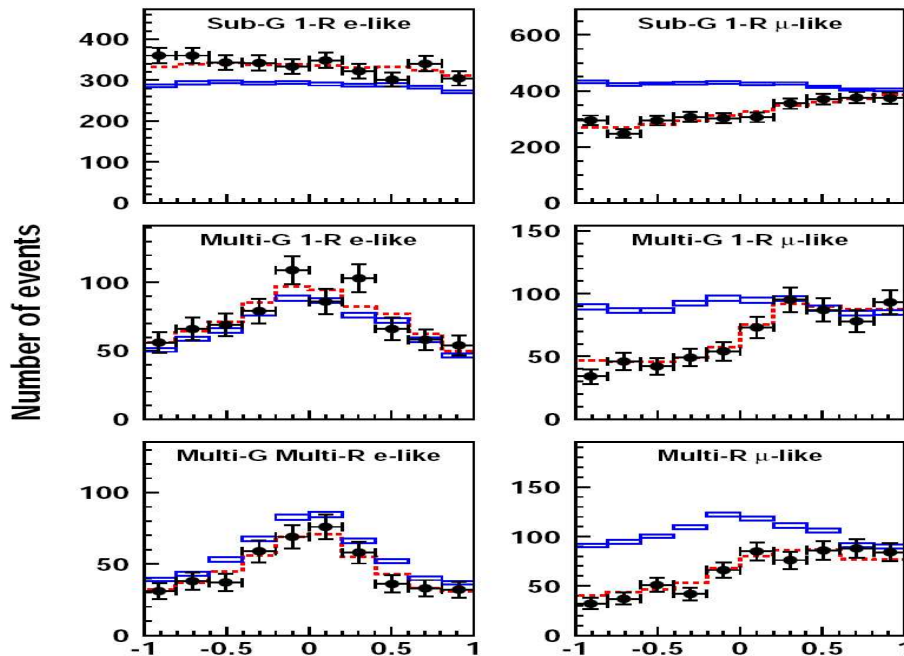


Figure 2.5: Zenith angle distributions for fully contained events with Monte Carlo zero oscillation prediction (blue) and data points (black circles), (left) electron-like, (right) muon-like in the Super-Kamiokande detector (taken from [8]).

The angular information available in SK means that in addition to the ratio of upwards to downwards going events, which is already an effective measure of the oscillation signal, the zenith angle dependence of the disappearance signal can be measured enabling measurement of oscillations with multiple L/E. The zenith angle distributions for events fully contained within the fiducial volume are shown in Fig. 2.5. Muon data shows a clear departure from the no oscillation expectation indicating disappearance whereas the electron data shows no spectral distortion.

A three flavour oscillation analysis of the the SK-I data set [8] finds best fit values for the large mass splitting and mixing angles at  $|\Delta m^2| = 2.5 \times 10^{-3} \text{ eV}^2$ ,  $\sin^2 \theta_{23} = 0.5$  and  $\sin^2 \theta_{13} = 0.0$  assuming that the large splitting dominates ( $|\Delta m_{12}^2| \ll |\Delta m_{23}^2|$ ). The allowed regions for  $\theta_{13}$  are consistent with the bound from Chooz (see section 2.3) for both the normal and inverted mass hierarchy scenarios (see Fig. 2.6 for confidence level plots).

A number of other atmospheric experiments were performed including the Soudan-2 [47], 1989-2001, and MACRO [48], 1989-2000, experiments. These experiments reported results consistent with those of Super-Kamiokande. For a review of atmospheric experiments see [24].

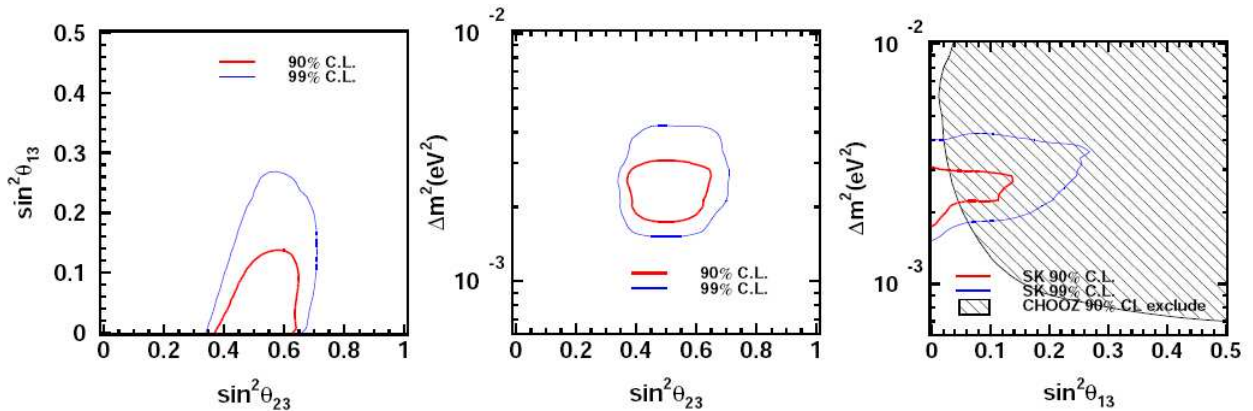


Figure 2.6: *Contours of three family oscillation analysis of SK data* (taken from [8]).

## 2.3 Reactor experiments

Reactor based oscillation experiments measure the disappearance of  $\bar{\nu}_e$  from beta decays in nuclear reactors. The range in energies available, high flux and well understood beam made this type of experiment unique up until the advent of Borexino in their ability to probe both mass splittings. In addition, as they can look for the same oscillation signal as solar neutrino experiments but in the anti-neutrino sector they act as a terrestrial check of the oscillation scenario. While there is an abundance of reactor neutrino experiments either proposed or under construction, including the Daya Bay and Double Chooz experiments, the main contributions in this sector have been from the experiments KamLAND and Chooz.

The KamLAND experiment [9], 2002-2007, constitutes a 1.2 ton ultra-pure liquid scintillator filled balloon 2700 metres-water-equivalent underground. It receives flux from various reactors in both Japan and South Korea resulting in a mean baseline of  $\sim 180$  km. High efficiency detection of the inverse beta decay interaction:  $\bar{\nu}_e + p \rightarrow e^+ + n$  is afforded via the characteristic correlated prompt scintillation light from positron annihilation with delayed light from neutron capture on hydrogen. The most recent high statistics run rejects the no oscillation hypothesis to  $>5\sigma$  as can be seen from Fig. 2.7. This data has stringently constrained the solar oscillation parameters (Fig. 2.7) to the level of excluding all scenarios save the LMA-I solution to  $>4\sigma$ . Incorporation of the results of SNO and solar flux experiments yields the best fit results for  $\theta_{12}$  and  $\Delta m_{21}^2$  to:  $\Delta m_{21}^2 = 7.59_{-0.21}^{+0.21} \times 10^{-5}$  eV<sup>2</sup> and  $\tan^2 \theta_{12} = 0.47_{-0.05}^{+0.06}$ .

The Chooz experiment [49], 1996-1998, took place in the Ardennes region of France. Neutrino spectra from two reactors with a combined thermal power of 8.5 GW<sub>th</sub> were used to detect inverse beta decay in the gadolinium loaded scintillator detector positioned at 1 km average distance from the neutrino source. The gadolinium was used due to the larger cross-

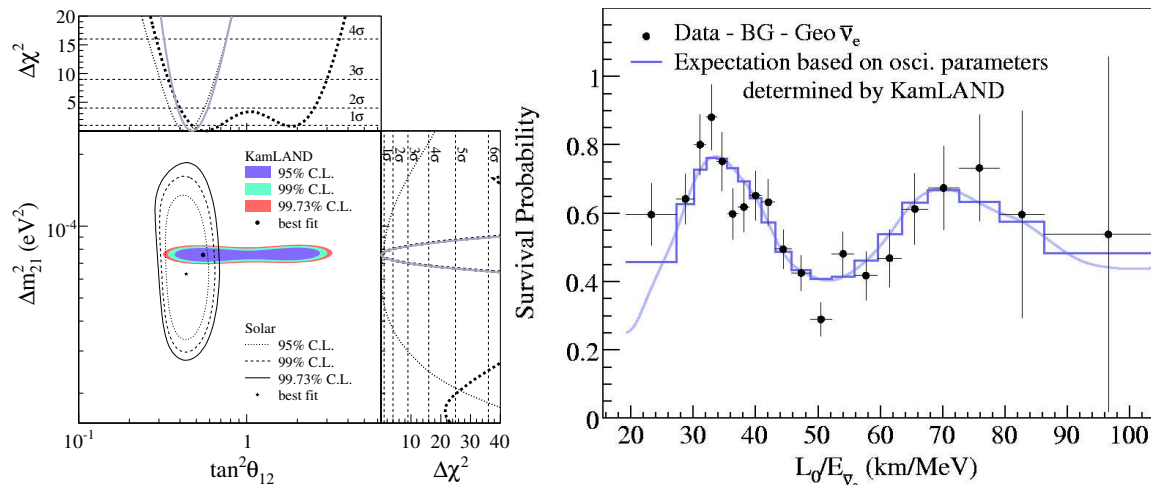


Figure 2.7: *KamLAND* results showing the allowed parameter region and comparison to solar neutrino data (left) and the oscillatory form of  $L/E$  data for the ratio of observed to no oscillation prediction (taken from [9]).

section for neutron capture on this isotope. Chooz did not detect any distortion in the expected  $\bar{\nu}_e$  spectrum over this distance and as such excluded to 90% confidence  $\sin^2 2\theta_{13} > 0.18$  in the oscillation scenario with  $\Delta m_{32}^2 > 0.9 \times 10^{-3}$ . This result constitutes the current best limit on the third mixing angle.

## 2.4 Accelerator experiments

Experiments using neutrino beams created as secondary or tertiary decay products from proton beam bombardment of a target have the advantage that the energy of the neutrino beam can be optimised for a suitable baseline as well as affording the possibility to repeat the same experiment with both neutrinos and antineutrinos. A number of experiments have operated with what are termed ‘conventional’ beams with the next generation of oscillation experiments set to be dominated by so called ‘superbeams’. In addition, there are proposals for a third generation of accelerator facilities which would be able to create intense well understood neutrino beams.

### 2.4.1 Conventional and Super beams

Standard accelerator based techniques rely on the production of muon type neutrinos from the decay of charged pions. The neutrino beam is produced by directing a proton beam onto a target optimised for charged pion production, capturing a specific charge using magnetic devices and then allowing the captured species to decay in the process  $\pi^{+(-)} \rightarrow \mu^{+(-)} + \nu_\mu(\bar{\nu}_\mu)$

with the main practical difference between a conventional and superbeam being increased power on target. However, bombardment of a nuclear target creates, in addition to pions, other charged mesons with decay modes containing neutrinos in amounts which are not easily calculated. These additional processes along with non zero probability of opposite charge pion capture and of prompt muon decay lead to some pollution of the desired  $\nu_\mu$  ( $\bar{\nu}_\mu$ ) beam with  $\bar{\nu}_\mu$  ( $\nu_\mu$ ),  $\nu_e$  and  $\bar{\nu}_e$  as well as distorting the expected spectrum. Two main techniques have and will be used to reduce the systematic uncertainties associated with these processes. Dedicated hadron production experiments like HARP [50] and NA61 [51] study in detail the production cross-sections of particular mesons while actual neutrino oscillation experiments employ near detectors. A detector placed close to the neutrino source and generally constructed at least partly of the same technology used for the main signal detector can be used to measure the initial flux of each neutrino type. Extrapolation of this measurement to the far site allows for the formation of the data/no-oscillation ratio and thus a measurement of  $\nu_\mu$  ( $\bar{\nu}_\mu$ ) disappearance oscillation. Accelerator experiments generally serve as an independent measure of the same parameters as atmospheric experiments, however, with an appropriate far detector and low beam systematic on the initial  $\nu_e$  ( $\bar{\nu}_e$ ) content of the beam, observation of appearance  $\nu_e$  at the far site would allow measurement of  $\theta_{13}$ .

K2K [10], *1999-2004*, was a conventional accelerator neutrino experiment which used the observed disappearance of  $\nu_\mu$  ( $\bar{\nu}_\mu$ ) created by 12 GeV protons at the KEK synchrotron after traversing the 250 km distance to the SuperKamiokande detector to measure oscillation parameters. Taking into account the full data taking run of 5 years K2K excluded the no oscillation scenario to  $4.3\sigma$  and measured the atmospheric parameters as shown in Fig. 2.8 with best fit points at  $\sin^2 2\theta_{23} = 1$  and  $|\Delta m_{23}^2| = 2.75 \times 10^{-3} \text{ eV}^2$ .

The MINOS experiment [52], *2005-present*, observed  $\nu_\mu$  ( $\bar{\nu}_\mu$ ) in a large magnetised steel and scintillator calorimeter situated in the Soudan Underground laboratory 735 km from the neutrino source at the NuMI beam line in Fermi National Laboratory. The neutrino beam spectrum ranged in energy between 1 GeV-30 GeV with the focusing horn currents tuned to select a peak energy of 3 GeV. Using the spectrum detected in the near detector situated 1 km from the production target it was possible to make a prediction of the expected non-oscillation spectrum at the far detector. A data run of 292 days yielded the measurements of the atmospheric parameters of  $|\Delta m_{23}^2| = 2.74_{-0.26}^{+0.44} \times 10^{-3} \text{ eV}^2$  and  $\sin^2 \theta_{23} > 0.87$ . While such a detector is not optimised for the detection of electrons some efficiency can be achieved. MINOS has begun data taking to perform an analysis of electron neutrino appearance with initial results showing 35 electron-like events from an expectation of  $27 \pm 5(\text{stat.}) \pm 2(\text{syst.})$  [53]. Results of an anti-neutrino run involving  $1.71 \times 10^{20}$  protons on target yield best fit values for the mass squared difference and mixing angle

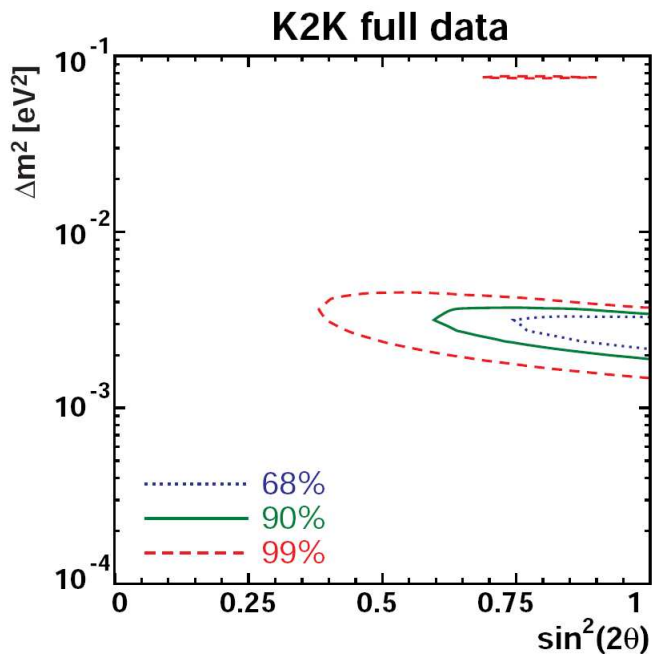


Figure 2.8: *K2K measurement of atmospheric oscillation parameters* (taken from [10]).

of a 2 flavour hypothesis of  $\Delta m^2 = (3.36_{-0.40}^{+0.45}(stat.) \pm 0.06(syst.)) \times 10^{-3} \text{ eV}^2$  and  $\sin^2 2\theta = 0.86 \pm 0.11(stat.) \pm 0.01(syst.)$  [11] which are inconsistent with the measurements made in the MINOS neutrino data run at 68% CL (see Fig. 2.9). Further data taking and a full three flavour analysis will confirm if this potentially important result is significant. Another important result came from the LSND experiment which used low energy  $\bar{\nu}_\mu$  ( $20 < E < 60 \text{ MeV}$ ) from  $\mu^+$  decay at rest to search for  $\bar{\nu}_e$  appearance via the same signal channel used by reactor experiments. They reported an excess consistent with a mass splitting  $\Delta m^2 \sim 1 \text{ eV}^2$  [54]. This result was then followed by a search for  $\nu_e$  appearance in a  $\nu_\mu$  beam ( $60 < E < 200 \text{ MeV}$ ) which yielded a result consistent with the antineutrino observation [55]. This result was inconsistent with the three flavour oscillation results from all other experiments and has been interpreted via two flavour oscillation to a sterile neutrino. In order to test this prediction another experiment MINIBoONE [12] was designed with a similar L/E to LSND. The first data run with neutrinos excluded the LSND result to 98% confidence level but detected an excess of  $\nu_e$  at low energy (see Fig. 2.10). Recently presented antineutrino analysis results indicate a  $2.5\sigma$  excess consistent with the LSND result [56].

The T2K experiment [57] recently commissioned its beam. It will search for the appearance of electron neutrinos in a predominantly muon type beam at SK after the beam has traversed 295 km from the new JPARC facility in Tokai. With a design proton beam on target power of 0.75 MW, T2K is considered the first superbeam. In addition, by using

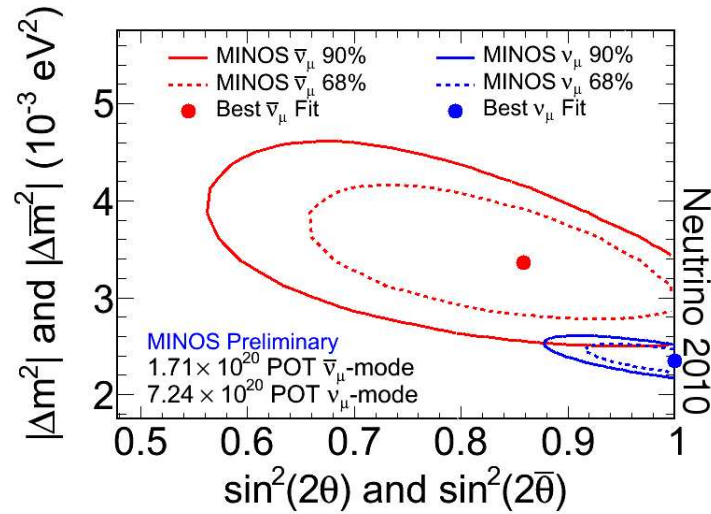


Figure 2.9: Confidence Interval contours in the fit of the MINOS Far Detector antineutrino data (red) to the hypothesis of two-flavor oscillations (taken from [11]).

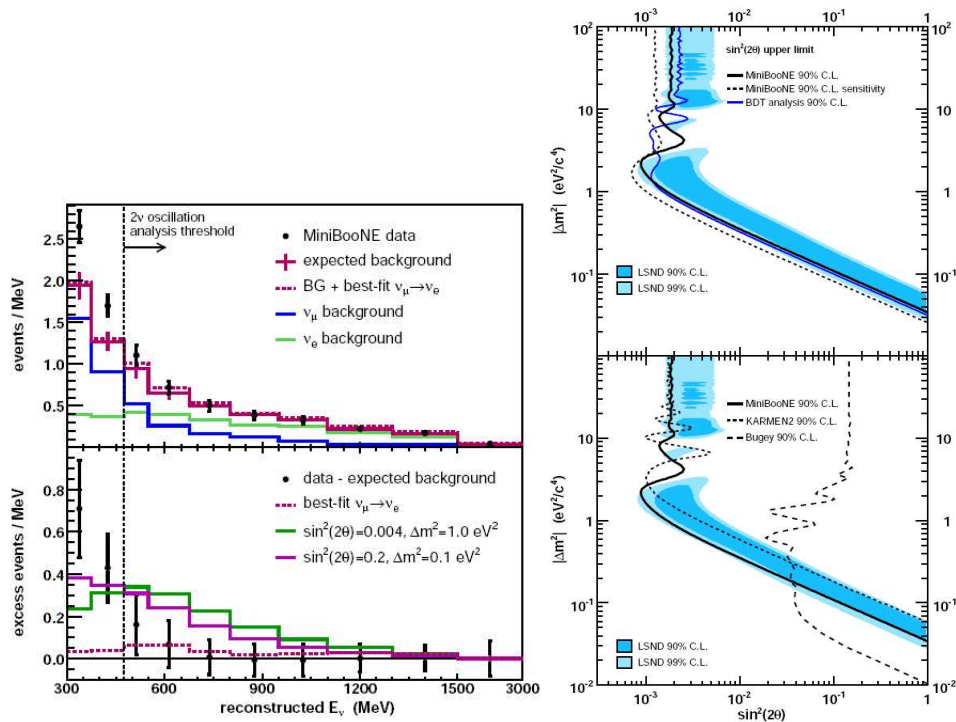


Figure 2.10: Observed  $\nu_e$  spectrum in MINIBOO NE with expected background and comparison to LSND (left) and exclusion plot based on MINIBOO NE observation (right) (taken from [12]).

a variable off axis angle T2K can create an almost monoenergetic beam with peak energy between 0.5-0.9 GeV.

The NO $\nu$ A experiment [58] is currently under construction in FermiLab and Minnesota. It will use a 220 tonne liquid scintillator near detector in an off-axis position in the NuMI beam to measure the neutrino spectrum at this angle. It will seek to measure the appearance  $\nu_e$  ( $\bar{\nu}_e$ ) signal in a 15 kT liquid scintillator detector on the same off-axis angle 835 km from the neutrino source. Measurement of the mass hierarchy and CP-violating phase will be possible for part of the parameter space by running in both neutrino and antineutrino mode.

## 2.4.2 New accelerator concepts

Producing a high energy, well understood beam of neutrinos could also be achieved using other techniques. One possible facility could use high Q-factor beta emitting ions accelerated to high gamma. Such a facility, known as a beta beam, was first proposed in [59]. The original proposal considered accelerating  ${}^6\text{He}$  ions to  $\gamma = 150$  using the production and acceleration infrastructure studied by ISOLDE [60] and to achieve the CP conjugate measurement using  ${}^{18}\text{Ne}$  accelerated to  $\gamma = 100$  (schematic shown in Fig. 2.11). Subsequent studies of the physics potential of such a neutrino source have advocated the use of higher  $\gamma$  factors [61] while novel designs including a recycling production allowing the use of the higher Q  $\beta$ -emitters  ${}^8\text{Li}$  and  ${}^{18}\text{B}$  in a beam with very low transverse emittance [62] and the use of electron capture isotopes to produce an essentially monochromatic beam [63] have also been proposed. Another facility which could be used to probe the remaining oscillation parameters is a Neutrino Factory producing a multi-species beam from the decay of muons. The current design status of such a facility is described in greater detail in chapter 3.

## 2.5 Conclusion

The existence of neutrino masses and oscillation has been clearly established through the measurements of many experiments using a variety of neutrino sources. Solar neutrino experiments have excluded all other descriptions of the solar neutrino deficit other than oscillations with consistent results using reactor neutrinos having given a terrestrial confirmation of these results. Furthermore, atmospheric and accelerator neutrino sources have confirmed the model for muon neutrinos. A combination of all results (excluding those from LSND) yields the current best fit to the known parameters as those shown in equation 2.4 [25]. Future oscillation experiments are left with the challenge of measuring the small mixing angle  $\theta_{13}$ , establishing the mass hierarchy and the possible measurement of leptonic CP violation

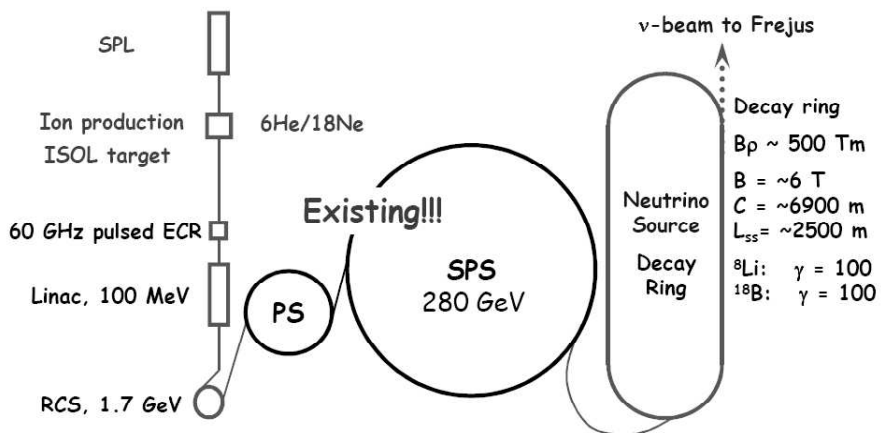


Figure 2.11: Schematic of Beta Beam facility to accelerate and store  ${}^6\text{He}$  and  ${}^{18}\text{Ne}$  (or  ${}^8\text{Li}$  and  ${}^{18}\text{B}$ ) ions.

with discovery of a non zero  $\delta_{CP}$ .

$$\begin{aligned}
 \sin^2 2\theta_{12} &= 0.87 \pm 0.03 \\
 \Delta m_{21}^2 &= (7.59 \pm 0.20) \times 10^{-5} \text{ eV}^2 \\
 \sin^2 2\theta_{23} &> 0.92 \\
 |\Delta m_{32}^2| &= (2.43 \pm 0.13) \times 10^{-3} \text{ eV}^2 \\
 \sin^2 2\theta_{13} &< 0.19, \text{ at } 90\% \text{ CL.}
 \end{aligned}
 \tag{2.4}$$

# Chapter 3

## The Neutrino Factory

### 3.1 Introduction

The Neutrino Factory was first proposed in [64, 65] as a means to create an intense, well understood multi-flavour beam of neutrinos from muon decay, with the first full oscillation physics potential study being presented in 1997 by Geer [66]. It was envisaged that a flux of  $10^{21}$  neutrinos per operational year could be achieved, however, the technical challenges in constructing a facility capable of this are many fold. The current design thinking for the neutrino factory facility and detectors is described below, with Fig. 3.1 showing the facility as proposed by the international scoping study for a neutrino factory whose outcomes are discussed in greater detail in [14, 67, 68].

### 3.2 Muon production

The first step in producing a high flux of muons is the production of charged pions. These must then be captured and allowed to decay to muons. While charge pion production is a well studied field, having been used in the context of standard accelerator neutrino facilities (described in 2.4) and extensively studied at various energies (for example in [50, 51]), the high fluxes required by the neutrino factory demand certain technical effort to achieve an optimised design.

#### 3.2.1 Proton driver

In order to achieve sufficient flux of charge pions it is envisaged that a proton driver with a power on target of 4 MW is required. The optimum proton energy as well as the appropriate repetition rate, bunch length and the best accelerator technology or combination of technolo-

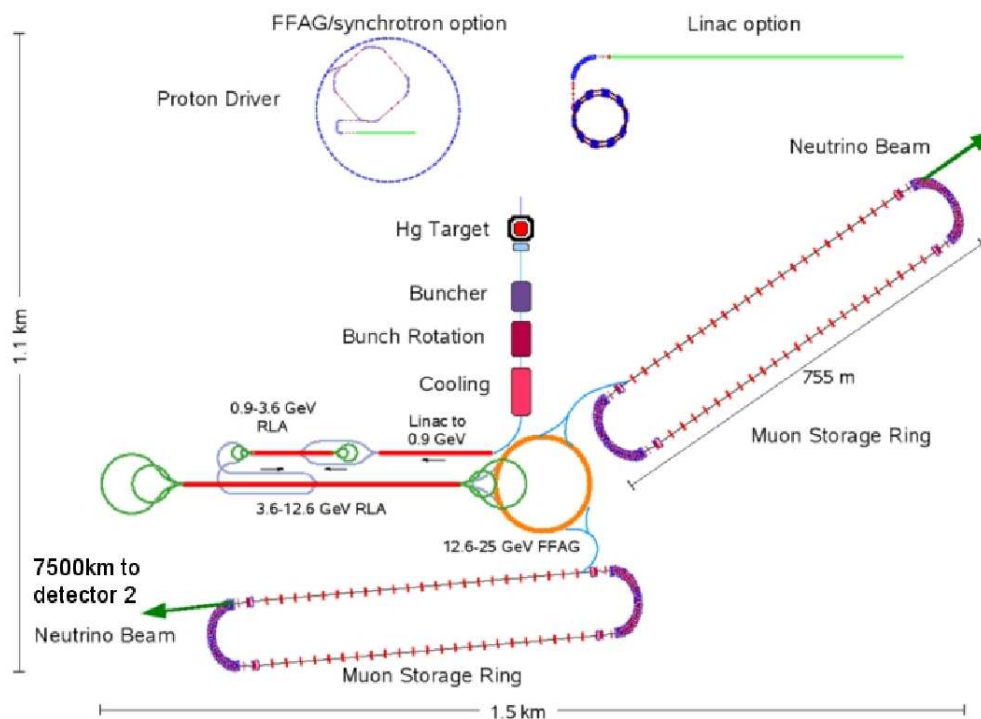


Figure 3.1: *The neutrino factory facility.*

gies to achieve these goals must be determined. Conceptual designs have been proposed in [67] with the current baseline design using a sychrotron to achieve a proton energy in the range 5-10 GeV, however, there are other possible accelerator designs utilising non-scaling FFAGs which have the potential to achieve the required power. The highest power proton target interactions used by existing facilities provide 0.75 MW in the case of the JPARC neutrino beam recently commissioned for the T2K experiment in Japan and the 1.4 MW beam to be used at SNS in the USA. The required increase in intensity for an optimum neutrino factory will be a great challenge. The project X proposal to build a 2 MW source at FNAL in USA incorporates design traits allowing for potential upgrades to serve as a 4 MW Neutrino factory source [69] allowing an active R&D program alongside experimental data taking.

### 3.2.2 Target, capture and decay

The design of an appropriate target is dictated by optimisation of production while limiting re-absorption. The main problem is the huge energy density created in the target when the proton beam is incident. The exact design with respect to geometry, material and state will feed back into the optimisation of the proton driver described in 3.2.1 as well as determining what level and form of secondary shielding and what type of beam dump will be required. A large fraction of the incident protons will not be fully absorbed so a suitable absorber

positioned as to not interfere with the experiment is required.

A solid target would have the advantage of greater density of nucleons to act as interaction centres and has many precedents such as the graphite target developed for the T2K experiment [70]. However, it is unclear whether such a target would be able to withstand the thermal shock produced by the energy deposition of a 4 MW beam for a sufficiently long period of time to be a worthwhile option for the neutrino factory. There are two main proposed schemes currently under study. A liquid mercury jet is currently considered the baseline option. In the scenario envisaged by the ISS, the proton beam and Hg jet would cross at an angle of 33 mrad and the pool of Hg from the jet would act as the beam dump before being passed through a heat exchanger and re-circulated. An Hg jet target was tested in the guise of the MERIT experiment [71] particularly to quantify the dispersion of the jet caused by beam interaction and related effects. There is also the possibility of using a fluidised powder target [72] which could avoid some of the radiological and chemical difficulties of the mercury jet solution while avoiding the disadvantages of solid targets.

### 3.2.2.1 Pion capture

A solenoidal focusing system would allow for the simultaneous capture and focus of both positively and negatively charged pions. In this way it is possible to either run with opposite polarities to two different detector sites or pulse the beam between each polarity. As such the favoured technology for pion capture is that the target will be housed within a 20 T hybrid solenoid (superconducting outer and resistive inner coil) and that the capture region will be comprised of a series of superconducting solenoids to taper the field adiabatically down to 1.75 T. Once captured, the pions will be allowed to decay in a 100 m long drift region with minimal time dependent RF producing a  $\mu^\pm$  beam of with momentum spread related to position within the bunch.

## 3.3 Muon Phase Rotation and Cooling

Pion-muon decay kinematics result in the bunch length of the produced muons being short but having a large momentum spread of between  $100 \rightarrow 300$  MeV/c. Such a momentum spread cannot easily be accelerated and must be reduced. The first technique employed to achieve this goal is phase rotation. Phase rotation involves using Radio Frequency (RF) acceleration to speed up slower muons and slow quicker ones resulting in a long bunch length with a very dense core in energy narrowly centered around  $100$  MeV/c<sup>2</sup>. The current favoured design adopted by two major studies [67, 73] involves the use of two induction linacs surrounding a drift space.

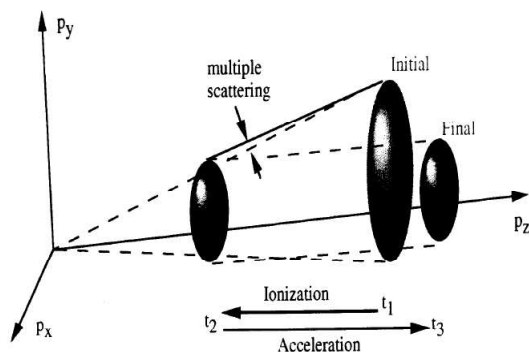


Figure 3.2: *Schematic of expected momentum rotation due to an ionization cooling channel* (taken from [13]).

Even after phase rotation, the muon beam occupies too large a phase space volume to be injected into a conventional accelerator. In order to solve this problem the beam must have its transverse emittance reduced. Where the transverse emittance is related to the momentum and angular distribution of the beam and the reduction of this parameter being termed cooling. Standard methods for cooling particle beams such as stochastic, electron and laser cooling take of order a few seconds to minutes to cool a beam by a sufficient amount and are, as such, inappropriate for a muon beam due to the mean lifetime of the muon being only  $2.2\mu\text{s}$  at rest. A more novel approach is required, muon ionization cooling.

Muon ionization cooling involves, as the name suggests, using ionization losses in material to cool the beam. On passing through an absorber a muon loses both transverse and longitudinal momentum but, to first order, does not change the beam size. Longitudinal loss is undesirable and as such RF cavities are used to re-accelerate the muons longitudinally. The net effect is the rotation of the muon momentum vector towards the forward direction as illustrated in Fig. 3.2. The Muon Ionization Cooling Experiment (MICE) [74] exists to test this technology.

### 3.3.1 MICE

MICE seeks to prove muon ionization cooling technologically by performing measurements of muon beam transverse emittance both before and after a cooling channel constructed of liquid hydrogen absorbers and RF cavities for re-acceleration.

Liquid Hydrogen was chosen as the absorber material as low  $Z$  materials tend to cause less multiple scattering. Multiple scattering is a second order effect which can cause an increase in the beam emittance. MICE is positioned on a dedicated beamline at the ISIS

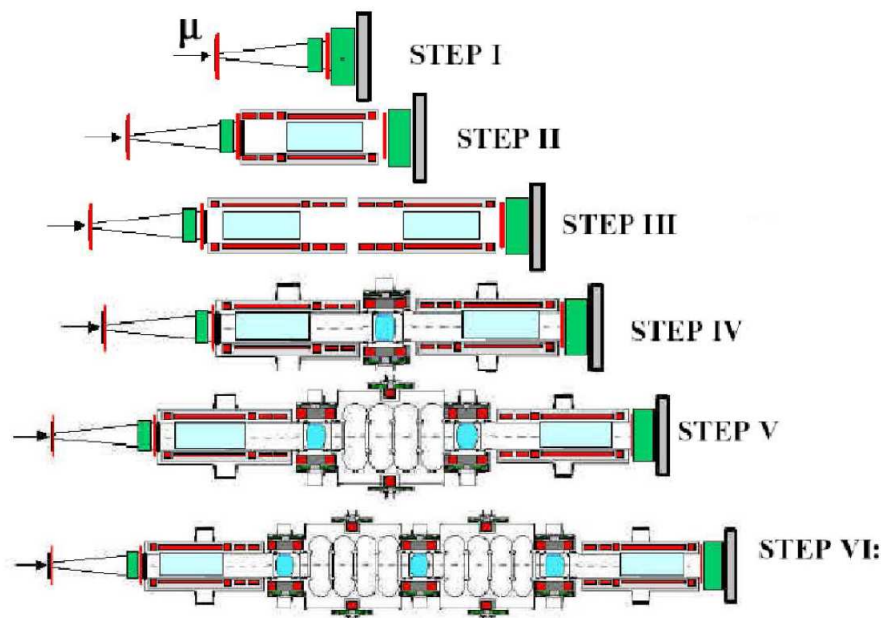


Figure 3.3: *Planned staged evolution of the MICE experiment.*

accelerator facility and will aim to measure the emittance of the muons produced on target and after absorption and re-acceleration by the staged introduction of absorbers and RF as illustrated in Fig. 3.3.

### 3.4 Re-acceleration and storage

After cooling the muon beam kinetic energy will have reduced to a mean level of 138 MeV. Quick and effective re-acceleration of the beam will be required to limit decay loss and to reach the desired energy at the decay region. Current physics studies envisage a 25 GeV muon energy in the decay ring. The ISS presented the baseline schemes as a combination of recirculating linear accelerator (RLA) and fixed-field alternating gradient (FFAG) technologies. These were chosen as the time required to cycle the magnets in even a fast-cycling synchrotron is too great for this technology to be considered.

Once accelerated to the desired energy the muons will be injected into two ‘racetrack’ storage rings. In the baseline design, injection into a particular storage ring will oscillate between the two polarities for each bunch. These storage rings must be optimised to have as large a straight side to arc ratio as possible so that the majority of the muons can decay in the straight sections pointing towards the detectors. Straight sections of 600 m in length with total racetrack length  $\sim 1600$  m are envisaged as an achievable design able to fulfill all

the requirements of the facility. They would have to store  $10^{21}$  muons to achieve the baseline requirement of  $2 \times 10^{20}$  decays in the straight section pointing towards the detector per year.

## 3.5 Detector Concepts

The decay pipes will point at two far sites chosen to optimise the physics possible with the detector technology under use. In the region close to the decay pipes there will be one or more detectors termed Near Detectors (ND). These detectors should be high granularity tracking calorimeters designed to take advantage of the unprecedented flux available at the NF facility. The oscillation signal detectors or Far Detectors (FD) will be high mass magnetised calorimeters capable of high efficiency  $\nu_\mu$  ( $\bar{\nu}_\mu$ ) charge current (CC) interaction identification and calorimetry, positioned thousands of kilometres from the facility and optimised for measurement of the golden channel signal described in section 1.4.1.

### 3.5.1 Near detectors

The primary function of the near detectors will be to measure to high accuracy the cross sections of the interactions of interest at the far detector. Moreover, there are certain background processes to the oscillation signal at the far detector which cannot be measured accurately there and thus must be quantified at the near site. First among these is the measurement of the production of Charm containing mesons in Deep Inelastic Scattering (DIS) events whose leptonic decays can constitute background (described in greater detail in 4.2.1). Moreover, the ND will be required to measure the absolute flux from the beam pipe and could even be used to predict the far detector non-oscillation flux, a technique for which is described in chapter 7.

In addition, the huge number of interactions available for analysis open up the possibility of a rich tapestry of physics studies [75, 76].

### 3.5.2 Far detectors

There are likely to be two far detector sites positioned at  $\sim 2000$ - $4000$  km and  $\sim 7500$  km from the facility. The two sites allow for the disentanglement of the degeneracies described in section 1.4 with the 7500 km site being of particular use in the determination of the matter effect parameter and the mass hierarchy. The basic requirement for both far detectors will be the measurement of the golden channel. There are many technologies which have been proposed as being capable of performing this task. A large magnetised Liquid Argon TPC is likely to be restrictively expensive even in the scenario where the technological leap required

to make such a detector viable were made. It is more likely that a solid state detector will be used as achievement of the required mass would be far easier. A sampling calorimeter made of iron interspersed with plastic scintillator and based on technology exploited by the MINOS experiment [77] was originally studied in the context of a neutrino factory in [17]. This Magnetised Iron Neutrino detector (MIND) is described in greater detail in chapters 5 and 6 where work to develop and exploit a modern simulation and analysis framework to optimise the sensitivity of a neutrino factory with MIND like detectors is presented. Studies of the limit of this technology as the proportion of iron tends to zero, the totally active scintillating detector (TASD) have been presented in [78].

### 3.6 Physics at a neutrino factory

Although the muons seen by the detectors will come from multiple sources along the length of the storage rings this length is so small in comparison to the distance to the far detectors ( $> 2500$  km) that the expected neutrino spectra there are accurately calculated using the point source approximations:

$$\begin{aligned}
 \frac{d^2 N_{\bar{\nu}_\mu, \nu_\mu}}{dy d\Omega} &= \frac{4n_\mu}{\pi L^2 m_\mu^6} E_\mu^4 y^2 (1 - \beta \cos \varphi) \{ [3m_\mu^2 - 4E_\mu^2 y (1 - \beta \cos \varphi)] \\
 &\quad \mp \mathcal{P}_\mu [m_\mu^2 - 4E_\mu^2 y (1 - \beta \cos \varphi)] \} \\
 \frac{d^2 N_{\nu_e, \bar{\nu}_e}}{dy d\Omega} &= \frac{24n_\mu}{\pi L^2 m_\mu^6} E_\mu^4 y^2 (1 - \beta \cos \varphi) \{ [m_\mu^2 - 2E_\mu^2 y (1 - \beta \cos \varphi)] \\
 &\quad \mp \mathcal{P}_\mu [m_\mu^2 - 2E_\mu^2 y (1 - \beta \cos \varphi)] \}
 \end{aligned} \tag{3.1}$$

where  $\beta = \sqrt{1 - \frac{m_\mu^2}{E_\mu^2}}$ ,  $E_\mu$  is the parent muon energy,  $y = E_\nu/E_\mu$ ,  $L$  is the distance to the detector,  $\mathcal{P}_\mu$  is the polarisation of the muons and  $\varphi$  is the angle between the beam axis and the direction to the detector. Since the far detector is essentially a point as seen by the beam, it is only necessary to replace  $L$  with  $L + s$ , where  $s$  is the position in the decay region where a decay takes place, and integrate along the straight section length to achieve the line source versions of eqs. 3.1. A near detector positioned within  $\sim 1$  km of the beam pipe will, however, see a different spectrum due to the transverse spread of the beam being a significant fraction of the detector diameter, the straight section length ranging from  $0.6 \rightarrow 7.5$  times the detector baseline (assuming a minimum baseline of 80 m and a 600 m straight section), meaning both multiple  $\varphi$  and additional contributions from other sections of the storage ring are possible. These additional contributions tend to increase the low energy content of the spectrum seen by the near detector particularly due to the tendency of low energy neutrinos to be emitted at larger angles to the beam direction.

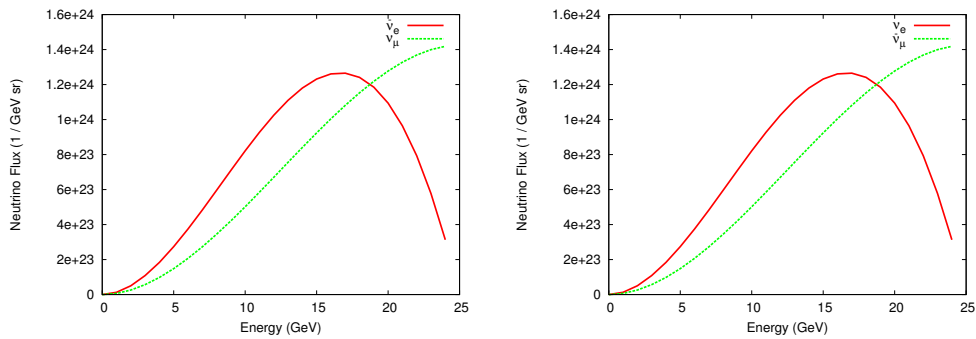


Figure 3.4: Expected fluxes at source from stored  $\nu_\mu$  (left) and stored  $\bar{\nu}_\mu$  (right) at 25 GeV.

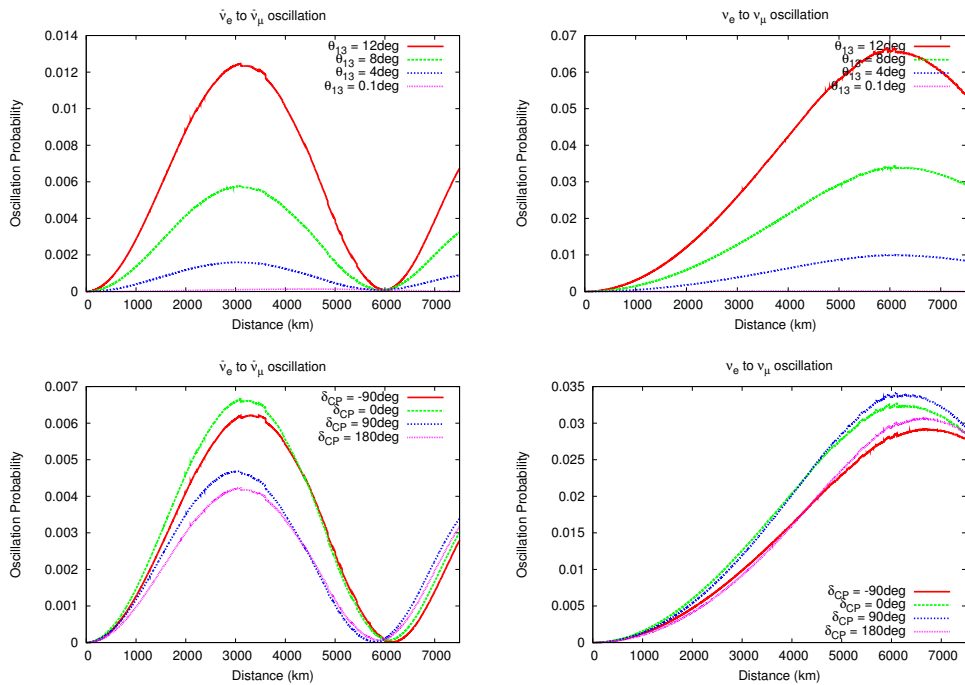


Figure 3.5: Variation of golden channel oscillation probability ( $\bar{\nu}_\mu$  app. (left)  $\nu_\mu$  app. (right)) with distance for fixed  $E_\nu = 17$  GeV and (top) fixed  $\delta_{CP} = 45^\circ$ , (bottom) fixed  $\theta_{13} = 8^\circ$ .

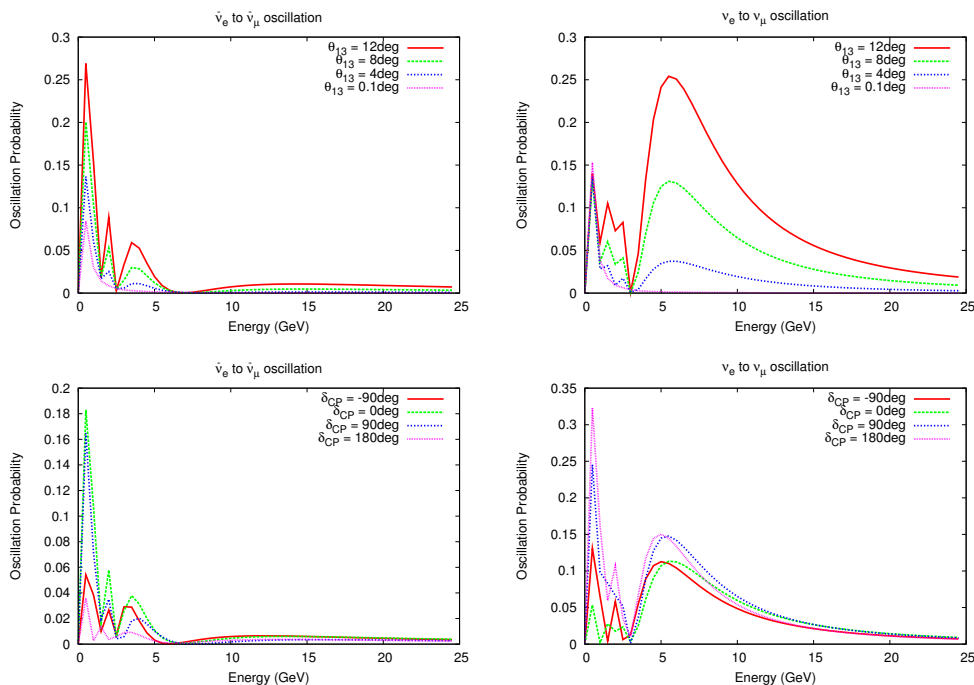


Figure 3.6: Variation of golden channel oscillation probability ( $\bar{\nu}_\mu$  app. (left)  $\nu_\mu$  app. (right)) with energy for fixed  $L = 4000$  km and (top) fixed  $\delta_{CP} = 45^\circ$ , (bottom) fixed  $\theta_{13} = 8^\circ$ .

The fluxes per steradian calculated from equation 3.1 with  $\mathcal{P}_\mu = 0$  are shown in Fig. 3.4. As can be seen the peak energy of the  $\nu_e$  ( $\bar{\nu}_e$ ) spectrum is at  $\sim 17$  GeV but is very broad. Choosing the peak energy and the values for the measured oscillation parameters as published in [79] Fig. 3.5 shows how the golden channel oscillation probability varies with distance for various values of  $\theta_{13}$  and  $\delta_{CP}$ . Larger distances would be interesting at this energy but since statistics will be smaller as the distance increases the experimental sensitivity is reduced. Considering instead the full spectrum of energy at a fixed distance of 4000 km, the variation of the probability can be seen in Fig. 3.6, where it is clear that understanding the low energy region fully would require very good energy resolution and high statistics. Clearly the energy dependence of the oscillation probability is a useful tool in understanding the values of the remaining unmeasured parameters, but how well this can be exploited, of course, relies on the energy resolution of the detector. Combining the neutrino factory flux and the oscillation probability it can be seen (Fig 3.7) that measurement of  $\delta_{CP}$  would be aided significantly by using a detector with efficiency below 5 GeV and good energy resolution, especially when cross-section energy dependence is considered. As described in chapters 1 and 2, the Neutrino factory would perhaps need to measure the last mixing angle and CP phase simultaneously and to do that the detector distances and analyses should be optimised to resolve certain ambiguities which arise in the golden channel.

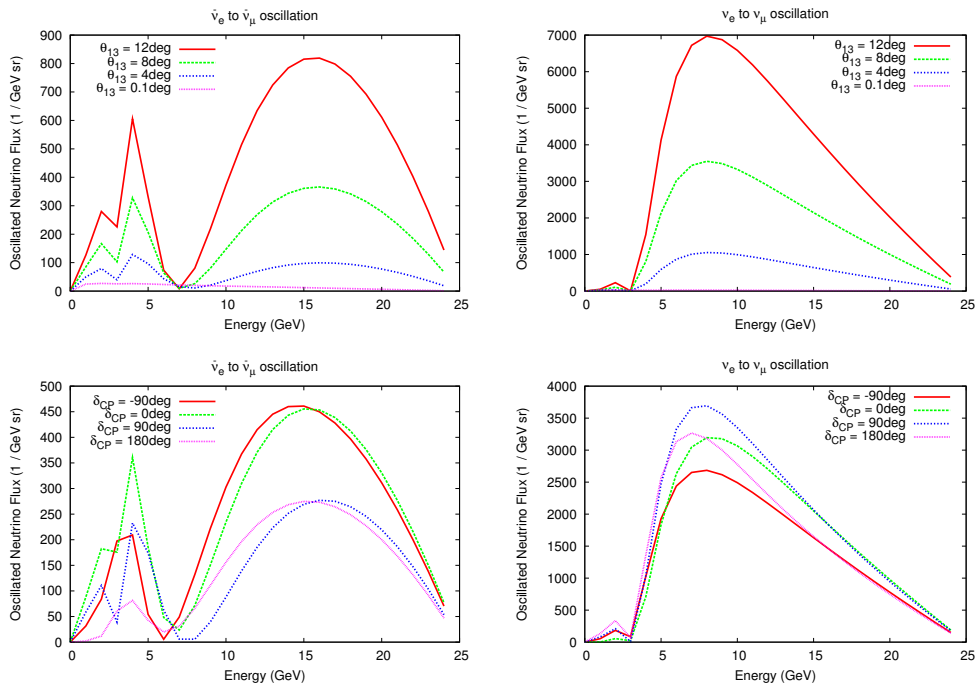


Figure 3.7: Variation of  $\nu_\mu$  appearance flux ( $\bar{\nu}_\mu$  app. (left)  $\nu_\mu$  app. (right)) with energy for fixed  $L = 4000$  km and (top) fixed  $\delta_{CP} = 45^\circ$ , (bottom) fixed  $\theta_{13} = 8^\circ$

Sensitivity of the baseline neutrino factory to the key goals of  $\theta_{13}$ ,  $\delta_{CP}$  and  $\text{sign}(\Delta m_{23}^2)$  determination as well as to the resolution of the degeneracies mentioned in section 1.4.1 has been carried out in the context of the International Scoping Study for the neutrino factory [14]. Since the optimal  $L/E$  for the study of different parameters and resolution of different degeneracies are not the same, the physics optimisation took into account how sensitivity varies from optimal as different combinations of muon energy and baseline are used. As can be seen in figures 3.8, 3.9 and 3.10, the optimum baseline and energy combination for the discovery of  $\theta_{13}$ ,  $\delta_{CP}$  and the mass hierarchy differ significantly with shorter baselines clearly favoured for the discovery of CP violation and longer for the mass hierarchy. However, in all cases a combination of two detectors, one at  $\sim 4000$  km and another at  $\sim 7500$  km, receiving neutrinos from muons stored at between 20–30 GeV is a good compromise. For this reason the current design study favours a 25 GeV neutrino factory with 2 detectors with baselines of this order.

Another important study looked at how sensitivity to  $\delta_{CP}$  changed as the signal efficiency threshold of the detectors was changed. As  $\delta_{CP}$  affects the phase of the oscillation, the efficiency at lower energies allows greater sensitivity due to increased coverage of the second maximum of the oscillation, as shown in Fig. 3.11.

The study concluded that a combination of one detector at a distance of  $\sim 3000$ – $5000$  km

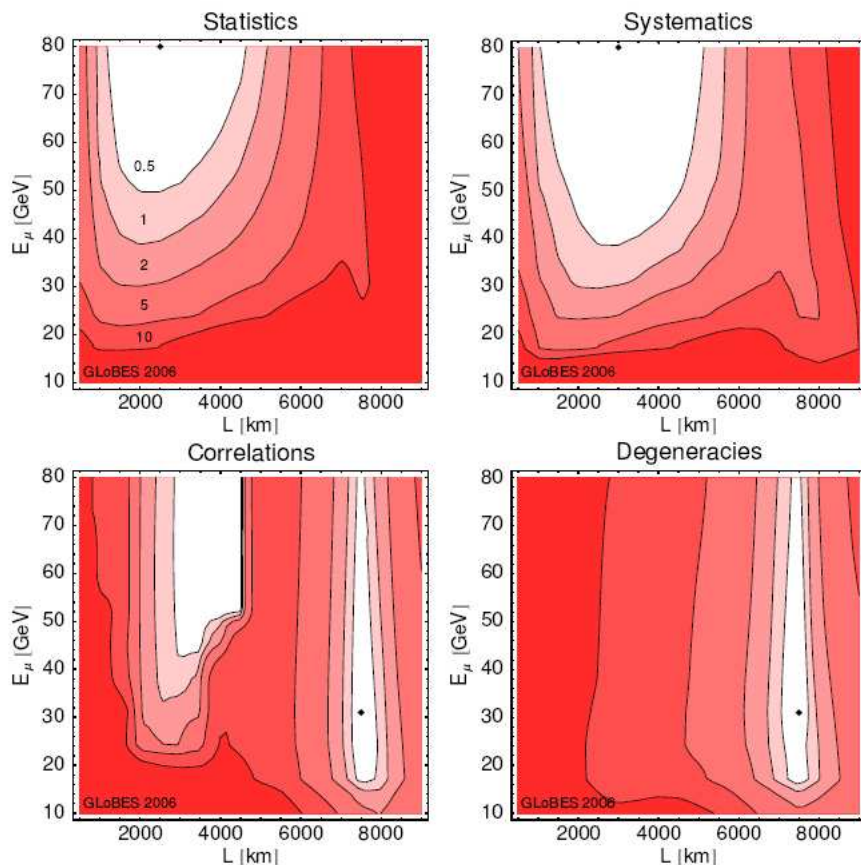


Figure 3.8: Sensitivity to  $\sin^2 2\theta_{13}$  at  $5\sigma$  relative to optimal (white) successively taking into account statistics, systematics, correlations and degeneracies. The diamond marks the optimal combination in each case (taken from [14]).

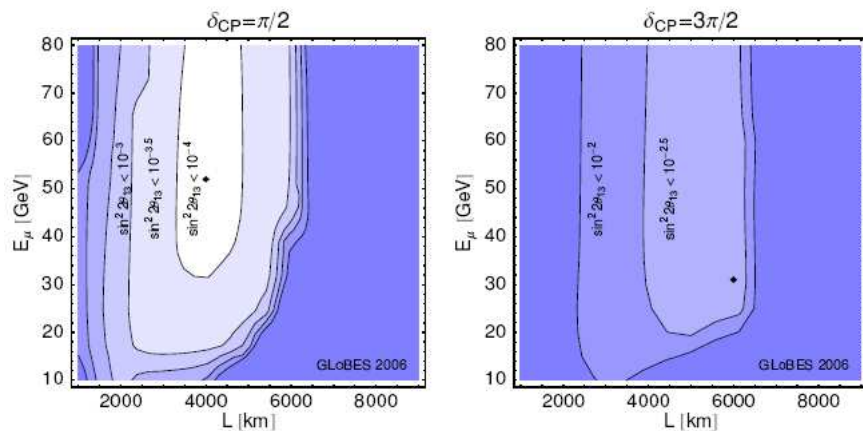


Figure 3.9: Sensitivity to maximal CP-violation ( $\delta_{CP} = \pi/2$  or  $\delta_{CP} = 3\pi/2$ ) for true mass hierarchy normal (taken from [14]).

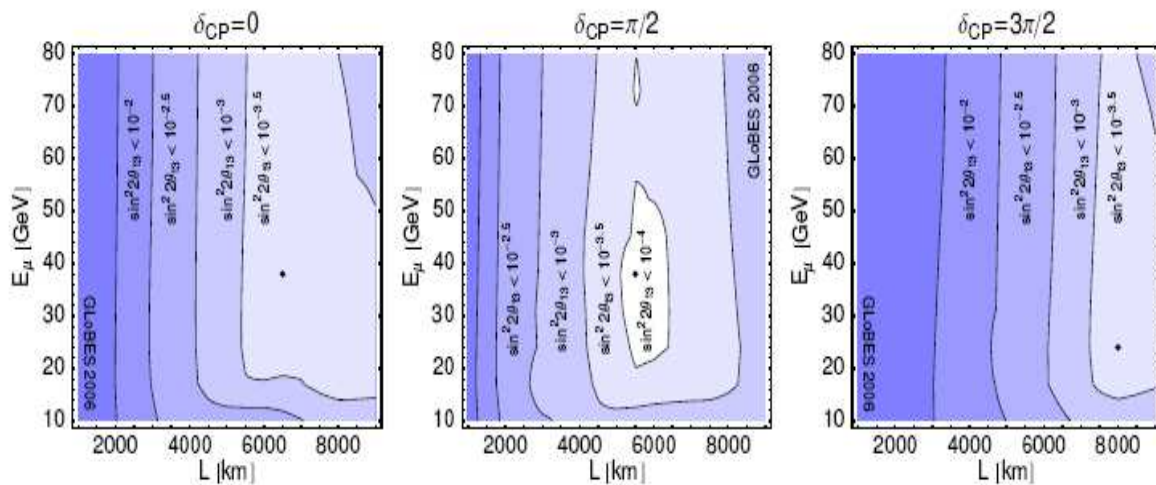


Figure 3.10: Sensitivity to normal hierarchy for different values of  $\delta_{CP}$  (taken from [14]).

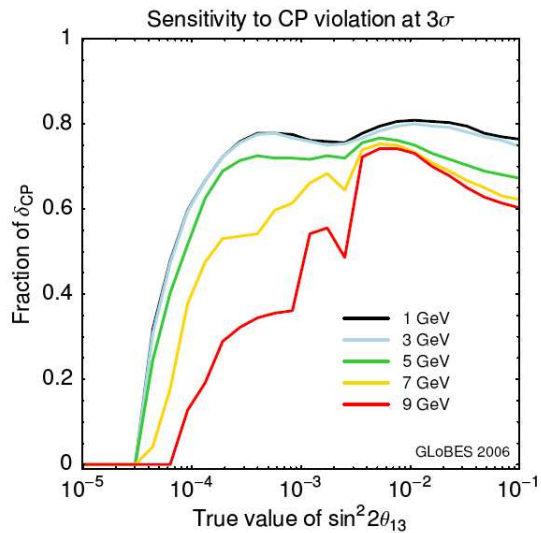


Figure 3.11: Sensitivity to  $\delta_{CP}$  for different detector threshold energies (taken from [14]).

and another at  $\simeq 7500$  km fed by a stored muon beam of energy 25 GeV gave the best sensitivity to all required measurements and disambiguities.

### **3.7 Conclusion**

The Neutrino Factory facility has the potential to provide an unprecedented level of neutrino flux allowing studies of oscillations and other physics. Work to optimise the facility detectors and physics reach is ongoing under the guise of the International Design Study for the neutrino factory (IDS-NF) and Euro- $\nu$  projects. The IDS-NF seeks to produce a reference design report detailing the optimum specifications of the facility and detectors by 2013. Such a document would be used as the spring board to begin full engineering designs and ultimate construction of the neutrino factory.

# Chapter 4

## Active Pixel Sensors for vertex detection at the Near Detector

### 4.1 Introduction

The Neutrino Factory near detector facility will be comprised of either one multi-purpose detector or many smaller task specific detectors. The primary studies required to be performed at any near detector facility will be the measurement of cross-sections, quantification of the absolute flux from the beam pipe in both polarities and measurement of processes which could constitute background to the wrong-sign muon search at the far detector. Moreover, a number of other physics studies could be performed taking advantage of the large, multiflavour neutrino flux.

### 4.2 Physics at the near detector

The neutrino flux achieved from muon decays is very well understood and calculable. Hence, the flux of neutrinos at the near detector of a neutrino factory could be calculated to a high degree of accuracy using only the beam monitoring available in the decay ring. This knowledge could be improved further due to the high interaction statistics expected at the near site, making suppressed interaction processes like inverse muon decay and electron scattering statistically significant. The cross-section for these processes can also be calculated accurately in the standard model and as such, using high granularity tracking and calorimetry, the near detector would be able to understand the neutrino flux, particularly at high energies, to a high degree of accuracy. Thus, it is possible to decouple the measurement of other cross-sections from the flux and seek to measure exclusive neutrino and antineutrino cross-sections across the full energy range to at least the 1% level. This well understood, high flux

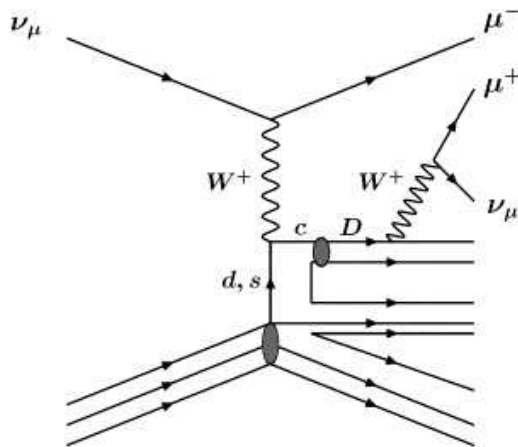


Figure 4.1: *Feynman diagram for DIS charm production* (figure taken from [15]).

beam could also be used to perform other physics studies including the measurement of the Weinberg angle,  $\sin^2 \theta_w$ , using the ratio of neutral current to charged current interactions, nucleon Parton Distribution Function (PDF) measurements, nuclear re-interactions using a range of target materials and, if placed at an appropriate distance from the source, perform beyond the standard model searches using non-standard interactions or non-standard oscillations [75, 76, 80]. One of the most important cross-section measurements to be undertaken is that of charm production in deep inelastic scattering interactions, due to its importance as a background to the neutrino oscillation search (see chapters 5 and 6).

### 4.2.1 Charm production background

Neutrino interactions on nuclear targets can produce charm containing mesons as part of the hadronic shower produced in deep inelastic scattering events (DIS) (see Fig. 4.1), particularly at high neutrino energies. Charm quarks can be produced in charged current interactions through the Cabibbo favoured transition  $s (\bar{s}) \rightarrow c (\bar{c})$ , which can be used to measure the strange content of the nucleon, in addition to more suppressed transitions from  $d$  quarks and via charm production at fragmentation, which is also possible in neutral current interactions [15]. With appropriate detector resolution and analysis the relative production of the charmed particles  $D^+$ ,  $D^0$  and  $\Lambda_c$  can be measured for neutrino and the conjugate channels for antineutrino beams. The combination of these measurements can be used to extract the Cabibbo-Kobayashi-Maskawa (CKM) matrix element  $|V_{cd}|$ . In addition to the study of nucleon structure, the production of charm mesons (particularly  $D^{+/-}$ ) is interesting for neutrino factory experiments since these processes constitute possible background to the wrong sign muon signal at the far detectors through muon containing leptonic and semileptonic

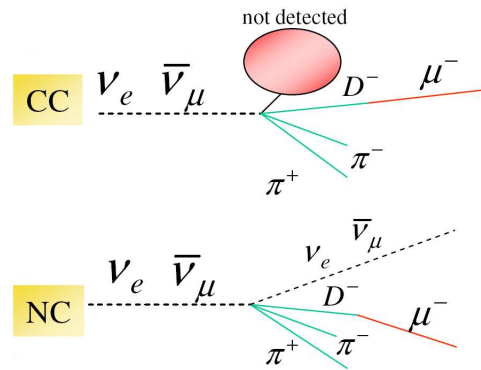


Figure 4.2: Possible backgrounds to a wrong sign muon search from charm meson decays.

decays as demonstrated in Fig. 4.2. Charm decays are of particular interest because of their kinematics. The short lifetime of these mesons and the relatively high momentum of the produced muon means that they can mimic the primary muon of a charged current interaction, particularly where the primary muon itself is short enough not to be disentangled from the hadronic activity. While many of these events should be excluded by the analysis performed on the far detector data, the expected abundance of these events must be understood in order to calculate the remaining background. The current best measurements of the cross-sections for charm meson production come from the NOMAD [81] and CHORUS [82] experiments. However, these results have errors of between 6% and 10% and only cover part of the energy region of interest to the NF. In order to measure this cross-section accurately, a fast, high resolution detector is required to locate the displaced vertex of the meson decay.

## 4.2.2 A silicon vertex detector at the near detector

A vertex detector composed of silicon sensors interspersed with passive target material similar to the NOMAD-STAR detector [83] could be used in conjunction with a fully active scintillator detector or indeed a NOMAD-like detector to perform the required studies of a neutrino factory. The vertex detector would be used to search for charm production in neutrino interactions by either looking for an impact parameter, indicative of  $D^{+/-}$  decay, or a double vertex in the case of neutral meson decays. Such a study would require any vertex detector to have position resolution of  $\sim 30 \mu\text{m}$  [83] which would enable resolution of the impact parameter down to  $\sim 90 \mu\text{m}$ . While the  $50 \mu\text{m}$  pitch strip detector of NOMAD-STAR achieved such resolution, the conditions at a neutrino factory demand a re-optimised design for the vertex detector to be able to achieve the required resolution. Using pixelated detectors would allow for the measurement of 3D position in each plane. 3D resolution would allow

for the measurement of the actual impact parameter instead of its projection into a plane as was the case for NOMAD-STAR [83] which has the potential to improve the minimum impact parameter visible to the detector and reduce the possibility of inclusion of hits due to non-beam related interactions. Moreover, the event rate expected at a neutrino factory near detector means that inclusion of additional hits due to event pile up could be possible without 3D position reconstruction per layer. In one year (defined as the Snowmass year of  $10^7$  s) the combination of all CC and NC interaction channels would result in  $\sim 7 \times 10^{13}$  interactions in a 100 kg detector placed 100 m from the end of one of the decay ring straight sections. Taking into account the expected duty cycle of  $\sim 10\%$  this translates to a total interaction rate in a data taking window of  $> 10^7$  neutrino interactions per second. Considering the current best measurements of the charged current charm induced dimuon cross-section [81] and a selection efficiency of 10%, a 100 kg vertex detector would have  $\sim 10^8$  dimuon charm events per year to study potential background to the oscillation signal.

### 4.3 APS technology

A possible technology for the active layers of the silicon detector is that of Active Pixel Sensors (APS). APS are silicon pixel devices based on basic CMOS technology and as such are low cost and widely available. This manufacture technique affords the possibility of integration of first stage amplification within the pixel and is relatively low in cost. Moreover, the monolithic nature of these devices, where all parts are integrated into a single silicon wafer, removes the need for high voltage for depletion. Although this technology was originally developed for photon detection, the flexibility of design could have huge potential for application in particle physics and be of particular use for the application described above.

The sensitive element in such a device is an n-well in a p-type epitaxial (epi-)layer which forms a pn photodiode. Electrons are excited to the conduction band when ionising radiation passes through the epi-layer and then subsequently spread out by diffusion to be collected when they come sufficiently close to the photodiode. While the thin epitaxial layer – ranging from a few  $\mu\text{m}$  in width to  $\sim 25 \mu\text{m}$  – means that the collected charge for a MIP is less than that in competing similar technologies, the integrated nature of this type of device makes it possible to design pixels with low noise. However, this structure is susceptible to other sources of noise, including reset noise. Therefore, novel designs are required to achieve the stability and low level of noise required for the above application.

Two devices were considered: the Vanilla detector, which was designed primarily as a test device for a novel reset technique used to reduce noise and the HEPAPS4 device designed specifically for charged particle detection and using a standard three transistor design where

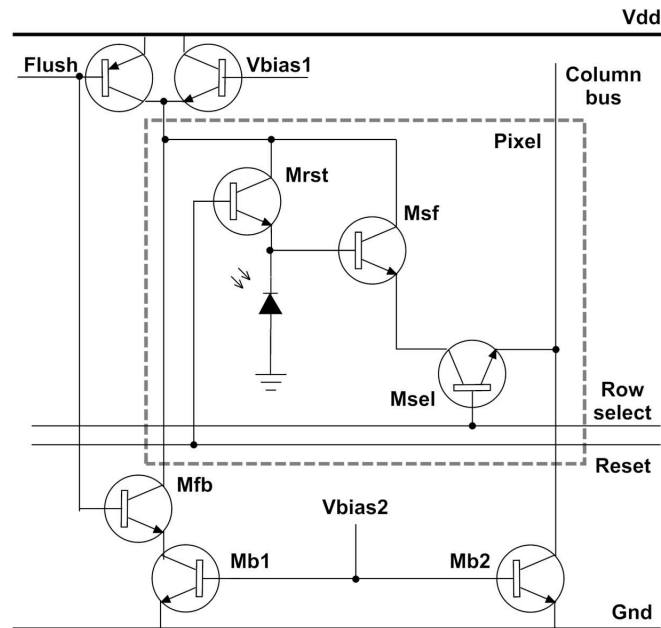


Figure 4.3: An APS pixel. Basic pixel structure common to Vanilla and HEPAPS4 within dotted line; additional electronics for Vanilla flushed reset outside.

the transistors control reset, amplification and readout. Both detectors were designed at the Rutherford Appleton Laboratory as parts of the UK MAPS [84] and the MI3 projects [85].

## 4.4 The Vanilla detector

The Vanilla APS comprises an array of  $520 \times 520$  pixels each of  $25 \mu\text{m}$  pitch with integrated analogue to digital converters (ADC). This structure allows for in-pixel digitisation and output at a rate of 12 bits for full frame mode, although it can also be read out in analogue mode, where digitization is handled off chip. The sensor can operate at a readout rate of up to 100 frames/s for full frame, and at 20 kHz (in analogue mode) at 10 bits resolution for ROI. In addition to Vanilla's standard three transistor pixel architecture there is additional structure allowing for 3 reset modes – soft, hard and flushed.

A hard reset involves applying a voltage to the gate of the transistor  $M_{rst}$  which is higher than the voltage applied to the drain by more than the threshold voltage of the transistor and results in a noise level of  $\sim \sqrt{kTC}$  – where  $kTC$  is the base level noise of a device calculated from the temperature,  $T$ , and the main collection node capacitance,  $C$  with  $k$  Boltzmann's constant – while a soft reset involves holding both the gate and drain voltage at  $V_{dd}$  and allowing the charge to flow out and can reduce the noise base to  $\sqrt{\frac{kTC}{2}}$  but can suffer

from image lag. Image lag occurs when the charge from a previous frame is not completely removed at reset and, as such, subsequent frames are affected. This leads to a non-uniform base level in the pixel. Vanilla pixels contain an additional in-pixel structure (see Fig. 4.3) which enables the use of a hard reset immediately followed by a soft reset in one reset cycle. This ‘flushed’ reset was designed to achieve the noise base level of a soft reset while avoiding image lag [86].

#### 4.4.1 Gain determination using photon transfer curve method

Although sensitivity to charged particles is of greatest interest in determining the suitability of a detector to the application, photonic techniques are useful to determine the basic performance parameters, such as the conversion gain, which are required to fully understand the response of the device to charged particles. The gain of pixelated devices can be efficiently determined using the photon transfer curve technique (PTC) [87].

The PTC technique utilises the fact that the arrival of photons to a pixel is a Poisson process where the variance is equal to the mean. The method involves illuminating the sensor uniformly across the region under test and gradually increasing the intensity while recording several frames at each setting. The measured ADC signal can be understood as  $S_{ADC} = G \times n_e$  where  $G$  is the camera gain and  $n_e$  is the number of electrons excited to the conduction band. Above a certain irradiance level the noise of the device will be dominated by the noise of the arriving photons, the shot noise; in this region the signal variance in ADC units is  $\sigma_{ADC}^2 = (G \times \sigma_e)^2$  where  $\sigma_e$  is the standard deviation of the number of excited electrons and since shot noise satisfies Poisson statistics then  $\sigma_e^2 = n_e$ . As a result the variance and signal are related by  $\sigma_{ADC}^2 = G \times G n_e = G S_{ADC}$  and a plot of variance with Signal should exhibit a linear region with gradient equal to  $G$ .

Using several frames taken without any illumination, a pedestal frame is calculated where each ‘pixel’ is the mean dark level recorded in the corresponding device pixel. The mean at each illumination level for a pixel is then calculated as the mean of the pedestal subtracted value recorded at that level. The corresponding pixel variance is  $\sigma_{true}^2 = \sigma_{sub.}^2 - \sigma_{ped.}^2$  since subtraction of the pedestal frame will introduce additional variance. When fitted, the linear region of the variance/mean plot should have gradient equal to the gain for the pixel under consideration in the shot noise dominated region. Fig. 4.4 shows a PTC curve where the mean and variance averaged across many pixels has been used, the gradient of the linear region in this plot should give an indication of the mean gain across those pixels used. However, assessing the gain in this way does not properly take into account the possibility of variable gain across the device. Calculating the gain for each pixel individually requires a greater number of frames at each setting but allows for a better assessment of the gain sta-

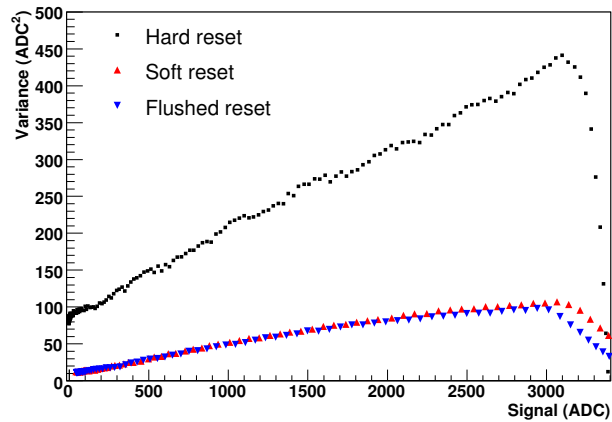


Figure 4.4: *Examples of PTC curves for three reset modes.*

Reset mode	Mean Gain ( $e^-/ADC$ )	Read noise (ADC)
Soft	23.97	3.31
Hard	6.67	9.17
Flushed	26.33	3.04

Table 4.1: *Summary of measured gains for each reset type and read noise level.*

bility across the device. Particularly when in-pixel conversion is used this can be important. The distribution of calculated gain values per pixel yields a mean value for the gain of the device.

Measurements were taken using a LED (with  $\lambda = 520\text{nm}$ ), with a diffuser utilized to give uniform illumination of the active region to within 1%. The device was run in digital readout mode and all reset types were tested using a central  $100 \times 100$  pixel region. Fig. 4.5 shows the achieved gain spread expressed in  $e^-/ADC$  (the inverse of the PTC curve gradient) for each reset mode with the mean gain values summarised in table 4.1. The measured gain using hard reset differs significantly from that measured in the other reset modes. While no definitive reason has been found for the difference, it is interesting to note that this difference is not seen when using analogue readout [88] and that flushed and soft reset modes demonstrate significant non-linearity in analogue mode which is not seen in digital mode (see section 4.4.2). Non-linearity has been observed in MAPS before [89] and was attributed to varying capacitance of the diode during charging, compensation in the on-chip ADC could account at least partially for the observed difference in the gains. The intercept of the PTC curve with the variance axis can also be used to give an indication of the device base level read noise [90] as this should be a constant value and dominate at low illumination.

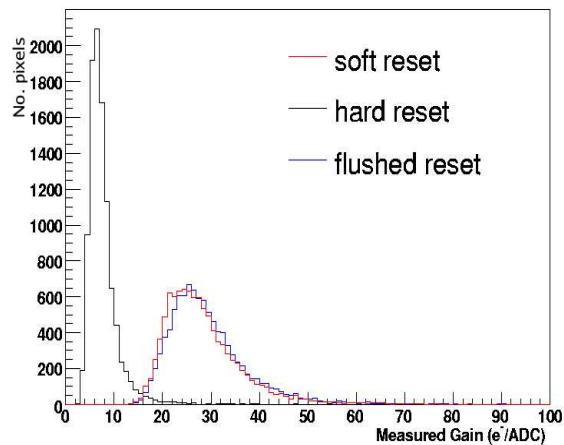


Figure 4.5: *Distribution of calculated pixel gains for Vanilla working in Digital readout mode for the three possible reset modes.*

#### 4.4.2 Device Linearity

The linearity of any device is a measure of how closely its response follows a simple linear relation with illumination across its entire dynamic range. Significant variance from linearity would indicate a varying gain making reliable reconstruction of any signal problematic. Such a characteristic would complicate the characterisation of a device to particle passage as a reliable measurement of the device gain is required to properly classify the energy deposited by a minimum ionising particle (MIP).

Using the same data set as in the PTC measurement to plot the mean response averaged across the whole detector against illumination allows for an accurate measure of this quantity. Accurate knowledge of the irradiance of the LED at different settings used was achieved through the use of a calibrated Hamamatsu photodiode. Results show that the Vanilla digital readout mode exhibits linear response (with less than 1% non-linearity up to 3000 ADC) across the whole dynamic range, Fig. 4.6, for all reset modes.

### 4.5 HEPAPS4

HEPAPS4 [91] utilises standard NMOS technology and was designed specifically for low noise readout of particle hit information at the speeds required for a lepton collider. The  $1024 \times 384$  pixel array is comprised of  $15 \mu\text{m} \times 15 \mu\text{m}$  pitch pixels. Traversing particles deposit charge in the  $20 \mu\text{m}$  p-type epitaxial layer. The charge then diffuses to the n-type well to be collected, normally in more than one pixel. HEPAPS4 is the latest in a line of

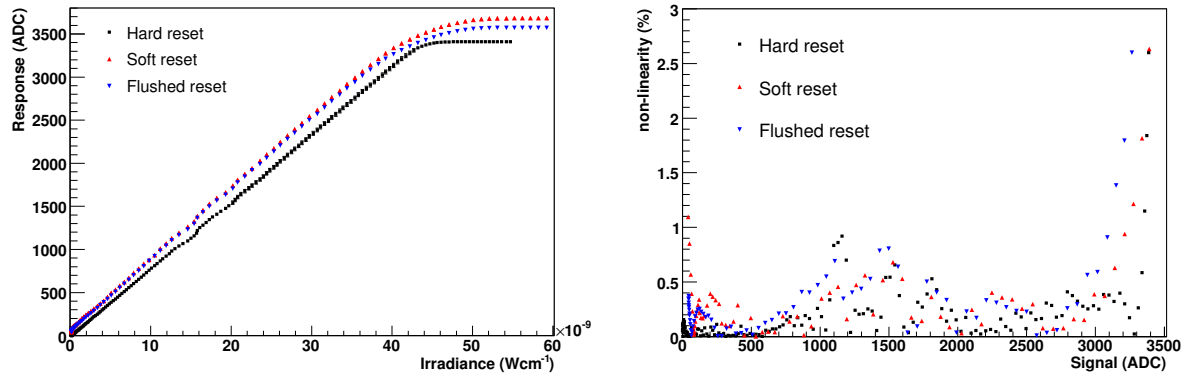


Figure 4.6: *Response versus irradiance for Vanilla with the three reset modes (left) and variance from a linear fit to the non-saturation region as % of the measured range (right)*

Diode size ( $\mu\text{m}^2$ )	Gain ( $e^-/ADC$ )	Noise ( $e^-$ )
$1.7 \times 1.7$	5.1	54

Table 4.2: *Summary of key characteristics of the HEPAPS4 chip.*

monolithic active pixel sensors (MAPS) designed for particle physics experiments by the UK MAPS Project [84].

### 4.5.1 Sensitivity of HEPAPS4 to electron passage

Suitable vertex detectors must be sensitive to particle passage at a range of energies with high position resolution. The sensitivity to minimum ionising particles (MIP) can test accurately this characteristic. While electrons do not act exactly as MIPs – due to their energy loss being dominated by radiation losses – the ready availability of  $\beta^-$  sources and of electron testbeams allows for extensive multi-energy testing of devices. HEPAPS4 was tested under the passage of 6 GeV electrons from the DESY synchrotron and MIP energy electrons from a strontium-90  $\beta$ -source (the Q-value of  $^{90}\text{Sr}$  is 0.546 MeV and that of its short lived daughter product  $^{90}\text{Y}$  is 2.28 MeV). Photonic studies were performed and presented in both [92, 93] with relevant results summarised in table 4.2. HEPAPS4 was measured to have a conversion gain of  $5.1 e^-/ADC$ , the detection of Minimum Ionising Particles (MIP) should be more efficient with a detector producing more ADCs per electron, however, the noise level is somewhat high. Collider applications require as low a noise level as possible for efficient tracking.

## 4.5.2 Exposure to 6 GeV electrons at DESY

As a test of the triggering logic implemented in the firmware of HEPAPS4 and as a first step towards testing the response of the device to charged particles, HEPAPS4 was exposed to 6 GeV  $e^-$  at DESY (Hamburg). Tracking data was provided by 5 silicon pixel devices (named ISIS [94]).

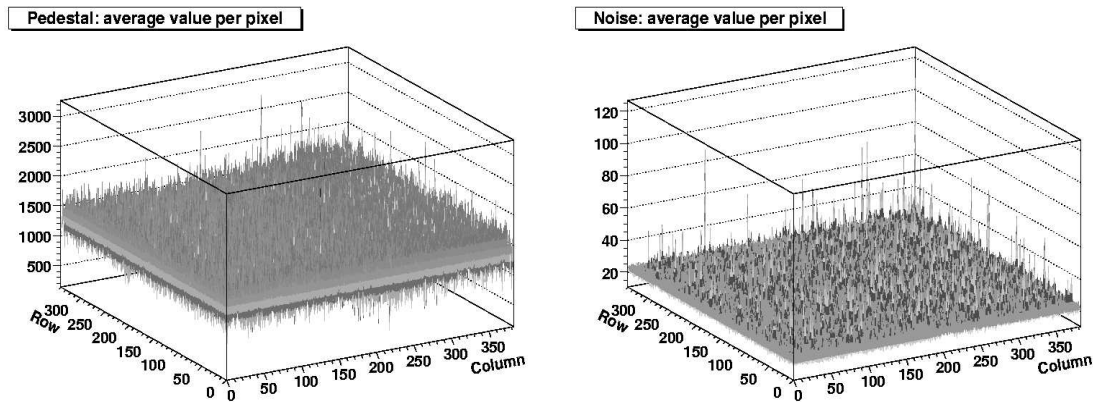


Figure 4.7: *Pedestal and Noise for each pixel in one region of interest.*

Pedestal frames were calculated from data taken in situ without beam and were used in the analysis to correct data frames. In addition, the noise of the pedestal corrected frames was calculated (examples of both pedestal and noise found in Fig. 4.7). A potential signal could then be assessed according to its significance as a multiple of the noise level calculated for that pixel; for the analysis described a pixel with a significance of  $7\sigma$  or greater could act as a seed. A seed was accepted as such if the pixels directly adjacent to it were of lesser significance and that beyond the  $3\times 3$  region directly adjacent no other pixel had a significance of greater than  $7\sigma$ . Those seeds found were then used as the central base to form a cluster. Any pixel in the surrounding  $5\times 5$  region with a significance greater than  $3\sigma$  was added to the pixels considered part of the particle's deposited energy. This technique ensures that all or most of the diffused electrons excited by the passage of the particle were collected.

The hit map shown in Fig. 4.8 was the first indication of beam sensitivity. Although the full circular beam profile is not seen, a large enough section of the beam is in the field of view of the detector. Full analysis of the clusters associated with these seeds yields a measurement of the most likely signal strength and cluster size at this energy, shown in Fig. 4.9.

While the results of the beam test confirmed that the device responded to charged particles, the setup was found to be dominated by non-uniform system noise with a mean level of 23 ADC counts. Sub-optimal sample timing resulted in a non-uniform gain across the array so that conversion to electron charge was not possible. In addition, the low energy

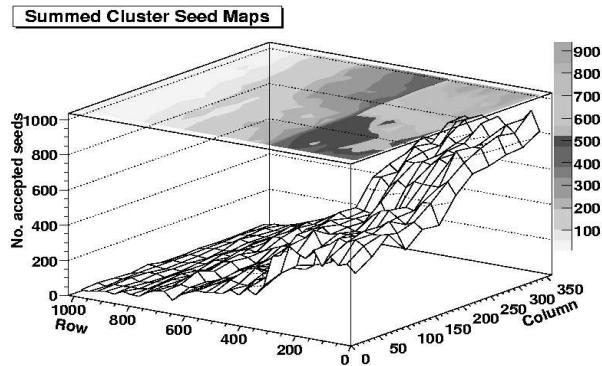


Figure 4.8: *Distribution of accepted seeds in one ROI. Center of beam indicated from row 150.*

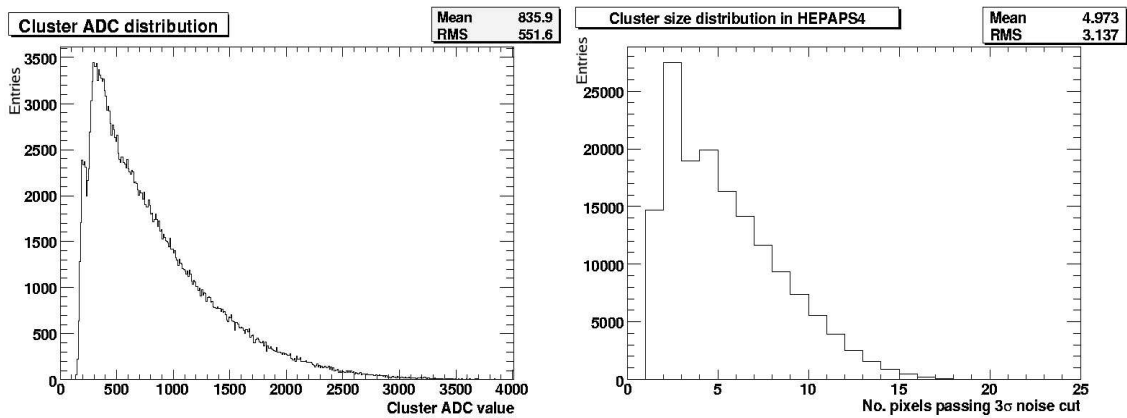


Figure 4.9: *Cluster analysis results for DESY testbeam. Left: Signal distribution in ADC. Right: Signal distribution in number of pixels.*

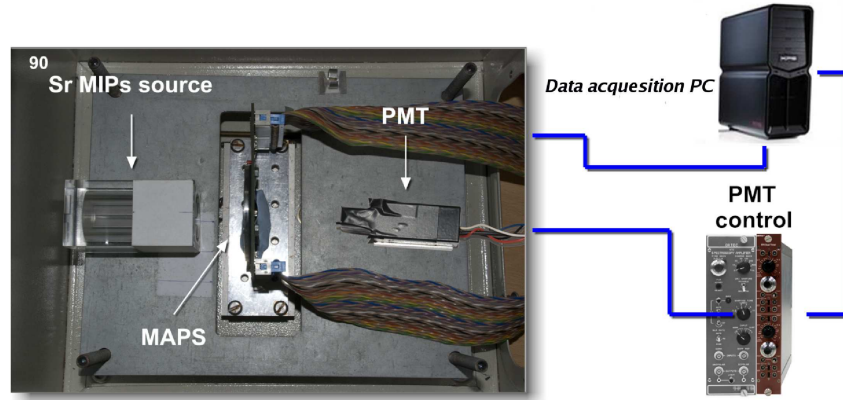


Figure 4.10: *Source testing setup.*

of the electron beam and the larger pixel size of the telescope devices meant that efficient correlation and position resolution was not possible. Optimisation of the system – including improved timing settings and the use of shorter, higher quality cables with greater shielding – before source testing was necessary to fully understand the response of the detector.

### 4.5.3 Exposure to $^{90}\text{Sr}$ $\beta$ source

A high activity (4MBq)  $^{90}\text{Sr}$   $\beta$  source was used to test the device with the newly optimised settings. Experiments were carried out using a setup, developed by the author and shown in Fig. 4.10, containing a PMT read out scintillator for triggering. The device was placed in a continuous scan of all pixels within a central region of the array with a pulse from the PMT causing a digital signal to be sent to the device triggering a readout of these pixels. While an accelerator beam can be tuned to a well defined energy a  $\beta$  source is by its very nature a continuous spectrum. However, only a restricted energy range of particles should be able to fully traverse the device and cause a trigger. While the activity of the source means that frames may contain multiple clusters, some of which correspond to particles which did not cause the trigger, the dominant signal should be that of electrons with energy close to the MIP energy region.

Considering a Region of Interest (ROI) consisting of the central 600 rows and the full 384 columns we find the noise level distributed with a most probable value at  $\sim 13$  ADC (see Fig. 4.11) and a mean noise of 15 ADC. As can be seen from table 4.2 the device gain for the optimised settings was measured to be  $5.1 e^-/\text{ADC}$ . This value was obtained using the PTC method described in 4.4.1 with the row and column sampling and reset times optimised using a setup designed to limit all external noise (see [93] for details). The resulting mean noise level of  $\sim 77 e^-$  is slightly greater than the  $54 e^-$  expected from the photonic studies,

however, the nature of the source testing set-up meant that longer cables with less shielding had to be used. It is possible that some external noise may have been measured in this case. In addition, a larger region of interest was used in order to ensure as great a statistical sample as possible; introduction of a larger number of pixels and pixels from the edge of the device could also have increased the mean noise due to the proximity to the readout electronics.

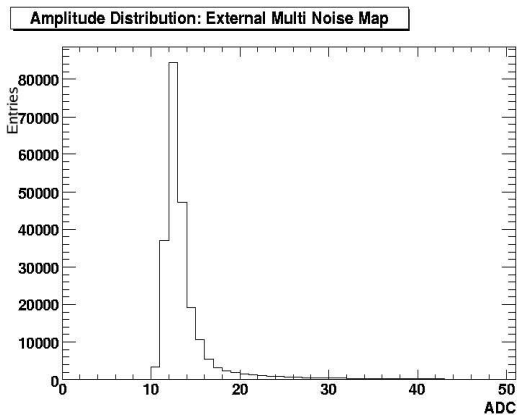


Figure 4.11: *Noise distribution calculated from 1800 dark frames.*

The data was analysed using the same clustering algorithm as in section 4.5.2 with significance cuts also as described above. As mentioned before, electrons never exactly act as MIPS due to their low mass. Considering the straggling functions described in [95] it is expected that the distribution would be broadened by additional processes and as such a broad peaked distribution somewhat dissimilar to the standard MIP convoluted Landau and Gaussian should be expected.

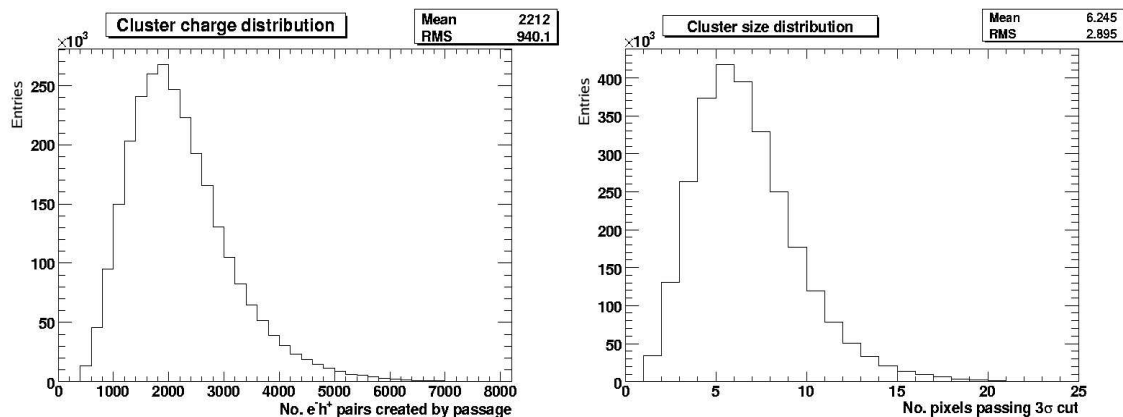


Figure 4.12: *Source cluster analysis results. Left: Cluster signal distribution, Right: Cluster size distribution.*

The measured distribution has a most probable value at 1775 electrons created per cluster. The straggling functions mentioned above calculate a most probable value for the energy

loss of a particle traversing  $20 \mu\text{m}$  of silicon as  $\sim 3.94 \text{ keV}$  which corresponds to  $\sim 1100$  electrons, assuming an ionization constant of  $3.6 \text{ eV/electron-hole pair}$  for silicon. Considering the true situation where diffusion of electrons from the inner surfaces of parts adjacent to the epi-layer is possible and the finite probability of including deposits from non-traversing electrons deviation from this theoretical calculation is not unexpected.

## 4.6 Discussion

The results obtained for both devices are promising with regard to the suitability of MAPS to vertexing at a neutrino factory near detector. The noise reduction obtained in the more modern Vanilla detector indicates a promising trend in the development of this technology. The lack of built in logic to perform triggering in Vanilla meant that it was not possible to test this device in a testbeam scenario. However, a number of ongoing studies will develop similar devices specifically designed for low noise performance [85] which will be tested as possible vertex detectors for lepton colliders. While the noise requirements are not so stringent for a vertex detector at a neutrino factory near detector any technology capable of performing vertexing at a lepton collider would be ideal for this application.

The signal to noise of HEPAPS4 for MIP energy electron detection, measured as  $S/N \simeq 23$ , is sufficient for use as a vertex detector at a neutrino factory. With proper development and proof that sufficient position resolution can be achieved a MAPS based vertex detector could be a viable option. It is unlikely that such a detector would require pixels as small as those present in either of the devices to achieve the required position resolution which could further reduce cost for both electronics and the silicon devices themselves to make the vertex detector.

## 4.7 Conclusions

Two APS devices have been tested with electron testing indicating the suitability of such technology to the detection of MIP energy particles. Development of the technology with additional structures such as those still under test in the Vanilla device indicate that competitive noise levels could be reached and as such the flexibility of APS technology could win out in selecting devices for future particle physics detectors. Ongoing studies using back-thinned versions of Vanilla – where the substrate is etched off – are being used to demonstrate that the technology can be used with significantly reduced non-active material [96] another advantage for particle detectors.

Further development of the technology to reduce noise and demonstrate scalability is

necessary before APS technology becomes a clear candidate for the vertex detector at a neutrino factory. However, the current trend in the development of the technology indicates that MAPS could be an ideal option for the application.

# Chapter 5

## Development of reconstruction and analysis software for a Magnetised Iron Neutrino Detector

### 5.1 Introduction

Early papers on the physics outcomes of a Neutrino Factory concentrated on the sub-dominant  $\nu_e \rightarrow \nu_\mu$  oscillation [31] in which a muon of opposite charge to that stored in the facility storage ring (wrong-sign muon) would be produced in a far detector by the charge current (CC) interactions of the oscillated  $\nu_\mu$ . The first analysis of the capabilities of a large magnetised iron detector to detect the wrong-sign muon signature was discussed in [17] (termed the Golden Channel), where it was demonstrated that this combination was capable of the extraction of the remaining unknown parameters in the neutrino sector, the third mixing angle  $\theta_{13}$  of the Pontecorvo-Maki-Nakagawa-Sakata (PMNS) matrix [97, 98, 26] and the  $CP$  violating phase  $\delta_{CP}$ .

The Magnetised Iron Neutrino Detector (MIND) is a large scale iron and scintillator sampling calorimeter. As a result of the studies mentioned above it is considered the baseline detector for a Neutrino Factory (NF) storing muons in the energy range 20-50 GeV [68]. Under the remit of EUROnu [99] and the International Design Study for a Neutrino Factory [100] all aspects of possible future neutrino beam facilities including accelerator, detectors and physics must be studied and compared to select the best option to determine the remaining oscillation parameters.

Previous studies of MIND focused on the topology and kinematics of neutrino events in the detector, assuming perfect pattern recognition. By smearing the kinematic variables of the participant muon and hadronic shower it was demonstrated that using a combination of

cuts on the relative length of the two longest particles in the event and the momentum and isolation of this candidate, high signal identification efficiency and background suppression could be achieved [101, 19]. However, a full study without such assumptions is necessary to fully characterise the detector response.

While MIND is essentially a large scale version of the MINOS detector [77], the nature of the NF beam – containing 50%  $\nu_e$  and 50%  $\bar{\nu}_\mu$  in the case of stored  $\mu^+$  – means that the optimisation of the analysis is somewhat different. Incorrect charge assignment (charge misidentification) of non-oscillated  $\bar{\nu}_\mu$  CC interactions present a significant possible background in this beam configuration, in addition to backgrounds from meson decays in the hadronic shower and misidentification of Neutral Current (NC) and  $\nu_e$  CC events.

This current study re-visits the problem by taking an un-biased look at the visible part of a large sample of neutrino interactions – generated using the same GEANT3 [102] simulation as in the above mentioned studies with a uniform distribution in neutrino energy – and developing pattern recognition algorithms (first presented in [103]) – described in Sec. 5.3 – to extract a candidate muon for fitting using a Kalman filter. Successful fits are then subject to offline analyses – described in Sec. 5.4 – to determine the validity of those wrong sign candidates. Analysis results are presented in Sec 5.5.

## 5.2 MIND parameterisation and expected event yields

For the purpose of the described study, MIND is a cuboidal detector of 14 m  $\times$  14 m cross-section and 40 m length, segmented longitudinally as 4 cm of iron and 1 cm of plastic scintillator for a total mass of  $\sim$ 51.0 ktonnes. No transverse segmentation was simulated, but transverse position smearing of  $\sigma = 1$  cm was carried out, corresponding to an effective segmentation of 3.5 cm. Each scintillator plane currently represents 2 view matched planes. A dipole magnetic field of mean induction 1 T in the transverse plane provides the field necessary for charge and momentum measurements.

In the first part of the analysis, event vertices were generated centred in the detector plane at 1.5 m from the front of the detector in the beam direction ( $z$ ) in order to study the nature of the backgrounds without detector edge effects. Sec. 5.4.3 discusses the expected fiducial effects when a more realistic randomly generated vertex is considered.

At a MIND placed 4000 km from the neutrino source and assuming the current best global fit oscillation parameters:  $\theta_{12} = 33.5^\circ$ ,  $\theta_{23} = 45^\circ$ ,  $\Delta m_{21}^2 = 7.65 \times 10^{-5}$  eV<sup>2</sup>,  $\Delta m_{32}^2 = 2.40 \times 10^{-3}$  eV<sup>2</sup> [79], setting  $\delta_{CP} = 45^\circ$  and calculating matter effects using the PREM model [104], the expected total number of interactions due to  $10^{21}$   $\mu^+$  decays at 25 GeV energy would be of order those shown in table 5.1, for  $\theta_{13} = 5.7^\circ$  and  $\theta_{13} = 0.2^\circ$ .

$\theta_{13}$	$\bar{\nu}_\mu$ CC	$\nu_e$ CC	$\bar{\nu}_\mu + \nu_e$ NC	$\nu_\mu$ (Signal)
$5.7^\circ$	$1.27 \times 10^5$	$3.50 \times 10^5$	$1.56 \times 10^5$	$5.92 \times 10^3$
$0.2^\circ$	$1.27 \times 10^5$	$3.60 \times 10^5$	$1.59 \times 10^5$	$1.12 \times 10^2$

Table 5.1: *Expected absolute number of interactions in a 51 ktonne MIND at a distance of 4000 km from  $10^{21} \mu^+$  decays at 25 GeV in a NF storage ring.*

Thus in order to successfully extract oscillation parameters from the golden channel, potential backgrounds from non-signal interactions must be suppressed to at most the  $10^{-3}$  level in absolute terms with sensitivity to smaller values of  $\theta_{13}$  requiring even more stringent suppression. Moreover, the existence of possible degenerate solutions due to uncertainty in the measured parameters and due to the nature of the oscillation probability (see [105, 38]) means that spectral information is required to reliably determine  $\delta_{CP}$ . This additional requirement dictates that backgrounds must be suppressed to below  $10^{-3}$  in each energy bin while maintaining an efficiency threshold below 5 GeV so that information on the rise of the first oscillation maximum is available.

## 5.3 Reconstruction tools

The reconstruction package was used to analyse a large data set comprised of Deep Inelastic Scattering (DIS) neutrino interactions of  $\bar{\nu}_\mu$  and  $\nu_e$  generated by the LEPTO61 [106] package in the energy range 0-30 GeV and tracked through the GEANT3 simulation of MIND. Considering  $\sim 10^6$  interactions each of  $\bar{\nu}_\mu$  and  $\nu_e$  CC with a dedicated study of events containing wrong sign muons from meson decay  $\nu_\mu$  CC (performed with statistics equivalent to  $5 \times 10^6$  interactions to give  $\sim 6 \times 10^5$  wrong-sign events) and  $\sim 2.5 \times 10^6$  NC interactions, the main expected backgrounds were studied.

Each event considered comprised all three dimensional points with their associated energy deposit, which were recorded in the scintillator sections of the MIND simulation, with the  $x, y$  position of these hits smeared according to a  $\sigma = 1$  cm Gaussian before analysis began.

### 5.3.1 Muon candidate extraction

After ordering the hits from smallest to greatest  $z$  position in the detector the first step of the reconstruction was to extract a candidate muon from the event. Two methods were employed to perform this task depending on the event topology: a Kalman filter incremental fit was

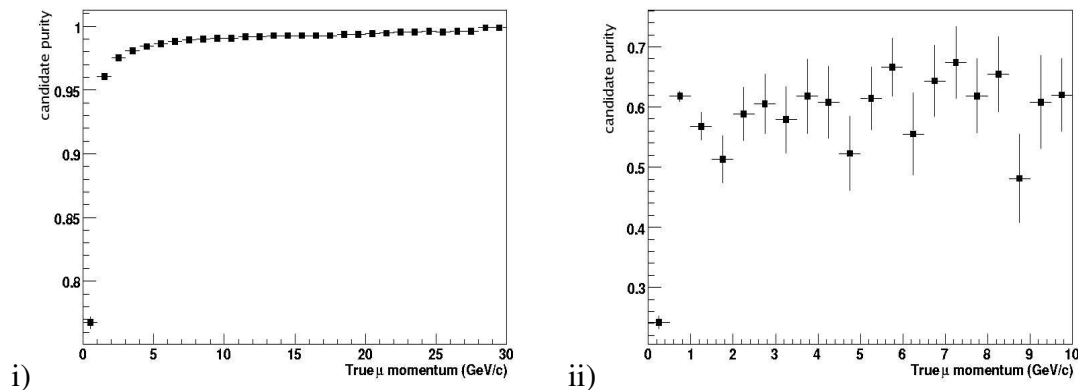


Figure 5.1: *Muon candidate purity as a function of true muon momentum for i) the Kalman filter extraction method and ii) the Cellular Automaton method.*

used to extract candidates from those events with one particle clearly longer than the others (described in Sec. 5.3.1.1), while a Cellular Automaton method was used in those events not viable for reconstruction through the first method (see Sec. 5.3.1.2). The criterion for the first category was that the five planes with activity furthest downstream should contain no more than one hit per plane.

### 5.3.1.1 Kalman Filter candidate extraction

Using the Kalman filter algorithm provided by RecPack [107] it is possible to propagate the track parameters back through the planes using a helix model, which takes into account multiple scattering and energy loss. Since, in general, a muon will act as a Minimum Ionising Particle (MIP) and will travel further in the detector than the hadronic particles, those hits furthest downstream can be assumed to be muon hits and used as a seed for the Kalman filter. The seed state is then propagated back to each plane with multiple hits and the matching  $\chi^2$  to each of the hits is computed. Hits with matching  $\chi^2$  below 20 are considered and in each plane the one with the best matching among these is added to the trajectory and filtered (the track parameters are updated with the new information). All accepted hits constitute the candidate muon and are presented for fitting (Sec. 5.3.2), with the remaining hits being considered as hadronic activity. Fig. 5.1-(left) shows the fraction of true muon hits in the candidate when using this method.

### 5.3.1.2 Cellular Automaton candidate extraction

Events with high  $Q^2$  transfer or low neutrino energy can tend to be rejected by the first method, since in general the muon will not escape the region of hadronic activity. Should this

be the case reconstruction is attempted using a Cellular Automaton. The Cellular Automaton method (based on the method described in [108]) uses a neighbourhood function to first rank all the hits and then form all viable combinations into possible trajectories.

A ‘neighbour’ is defined as a hit in an adjacent plane within a pre-defined transverse distance of the projection into that plane of the straight line connecting hits in the previous two planes. Starting from the plane with lowest  $z$  position, hits are given a rank one higher than their neighbour in the previous plane should they have one. Trajectories are then formed from every possible combination of one hit per plane starting with those of highest rank using the neighbourhood function with a stricter condition.

Those trajectories formed using this method are then subject to a number of tests to determine which is most likely to be a muon. After having a basic helix fit performed and being assessed according to their length, trajectories are rejected for being short, having high  $\chi^2$  fit or high relative curvature error (described in Sec. 5.4.1). The candidate muon is then selected as the longest remaining trajectory with the lowest  $\chi^2$ . All other hits in the event are considered to be from hadronic activity. Fig. 5.1-(right) shows the purity of the candidate when using this method.

### 5.3.2 Candidate fitting

All candidates successfully extracted from their event that have greater than six hits are presented to the fitter as a candidate muon. The same Kalman filter algorithm is used here as in Sec. 5.3.1.1. Fitting the candidate iteratively improves seeding and thus using a more constricted  $\chi^2$  condition than in the pattern recognition, the maximum number of successful, reliable fits was achieved.

With the trajectory hits ordered in increasing  $z$  position, a least squares quartic fit was performed on the section outside the planes where there was hadronic activity. This fit was used to estimate the slopes in  $x$  and  $y$  and the momentum of the candidate, to be used as a seed for the Kalman filter helix fit in the forward direction. The matching  $\chi^2$  was once again checked at each hit. Hits with greater than the pre-determined maximum (20) were ignored. In addition, the filtering process only allows a pre-determined maximum number of hits (5) to be ignored. Should this number be reached, the filtering process is aborted and the smoother uses only those hits up to this point in the candidate. This method efficiently rejects hits beyond any large angle scatter which could cause charge misidentification. Successful fits were re-seeded with the state vector at the first fitted hit and a scalar multiple (5) of the corresponding covariance matrix (taking only the diagonal elements) and then refitted.

Failed fits and those with less than 50% of their hits fitted are then fitted again in the backwards direction using the seed from the pattern recognition. Two iterations are once again

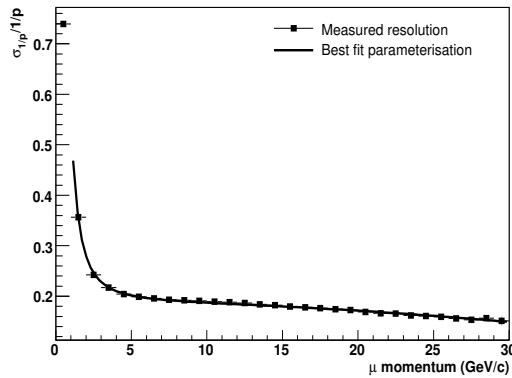


Figure 5.2: *Momentum resolution for as a function of  $\mu$  momentum.*

performed, with successful fits being accepted and those which are unsuccessful reverting to the result of the original fit.

The result of a fit being the track parameters at the projection to the event true vertex  $z$  position (3-momenta, position and charge) The momentum resolution as a function of the true primary muon momentum is shown in Fig. 5.2. Resolution is below 20% at high energies and can be parameterised as

$$\frac{\sigma_{1/p}}{1/p} = 0.19 - 4.38 \times 10^{-5} p^2 + \frac{0.37}{p^2}. \quad (5.1)$$

### 5.3.3 Hadronic reconstruction

The hadronic activity must be used to reconstruct the energy of the hadronic shower in order to ultimately reconstruct the energy of the interacting neutrino. In the absence of a well developed algorithm to perform this task due to the simplification of the hadronic shower representation in the current simulation, the current study assumes reconstruction of the hadronic energy  $E_{had}$  with a resolution  $\delta E_{had}$  equal to that recorded by the MINOS CalDet testbeam [77, 109]:

$$\frac{\delta E_{had}}{E_{had}} = \frac{0.55}{\sqrt{E_{had}}} \oplus 0.03. \quad (5.2)$$

It was demonstrated in [17] that a cut based on the isolation of the muon candidate from the hadronic shower was a powerful handle for the rejection of hadronic backgrounds. This isolation was measured via the  $Q_t$  variable:

$$Q_t = P_\mu \sin^2 \vartheta, \quad (5.3)$$

where  $P_\mu$  is the muon momentum and  $\vartheta$  is the angle between the muon and the resultant hadronic vector. This requires the reconstruction of the direction vector of the shower. The

Monolith test-beam [110] measured an hadronic angular resolution described by:

$$\delta\theta_{had} = \frac{10.4}{\sqrt{E_{had}}} \oplus \frac{10.1}{E_{had}} \quad (5.4)$$

for a similar detector. This parameterization was used to smear the hadron shower direction vector, which in combination with the reconstructed muon momentum and direction (see Sec. 5.3.2) were used to compute the  $Q_t$  variable defined above. While the design of MonoLith, MINOS and MIND are not identical there is a great deal of similarity. MINOS consists of 2.5 cm low carbon steel plates interspersed with scintillator bars read out using multi-anode photo-tubes. The energy resolution of this detector is, therefore, a very good model for the expected resolution of MIND. However, the electronics used in MINOS do not allow a reliable measurement of the hadronic angle due predominantly to cross-talk. MonoLith comprised 6 cm iron plates read out using RPCs and measured the angular resolution using a pion test beam. While the resolution of a DIS neutrino event hadronic shower would be different, the combination of the additional information available from scintillator read-out, improved scintillator/iron spacing and improved electronics – using for example silicon photomultipliers – means that while ambitious the angular resolution used in this study is not unrealistic. In this analysis the  $Q_t$  cut is applied to all events demonstrating hadronic activity with energy above a minimum level, however, particularly when electronics noise is considered, there will be some events with too little activity for the hadronic angle to be reliably reconstructed. Since only DIS interactions are considered here those events falling into this category are unlikely to be cut since the cut is only applied to events reconstructed with high energy (see section 5.4.4) and the cut is most effective against events containing decay muons where the hadronic activity is necessarily higher.

## 5.4 Analysis tools and cuts

As mentioned in Sec. 5.1 there are four main possible sources of background to the wrong sign muon search: incorrect charge assignment and high energy wrong sign muons from meson decays in  $\bar{\nu}_\mu$  CC events, and NC and  $\nu_e$  CC events wrongly identified as  $\nu_\mu$  CC. In order to reduce these backgrounds while maintaining good efficiency a number of offline cuts were employed. They can be organised in four categories: i) muon candidate quality cuts, ii)  $\nu_\mu$  CC selection cuts, iii) fiducial cuts and iv) kinematic cuts.

### 5.4.1 Muon candidate quality cuts

These cuts are related to the quality of the candidate track fit and the determination of its curvature. Two observables are considered: the  $\chi^2$  probability of the Kalman filter fit and

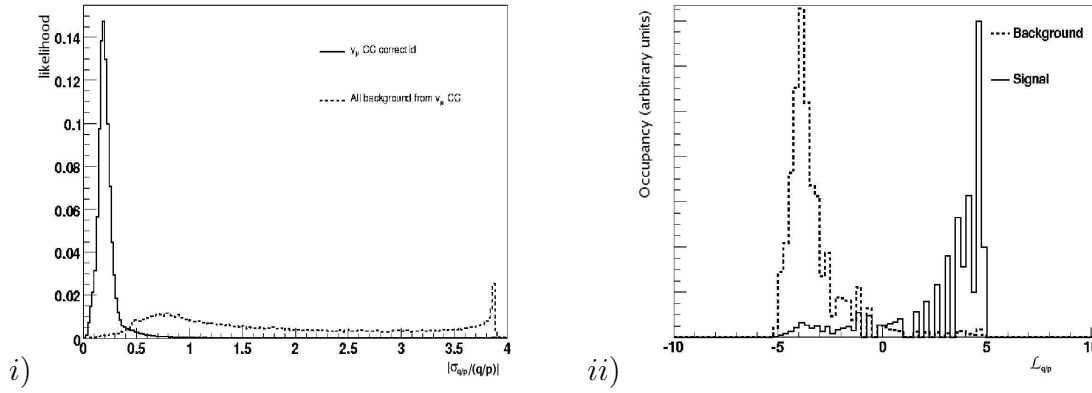


Figure 5.3: i)  $\frac{\sigma_{q/p}}{q/p}$  likelihood for signal and background from  $\bar{\nu}_\mu$  CC for all energies considered, and ii)  $\frac{\sigma_{q/p}}{q/p}$  log likelihood ratio ( $\mathcal{L}_{q/p}$ ).

the relative error of the determined curvature ( $\frac{\sigma_{q/p}}{q/p}$ ) where  $q$  is the charge as measured by the Kalman filter (1/-1). The first helps in rejecting high angle scatters or muon candidates with a large contamination from hadronic hits. The second variable is related with the probability of misidentifying the charge, and shows significant separation for correct and incorrect charge assignments for all neutrino events as shown in Fig. 5.3-(left).

It is possible to reject a large portion of possible backgrounds using sequential cuts on these two variables:

$$\left| \frac{\sigma_{q/p}}{q/p} \right| < 0.7 \text{ and } \chi_{prob}^2 > 0.9999, \quad (5.5)$$

(where  $\chi_{prob}^2$  is the  $\chi^2$  probability as calculated in the TMath class of the ROOT framework [111]). However, a slightly better rejection is found when the relative error cut is substituted by a cut on the log likelihood ratio of  $\frac{\sigma_{q/p}}{q/p}$  for signal and background (see Fig. 5.3-(right)):

$$\mathcal{L}_{q/p} > 2 \text{ and } \chi_{prob}^2 > 0.9999. \quad (5.6)$$

#### 5.4.2 $\nu_\mu$ CC selection cuts

The discrimination between  $\nu_\mu$  CC and NC interactions relies on three easily available or calculable parameters, which are those of the extracted muon candidate. Due to the similarity of MIND and MINOS the parameters employed in the MINOS analysis [52] were used. Using a high statistic data set with knowledge of the true nature of each event, distributions of these three parameters for both NC and CC events were formed into PDFs (or likelihoods).

The first parameter was the length of the candidate in terms of the number of hits which form it ( $l_{hit}$ ). This variable takes advantage of the nature of the muon as a penetrating particle and shows clear separation between  $\nu_\mu$  CC and NC events (see Fig. 5.4-(top-left)).

The second parameter is the fraction of the total visible energy – the sum of all scintillator deposits as reconstructed from the charge read-out – in the event which is in the candidate ( $l_{frac}$ ). This parameter is not useful for all events due to the high probability for both NC and CC events to have a fraction very close to or equal to one although no rise towards these values is present for NC since only DIS interactions are considered and the likelihood for a NC interaction to produce a viable candidate along with few other deposits in a DIS event is smaller than that to produce a single unaccompanied track or multiple tracks. Thus, events that fall into this category, low  $Q^2$  CC events or single pion production NC predominantly, are excluded from this distribution and do not use this parameter in their analysis. Here, while NC events demonstrate the full spectrum of possible values, signal events tend to be more concentrated at high fractions (see Fig. 5.4-(top-right)). However, high  $Q^2$  CC events will tend to exhibit NC like behaviour.

While the third parameter used by MINOS is the mean energy deposited per plane for the candidate, the current simulation setup of MIND does not exhibit sufficient separation in this parameter for effective analysis. This effect is most likely due to the simplification of the hadronic shower development in the current version of the simulation. Thus, in place of this parameter the variance of the deposit is used ( $l_{var}$ ), shown in Fig. 5.4-(bottom).

The likelihood ratio for each of the three observables was computed and combined in three main log likelihood discriminators described in Eqs. 5.7 to 5.9:

$$\mathcal{L}_1 = \log \left( \frac{l_{hit}^{CC} \times l_{frac}^{CC} \times l_{var}^{CC}}{l_{hit}^{NC} \times l_{frac}^{NC} \times l_{var}^{NC}} \right) \quad (5.7)$$

$$\mathcal{L}_2 = \log \left( \frac{l_{2D}^{CC} \times l_{hit}^{CC}}{l_{2D}^{NC} \times l_{hit}^{NC}} \right) \quad (5.8)$$

$$\mathcal{L}_3 = \log \left( \frac{l_{hit}^{CC^{frac=1}} \times l_{var}^{CC^{frac=1}}}{l_{hit}^{NC^{frac=1}} \times l_{var}^{NC^{frac=1}}} \right) \quad (5.9)$$

$\mathcal{L}_1$  is formed from the multiplication of the likelihoods mentioned above while  $\mathcal{L}_2$  is formed by the multiplication of the  $l_{hit}$  likelihood and a 2 dimensional likelihood of the variance and energy fraction ( $l_{2D} = l_{hit} : l_{frac}$ ), such a distribution allows for the consideration of correlations between the parameters.  $\mathcal{L}_1$  or  $\mathcal{L}_2$  are used when the energy fraction is less than 0.999 and  $\mathcal{L}_3$  otherwise. Distributions of these discriminators for samples of  $\nu_\mu$  NC and CC events are shown in Fig. 5.5.

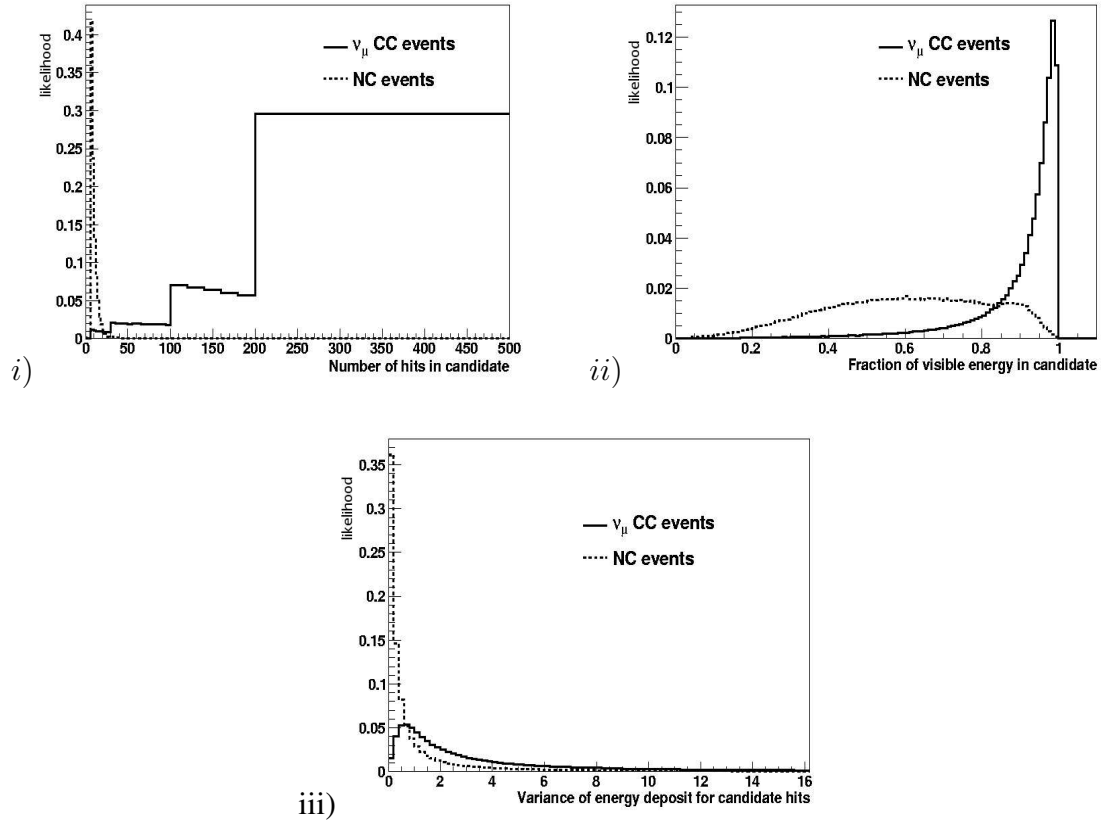


Figure 5.4: *PDFs of the three parameters used for NC/CC likelihood separation. i) Number of hits in candidate  $l_{hit}$ , ii) Fraction of visible energy in candidate  $l_{frac}$  and iii) Variance of energy deposit in candidate  $l_{var}$ .*

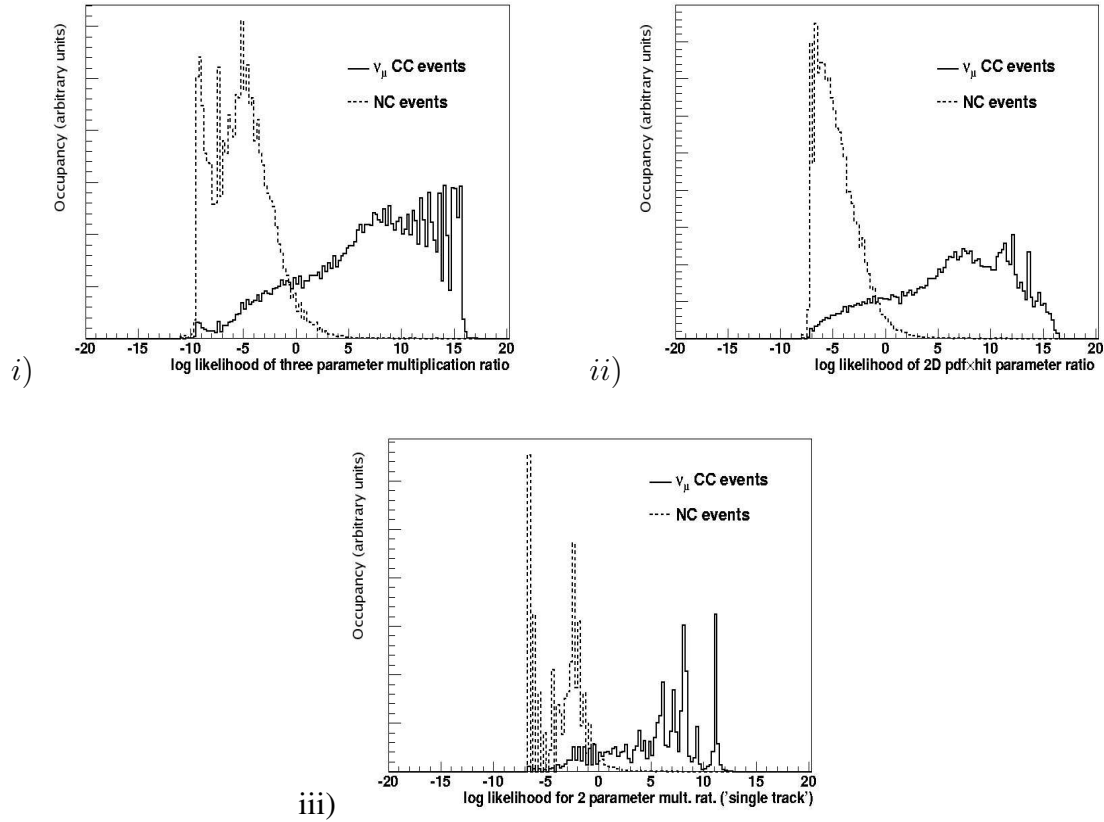


Figure 5.5: Log likelihood discriminator distributions for energy fraction  $< 0.999$ , i)  $\mathcal{L}_1$ , defined in Eq. 5.7, ii)  $\mathcal{L}_2$ , defined in Eq. 5.8 and iii) for energy fraction  $\geq 0.999$ ,  $\mathcal{L}_3$ , defined in Eq. 5.9.

### 5.4.3 Fiducial cuts

Events originating near the edges of the detector can leave the sensitive volume. This will result not only in the loss of event energy and thus worsened energy resolution but, due to the shortening of the event, can cause a misidentification of the charge of a candidate. While the shortening of the event has the potential to reduce backgrounds from NC and  $\nu_e$  CC as there should be less viable candidates, viable signal can also be lost, with a corresponding increase in charge misidentification background. Therefore, it is recommendable to apply a fiducial volume cut so that these pathologies are minimised. Specifically, events are rejected should their candidate have both its first hit within 50 cm of the sides or back of the detector and its last within 10 cm. In sec. 5.5.1.3, the edge effects and their suppression are presented using  $\bar{\nu}_\mu$  CC events as a model since they should affect little or no increase on NC and  $\nu_e$  CC backgrounds and any small variation should be of the same spectral form as those seen in  $\bar{\nu}_\mu$  CC events.

### 5.4.4 Kinematic cuts

Considering the remaining signal and background after applying all cuts described above, the  $Q_t$  (see Sec. 5.3.3) and muon candidate momentum ( $P_\mu$ ) distributions are those shown in Fig. 5.6. A clear separation between signal and background events is observed. In particular, background events are concentrated at very low  $Q_t$ , while the signal exhibits much larger  $Q_t$  values. In order not to reduce the efficiency at low neutrino energy, cuts on these two variables are only applied for reconstructed neutrino energy ( $E_\nu$ ) above 7 GeV. The applied cuts are those of Eq. 5.10:

$$P_\mu \geq 0.2 \cdot E_\nu \quad \text{and} \quad Q_t > 0.25 \text{ GeV}/c \quad \text{for } E_\nu > 7 \text{ GeV}. \quad (5.10)$$

### 5.4.5 Summary of analysis cuts

As will be dicussed in the next section the most successful set of cuts is given below in table 5.2.

## 5.5 Analysis Results

Using a large data set and the analyses described above the efficiency and rejection power of MIND has been studied.

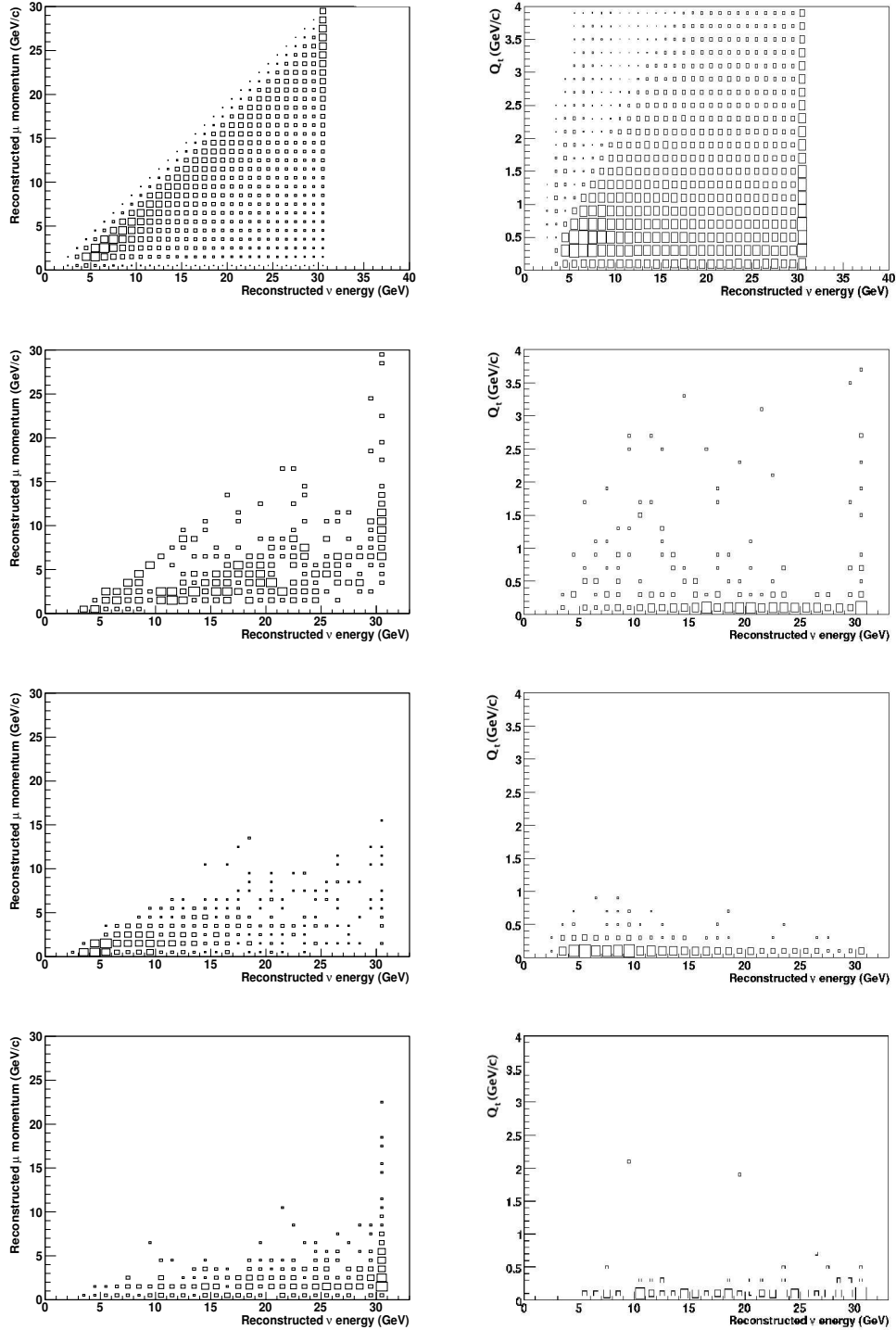


Figure 5.6: *Distributions of kinematic variables: Reconstructed muon momentum (left) and  $Q_t$  variable in GeV/c units (right) versus reconstructed neutrino energy, for (top→bottom) signal,  $\bar{\nu}_\mu$  CC backgrounds, NC background and  $\nu_e$  CC background. All events reconstructed with energy  $> 30$  GeV are shown in an overflow bin.*

Cut type	Cut value
Fiducial	if $ r_i^{first} - r_i^{det}  \leq 50 \text{ cm}$ , $ r_i^{last} - r_i^{det}  > 10 \text{ cm}$ for $r_i = x, y, z$
Track quality	$\mathcal{L}_{q/p} > 2.0$ and $\chi_{prob}^2 > 0.9999$
$\nu_\mu$ CC selection	$\mathcal{L}_1 > 0$ for $l_{frac} < 0.999$ $\mathcal{L}_3 > 0$ for $l_{frac} \geq 0.999$
Kinematic	$P_\mu \geq 0.2 \cdot E_\nu$ and $Q_t > 0.25 \text{ GeV}/c$ for $E_\nu > 7 \text{ GeV}$

Table 5.2: Summary of analysis cuts.

### 5.5.1 $\bar{\nu}_\mu$ charge current interactions

The background from  $\bar{\nu}_\mu$  interactions can be separated in two different contributions: i) fake wrong-sign muons from charge misidentification of the primary muon (mainly) and from pion to muon confusion, and ii) true wrong-sign muons from the decay of hadrons.

#### 5.5.1.1 Incorrect charge assignment

The charge misidentification background was studied using  $\bar{\nu}_\mu$  interactions where events containing hadronic decays to  $\mu^-$  were excluded to be considered separately (Sec. 5.5.1.2). An event is considered background if a candidate is successfully extracted and fitted with charge opposite to that of the true primary muon. Background events are mainly due to incorrect charge assignment to the true primary muon (due to multiple scattering or impurity of the candidate), but have a small contribution from penetrating hadrons (mainly pions) which are identified as muon candidates when the true primary muon has low momentum and is not correctly identified.

As shown in Fig. 5.7-(left) this background can be efficiently suppressed by cutting on the track quality variables, described in Sec. 5.4.1. Further rejection is obtained by applying  $\nu_\mu$  CC selection cuts (see Fig. 5.7-(right)).

#### 5.5.1.2 Wrong sign muons from hadron decays

The production and decay of negatively charged mesons in the hadronic part of a DIS interaction has high probability to produce a  $\mu^-$ . Particularly mesons containing charm will decay promptly and produce high energy muons which can be selected as primary muon candidates when the true primary muon is not correctly identified (in general when it has low momentum). Suppression of this background is particularly important due to the high level of uncertainty on the value of the charm production cross section [82]. Track quality and

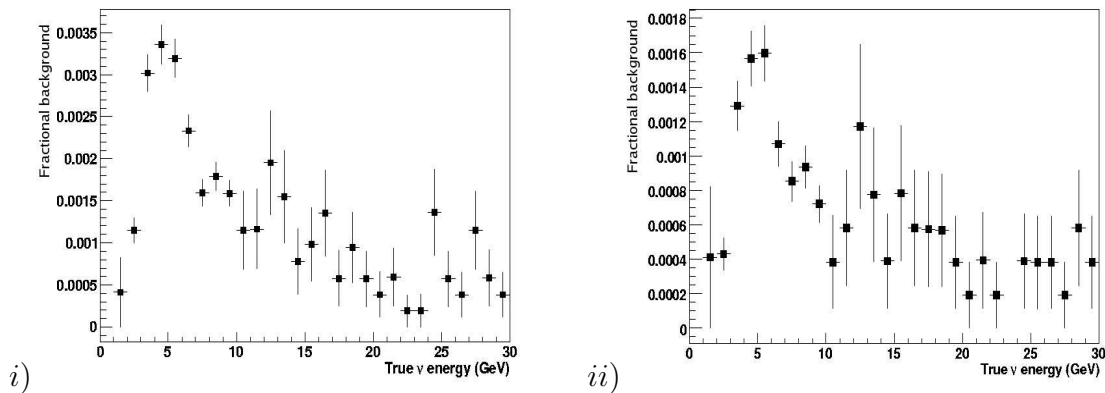


Figure 5.7: Charge mis-assignment and hadron to muon mis-identification background i) with track quality cuts only and ii) including  $\nu_\mu$  CC selection cuts.

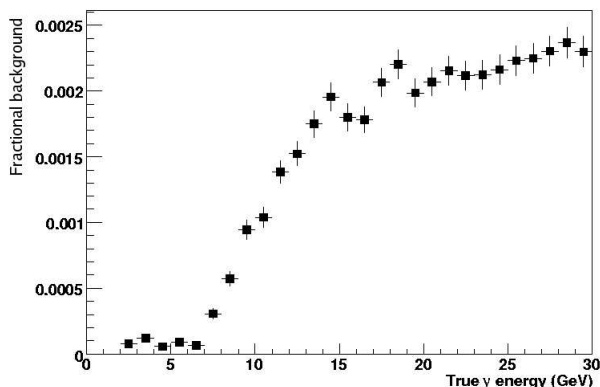


Figure 5.8: Wrong sign muon decay background with track quality and  $\nu_\mu$  CC selection cuts.

$\nu_\mu$  CC selection cuts are effective in reducing this type of background for low neutrino energies, but the suppression of high energy background requires further cuts, which are described below.

### 5.5.1.3 Inclusive $\bar{\nu}_\mu$ background with fiducial and kinematic cuts

Considering a set of  $\bar{\nu}_\mu$  CC events generated randomly throughout the detector volume the inclusive background from this type of interaction has been studied. An additional cut on those events with a candidate failing the fiducial volume cut, defined in Sec. 5.4.3, is used to suppress background caused by edge effects. As can be seen in Fig. 5.9-(left), the additional background introduced by edge effects is almost compensated by the fiducial cut, leading to an inclusive  $\bar{\nu}_\mu$  background similar to the addition of the ones shown in Figs. 5.7-(right) and 5.8.

The high energy background of Fig. 5.9-(left) is mainly due to very hard muons from the decay of charm mesons. Fortunately these muons, due to their decay origin, tend to be embedded in the hadron shower unlike a true primary muon. Thus the  $Q_t$  variable should be very effective in rejecting this kind of event. As can be seen in Fig. 5.9-(right) the kinematic cuts afford a sizeable suppression, particularly at higher neutrino energy.

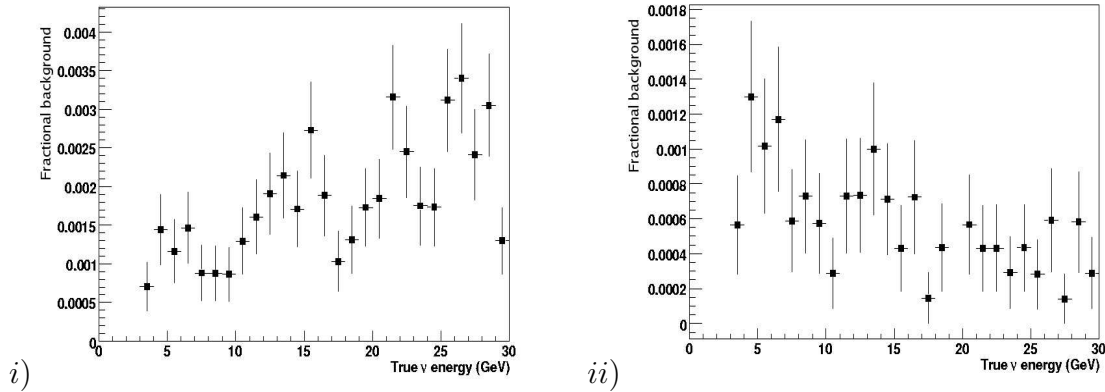


Figure 5.9: *Expected background from  $\bar{\nu}_\mu$  CC interactions when events are randomly generated in the entire detector: i) after track quality,  $\nu_\mu$  CC selection and fiducial cuts, and ii) including kinematic cuts.*

## 5.5.2 Neutral current interactions

Neutral current interactions should be of the same nature for all species. Background events will tend to originate from penetrating pions or muons from the decay of hadrons. Moreover, since there will always be missing energy in the event, those events successfully fitted will tend to be reconstructed at lower energy than the true neutrino energy. As such and due to the large amount of NC events expected in the detector, this background must be suppressed efficiently. Fig. 5.10 shows the evolution of the NC background when different cuts are included.

## 5.5.3 $\nu_e$ charge current interactions

The interactions of  $\nu_e$  present in the beam can also produce some background to the signal. While the electron itself will be stopped quickly and will shower far more than a muon, penetrating pions or decay muons originating in the hadronic shower can be mistaken for primary muons.

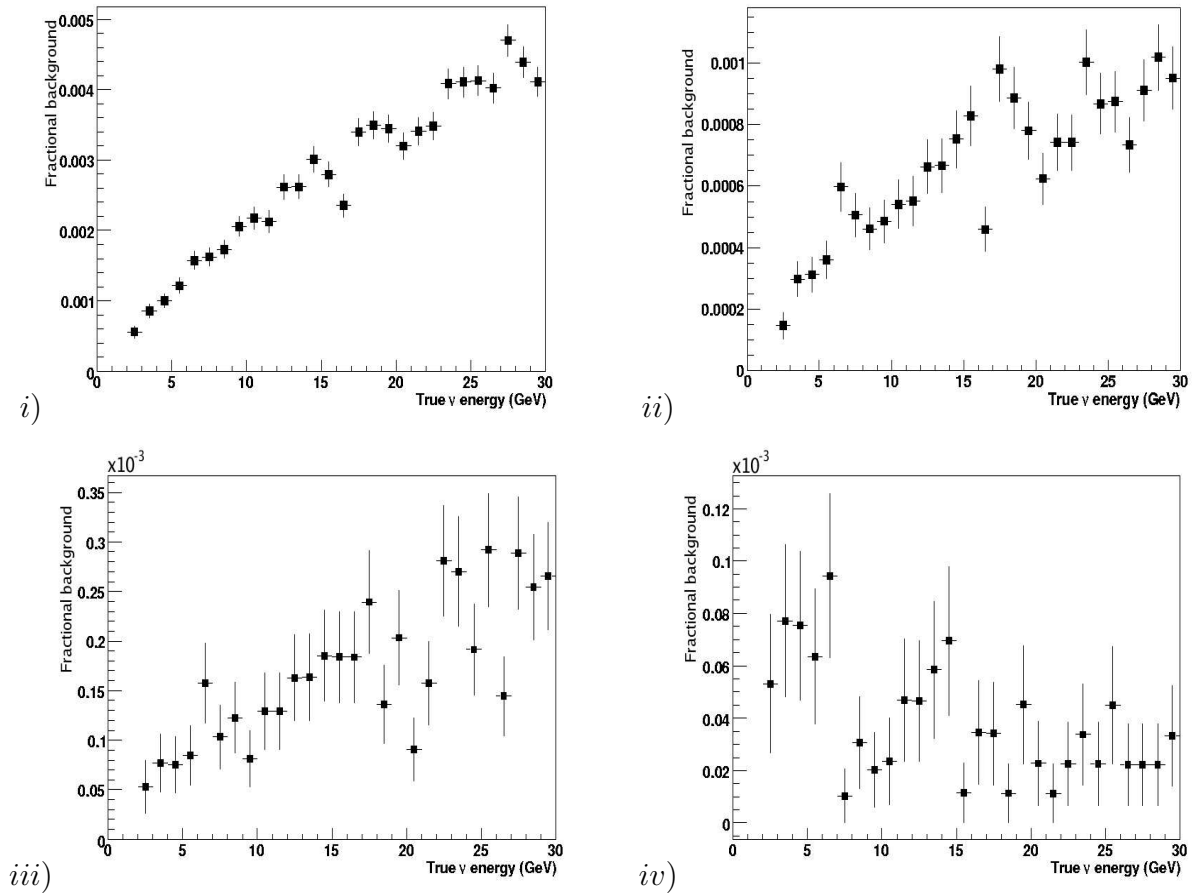


Figure 5.10: *Expected background from  $\bar{\nu}_\mu$  NC interactions, i) with track quality cuts (Eq. 5.5) only, ii) including  $\nu_\mu$  CC selection cuts, iii) substituting track quality cuts of Eq. 5.5 by those of Eq. 5.6 and iv) including kinematic cuts.*

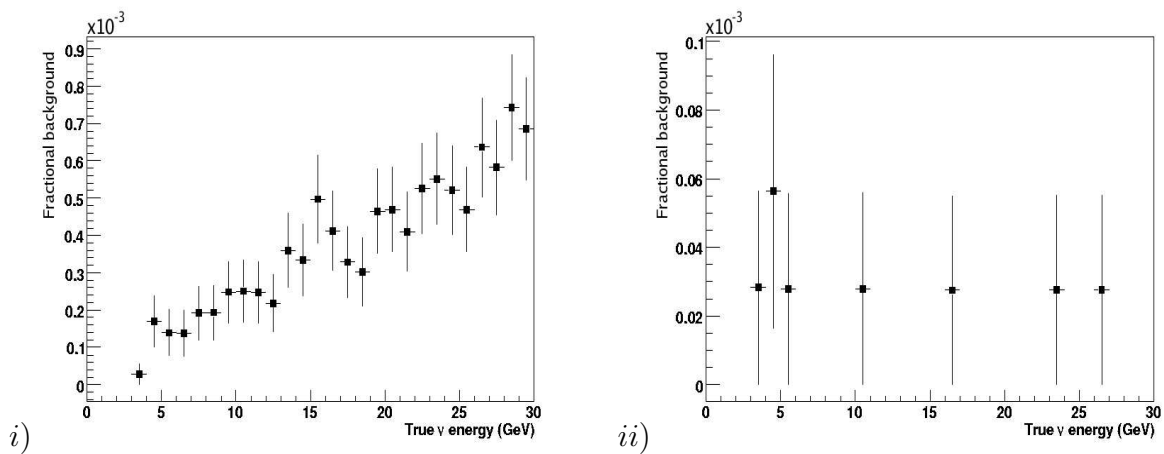


Figure 5.11:  *$\nu_e$  CC background to golden channel signal, i) with track quality and  $\nu_\mu$  CC selection cuts, and ii) including kinematic cuts.*

After application of track quality and  $\nu_\mu$  CC selection cuts it can be seen in Fig. 5.11-(left) that the  $\nu_e$  CC background can be reduced to a similar level as the NC background when the same cuts are applied. Moreover, excellent rejection for high energy neutrinos is obtained by applying kinematic cuts, as shown in Fig. 5.11-(right). This is because the candidate muon in  $\nu_e$  events tends to have lower momentum than in NC events, as shown in Fig. 5.6 .

### 5.5.4 Summary

	Total	0 – 5 GeV	5 – 10 GeV	10 – 30 GeV
$\bar{\nu}_\mu$ CC	$5.5 \times 10^{-4}$	$6.6 \times 10^{-4}$	$8.2 \times 10^{-4}$	$4.6 \times 10^{-4}$
$\nu_e$ CC	$7.8 \times 10^{-6}$	$2.6 \times 10^{-5}$	$5.5 \times 10^{-6}$	$5.5 \times 10^{-6}$
$\bar{\nu}_\mu + \nu_e$ NC	$3.8 \times 10^{-5}$	$6.8 \times 10^{-5}$	$4.3 \times 10^{-5}$	$3.1 \times 10^{-5}$
$\nu_\mu$ (signal)	0.64	0.25	0.66	0.69

Table 5.3: *Summary of expected fractional signal and background with true neutrino energy.*

Considering all types of events mentioned above and applying the most successful analysis chain described in table 5.2 the resulting signal efficiency and fractional backgrounds are those summarized in table 5.3. The evolution of the backgrounds for the different cuts is in Figs. 5.9, 5.10 and 5.11, while similar plots for the signal efficiency are those of Fig. 5.12. While it is obvious that the effect of the kinematic cuts below 7 GeV true neutrino energy is small due to their application only to events reconstructed with energy greater than this value, it is important to remark that fiducial cuts do not affect the efficiency at low energies either.

Another important question is that of the relation between the true and the reconstructed neutrino energy for the different interaction types. The response matrices are shown in Fig. 5.13 and presented numerically in appendix A.

## 5.6 Conclusions

Through a combination of fiducial, track quality,  $\nu_\mu$  CC selection and kinematical cuts, an analysis has been applied demonstrating the power of MIND to detect and identify  $\nu_\mu$  CC DIS interactions in the presence of realistic reconstruction of the primary muon. The efficiency threshold currently lies between 3 and 4 GeV, and an efficiency plateau of 70% is reached at about 6 GeV. While improved sensitivity could be achieved by lowering the

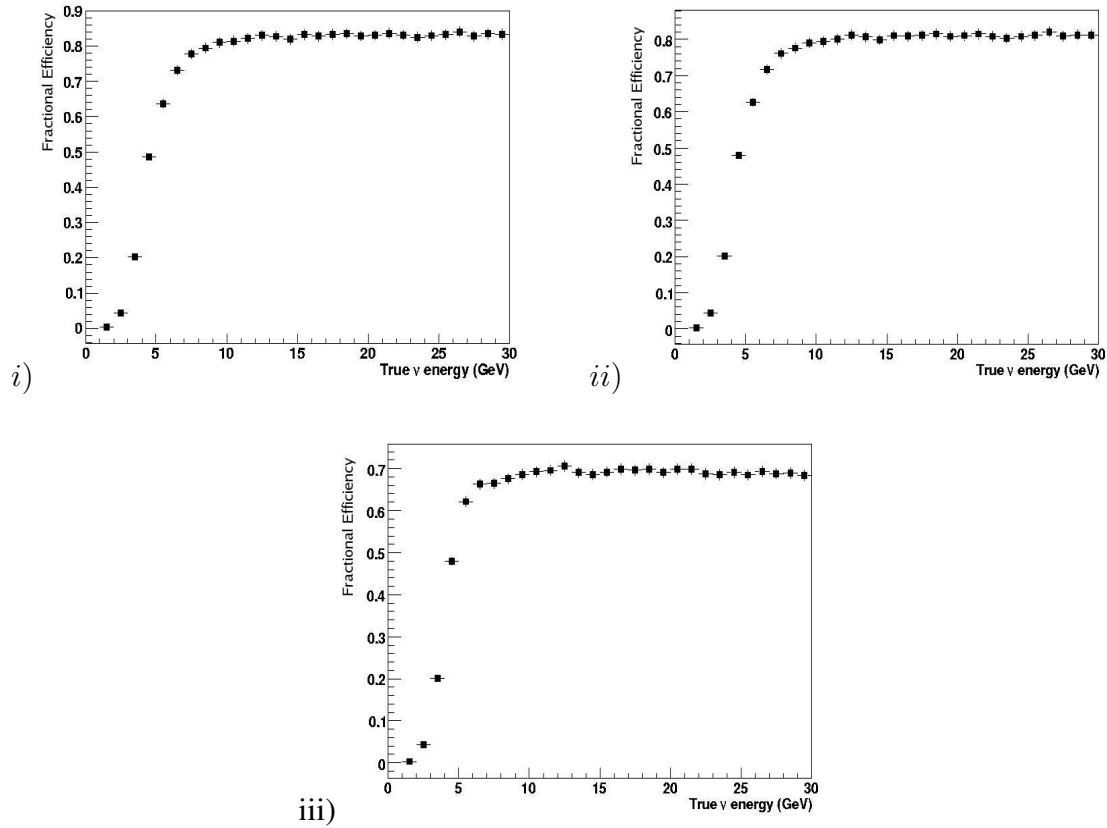


Figure 5.12: *Expected signal identification efficiency: i) after track quality and  $\nu_\mu$  CC selection cuts, ii) including fiducial cuts, and iii) including kinematic cuts.*

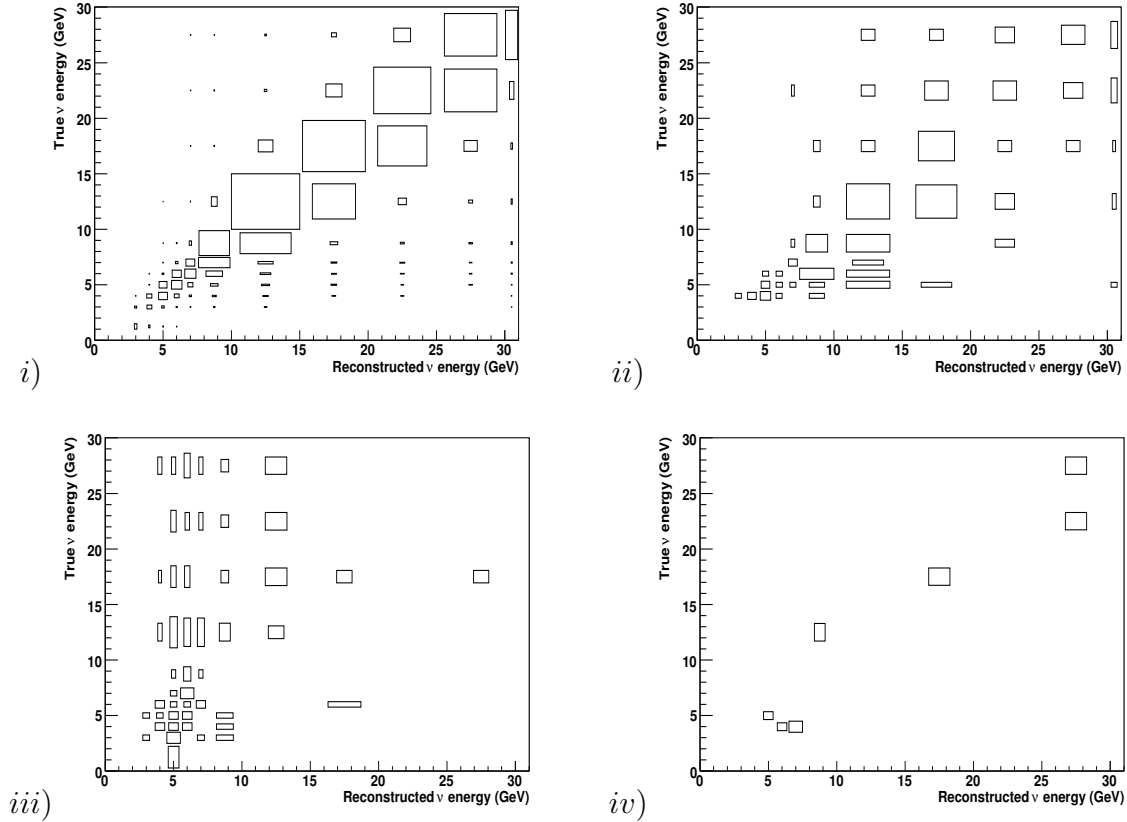


Figure 5.13: Response matrix in true/reconstructed neutrino energy for signal and backgrounds: *i*) signal efficiency, *ii*) backgrounds from  $\nu_\mu$  CC, *iii*) NC and *iv*)  $\nu_e$  CC. The area of the rectangles is proportional to the relative size of the response matrix element.

threshold, as mentioned in Sec. 5.2, this region would be dominated by quasi-elastic and resonance interactions which have not yet been considered due to the overall dominance of DIS interactions. This study was carried out using LEPTO61, which contains only DIS interactions, in order to perform a direct comparison to the efficiencies obtained in previous studies [17, 68, 19]. Especially quasi-elastic interactions should contain less hadronic activity and thus the low energy pattern recognition efficiency should improve. An increased sample of successfully reconstructed events in this region should increase the efficiency of the golden channel analysis particularly since other methods for neutrino energy reconstruction exist in this region which do not require hadronic calorimetry. While it is likely any background present due to these low energy interactions could not be excluded using the kinematic cuts mentioned above, isolation from the hadronic shower becomes irrelevant and exclusion can be achieved through the combination of the neutral current rejection parameters and fit quality.

The powerful rejection afforded by the inclusion of the hadronic energy and direction vector highlights the importance of good hadronic reconstruction. While the hadronic energy has been reconstructed well in other similar experiments the direction vector requires careful consideration of both technology and analysis to achieve the required resolution. In the next chapter, an optimised MIND design will be included, within a GEANT4 framework, where low energy quasi-elastic and resonance interactions will also be taken into account.

Compared to the baseline MIND presented in [68], where perfect pattern recognition was assumed, these new results show some improvement. The aforementioned study considered the charge and NC backgrounds and in both cases the results presented here are of similar level. The signal efficiency curve reaches a plateau at 70% in the bin of 6 – 7 GeV. The corresponding curve in the previous study reaches approximately the same level at a similar or slightly higher energy depending on the particular analysis. Using the efficiency curve in [68], Neutrino Factory sensitivity studies were carried out in the context of the International Scoping Study (ISS) for a future neutrino facility [112], demonstrating that a NF with two 50 ktonne MIND detectors at two different baselines has the largest  $\theta_{13} - \delta_{CP}$  coverage out of all possible facilities. This paper reinforces the conclusions from that study by showing that the pattern recognition and reconstruction of events in MIND do not degrade the selection efficiency for the oscillated signal.

# Chapter 6

## The Golden Channel oscillation signal with a Magnetised Iron Neutrino Detector

### 6.1 Introduction

In conjunction with the development of reconstruction algorithms for MIND, an entirely new simulation was developed in collaboration with colleagues at IFIC, Valencia, using the Nuance event generator and Geant4. This simulation will ultimately allow for a full optimisation of MIND in terms of segmentation, technology and analysis. Described here is work undertaken by the author in developing the simulation and digitization as well as the application and re-optimization of the reconstruction algorithm described in chapter 5. Additionally, the analysis described in chapter 5 was re-optimised and the resultant efficiencies were used in chapter 7 to evaluate the expected sensitivity of the combination of MIND and a 25 GeV Neutrino Factory to key oscillation parameters.

### 6.2 Neutrino event generation

As mentioned in chapter 5, generation of neutrino events in MIND was previously performed using the LEPTO61 package. Although, the deep inelastic scattering (DIS) events generated using this program will dominate over the majority of the energy region of interest for the neutrino factory there are other important processes which must be considered especially at low energies where the oscillation signals exhibit most variation.

As can be seen from Fig. 6.1, there are three processes of significant importance in the NF energy range. Particularly at energies below 5 GeV there should be a large contribution from

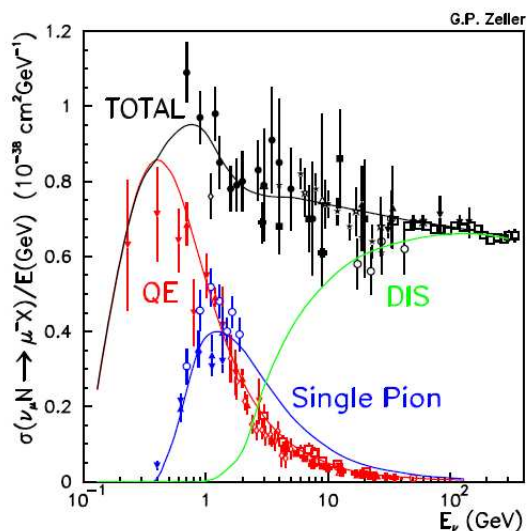


Figure 6.1: Experimentally measured cross-sections for Quasi-elastic, single pion and deep inelastic  $\nu_\mu$  CC interactions with the predictions made by Nuance [16].

quasi-elastic (QE) and single pion production (1pi) events. A QE event is well described by the interaction of the neutrino with a nucleon as a whole in a process of the form:  $\nu_\mu + n \rightarrow \mu^- + p$ . The energy of such an event is very easily reconstructed from the momentum of the muon and the angle it makes with the beam direction. In addition, the low multiplicity of the event makes muon reconstruction simpler. 1pi events should also improve the purity of low energy region candidates due to their low multiplicity, however, in cases where the pion produced is penetrating or decays to a muon there is also the possibility of increased background due to reconstruction of a candidate which is not a  $\nu_\mu$  ( $\bar{\nu}_\mu$ ) CC primary muon. There are also other types of interaction which are more highly suppressed. There will be contributions from nuclear resonances, particularly those classified as producing 2 or 3 pions, as well as small contributions from diffractive and coherent production.

Generation of all types of interaction was achieved using the Nuance framework [113]. The relative proportions of interaction types generated by Nuance are shown in Fig. 6.2 where ‘other’ interactions include the resonant and diffractive processes other than single pion production mentioned above. These distributions are consistent with that expected and as such can be passed to a simulation of the detector with confidence. Nuance attempts also to simulate the effect of re-interaction within the participant nucleon which is particularly important for low energy interactions in high Z targets like iron. The interacting and resultant particles are listed in text format along with information on their energies and momenta and the type of neutrino interaction. These events can easily be read into a detector simulation.

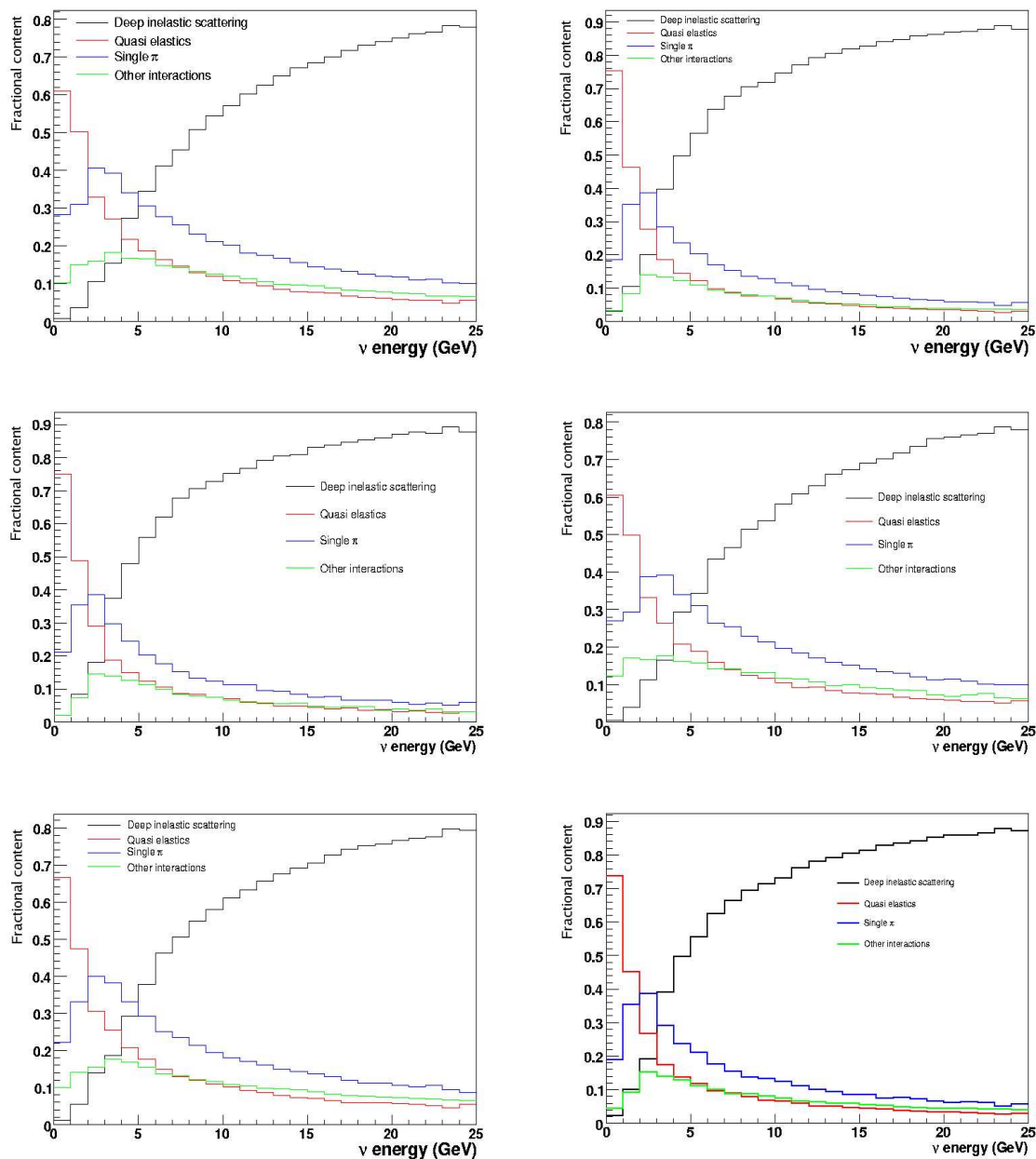


Figure 6.2: Proportion of total number of interactions of different  $\nu$  interaction processes for events generated using Nuance and passed to the G4mind simulation. (top)  $\bar{\nu}_\mu$  (left) and  $\nu_e$  CC (right), (middle)  $\nu_\mu$  (left) and  $\bar{\nu}_e$  CC (right) and (bottom) NC from antineutrinos (left) and neutrinos (right).

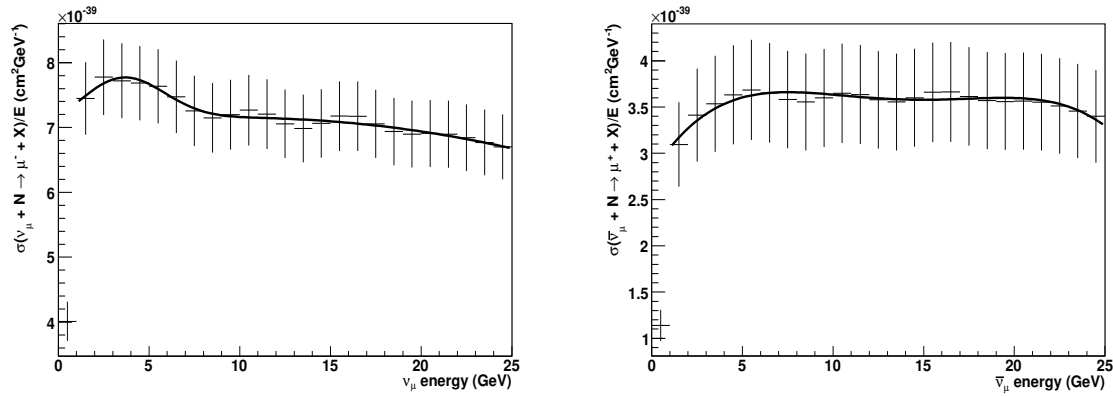


Figure 6.3: *Exclusive cross-section parameterisation for  $\nu_\mu$  CC (left) and  $\bar{\nu}_\mu$  CC interactions (right).*

Using the flux spectrum used to generate the events and the resultant interaction spectrum the cross-section as a function of energy can be estimated by normalising the highest energy bin to the high energy limit –  $0.67 \times 10^{-38} \text{ cm}^2 \text{ GeV}^{-1}$  for  $\nu_\mu$  and  $0.34 \times 10^{-38} \text{ cm}^2 \text{ GeV}^{-1}$  for  $\bar{\nu}_\mu$  [25]. As can be seen in Fig. 6.3 a parameterisation can be fitted to the cross-section distribution and used to calculate absolute number of interactions expected for a given flux. The parameterisations extracted here will be discussed in greater detail in section 7.1 where they will be used to calculate expected interaction spectra in MIND.

### 6.3 Simulation of MIND using Geant4

A new simulation of MIND utilising the Geant4 toolkit [114] has been developed in collaboration with colleagues in Glasgow and Valencia. The simulation was designed to give as much flexibility to the geometry as possible so that an optimisation of all aspects of the detector could be carried out. The dimensions and spacing of all scintillator and iron pieces as well as all external dimensions of the detector can be controlled. This will allow for easy comparison of the simulation itself and the subsequent analyses to other potential NF detectors. Moreover, the ability to perform a direct comparison with an existing detector like MINOS [77] would lend considerable weight to any results published from this exercise.

In the iteration of the MIND design presented here a rectangular detector cross-section is used in which the transverse extent (*x and y dimensions*) and length in the beam direction (taken as transverse to the detector face, *z dimension*) are controlled from a parameter file. A dipole magnetic field of mean induction 1 T pervades the detector volume in the positive *y* direction. Data files generated using Nuance were read into the simulation with all final state

particles of the Nuance interaction being treated as primary particles for tracking through the MIND volume. Two data files are provided: one with events generated on iron nuclei and another where the events are generated on the nuclei in polystyrene. The file to be read for a given event is selected by a random generator according to the relative number of nucleons available in the two materials. An event vertex is then generated within one of the slabs of the appropriate material randomly positioned in three dimensions. Physics processes are modelled using the QGSP\_BERT physics lists provided by Geant4. This particular set was chosen due to its recommendation for calorimetry and tracking detectors (the implementation of the physics list is described in [115]). In addition, optimisation of the simulation requires the introduction of certain cuts selected to reduce simulation time without reducing the quality of the model.

In the current set-up, secondary particles are required to be predicted to travel at least 30 mm from their production point or to cross a material boundary between the detector subvolumes to have their trajectory fully tracked. In the case where they do not pass this cut, particles are only considered by processes which control the production of other particles. In addition, all particle types other than gammas and positive and negative muons are only fully tracked until their kinetic energy reduces to 100 MeV with the same processes as mentioned above still considered beyond this point. Gammas are excluded from this cut because they only take part in discrete processes. Muons were excluded as their interactions at the end point could be important to the pattern recognition.

In order to obtain the optimal amount of information from the simulation without increasing simulation time due to excessive readout, an event model must be defined. The studies of MIND require the truth information of the primary particles and any particles resultant of hadronic decays which could constitute background to the oscillation signal. Additionally, as much information as possible about the energy deposits in the scintillator layers is required. Persistency is achieved using the BHEP framework<sup>1</sup> which uses C++ classes to represent particles and events and uses ROOT trees to hold the data. Kinematic information about the initial interacting neutrino and nucleon is stored along with all kinematic and tracking information about the primary resultant particles. Particles from decays and those resultant from the nuclear interactions of the primary particles also have all kinematic variables saved and additionally are symbolically linked from the particle whose decay they originate (their mother particle). All of these particles have any scintillator deposits which they leave associated to them with full three dimensional position and energy deposit being saved. The kinematical information of all remaining particles – particularly those from showering – is not necessary to understand the event and as such is not saved. However, should one of these

---

<sup>1</sup>BHEP is a data persistency tool which was used by the HARP and K2K collaborations.

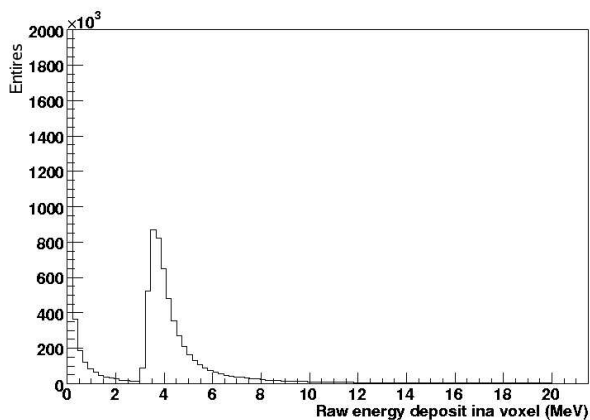


Figure 6.4: *Voxel raw energy deposit showing a peak at  $\sim 4$  MeV above a noise background.*

additional particles deposit energy in a scintillator plane, the position and energy of this deposit is associated to one of two 'shower particles'. The shower particles are essentially maps of hits with one containing the deposits of particles who ultimately find their origin in the hadronic part of the interaction and the other containing those whose origin is associated to any primary lepton present (that is the lepton resultant from the charge current interaction of a neutrino).

The analysis results described below were carried out using a MIND with a cross section of  $14\text{ m} \times 14\text{ m}$  and 3 cm of iron for every 2 cm of polystyrene extruded plastic scintillator. The simulated length of 40 m would correspond to a mass of just greater than 40 kTon, however, since the detector is already larger than the greatest longitudinal extent of any particle from a 25 GeV interaction, the efficiency curves can be applied without loss of generality to a larger detector of the same geometry.

## 6.4 Digitization

Ultimately the digitization of the hit information from Geant4 will be carried out by a full light passage simulation of appropriately shaped scintillator bars. However, for the purpose of these studies a simplified parameterisation is considered where two dimensional boxes – termed voxels – represent view matched x,y readout positions. Any deposit which falls within a voxel has its energy deposit added to the voxel total raw energy deposit. The thickness of two centimetres of scintillator per plane assumes 1 cm per view. Fig. 6.4 shows the distribution of raw energy deposit in the voxels.

Voxels with edge lengths of 3.5 cm were chosen. As can be seen from Fig. 6.5 deposits are evenly distributed across the voxels. This results in a position resolution of

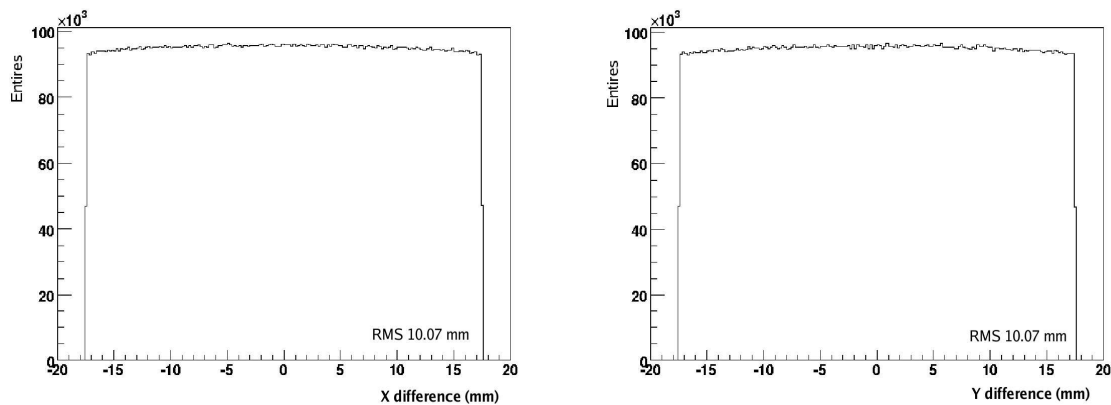


Figure 6.5: *Difference of voxel position and contained deposit positions.*

$3.5/\sqrt{12} \cong 1$  cm, analogous to the resolution assumed in the initial reconstruction studies of MIND presented in chapter 5. The raw deposit energy of each voxel is used to approximate the response of the scintillator bars assuming readout using wavelength shifting (WLS) fibres with attenuation length  $\lambda = 5$  m as reported by the MINERvA collaboration [116]. Assuming that approximately half of the energy will come from each view the deposit is halved and the remaining energy at each edge in x and y is calculated. This energy is then smeared according to a gaussian with  $\sigma/E = 6\%$  to represent the response of the electronics and then recombined into x, y and total = x+y energy deposit per voxel. At this point the size of the deposits in each plane must be assessed as to whether they are viable. Assuming an output wavelength of 525 nm and that electronics with a quantum efficiency of  $\sim 30\%$  could be achieved, it was required that there should be enough energy remaining at the readout planes to make at least 4.7 photo electrons (pe) as in MINOS [77]. Any voxel whoses two views do not make this cut is not saved. Should only one view pass, the failing view is excluded from any subsequent calculations (described in section 6.5). The digitization of an example event is shown in Fig. 6.6.

## 6.5 Reconstruction and analysis of Geant4 MIND

The reconstruction and analysis packages are described in detail in chapter 5. However, the added complexity of events generated in the new framework require some changes to both. All events used here in the optimisation of cuts and extraction of efficiencies were generated using a flux profile, designed to maximise statistics in all energy bins of interest. While a slight change in the likelihood distributions would be expected using a neutrino factory flux profile any slight change in the efficiencies is outweighed by the loss of statistics in key low

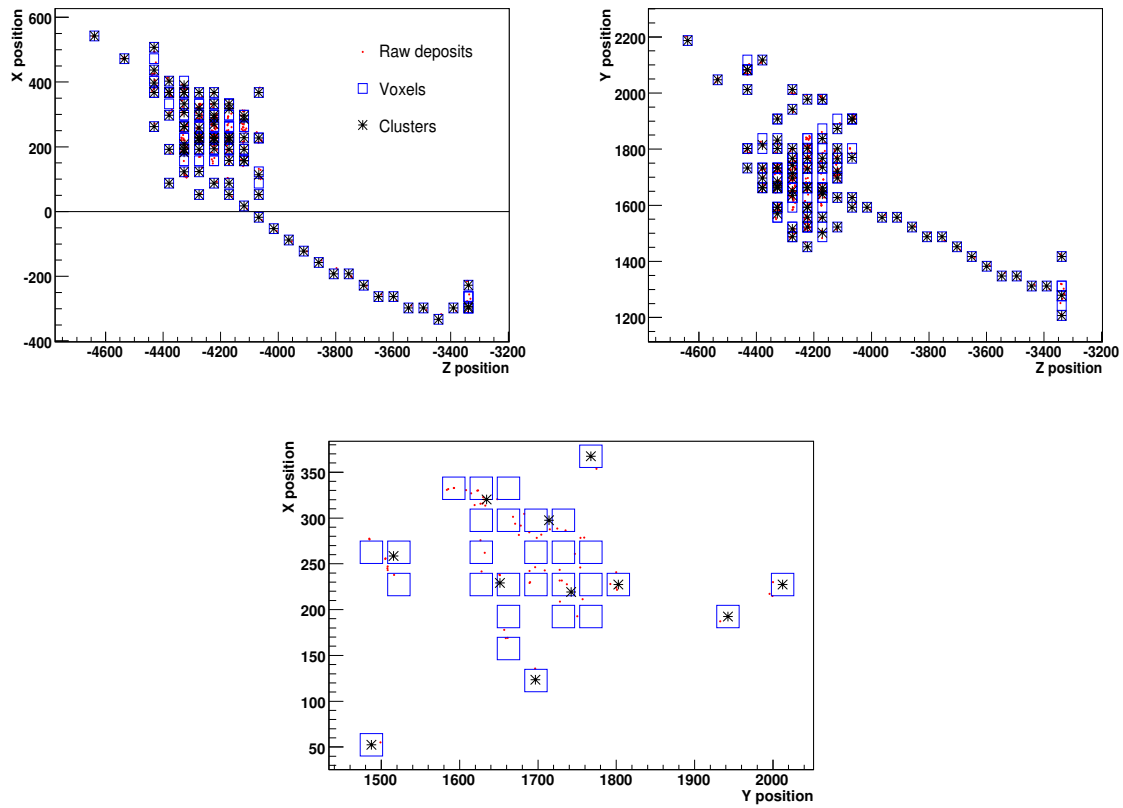


Figure 6.6: *The digitization and voxel clustering of an example event: (top left) bending plane view, (top right) non bending plane, (bottom) an individual scintillator plane. The individual hits are small dots (in red), the blue squares are the voxels and the black asterisks represent the centroid positions of the clusters.*

energy bins. Thus the response matrices, when multiplied by the expected interactions from a neutrino factory should give an accurate representation of the observed spectra at a MIND of this design used for a neutrino factory experiment.

### 6.5.1 Event reconstruction

Many traversing particles, particularly hadronic particles, will deposit energy in more than one voxel. Forming clusters of adjacent voxels reduces event complexity and can improve pattern recognition in the region of the hadron shower.

The clustering algorithm is invoked at the start of each event. The voxels of every plane with deposited charge are considered in sequence. Where an active voxel is in contact with no other active voxel this voxel becomes a measurement for the fit. If there are adjacent voxels, the voxel with the largest total deposit (at scintillator edge) is sought and all active voxels in the surrounding  $3 \times 3$  area are considered part of the cluster. Adjacent deposits which do not fall into this area are considered separate.

The cluster position is calculated independently in the x and y views as the weighted sum of the individual voxels:

$$X_c = \frac{\sum_i x_i E_i^x}{\sum_i E_i^x}, Y_c = \frac{\sum_i y_i E_i^y}{\sum_i E_i^y}. \quad (6.1)$$

Any deposit below the noise cut applied in the digitization is ignored. The positions calculated for the clusters in one test event are shown as black asterisks in Fig. 6.6. Comparison of the calculated weighted sums for the clusters to the weighted sum of all raw deposits in the included voxels (shown in Fig. 6.7) gives an estimate of the resolution appropriate for different classes of cluster. A single voxel forming a cluster has the position resolution of the voxels as described in section 6.4. Charge sharing results in improved position resolution for clusters formed from more than one cluster, which is clearly visible in the RMS of the 2 and 3 voxel distributions. As such, the resolution attributed to such clusters is the standard 1 cm resolution scaled by the ratio of the RMS of the appropriate distribution to that of the 1 voxel distribution. If there is no voxel with deposit above the noise cut in a view, then that view is given an error large enough that it is not considered by the Kalman filter.

The clusters formed from the hit voxels of an event are then passed to the reconstruction algorithm. However, an additional step has been added before implementation of the Kalman filter or cellular automaton to take into account the added complexity induced by more complete simulation of the hadronic and muon decays in this iteration of MIND. Fully contained muons (particularly  $\mu^-$ ) can have additional deposits at their endpoint due to captures on nuclei or decay particles. The additional clusters present at the muon endpoint due to these processes could cause an event with a clear long track free of any planes contain-

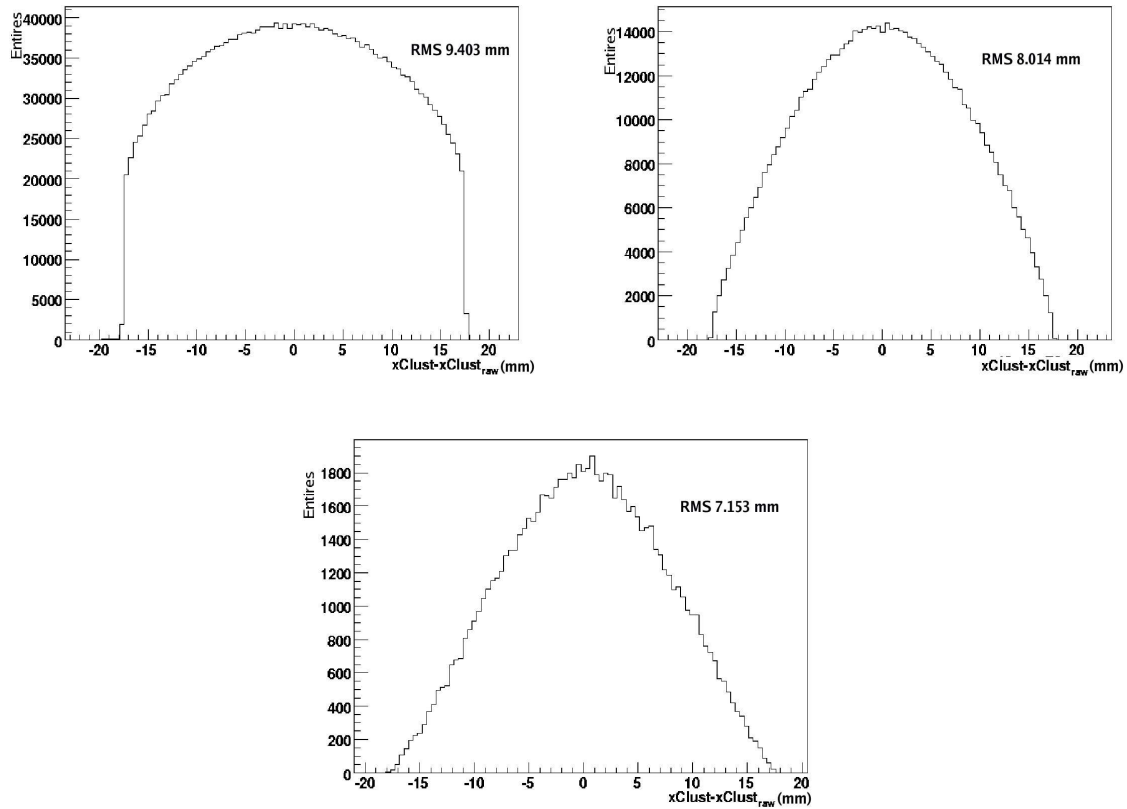


Figure 6.7: *Difference between calculated cluster position and weighted sum of raw deposits included for 1 voxel (top left), 2 voxels (top right) and 3 voxels (bottom).*

ing hadronic activity to be sent to the cellular automaton as the endpoint does not conform to the simple requirement that it be in such a ‘free’ plane. Since the cellular automaton is optimised for low energy events this often leads to long, well defined tracks being rejected. Therefore, after sorting clusters into increasing  $z$  position, the length and endpoint of the longest ‘free’ section is recorded. Those events which do not contain such a section with sufficient clusters to form a seed (set to 5 hits as in the Geant3 analysis) are immediately sent to the cellular automaton. Otherwise, if the ‘free’ section reaches the end of the event the only additional algorithm checks whether any of the last 2 hits lie more than 10 voxel lengths in transverse position away from the bulk of the track. This allows for the exclusion of any badly reconstructed clusters which at this point could cause bad seeding and for the filtering to fail. There are two other categories of events: those which have a high occupancy endpoint (mean occupancy of greater than 2 clusters per plane in the section following the ‘free’ section) and are associated with captures or the showering of the decay electron and those where the occupancy at the end point is low, the latter being associated with a more well defined decay or high curvature of the muon itself. The first category are only sent to the cellular automaton if the ‘free’ section ends outwith the final 20% of the event and the length of the ‘free’ section is less than twice the minimum number of seed hits, otherwise the high occupancy section is removed and not considered in subsequent assessments. The ‘free’ section is used to form a track to filter through the hadronic planes. The second type have a track formed from the ‘free’ section and are subject to an additional forward filtering through the planes in which only two clusters are present towards the endpoint after filtering through the hadronic region.

The only other change to the event pattern recognition is to the Kalman filter method. Where in the past an event was rejected should three planes in a row find no viable hit, here due to the greater complexity of the hadronic shower this cut is loosened. If three planes in a row have no viable hit the event can still be accepted if 70% of the planes not already identified as hadronic or due to muon decay (those skipped) have been filtered into the candidate trajectory. The complete pattern recognition chain using these additional algorithms leads to candidate purity (fraction of candidate hits of muon origin) for  $\nu_\mu$  ( $\bar{\nu}_\mu$ ) CC events as shown in Fig. 6.8. A cluster is considered to be of muon origin if greater than 80% of the raw deposits contained within the cluster were recorded as muon deposits.

Fitting of the candidates proceeds as in chapter 5 with a Kalman filter being used to fit a helix to the candidate using an initial seed estimated using a quartic fit and refitting any successes. Projecting successful trajectories back to the true vertex  $z$  position, the quality of the fitter can be estimated using the pulls of the different parameters in the fit vector (see Fig. 6.9). The pulls on the position and direction exhibit a larger sigma than expected indi-

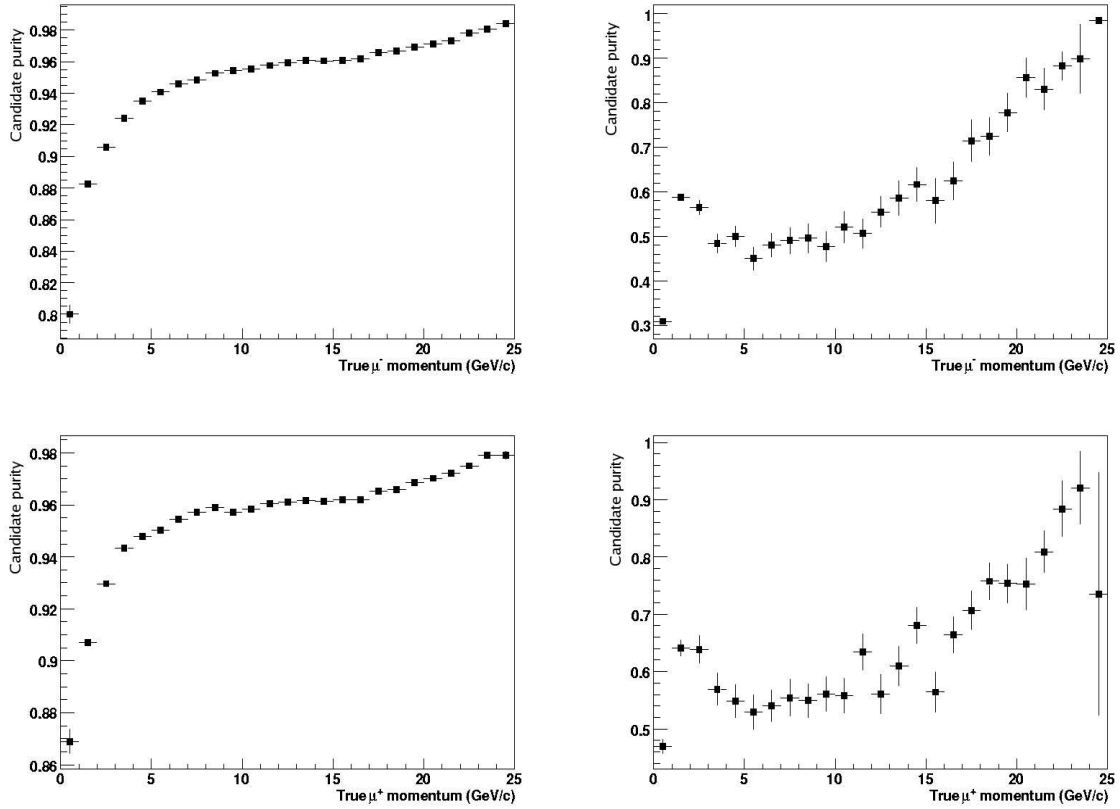


Figure 6.8: Muon candidate hit purity for  $\nu_\mu$  CC (top) and  $\bar{\nu}_\mu$  CC (bottom) interactions extracted using (left) Kalman filter method and (right) Cellular automaton method.

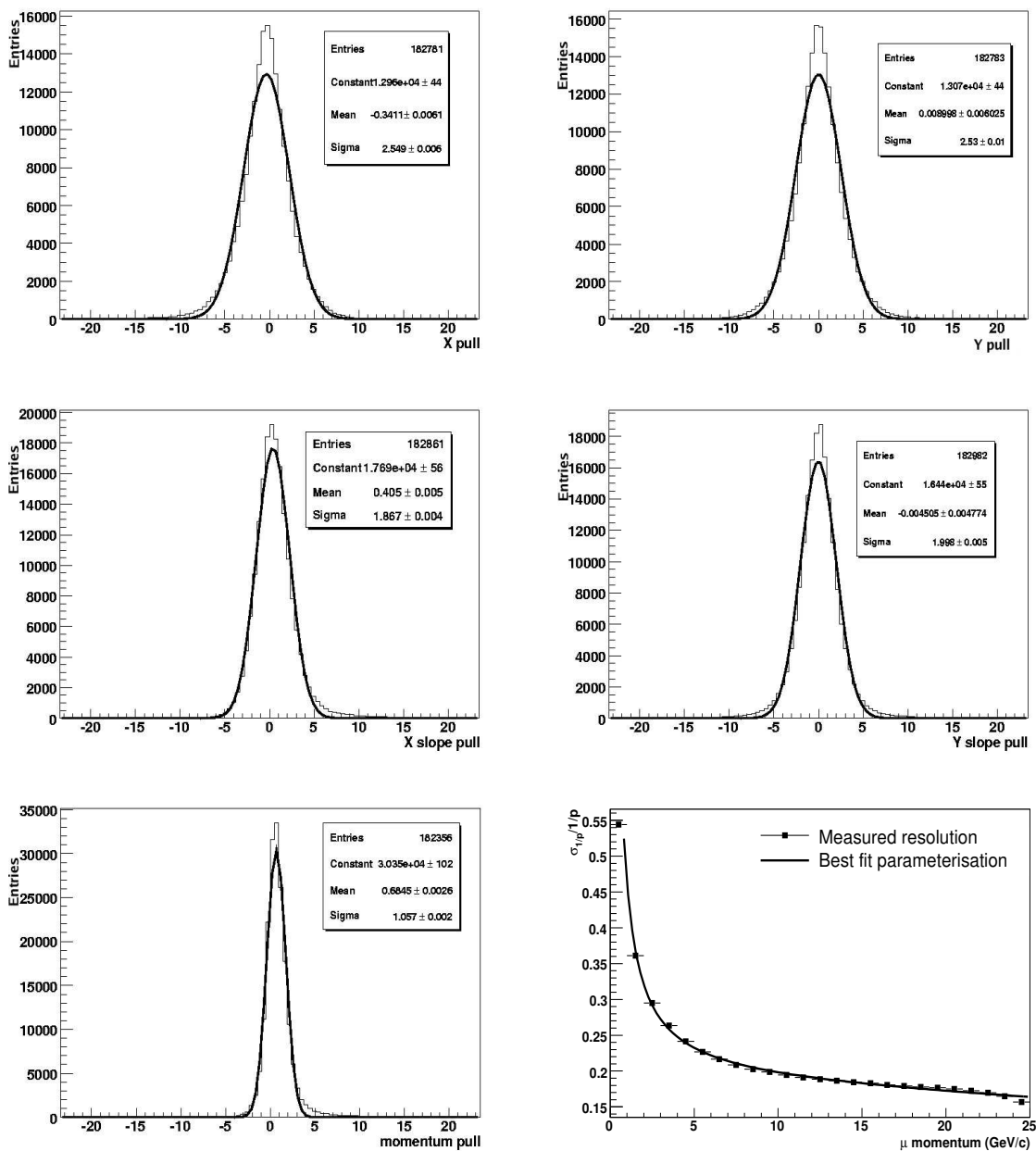


Figure 6.9: Pulls on the five Kalman filter vector parameters and the measured momentum resolution: (top) X (left) and Y (right) position, (middle) X (left) and Y (right) slopes and (bottom) momentum pull (left) and momentum resolution (right).

cating some underestimation of the position resolution. This underestimate is most likely in the vertex region where the plane occupancy will be high and it is likely that clusters will be formed from deposits from many different particles. This effect will be better understood as the digitization algorithms are improved and the position resolution is studied in more detail in specific regions of events. The momentum pull, however, behaves as expected but for a slight bias which can be attributed to the parameterisation of the energy loss in the version of RecPack used for the study. In this version the energy loss is not changed as the filter progresses along the track and can result in a bias. A new version with updated treatment of the energy loss will be implemented for the next stage of the study but was not available for use in the studies presented here. The muon momentum resolution is slightly improved from studies of chapter 5, particularly at low energies. The resolution can be parameterised as follows:

$$\frac{\sigma_{1/p}}{1/p} = 0.18 - \frac{0.28}{p} + 1.17 \times 10^{-3}p. \quad (6.2)$$

### 6.5.1.1 Hadron shower reconstruction

Hadronic reconstruction is predominantly performed using a smear on the true quantities as described in section 5.3.3. However, the presence of QE interactions in the sample allows for the reconstruction of certain events using the formula:

$$E_\nu = \frac{m_N E_\mu + \frac{m_{N_X}^2 - m_\mu^2 - m_N^2}{2}}{m_N - E_\mu + |p_\mu| \cos \vartheta}, \quad (6.3)$$

where  $\vartheta$  is the angle between the muon momentum vector and the beam direction,  $m_N$  is the mass of the initial state nucleon and  $m_{N_X}$  is the mass of the outgoing nucleon for the interactions  $\nu_\mu + n \rightarrow \mu^- + p$  and  $\bar{\nu}_\mu + p \rightarrow \mu^+ + n$  [117]. QE interactions can be selected using their distribution in  $\vartheta$  and their event plane occupancy among other parameters. For the current analysis an event is reconstructed using the appropriate version of equation 6.3, as dictated by the reconstructed charge of the candidate, if it contains 100% of the event visible energy (ignoring any skipped hits). Should the use of equation 6.3 result in a negative value for the energy it is recalculated as the total energy of a muon with  $p_{rec}$ .

## 6.5.2 Analysis of potential signal and background

Using the analysis technique developed for the Geant3 simulation and presented in chapter 5 the expected efficiencies and background suppressions for the appearance of both  $\nu_\mu$  and  $\bar{\nu}_\mu$  have been studied. The greater complexity of events as well as the changes to geometry and interaction spectra has, however, demanded the re-optimisation of existing cuts and the

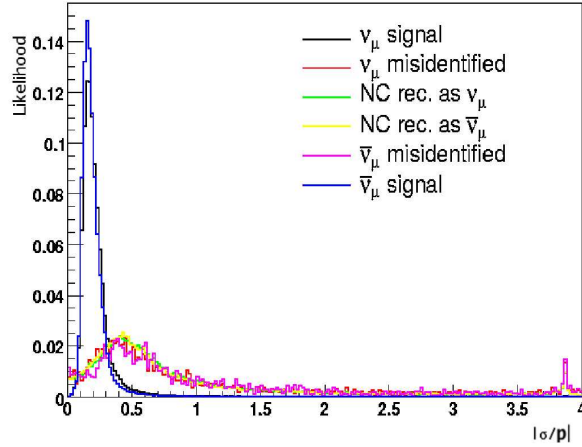


Figure 6.10: *Distribution of  $\frac{\sigma_{q/p}}{q/p}$  for signal and background processes.*

introduction of others. Cut levels and likelihood distributions have been defined using a test statistic of  $\nu_\mu$  and  $\bar{\nu}_\mu$  CC and NC events.

### 6.5.2.1 q/p relative error

The error on the momentum parameter of the Kalman filter is still a powerful handle in the rejection of background but as can be seen in Fig. 6.10 the distribution of calculated values of  $\frac{\sigma_{q/p}}{q/p}$  differs somewhat from those of the Geant3 case (shown in Fig. 5.3). The likelihood distributions for the combination of the two signals and of the neutral current and charge current backgrounds (re-normalising in the latter case to take account for the differing data sets) are used to assess events as signal or background (shown in Fig. 6.11-left).

Signal events are selected as those with a log likelihood parameter greater than -0.5 (where the parameter  $\mathcal{L}_{q/p}$  is defined as in section 5.4.1). As can be seen from Fig. 6.11-right this cut level effectively rejects much of the background.

### 6.5.2.2 Neutral current rejection

Rejection of neutral current events with fitted candidates is most efficient using the likelihood analysis of trajectory quantities. As in chapter 5 the MINOS parameters are employed. In this iteration, the three parameters of most use mirror those of the MINOS exactly: number of hits in the candidate, fraction of the total visible energy in the candidate and the mean deposit per plane of the candidate. The distributions of these variables for a test set of neutral current and charge current events were used to form the PDFs shown in Fig. 6.12.

The energy variables are calculated by first taking the summed deposits at the  $x$  and  $y$

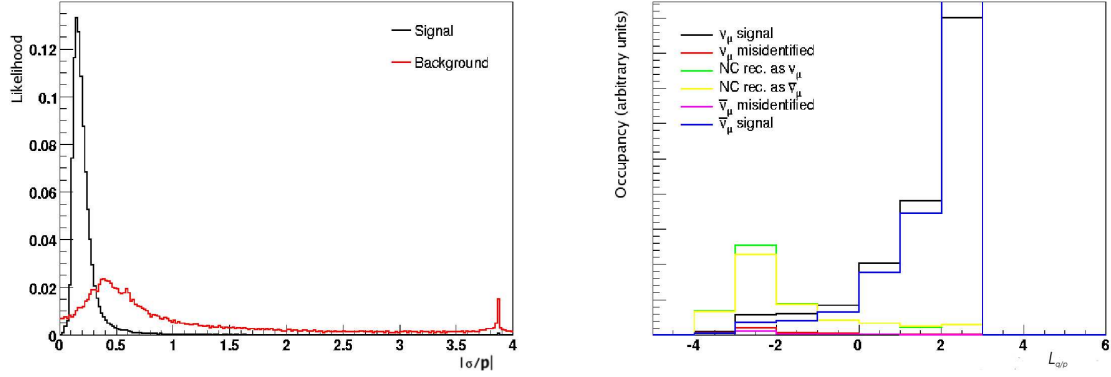


Figure 6.11: *PDF of  $\frac{\sigma_{q/p}}{q/p}$  (left) and the resulting log likelihood distribution ( $\mathcal{L}_{q/p}$ ) for a test statistic (right).*

edges and correcting for attenuation according to the cluster  $x$  and  $y$  position. The total visible energy is taken as the sum of these values over all clusters either in the candidate or hadronic shower vectors and the trajectory visible energy as the sum of those in the candidate. Since there are still a number of assumptions present in the scintillator readout and view matching and there is a high level of correlation between the energy variables, only the first likelihood parameter is used in the analysis presented. An alternative analysis introducing the likelihood functions derived from these energy parameters is discussed in section 6.7.1. Analysis using the likelihood parameter formed from the number of clusters proceeds as follows. Candidates with greater than 150 clusters are considered signal. This condition reflects the fact that the test statistic used for the likelihoods shown in Fig. 6.12 did not contain any NC event with a candidate in this region. Otherwise, samples are taken from the NC and CC PDFs to form the log likelihood rejection parameter

$$\mathcal{L}_1 = \log \left( \frac{I_{hit}^{CC}}{I_{hit}^{NC}} \right), \quad (6.4)$$

the distribution of which is shown in Fig. 6.13. Allowing only those candidates where the log parameter is  $> 1.0$  to remain in the sample ensures that the sample is pure.

### 6.5.2.3 Kinematic cuts

Kinematic cuts based on the momentum and isolation of the candidate as related to the reconstructed energy of the event can be used to reduce backgrounds from decays. Using the same definitions as in section 5.4.4 the distributions after the application of the preceding cuts are those shown in Fig. 6.14. While the remaining backgrounds from  $\nu_\mu$  and  $\bar{\nu}_\mu$  CC are not as concentrated at low  $Q_t$  as in the data of section 5.4.4, cuts based on these variables are

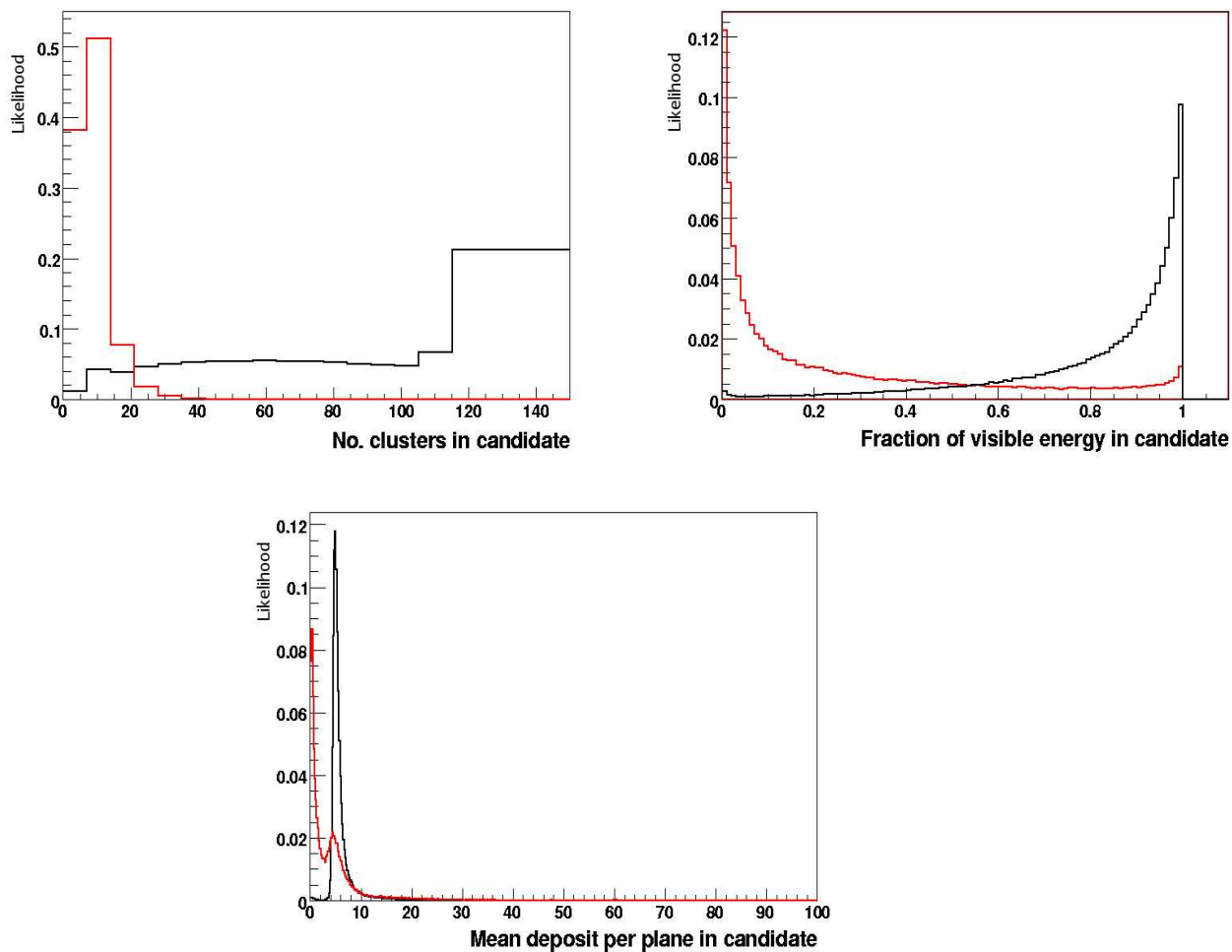


Figure 6.12: Likelihood distributions for the NC rejection parameters. (top left) Clusters in candidate, (top right) fraction of visible energy in candidate and (bottom) candidate mean deposit per plane. CC in black and NC in red.

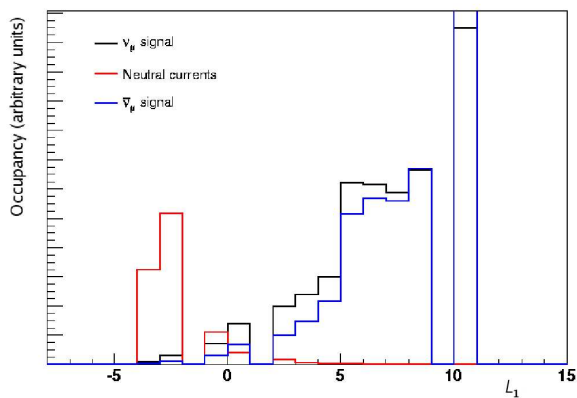


Figure 6.13: Distribution of log likelihood  $\mathcal{L}_1$ .

still an effective way to reduce all of the relevant beam related backgrounds.

$$E_{rec} \leq 5 \text{ GeV or } Q_t > 0.25 \text{ GeV}/c \quad (6.5)$$

$$E_{rec} \leq 7 \text{ GeV or } P_\mu \geq 0.3 \cdot E_{rec} \quad (6.6)$$

The acceptance level is described in equations 6.5 and 6.6. With the exception of those events whose energy is reconstructed using the quasi-elastic formula and hence do not have a hadronic shower whose separation can be calculated, events are subject to the  $Q_t$  cut if their reconstructed energy is greater than 5 GeV. Those events fulfilling the condition of equation 6.5 and those reconstructed using the quasi-elastic formula are then subject to the second cut if they have  $E_{rec} > 7$  GeV. All remaining events which fulfill the conditions of equation 6.6 (those above and to the left of the red lines in Fig. 6.14) are kept in the dataset for the next series of cuts.

#### 6.5.2.4 Additional cuts

A number of additional cuts have been developed and employed for the Geant4 data, particularly to reduce the background from identification of  $\nu_\mu$  ( $\bar{\nu}_\mu$ ) CC as the opposite polarity at high neutrino energy. A set of new cuts of two categories are used: 1) Those related to the range in  $z$ , displacement in the bending plane and reconstructed momentum of the candidate and 2) a cut utilising the results of a re-fit of the remaining events to a quadratic.

Additionally, a fiducial cut requiring that the first cluster in a candidate be at least 2 m from the end of the detector is employed to reduce the mis-identification of candidates originating at high  $z$ . Moreover, a high proportion of the mis-identified candidates are not fully fitted. The distribution of the ratio of the candidate clusters which are fitted with respect to the total number of candidate clusters for signal and background is shown in Fig. 6.15. Accepting only those events with a candidate with 60% of its clusters fitted reduces further the background levels.

The momentum of the muon candidate can be badly reconstructed due to multiple scattering and impurity in addition to other effects. These badly reconstructed events contribute significantly to the overall background. In order to reduce this effect three separate but related cuts are employed. Firstly, a maximum reconstructed momentum is enforced at 40 GeV. Knowledge that the true neutrino momentum cannot be greater than 25 GeV allows for this cut, however, the finite resolution of the detector demands that the cut not be as strict as  $< 25$  GeV. However, plotting the reconstructed momentum against the longitudinal extent of the candidate as well as the displacement in the bending plane as a proportion of the longitudinal extent against the number of hits in the candidate (see Fig. 6.16) further separation is possible. The background events tend to be concentrated at low relative displacement

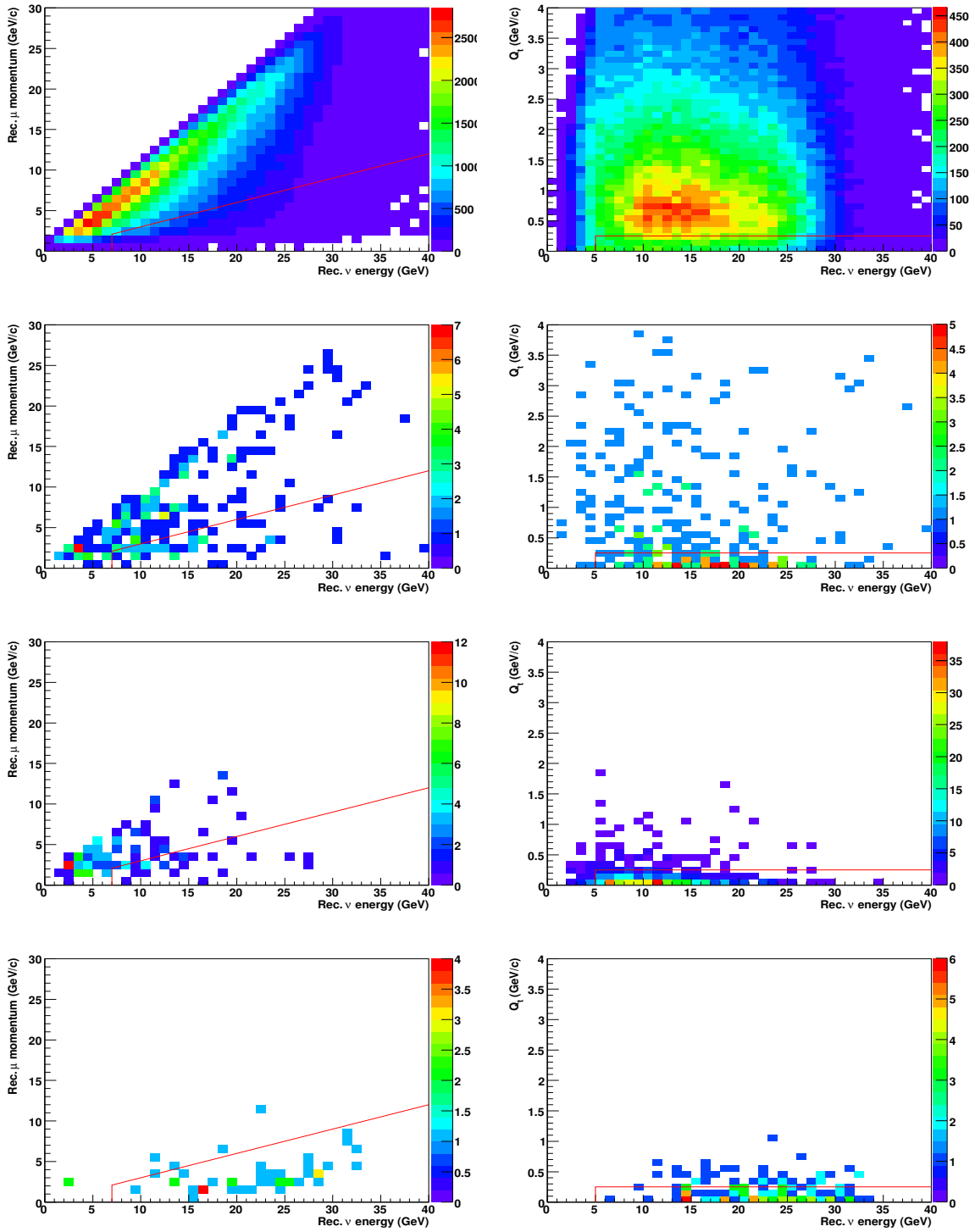


Figure 6.14: *Distributions of kinematic variables: (left) Reconstructed muon momentum with reconstructed neutrino energy for (top→bottom)  $\nu_\mu$  ( $\bar{\nu}_\mu$ ) signal,  $\nu_\mu$  ( $\bar{\nu}_\mu$ ) CC background, NC background,  $\nu_e$  ( $\bar{\nu}_e$ ) CC background and (right)  $Q_t$  variable (in the same order).*

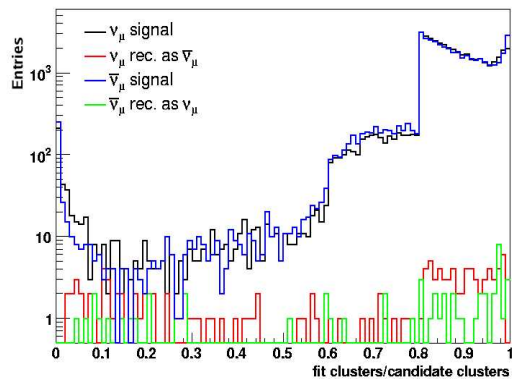


Figure 6.15: *Distribution of the proportion of clusters fitted in the trajectory.*

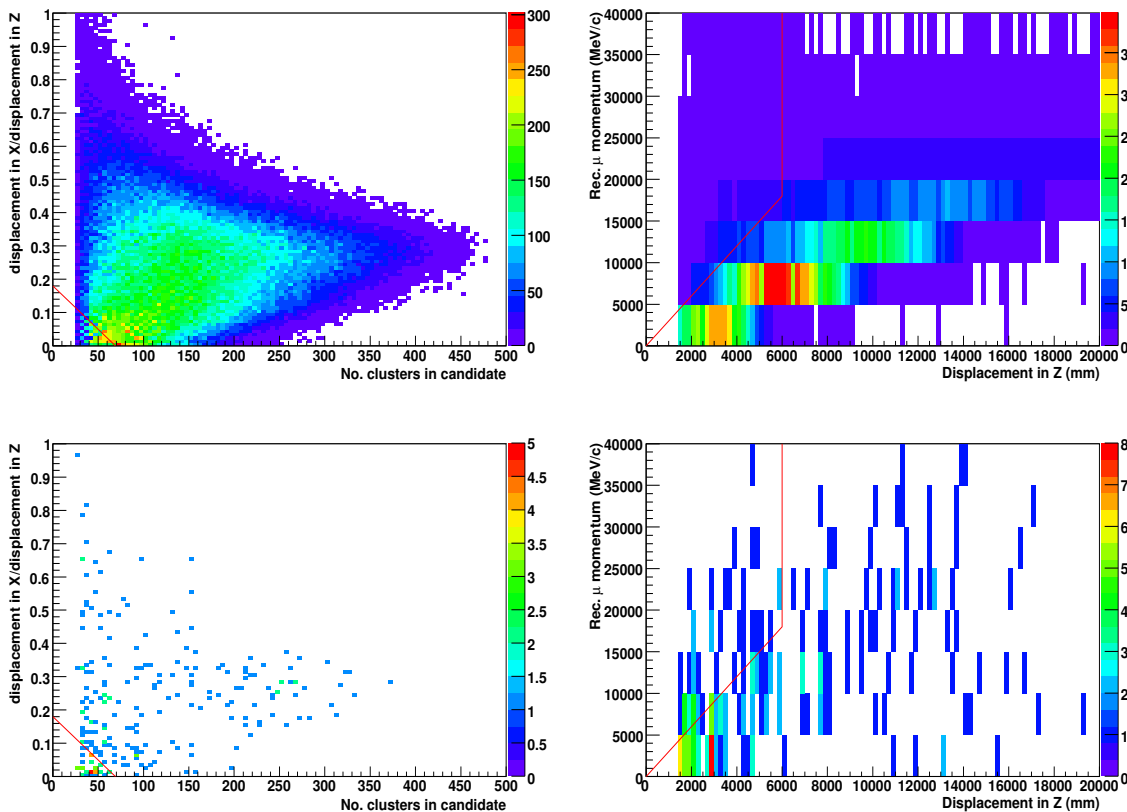


Figure 6.16: *Distributions of momentum and displacement with cut levels: (top left) relative displacement in the bending plane to the z direction against candidate hits for signal events, (top right) reconstructed momentum against displacement in z for signal events and (bottom) as top for  $\nu_\mu$  ( $\bar{\nu}_\mu$ ) CC backgrounds.*

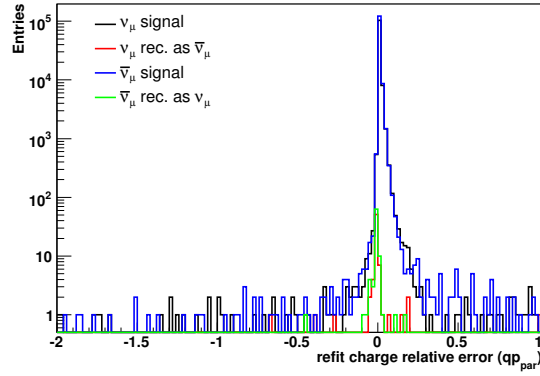


Figure 6.17: *Distribution of the  $qp_{par}$  variable with the region where the parameter is  $< 0$  representing those candidates fitted with charge opposite to the initial Kalman filter (region of highest occupancy shown).*

and low number of hits. Events are accepted should they meet the conditions described in equation 6.7 and illustrated by the red lines in Fig. 6.16:

$$\frac{dispX}{dispZ} > 0.18 - 0.0026 \cdot N_h \quad (6.7)$$

$$dispZ > 6000 \text{ mm} \quad \text{or} \quad P_\mu \leq 3 \cdot dispZ, \quad (6.8)$$

where  $N_h$  is the number of clusters in the candidate,  $dispZ$  is in units of mm and  $P_\mu$  in units of MeV/c.

The final cut involves fitting the candidates projection onto the bending plane to a parabola. If the charge fitted is opposite to that found by the Kalman filter (in the current simulation a negatively charged muon bends upwards so that for a parabola defined as  $a + bz + cz^2$  the  $c$  would be positive and the charge of the muon is  $Q_{par} = -sign(c)$ ) the quality of the fit is assessed using the variable:

$$qp_{par} = \begin{cases} \left| \frac{\sigma_c}{c} \right|, & \text{if } Q_{par} = Q_{kal}. \\ - \left| \frac{\sigma_c}{c} \right|, & \text{if } Q_{par} = -Q_{kal}. \end{cases} \quad (6.9)$$

where  $Q_{kal}$  is the charge fitted by the Kalman filter fit. Defining the parameter in this way assures that the cut is independent of the initial charge fitted. Accepting only those candidates with  $qp_{par} < -1.0$  or  $qp_{par} > 0.0$ , that is those without a change in charge and those fitted badly with a change, effectively reduces the background level from CC mis-identification as can be seen in Fig. 6.17.

Cut	Acceptance level	Eff. after		main back. ( $\times 10^{-3}$ )	
		$\nu_\mu$	$\bar{\nu}_\mu$	$\nu_e$	$\bar{\nu}_\mu$
Fiducial	$zI \leq 18000$ mm <small>where <math>zI</math> is the lowest <math>z</math> cluster in the candidate</small>	0.85	0.91	120 ( $\nu_e$ )	100 ( $\bar{\nu}_e$ )
Track quality	$\mathcal{L}_{q/p} > -0.5$	0.76	0.85	20 ( $\nu_e$ )	20 ( $\bar{\nu}_e$ )
Max. momentum	$P_\mu \leq 40$ GeV	0.76	0.84	20 ( $\nu_e$ )	20 ( $\bar{\nu}_e$ )
CC selection	$\mathcal{L}_1 > 1.0$	0.74	0.83	0.49 ( $\nu_e$ )	1.6 ( $\nu_\mu$ )
Fitted proportion	$N_{fit}/N_h \geq 0.6$	0.73	0.83	0.46 ( $\nu_e$ )	1.2 ( $\nu_\mu$ )
Kinematic	$E_{rec} \leq 5$ GeV or $Q_t > 0.25$ $E_{rec} \leq 7$ GeV or $P_\mu \geq 0.3E_{rec}$	0.63	0.77	0.65 ( $\bar{\nu}_\mu$ )	0.59 ( $\nu_\mu$ )
Displacement	$dispX/dispZ > 0.18 - 0.0026N_h$ $dispZ > 6000$ mm or $P_\mu \leq 3dispZ$	0.59	0.72	0.38 ( $\bar{\nu}_\mu$ )	0.38 ( $\nu_\mu$ )
Quadratic fit	$qp_{par} < -1.0$ or $qp_{par} > 0.0$	0.58	0.71	0.07 ( $\bar{\nu}_\mu$ )	0.07 ( $\nu_\mu$ )

Table 6.1: Summary of cuts applied to select the golden channel appearance signals. The level of absolute efficiency and the background level which would contribute the highest absolute number of background events (assuming the parameter values of table 5.1-row 1) after each cut are also shown.

### 6.5.2.5 Cut summary

In summary, the test statistic leads to the chain of cuts described above and in table 6.1. Application of this analysis and the resulting efficiencies and background suppressions are described in the following section.

## 6.6 MIND response to the Golden Channel

Using a high statistics dataset of  $3 \times 10^6$  events each of  $\nu_\mu$  CC,  $\bar{\nu}_\mu$  CC,  $\nu_e$  CC,  $\bar{\nu}_e$  CC and  $7 \times 10^6$  NC interactions from neutrinos and antineutrinos generated using Nuance and tracked through the Geant4 representation of MIND the expected efficiency and background suppression for the reconstruction and analysis of the golden channel appearance for both polarities of stored muons has been carried out. In addition, an estimate of the likely systematic error of the analysis has been made.

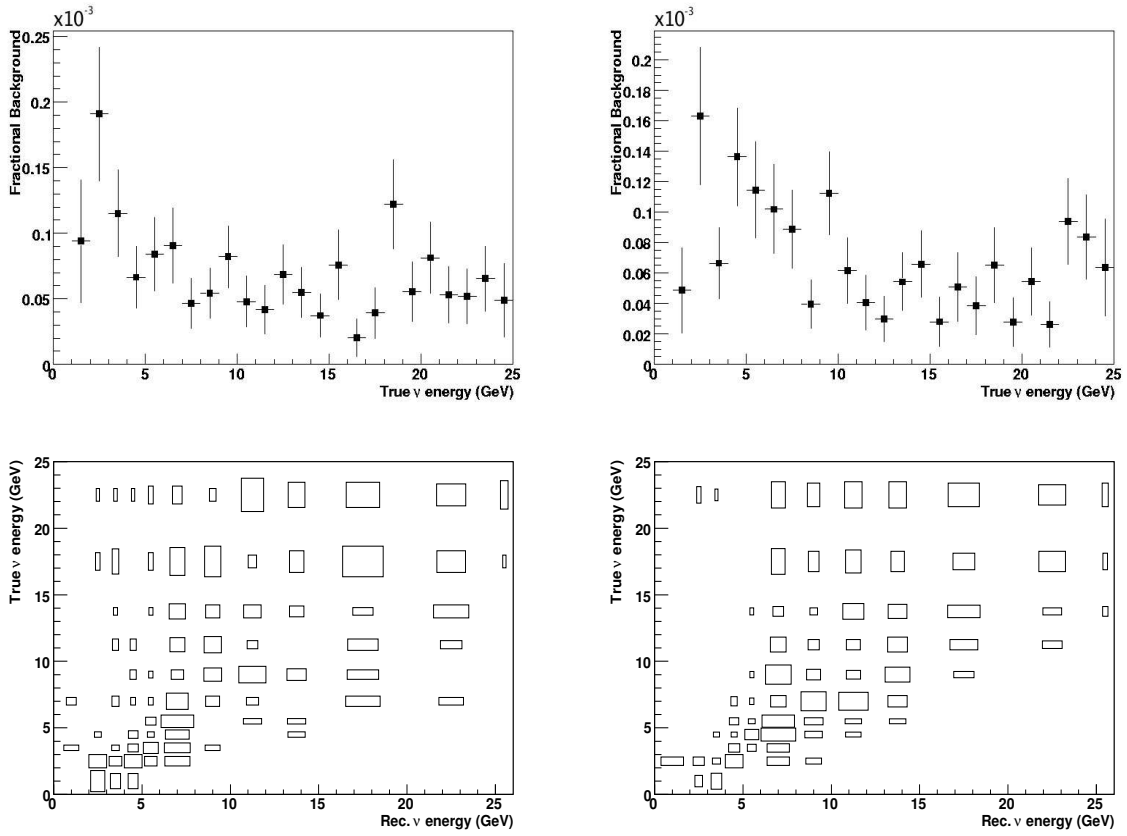


Figure 6.18: Background from mis-identification of  $\nu_\mu$  ( $\bar{\nu}_\mu$ ) CC interactions as the opposite polarity. (left)  $\bar{\nu}_\mu$  CC reconstructed as  $\nu_\mu$  CC, (right)  $\nu_\mu$  CC reconstructed as  $\bar{\nu}_\mu$  CC. (top) As a function of true energy, (bottom) response matrices in the true/reconstructed energy plane. Box sizes represent relative proportions with numeric values available in appendix B.

### 6.6.1 Analysis efficiency

The resultant efficiencies for both polarities and the corresponding background levels expected for the appearance channels are summarised in Figures 6.18 – 6.21. Numeric response matrices for each of the channels may be found in appendix B.

The background from mis-identification of the beam inherent muon type neutrino was in the case of the Geant3 study the largest of the main beam inherent backgrounds. As can be seen in Fig. 6.18 the expected level of background from these processes is significantly below  $10^{-3}$  at all energies for the new simulation and re-optimised analysis.

The background from neutral current interactions also lies at or below the  $10^{-4}$  level with the high energy region exhibiting a higher level than the low energy region due to the dominance of DIS interactions in this region making a viable candidate more likely because of the increased visible energy and particle multiplicity. As expected, the NC background

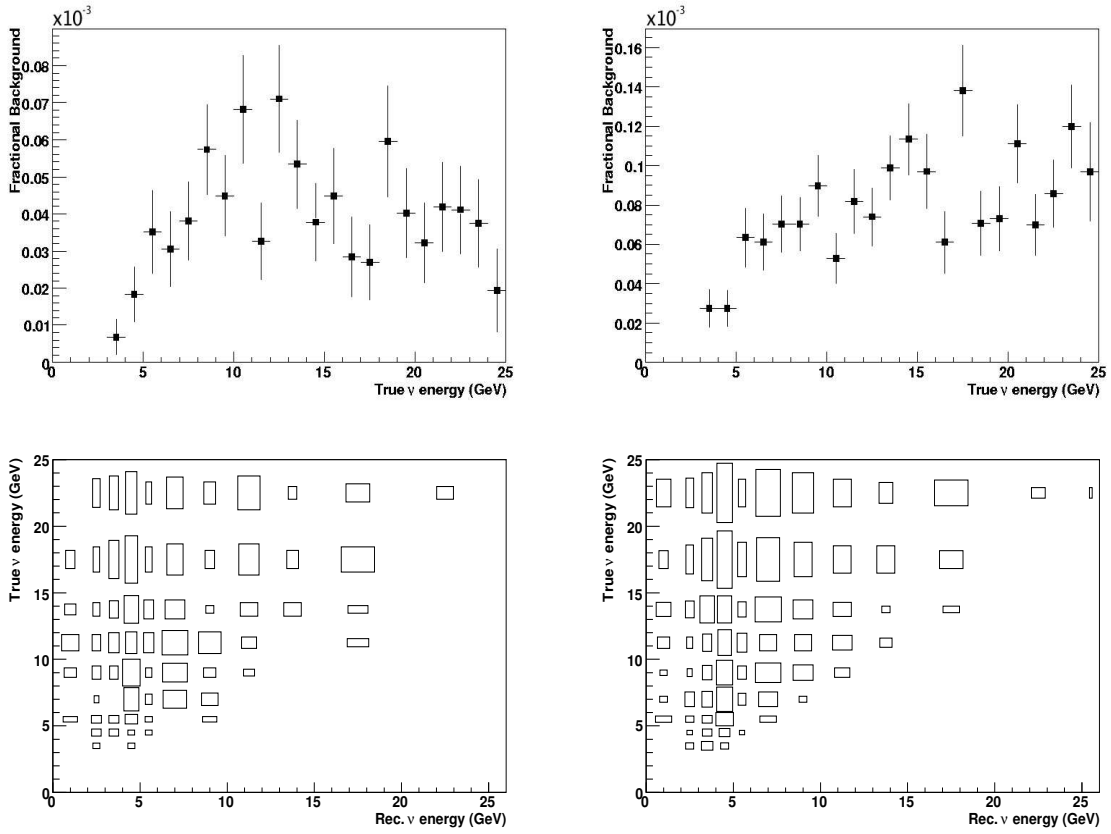


Figure 6.19: Background from mis-identification of NC interactions as  $\nu_\mu$  ( $\bar{\nu}_\mu$ ) CC interactions. (left) NC reconstructed as  $\nu_\mu$  CC, (right) NC reconstructed as  $\bar{\nu}_\mu$  CC. (top) As a function of true energy, (bottom) response matrices in the true/reconstructed energy plane. Box sizes represent relative proportions with numeric values available in appendix B.

tends to be reconstructed at low energy due to the missing energy.

The background from  $\nu_e$  ( $\bar{\nu}_e$ ) CC interactions are once again expected to constitute a very low level addition to the observed signal. This background is particularly well suppressed due to the thickness of the iron plates and the tendency for the electron shower to overlap with any hadronic activity.

The efficiency of detection of the two  $\nu_\mu$  polarities was expected to have a threshold lower than that seen in the study described in chapter 5 due to the presence of non-DIS interactions in the data sample. The efficiencies expected for the current analysis are shown in Fig. 6.21. Fig. 6.22 shows a comparison of the resultant  $\bar{\nu}_\mu$  efficiency to that extracted in chapter 5 and in the studies described in [17, 18, 19], the clear improvement in efficiency with development of the analysis has been made possible by the use of a more sophisticated approach to the application of cuts and by the introduction of the full spectrum of interactions. The presence of quasi-elastic interactions had a large impact on the threshold due to the lower multiplicity

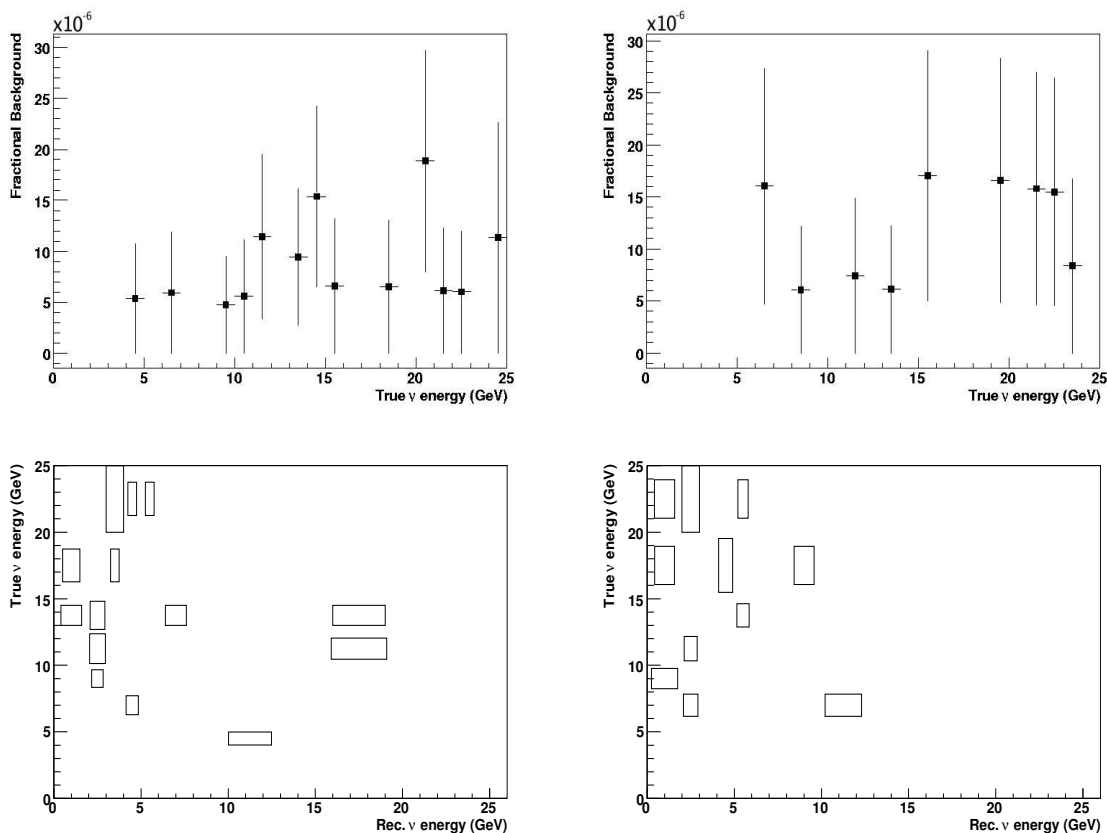


Figure 6.20: Background from mis-identification of  $\nu_e$  ( $\bar{\nu}_e$ ) CC interactions as  $\nu_\mu$  ( $\bar{\nu}_\mu$ ) CC interactions. (left)  $\nu_e$  CC reconstructed as  $\nu_\mu$  CC, (right)  $\bar{\nu}_e$  CC reconstructed as  $\bar{\nu}_\mu$  CC. (top) As a function of true energy, (bottom) response matrices in the true/reconstructed energy plane. Box sizes represent relative proportions with numeric values available in appendix B.

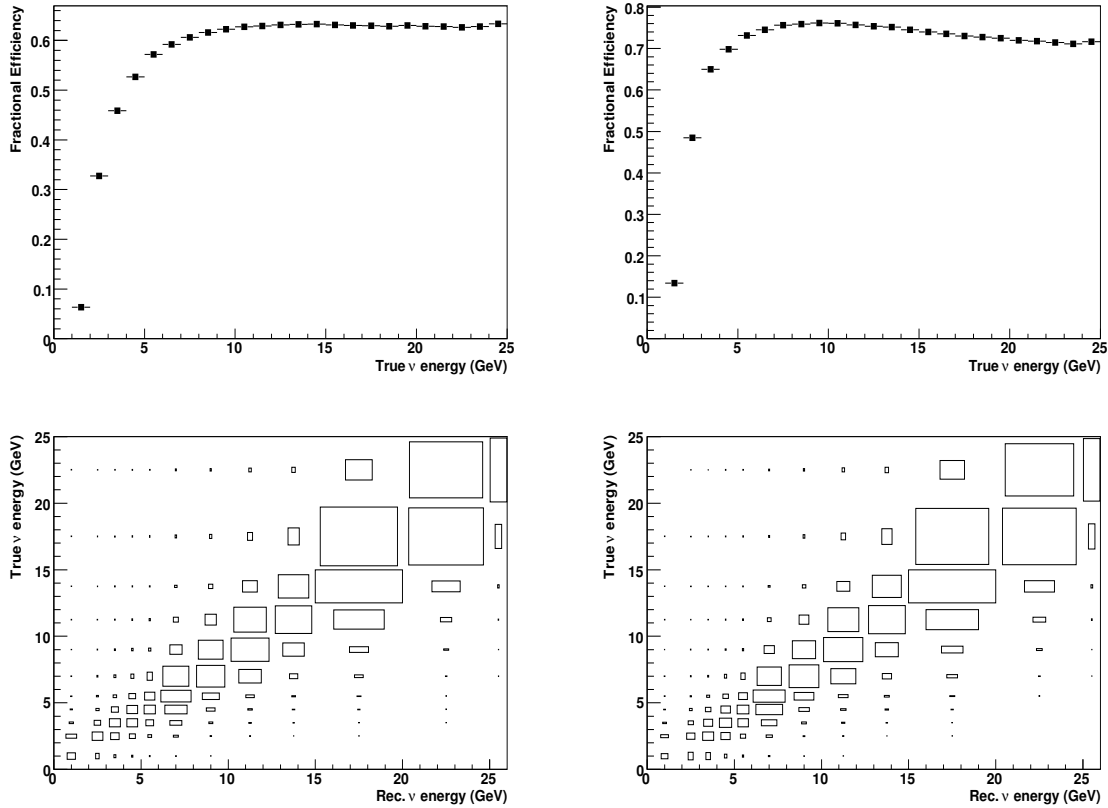


Figure 6.21: Efficiency of reconstruction of  $\nu_\mu$  ( $\bar{\nu}_\mu$ ) CC interactions. (left)  $\nu_\mu$  CC efficiency, (right)  $\bar{\nu}_\mu$  CC efficiency. (top) As a function of true energy, (bottom) response matrices in the true/reconstructed energy plane. Box sizes represent relative proportions with numeric values available in appendix B.

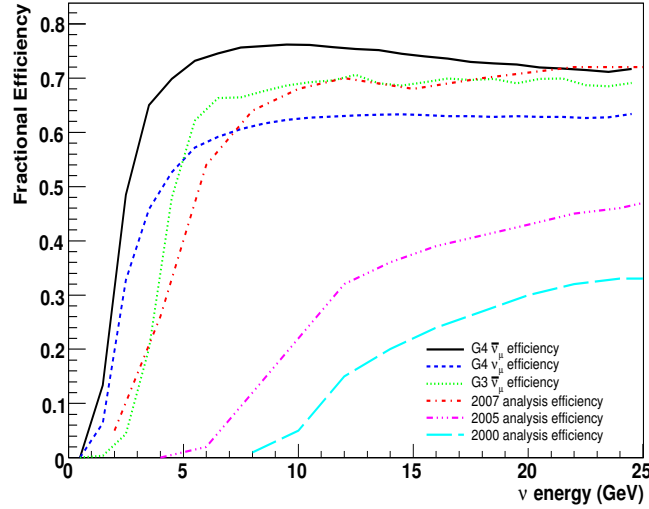


Figure 6.22: Evolution of the MIND  $\bar{\nu}_\mu$  CC detection efficiency. For 2000 analysis see [17], for 2005 see [18] and for 2007 see [19]

of low energy events of this kind. The thresholds of the newest results at between 2-3 GeV correspond well with the expected saturation point of sensitivity to the extraction of the oscillation parameters illustrated in Fig. 3.11.

The difference in efficiency between the two appearance channels is effectively described by the difference in inelasticity as described in the following section.

### 6.6.2 Inelasticity and the difference in efficiencies

The inelasticity of neutrino CC interactions are expected to follow an approximately flat distribution in the Bjorken variable

$$y = \frac{E_\nu - E_l}{E_\nu}, \quad (6.10)$$

with  $E_l$  the exiting lepton energy, due to neutrinos interacting mainly with quarks in DIS events. However, antineutrinos interacting with quarks tend to follow a distribution  $\propto (1 - y)^2$  [24]. As such neutrino interactions tend to involve a greater energy transfer to the target. As can be seen from Fig. 6.23-top left the efficiencies for the two species as a function of  $y$  after all cuts are the same to within error over the full  $y$  range. As such when the distribution of events with  $y$  is considered, the difference in efficiencies when translated into true  $\nu$  energy can be explained by the greater abundance of neutrino events at high  $y$ . However, since the cross-section for the interaction of neutrinos is approximately twice that for antineutrinos

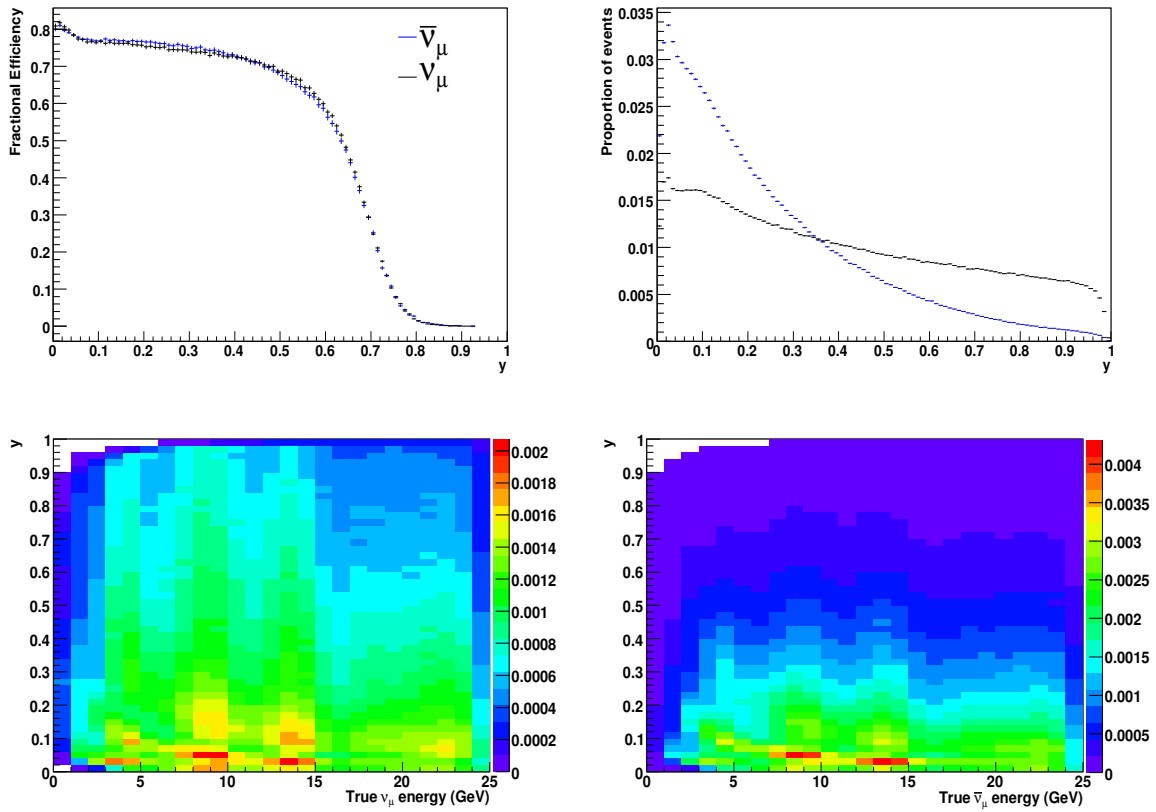


Figure 6.23:  $\nu_\mu$  CC and  $\bar{\nu}_\mu$  CC signal detection efficiency as a function of  $y$  (top left) and the normalised distribution of all events considered in each polarity as a function of  $y$  (top right). (bottom) Normalised distributions for  $\nu_\mu$  CC (left) and  $\bar{\nu}_\mu$  CC events in the  $y$ , true energy plane.

it is not expected that this reduced efficiency would affect the fit to the observed spectrum significantly.

### 6.6.3 Systematic study

The efficiencies described above will be affected by several systematic effects. There will be many contributing factors including uncertainty in the determination of the parameters used to form the cuts in the analysis, error in the determination of the hadronic shower energy and direction resolution, uncertainty in the relative proportions of the different interaction types and any assumptions in the representation of the detector and electronics. While exact determination of the overall systematic error in the efficiencies is complicated, an idea of the contribution of different factors can be obtained by setting certain variables to the extremes of their errors.

Since the neutrino energy is reconstructed generally from the sum of the hadron shower and primary muon energies and this reconstructed quantity is used in the kinematical cuts, uncertainty in the energy and direction resolution of the detector could contribute significantly to the systematic error in the efficiencies. Taking a 6% error as quoted for the energy scale uncertainty by the MINOS collaboration [77] and varying the constants of the energy and direction smears by this amount it can be seen (Fig. 6.24) that to this level the hadronic resolutions have little effect on the true neutrino energy efficiencies. However, the hadronic direction resolution is likely to have far greater uncertainty and would be very sensitive to noise in the electronics. Shown additionally in Fig. 6.24 are the efficiencies when the hadronic energy resolution parameters are 6% larger but with a 50% increase in the angular resolution parameters. Even at this level the observed difference in efficiency is only at the level of 1%.

The relative proportions of QE, DIS and other types of interaction in the data sample could have a significant effect on the signal efficiencies and backgrounds. Fig. 6.25 shows the change in efficiency if the data sample were purely DIS. Although experimental data is available confirming the presence of non-DIS interactions in the energy region of interest there are significant errors in the transition regions (see for example [118, 119]). These errors lead to an uncertainty in the proportion of the different types of interaction which can affect the efficiencies. In order to study the systematic error associated with this effect many runs over the dataset were performed using different random seeds to exclude events of a particular type from the dataset or alternatively exclude an equivalent proportion of the ‘rest’. As an illustration of the method consider the contribution from QE interactions. Taking the binned errors on the cross-section measurements from [118, 119] a run to reduce the QE content would exclude a proportion of events in a bin so that instead of contributing

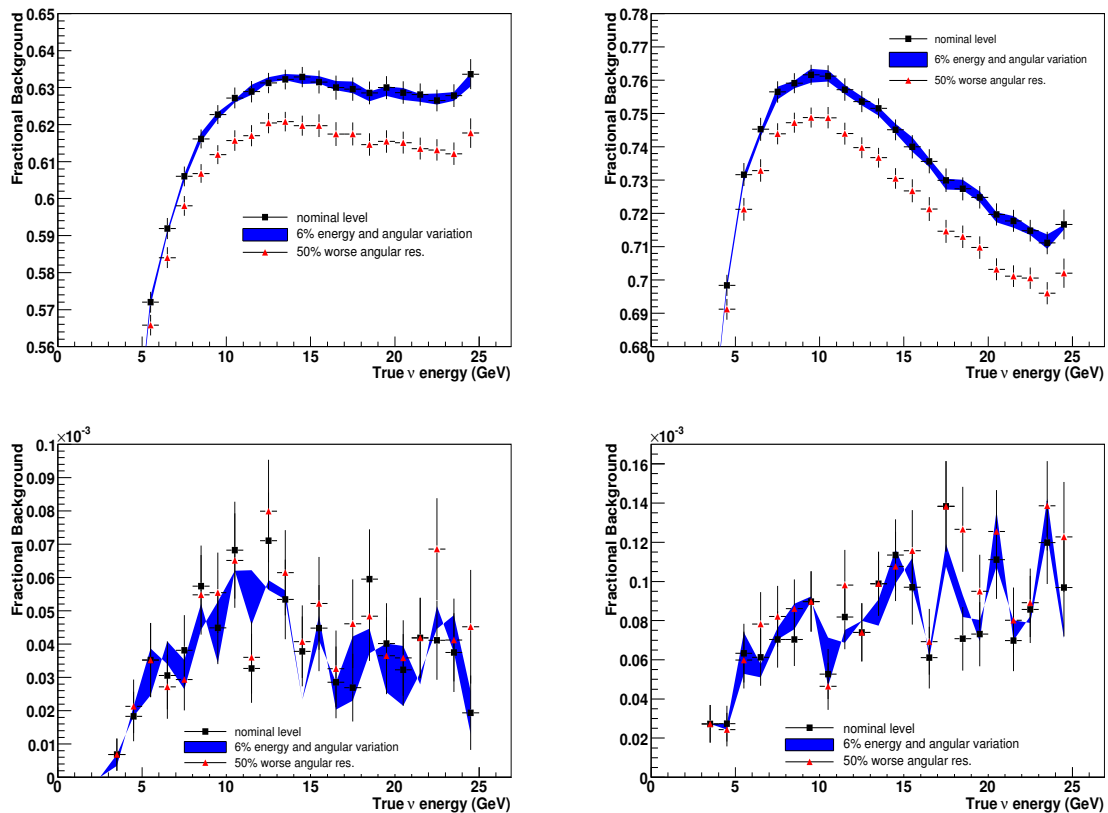


Figure 6.24: Variation of signal efficiency (top) and NC backgrounds (bottom) due to a 6% variation in the hadron shower energy and direction resolution and a more pessimistic 50% reduction in angular resolution (focused on region of greatest variation).

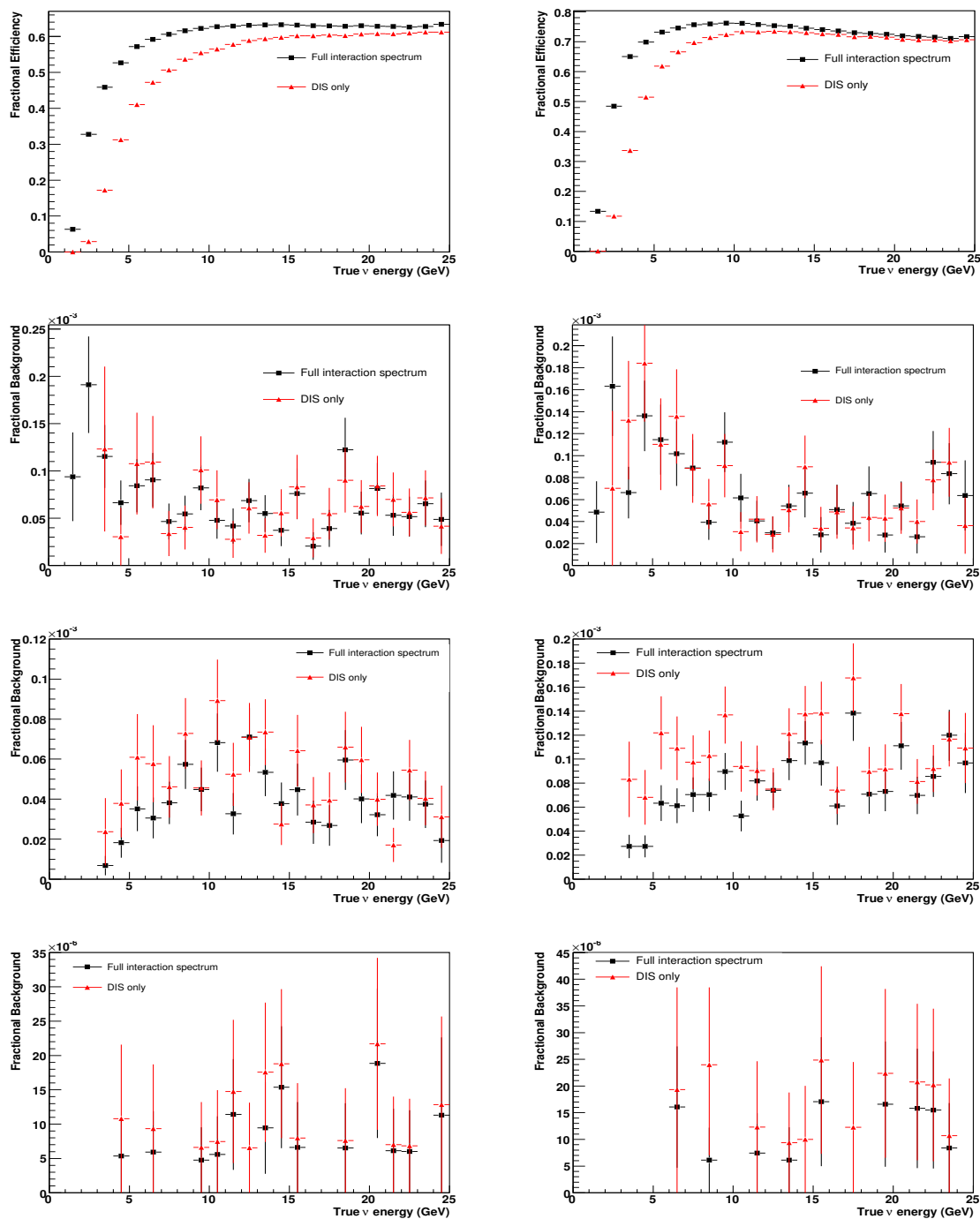


Figure 6.25: Efficiencies for a pure DIS sample compared to the nominal case. (top) Signal efficiency, (second line)  $\nu_\mu$  ( $\bar{\nu}_\mu$ ) CC background, (third line) NC background and (bottom)  $\nu_e$  ( $\bar{\nu}_e$ ) CC background.  $\nu_\mu$  appearance on the left and  $\bar{\nu}_\mu$  appearance on the right.

a proportion

$$\frac{N_{QE}}{N_{tot}}, \quad (6.11)$$

where  $N_{QE}$  is the total number of QE interactions in the bin of interest and  $N_{tot}$  is the total number of interactions in the bin, it would instead contribute

$$\frac{N_{QE} - \sigma_{QE}N_{QE}}{N_{tot} - \sigma_{QE}N_{QE}}, \quad (6.12)$$

where  $\sigma_{QE}$  is the proportional error on the QE cross-section for the bin. The equivalent run to increase the QE contribution reduces the contribution of the ‘rest’ by an amount calculated to give the corresponding proportional increase in QE interactions:

$$\frac{N_{QE} + \sigma_{QE}N_{QE}}{N_{tot} + \sigma_{QE}N_{QE}} = \frac{N_{QE}}{N_{tot} - \epsilon N_{rest}}, \quad (6.13)$$

where  $N_{rest}$  is the total number of non-QE interactions in the bin and  $\epsilon$  is the required proportional reduction in the ‘rest’. Solving for  $\epsilon$  yields the required reduction as

$$\epsilon = \frac{\sigma_{QE}}{1 + \sigma_{QE}}. \quad (6.14)$$

Sampling randomly and repeating runs ensures that any observed change in efficiency is not solely due to the particular events excluded. The  $1\sigma$  systematic error can be estimated as the mean difference between the nominal efficiency and the increase due to a higher QE proportion or decrease due to exclusion. Fig. 6.26 shows the errors in the true  $\nu_\mu$  and  $\bar{\nu}_\mu$  efficiencies extracted using this method to vary the contribution of QE, 1pi and other non-DIS interactions. Errors for 1pi resonant reactions are estimated at  $\sim 20\%$  below 5 GeV (as measured by the K2K near detector [120]) and at 30% above. Due to the large uncertainty both theoretically and experimentally on the models describing other resonances, coherent, diffractive and elastic processes a very conservative error of 50% is taken when varying the contribution of the ‘others’. As can be seen the systematic effect is on the level of 1% in the efficiency threshold region with increased QE and 1pi interactions generally increasing the efficiency and increased contribution of the ‘other’ interactions having the possibility to decrease efficiency. This last effect is likely to be predominantly due to resonances producing multiple tracks. The effect on backgrounds, while expected to be minimal, has not yet been studied due to the statistical limitations in the data sample making any calculation using this method unreliable.

## 6.7 Summary and future work

The efficiency of identification of  $\nu_\mu$  and  $\bar{\nu}_\mu$  CC interactions has been studied along with the associated beam inherent backgrounds. The efficiencies indicate rich possibilities in the

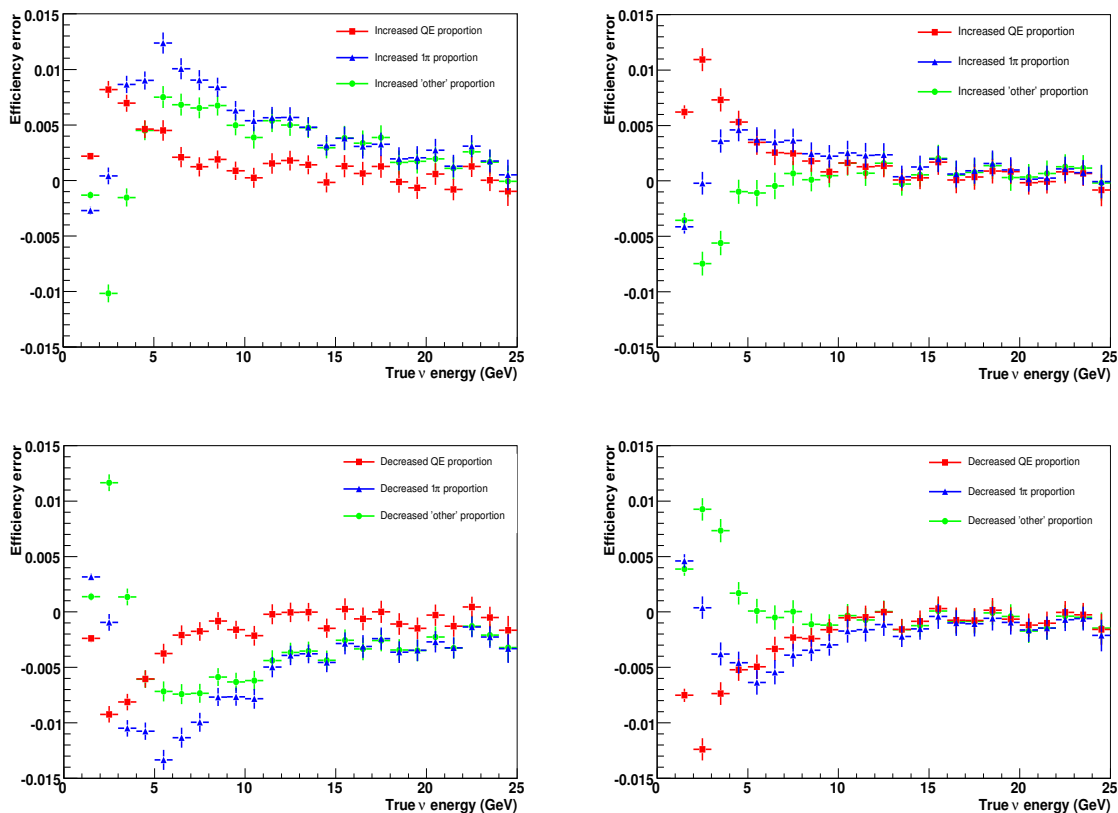


Figure 6.26: Calculated error on signal efficiencies on increasing (top) and decreasing (bottom) the proportion of non-DIS interactions in the dataset. (left) Errors on true energy  $\nu_\mu$  CC efficiency and (right) errors on true energy  $\bar{\nu}_\mu$  CC efficiency

study of the golden channel at a neutrino factory (which will be discussed in greater detail in the following chapter) with further improvement possible with the introduction of currently redundant energy deposit variables mentioned which are discussed in detail in section 6.7.1.

### 6.7.1 Development of the analysis

A number of additional steps will be required to fully benchmark the performance of MIND. This section presents some possible improvements to the analysis which have not yet been fully exploited.

#### 6.7.1.1 Energy deposit likelihood analysis

As mentioned in section 6.5.2.2, the two energy deposit based parameters used by MINOS were studied but not included in the analysis presented in this chapter. The standard implementation involving the multiplication of samples from the three likelihood distributions using the functions described in equations 6.15 – 6.18 was implemented as follows with the specific function used depending on the range which the other parameters fall into. If the candidate has more than 150 clusters it is considered as signal and is not subject to any likelihood function based on these parameters. The function  $\mathcal{L}_1$  was used in the case where the candidate has less than 150 clusters but the other two parameters are out of range (that is the fraction of the total visible energy in the candidate  $> 0.999$  and the mean deposit per plane in the candidate  $\geq 100$  MeV).  $\mathcal{L}_2$  was used when the number of clusters and energy fraction were in range,  $\mathcal{L}_3$  when the number of clusters and mean deposit were in range and  $\mathcal{L}_4$  when all three parameters were in range. Distributions of these functions for a test statistic are shown in Fig. 6.27.

$$\mathcal{L}_1 = \log \left( \frac{l_{hit}^{CC}}{l_{hit}^{NC}} \right) \quad (6.15)$$

$$\mathcal{L}_2 = \log \left( \frac{l_{hit}^{CC} \times l_{frac}^{CC}}{l_{hit}^{NC} \times l_{frac}^{NC}} \right) \quad (6.16)$$

$$\mathcal{L}_3 = \log \left( \frac{l_{hit}^{CC} \times l_{mean}^{CC}}{l_{hit}^{NC} \times l_{mean}^{NC}} \right) \quad (6.17)$$

$$\mathcal{L}_4 = \log \left( \frac{l_{hit}^{CC} \times l_{frac}^{CC} \times l_{mean}^{CC}}{l_{hit}^{NC} \times l_{frac}^{NC} \times l_{mean}^{NC}} \right) \quad (6.18)$$

While the separation of signal and background for all of the discriminators is good, application of the analysis was found to result only in improved efficiency at low energies while not yielding any clear advantage in background suppression. Indeed, for some choices of cut levels the signal efficiency was worse than that achieved for the single parameter analysis

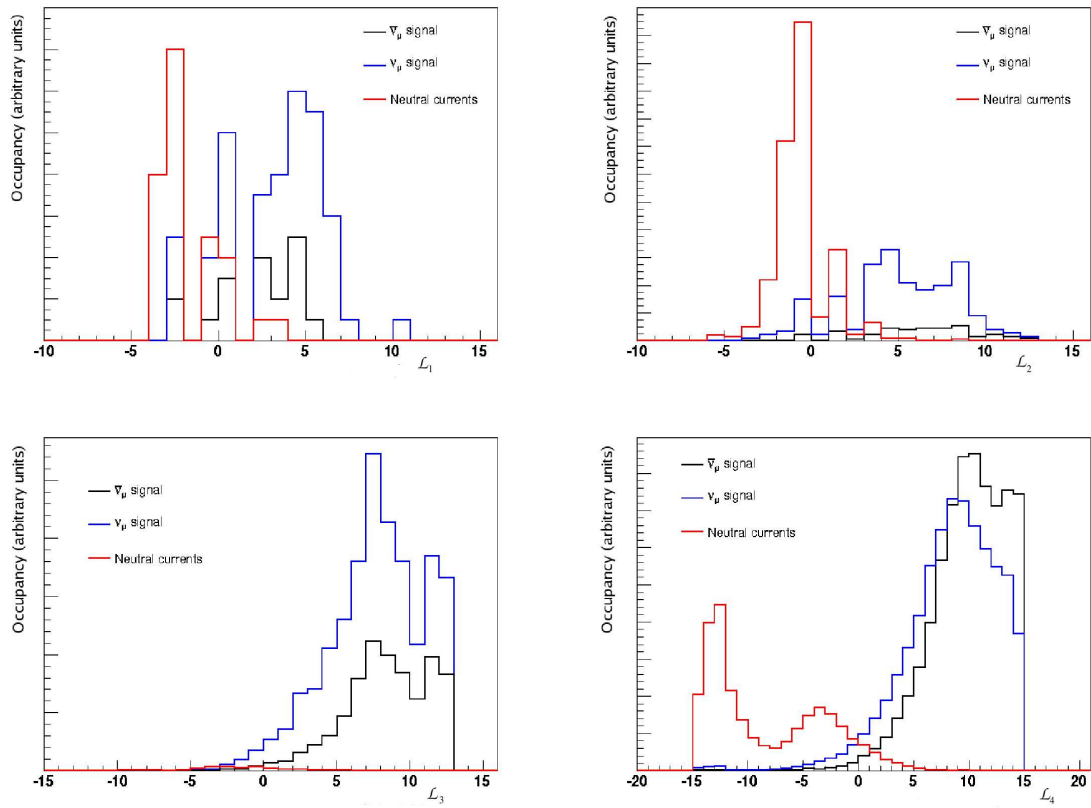


Figure 6.27: Log likelihood distributions for the four possible scenarios. (top left)  $\mathcal{L}_1$ , (top right)  $\mathcal{L}_2$ , (bottom left)  $\mathcal{L}_3$  and (bottom right)  $\mathcal{L}_4$

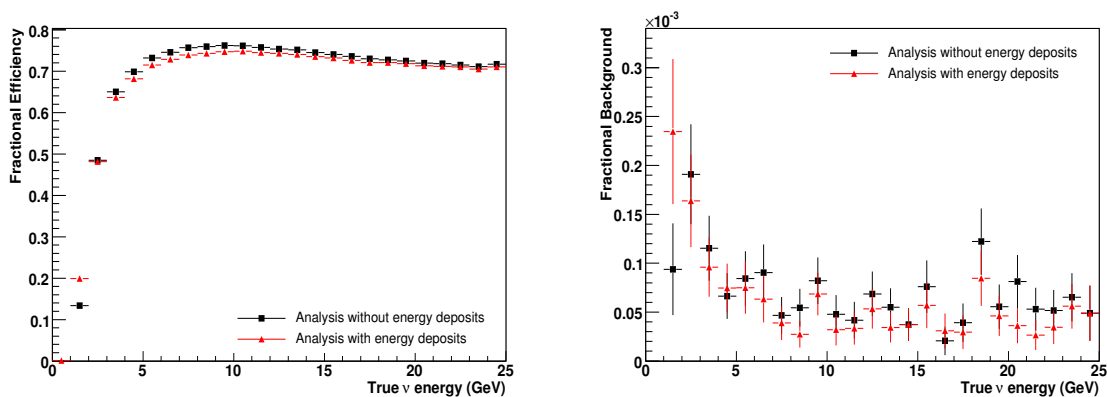


Figure 6.28: Comparison of signal efficiency (left) and  $\nu_\mu$  CC background (right) for analysis with cluster pdf only (black) and using the likelihood parameters of equations 6.15- 6.18.

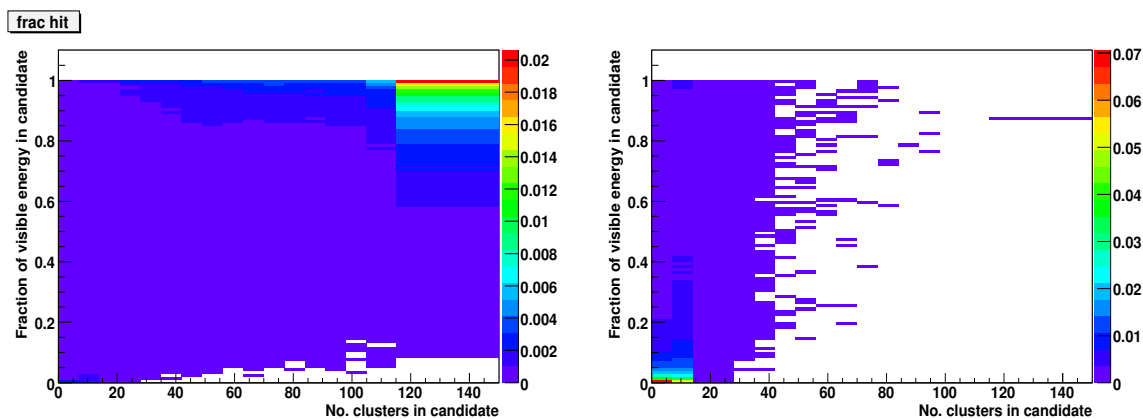


Figure 6.29: Two dimensional likelihoods for the fraction of visible energy in the candidate and its number of clusters for (left) signal and (right) NC interactions.

over most of the energy range and low energy backgrounds were significantly increased (see Fig. 6.28, for example). The assumptions made in the parameterisation of the scintillator response should not degrade the performance of these variables to this extent. However, there is significant correlation between these parameters (see, for example, Fig. 6.29) which, if ignored, could have a detrimental effect on their performance. Development of a multivariate analysis or neural net based on these variables (and, indeed, the other cuts used in the analysis) and taking their correlations into account could be beneficial to the ultimate analysis.

### 6.7.1.2 $\mu$ momentum measurement by range

Measurement of the muon momentum using the range of the candidate in the detector was shown to improve resolution, particularly at low momenta, by MINOS [52]. Moreover, an independent measure of the momentum could aid in the analysis. The cuts currently implemented via equations 6.7 and 6.8 are highly correlated with the range of the muon and their power to remove background is likely to be improved with the inclusion of the muon range measurement.

A full study of the range measurement was out of the scope of this thesis. Application of a range measurement based on a path integral of the fitted section of a candidate coupled with a scaling based on the expected range of muons in iron was found to be insufficient. However, calculation of muon ranges in an appropriate mixture of iron and scintillator and an improved measurement of the particle range should yield a muon range measurement of resolution comparable to that presented by MINOS.

### 6.7.1.3 Hadronic reconstruction

The studies presented use parameterisations based on results presented by Monolith and MINOS to estimate the quality of reconstruction of the hadronic energy and direction. These parameters are important both for the reconstruction of neutrino energy and for the formation of the kinematic cuts. In the ultimate analysis, reconstruction will be performed on an event by event basis using deposit charge and distribution information from that part of the event not associated to the candidate muon.

Full implementation of algorithms to perform the hadronic reconstruction was beyond the scope of this thesis. Initial studies using the recorded charge deposit and a simple scaling yielded a highly non-Gaussian distribution for both key parameters. The assumed view matching and assumptions in the scintillator response will have contributed to this result, however, a dedicated study will be required to fully understand the best method with which to perform the reconstruction. Using these directly observable quantities as well as the measured quantities of an identified primary muon from the event could be used to form a seed for a jet fitting algorithm which could reconstruct both the energy and momentum of the hadronic shower. .

## 6.7.2 Unaccounted backgrounds

There remain two backgrounds which have not yet been studied which, depending on the final detector design and location, could contribute significantly. The first is the background from cosmic rays and cosmic neutrinos. While understanding the timing of the accelerator

system and directional arguments will enable the rejection of many of these events it is clear that some level of rock overburden or active vetoing will be required especially when considering the surface area of a 50-100 ktonne MIND and the NF design requiring a duty cycle – the proportional time window when beam related interactions are possible – of  $\sim 10\%$ . The study of this potential background is also important in the selection of any potential detector site.

Another important study required is the contribution to the reconstructed spectrum from  $\nu_e \rightarrow \nu_\tau$  ( $\bar{\nu}_e \rightarrow \bar{\nu}_\tau$ ) interactions. This oscillation channel would be expected to produce a similar absolute flux of  $\nu_\tau$  ( $\bar{\nu}_\tau$ ) to that produced by the golden channel  $\nu_\mu$  ( $\bar{\nu}_\mu$ ) oscillation. While the high interaction threshold for these species means that fewer interactions will take place in the detector, tau interactions become significant above  $\sim 8$  GeV. As such since the  $\tau$  produced in CC interactions will decay promptly and has a branching fraction for  $\mu$  containing channels of  $(17.36 \pm 0.05)\%$  [25] it is possible that a not insignificant fraction of these events may survive the analysis. However, understanding of this background, if treated with care, can contribute information to the fit instead of detracting from it [121]. The distortion caused is highly sensitive to the oscillation parameters as would be expected of an appearance channel and as such fitting for this distortion could help in the removal of ambiguities in the determination of  $\theta_{13}$  and  $\delta_{CP}$ .

## 6.8 Conclusions

A new Geant4 simulation of MIND has been developed with enough redundancy to be developed further as MIND is optimised with the inclusion of all expected effects. Considering the spectrum of neutrino interactions in the energy region 0-25 GeV produced by the Nuance generator this simulation has been used to study the efficiency of the MIND detector and the expected sensitivity of a neutrino factory using this detector technology to the measurement of  $\theta_{13}$  and  $\delta_{CP}$ . The proportions of quasi-elastic, single pion production and deep inelastic events obtained from Nuance are consistent with that observed in experiment and a parameterisation of the total interaction spectrum has been found to have the expected form.

Digitization of the events tracked through the simulation assumes read-out of the scintillator using WLS fibres and electronics with 30% QE and a standard deviation on signal response of 6%. Both assumptions should be achievable in reality by the time of construction and could, perhaps, turn out to be conservative if the current trend in electronics cost and performance continues. These events have been used to study the efficiency and background suppression of MIND used in a search for wrong sign muons considering a neutrino factory storing both muon polarities. A reconstruction algorithm re-optimized from that introduced

in chapter 5 was used in conjunction with a re-optimised analysis using the same methodology. Application of these algorithms to data-sets comprising several million  $\nu_\mu$  ( $\bar{\nu}_\mu$ ) and  $\bar{\nu}_e$  ( $\nu_e$ ) CC and NC events calculated response matrices describing the expected response of the detector with efficiency plateaus from 5 GeV in true neutrino energy at  $\sim 60\%$  for  $\nu_\mu$  and  $\sim 80\%$  for  $\bar{\nu}_\mu$  and thresholds at  $\sim 2$  GeV with all beam inherent backgrounds simultaneously suppressed to at or below the  $10^{-4}$  level. The difference in efficiencies for the two polarities has been studied and found to be predominantly due to the difference in the inelasticity spectrum expected for neutrino and anti-neutrino interactions. Systematic errors due to hadronic energy resolution and relative errors in the different contributing interaction types indicate a maximum expected systematic error on the signal efficiency of  $\sim 1\%$ .

While the simulation still contains a number of assumptions concerning the digitization and the magnetic field, the results obtained in this study are expected to be indicative of the detection power of MIND for the golden channel.

# Chapter 7

## Sensitivity of MIND to the Neutrino Factory golden channel oscillation

### 7.1 Introduction

As described in section 3.6 the neutrino factory could be required to simultaneously measure the third mixing angle  $\theta_{13}$  and the CP-violating phase  $\delta_{CP}$  while removing ambiguity caused by degenerate solutions. An array of phenomenological studies have been performed to study the extent to which the remaining uncertainties can be understood in certain scenarios (see [14] for example).

Extracting the oscillation parameters from the observed signal at the far detectors requires the accurate prediction of the expected flux without oscillation which is used along with the calculated oscillation probabilities to fit the observed signal for the best value of  $\theta_{13}$  and  $\delta_{CP}$ . Due to the large distance to the far detectors the flux spectra expected from the decay rings of the neutrino factory are accurately approximated by the flux from a point source of muons travelling with appropriate Lorentz boost in the direction of the detector. Using this flux or, alternatively, a projection of the spectra observed in the near detector the number of true interactions expected in MIND can be calculated for a set of the parameters  $\theta_{13}$  and  $\delta$ . These spectra can then be multiplied by the response matrices extracted in chapter 6 to calculate the observed golden channel interaction spectrum expected for some hypothetical values of the oscillation parameters.

This study will use the response of MIND extracted in chapter 6 and shown numerically in appendix B in the current standard IDS baseline NF set-up. That is a neutrino factory storing muons of energy 25 GeV of which  $2 \times 10^{20}$  of each species decay in the straight sections pointing towards the far detectors. The two MIND far detectors will constitute 150 ktonnes of mass in total with 100 ktonnes placed at 4000 km from the facility and

50 ktonnes at 7500 km. The fit results obtained in this standard framework will then be compared to fits obtained using a near detector spectrum projection.

## 7.2 The NuTS framework

The Neutrino tool suite (NuTS) was developed for the studies presented in [37, 105, 61]. It provides a framework for the generation of appropriate fluxes for different neutrino accelerator facilities along with the necessary infrastructure to calculate the true neutrino oscillation probabilities for all channels. In addition, using the parameterisations of the total interaction spectra calculated in section 6.2, the expected number of events in a given energy bin can be calculated. Using this framework and the response matrices extracted for MIND, simulated data for an experiment can be generated as

$$Data_{sim} = smear \left( M_{sig}^i N_{sig}^{i,j} + \sum_k M_{back}^{i,k} N_{back}^{i,j,k} \right), \quad (7.1)$$

for each polarity and detector baseline of interest, where  $M_{sig}^i$  is the response matrix for MIND for a particular signal channel  $i$  (stored  $\mu^+$  or  $\mu^-$ ),  $N_{sig}^{i,j}$  is the 100% efficiency interaction spectrum in true  $\nu$  energy bins for a channel  $i$  at a detector baseline  $j$  (either 4000 km or 7500 km),  $M_{back}^{i,k}$  is the response matrix for a background  $k$  (mis-identification of CC interactions of other neutrino species or from NC) to the appearance channel  $i$ ,  $N_{back}^{i,j,k}$  is the 100% expectation spectrum for a background  $k$  to an appearance signal  $i$  at a detector baseline  $j$  and these expected values are used to calculate an observed number of interactions following a Poisson distribution.

## 7.3 Fitting for $\theta_{13}$ and $\delta_{CP}$ simultaneously

Due to the correlation between the two remaining unmeasured parameters of the mixing matrix it is possible that a simultaneous fit will be necessary. Defining a grid of  $\theta_{13}$  and  $\delta_{CP}$  values the  $\chi^2$  of a fit to  $Data_{sim}$  can be calculated using the function

$$\begin{aligned} \chi^2 = \sum_j \left\{ 2 \times \sum_e^{E_\mu} \left( A_j x_j N_{+,j}^e(\theta_{13}, \delta_{CP}) - n_{+,j}^e + n_{+,j}^e \log \left( \frac{n_{+,j}^e}{A_j x_j N_{+,j}^e(\theta_{13}, \delta_{CP})} \right) \right. \right. \\ \left. \left. + A_j N_{-,j}^e(\theta_{13}, \delta_{CP}) - n_{-,j}^e + n_{-,j}^e \log \left( \frac{n_{-,j}^e}{A_j N_{-,j}^e(\theta_{13}, \delta_{CP})} \right) \right) \right. \\ \left. + \frac{(A_j - 1)^2}{\sigma_A} + \frac{(x_j - 1)^2}{\sigma_x} \right\} [61], \quad (7.2) \end{aligned}$$

where  $n_{i,j}^e$  is the simulated data ( $data_{sim}$ ) for an energy bin  $e$ ,  $N_{i,j}^e(\theta_{13}, \delta_{CP})$  is the predicted spectrum for the values of  $\theta_{13}$  and  $\delta_{CP}$  represented by the grid point (calculated as in

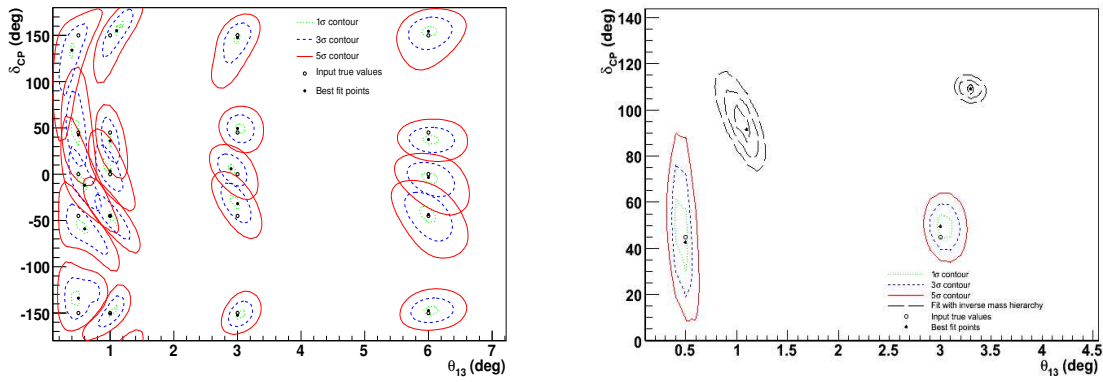


Figure 7.1: Examples of fits to simulated data for the standard IDS neutrino factory with normal mass hierarchy (left) and with a fit using the incorrect mass hierarchy (right).

equation 7.1 but without a smear),  $j$  represents the baseline as in equation 7.1 and the uncertainty in the expected number of interactions and expected difference in interactions between neutrinos and antineutrinos are represented by the additional free parameters  $A_j$  and  $x_j$  respectively and their corresponding errors which are set to  $\sigma_A = 0.05$  and  $\sigma_x = 0.01$ , which is equivalent to assuming a 5% error on the fiducial masses of the detectors and 1% error on the ratio of neutrino to antineutrino cross-sections which is the level to which the near detector would seek to measure the interaction cross-sections. The minimisation of the parameters  $A$  and  $x$  is performed analytically for each predicted dataset to leading order. The contours at  $\chi^2_{min} + 9$  represent approximately the  $3\sigma$  level of understanding. In such a fit, the measured oscillation parameters are considered fixed. While there would be some systematic error associated with uncertainty in these parameters, systematics from the fiducial masses and cross-section uncertainties are expected to dominate. Some examples for such fits are shown in Fig. 7.1. Superimposed in Fig. 7.1-right are the solutions found when the data is fitted with the incorrect mass hierarchy assumed. As can be seen the determination of  $\delta_{CP}$  becomes more difficult at lower  $\theta_{13}$  and the correlation between the two parameters becomes more apparent in the shape of the contours. Without the magic baseline this correlation would be even more evident since the correlation breaking allowed by the cancellation of the interference term would not be present. Although in Fig. 7.1-right the contours for those fits assuming the wrong mass hierarchy seem equivalent or even smaller than those for the correct hierarchy when one considers the fit  $\chi^2$  it becomes clear that the correct mass hierarchy fits the data far better.

One of the most important outcomes of phenomenological studies of future facilities is the definition of the sensitivity a particular set-up would have to the measurement of key variables and the exclusion of degeneracies. Generally such sensitivity is defined as the

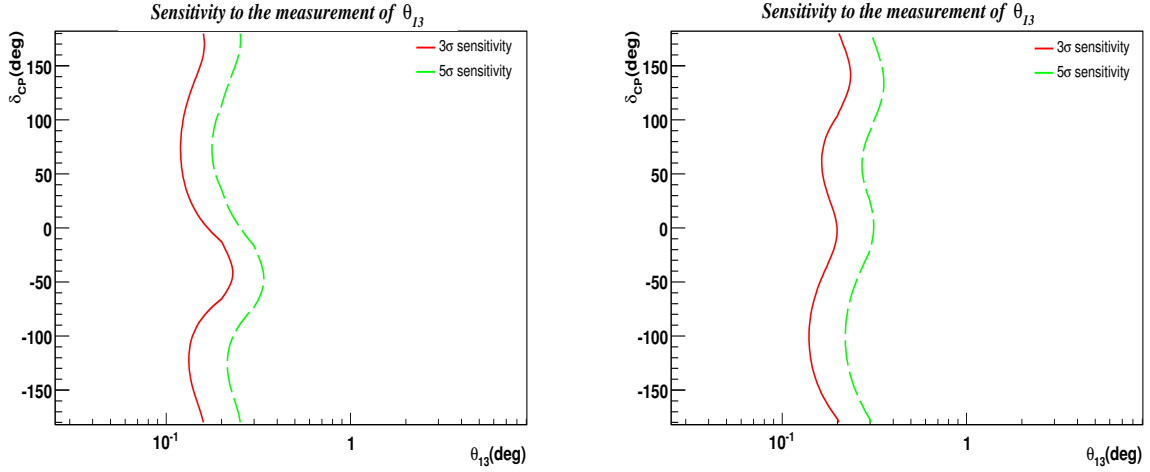


Figure 7.2: Sensitivity to  $\theta_{13}$  for true normal hierarchy (left) and true inverted hierarchy (right).

ability of a set-up to discern the true solution from a zero hypothesis to a certain level.

## 7.4 Sensitivity to $\theta_{13}$

A set-up is deemed sensitive to the measurement of  $\theta_{13}$  at the  $n\sigma$  level for a set of true values  $(\hat{\theta}_{13}, \hat{\delta}_{CP})$  if the minimum of equation 7.2 for a fit to data generated for these true values is distinguishable from the value of equation 7.2 obtained on fitting the data with  $\theta_{13} = 0$  to that level, that is:

$$\chi^2(\theta_{13} = 0) - \chi_{min}^2 \geq n^2. \quad (7.3)$$

Once again forming a grid on the  $(\theta_{13}, \delta_{CP})$  plane and performing a fit to every grid point as an ‘experiment’ the contour satisfying the condition described in equation 7.3 defines the limit of sensitivity to  $\theta_{13}$  of the set-up. For the purpose of these studies the ‘data’ is not smeared so that the contour strictly defines the transition between regions where the zero hypothesis could be excluded at  $n\sigma$  in less or more than 50% of any hypothetical experiments and is equivalent to the sensitivity defined in the studies mentioned above. Fig. 7.2 shows the sensitivities obtained for the standard neutrino factory set-up using the response matrices extracted in section 6.6.1. As can be seen  $3\sigma$  sensitivity is expected for all values of  $\delta_{CP}$  from  $\theta_{13} \simeq 0.25^\circ$  (equivalent to  $\sin^2 2\theta_{13} \simeq 7.6 \times 10^{-5}$ ). The exact positions in  $\delta_{CP}$  of maximum and minimum sensitivity coverage depends on the true mass hierarchy and the minimum is shifted from  $\delta_{CP} = 0$  due to the large matter effects present for the two detector baselines chosen for the study. The expected sensitivity compares favourably with the results of the ISS [14] where similar coverage was achieved.

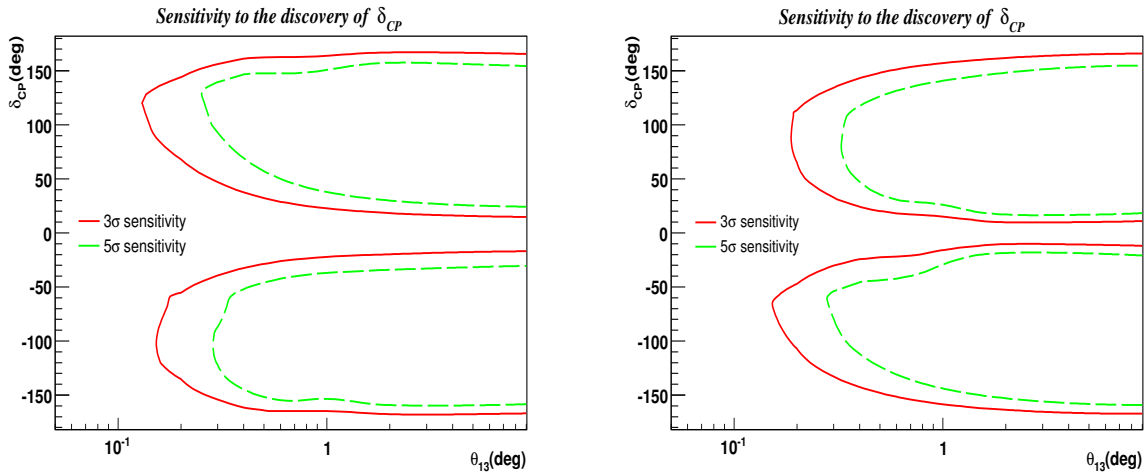


Figure 7.3: Sensitivity to  $\delta_{CP}$  for true normal hierarchy (left) and true inverted hierarchy (right).

## 7.5 Sensitivity to $\delta_{CP}$

Sensitivity to the measurement of  $\delta_{CP}$  is defined similarly as when the minimum  $\chi^2$  can be distinguished from the minimum obtained by fitting with  $CP$  conserving cases to the appropriate level, that is

$$\min(\chi^2(\delta_{CP} = 0), \chi^2(\delta_{CP} = 180), \chi^2(\delta_{CP} = -180)) - \chi_{min}^2 \geq n^2. \quad (7.4)$$

The contours of such sensitivity for the standard neutrino factory are shown in Fig. 7.3. The  $CP$  sensitivity reach at  $3\sigma$  extends below  $0.2^\circ$  for maximal violation. Maximum coverage is reached by  $\theta_{13} \sim 1^\circ$  for both positive and negative  $\delta_{CP}$  in the case of the inverted hierarchy and at slightly higher values for the normal hierarchy. The extended coverage seen when considering the inverted hierarchy is likely due to the increased antineutrino signal available in this scenario. Again the results compare favourably to those of the ISS particularly when one considers the drop in coverage observed for  $\sin^2 2\theta_{13} > 10^{-2}$  ( $\theta_{13} \gtrsim 2.85^\circ$ ) which is not seen in these results.

## 7.6 Sensitivity to the mass hierarchy

Distinguishing between the two possible mass hierarchies is not only important in the removal of degenerate solutions for  $\theta_{13}$  and  $\delta_{CP}$  but at a more fundamental level in the understanding of the neutrino mass sector as described in section 1.3. The sensitivity to the true mass hierarchy is defined here as when the true sign of  $\Delta m_{13}^2$  can be distinguished from the

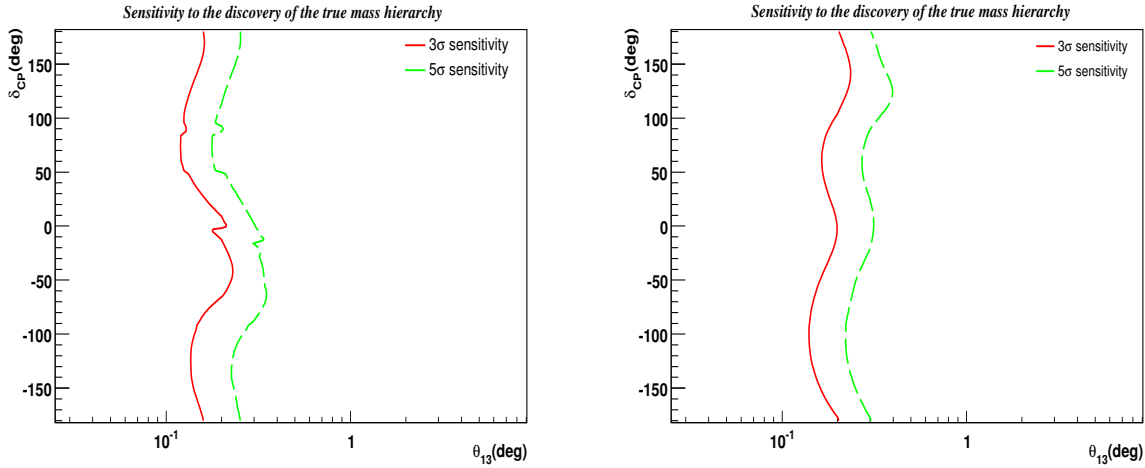


Figure 7.4: Sensitivity to the true mass hierarchy for true normal hierarchy (left) and true inverted hierarchy (right).

opposite sign to the appropriate level, that is

$$\chi_{min}^2(-\Delta m_{13}^2) - \chi_{min}^2(\Delta m_{13}^2) \geq n^2. \quad (7.5)$$

Contours of this condition for the standard neutrino factory are shown in Fig. 7.4.

Sensitivity to the mass hierarchy covers, as expected for this scenario where the magic baseline is combined with an intermediate baseline, the whole region where there is sensitivity to  $\theta_{13}$ . There is no detrimental effect observed due to the difference in efficiencies between the two channels which has not been included in an analysis of the neutrino factory before.

## 7.7 Influence of near detector data

Any neutrino near detector facility will have many possible functions, as described in section 4.2. Among these will be the measurement of the absolute flux in the direction of the far detectors. There is the possibility that this measurement could be used, in addition to the determination of the absolute normalisation, to project a non-oscillation flux prediction to the far detector site to be used in the determination of the oscillation parameters. This would require the reconstruction of the whole flux spectrum at the near detector so that the projection could be carried out reliably. Described here are the initial studies into the power of a technique for the projection of the near detector flux spectrum as a means of extracting oscillation parameters.

### 7.7.1 Flux measurement

Comparison of neutrino flux at the near and far sites is problematic for various reasons. However small, a detector within  $\sim 1$  km of the beam pipe subtends a far greater beam solid angle than a large scale detector positioned thousands of kilometres from the source and the solid angle subtended by the near detector as seen from different parts of the decay pipe varies considerably. Considering a 1 m radius near detector placed 100 m from the end of a 600 m long straight decay length and the the  $14 \times 14 \text{ m}^2$  cross section MIND at 4000 km from the same decay pipe it can be seen that the solid angle of the near detector as seen from the two ends of the decay pipe ranges from  $6.41 \times 10^{-6} - 3.14 \times 10^{-4}$  sr, a range of two orders of magnitude, whereas for the far detector the solid angle ranges between  $1.22 - 1.23 \times 10^{-11}$  sr, up to 7 orders of magnitude smaller and varying by only 1% of the larger value. As can be seen in Fig. 7.5, this results in a differing energy spectrum for near detector distances up to a distance of  $\sim 1$  km. Due to the steep angle of the beam direction, positioning the ND facility at 1 km would be restrictively expensive as well as problematic from an engineering standpoint. As such, one of the main focuses of this study must be to determine whether it is still possible to extract a prediction for the FD flux, even if the ND flux differs considerably from the FD spectrum, when the ND is positioned close to the end of the decay straight.

Direct comparison of expected fluxes at the two sites allows for a clear determination of the expected reduction in certain energy bins. This technique would require any ND to have excellent energy resolution to reduce the errors in the determination of the ND flux before projection. However, the proximity of the detector to the beam source means that a large mass is not a requirement from a statistical point of view (see interaction rates calculated in chapter 4) and hence a high resolution detector constructed of multiple subdetectors could be built with designs based on upgrades to the NOMAD [83] or Minerva [122] detectors as possible candidates. The studies described below focus on the determination of oscillation parameters via the neutrino factory golden channel using a matrix representation of all aspects of the set-up and is inspired by the technique utilised by the MINOS collaboration [123].

## 7.8 Flux projection for non-oscillation prediction

The technique essentially involves three matrices describing the set-up: near detector response, flux projection and far detector response; in addition to cross-section matrices for the relevant processes and a parameterisation of the oscillation probability which is ultimately used in the determination of the sensitivity to oscillation parameters. Through purely mathematical arguments one can prove that the oscillation probability is related to the two

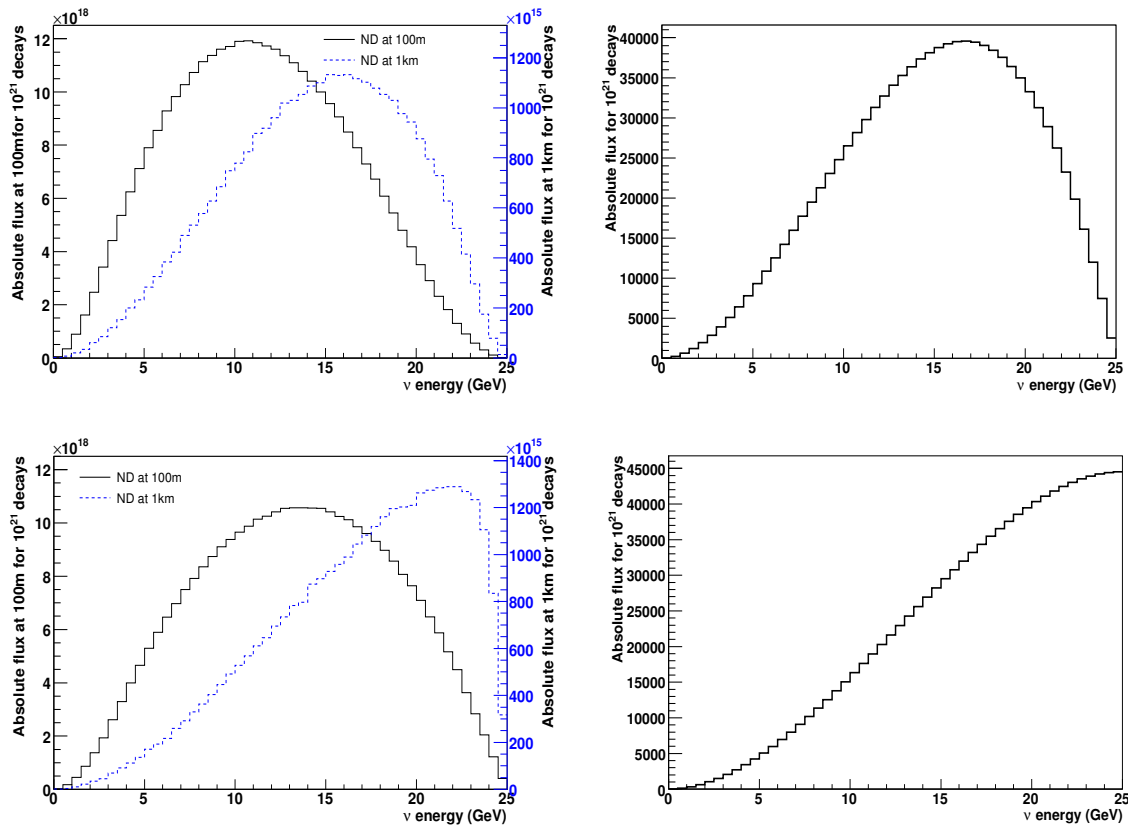


Figure 7.5: *Difference in expected fluxes at near and far sites: (top)  $\nu_e$  flux through a 1 m radius detector 100 m and 1 km from a 600 m decay straight (left) and at a 7 m radius detector 4000 km from the Neutrino factory; (bottom)  $\nu_\mu$  flux for the same detectors (using unpolarised muon expectation).*

observed signals via the relationship

$$P_{osc} = M_{FD}^{-1} M_{dat} M_{ND} M_{nOsc}^{-1}, \quad (7.6)$$

where  $M_{FD}$  and  $M_{ND}$  are matrices representing the combination of cross-section and response for  $\nu_\mu$  ( $\bar{\nu}_\mu$ ) at the far detector and  $\nu_e$  ( $\bar{\nu}_e$ ) at the near detector respectively,  $M_{nOsc}$  relates the expected FD  $\nu_e$  ( $\bar{\nu}_e$ ) flux without oscillations to the expected  $\nu_e$  ( $\bar{\nu}_e$ ) flux at the near detector and  $M_{dat}$  is the ratio of the observed  $\nu_\mu$  ( $\bar{\nu}_\mu$ ) interaction spectrum at the far detector to the observed  $\nu_e$  ( $\bar{\nu}_e$ ) interaction spectrum at the near detector. The extracted function would then be fit to the oscillation probability formulae to find the best fit values of the  $\theta_{13}$  and  $\delta_{CP}$ . This technique formed the basis of the first basic study of the matrix method which was presented in [124].

There are, however, a number of problems with this direct method. The finite resolutions of both detectors would mean the direct ratio of observed signals could not be used without some correction but, more importantly, fitting such a complex function as the oscillation formula, particularly in the low energy region, can be problematic. Inversion of the response of a detector, particularly a course grained calorimeter like the far detector can lead to statistical instabilities or bias in the prediction of the true energy interactions (see [125] for a more detailed discussion of this inverse problem). For these reasons the next step in the study involved a re-definition of the fitted quantity.

In analogy to the technique used in section 7.1 the updated method attempts to fit the observed far detector spectrum directly by using the projection of the observed near detector spectrum. That is, the predicted spectrum for a given grid point on the  $(\theta_{13}, \delta_{CP})$  plane is calculated as:

$$N_{FD} = M_{FD} P_{osc}(\theta_{13}, \delta_{CP}) M_{nOsc} M_{ND}^{-1} N_{ND}, \quad (7.7)$$

where  $N_{FD}$  and  $N_{ND}$  are the observed far and near detector spectra respectively with other symbols defined as in equation 7.6. In this way only the higher resolution near detector response need be inverted. The prediction here would, however, use binned data as opposed to using the integration of the flux calculations and as such the binning used at the near detector would have to be optimised for the projection. Calculation of the expected appearance spectrum from the no-oscillation flux spectrum is aided by fine binning, however, statistical significance and detector resolution limit how fine the binning can be in reality. An initial study using the golden channel oscillation without backgrounds was performed and presented in [126] using a near detector with  $\nu_e$  ( $\bar{\nu}_e$ ) detection threshold of 5 GeV and energy resolution of  $35\%/\sqrt{E}$ .

In order to predict the interaction spectra at the far detector the near detector would be required to measure both the  $\nu_\mu$  ( $\bar{\nu}_\mu$ ) and  $\bar{\nu}_e$  ( $\nu_e$ ) interaction spectra. The only background

to the  $\nu_\mu$  ( $\bar{\nu}_\mu$ ) measurement is likely to be from neutral current interactions. Using a combination of missing  $p_T$  and vertexing resolution, both of which should be possible to high resolution at a near detector, this could be suppressed to at least the level in the far detector. The  $\bar{\nu}_e$  ( $\nu_e$ ) measurement would require a more sophisticated analysis to achieve a pure sample. Both channels could benefit from the study of low background processes such as electron scattering but these processes are limited by statistics and take place often in restricted energy ranges and as such could not be used alone to perform this analysis. Any final analysis is likely to utilise a combination of channels and analyses to maximise statistics and purity.

Projection of the predicted flux is carried out using scaling matrices calculated using a comparison of the true fluxes at the near and far sites. The ultimate analysis would benefit from the use of a Monte Carlo study to either quantify the additional neutrinos expected in the beam from neutral current interactions and the corrections required to take into account the near detector resolution or to construct a probability matrix relating directly ND interactions to FD no oscillation interactions which is the method favoured in the MINOS analysis [123]. However, a simple scaling argument allows for the understanding of the ND effects and can be directly compared to existing studies which do not yet take into account the effect of additional neutrinos scattered into the beam by interactions.

## 7.9 Comparison of near detector projection to standard fit method

An initial study of the power of this technique has been carried out assuming a 100 kg cylindrical detector of 1 m radius placed 100 m from the end of a 600 m straight decay section. The flux expected at the near detector site is predicted by randomly generating muon decays along a straight line with an appropriate beam divergence and calculating the expected spectrum from the detector acceptance as calculated for each decay position. The detector is modelled using a conservative estimate of the  $\bar{\nu}_e$  ( $\nu_e$ ) energy resolution of  $35\%/\sqrt{E}(\text{GeV})$  with efficiency of 70% above 4 GeV with a straight line rise from 0% at 0 GeV.  $\nu_\mu$  ( $\bar{\nu}_\mu$ ) resolution is set at  $20\%/\sqrt{E}(\text{GeV})$  with efficiency of 80% for  $\bar{\nu}_\mu$  and 60% for  $\nu_\mu$  above 4 GeV (similar to the FD). A full detector simulation is not yet available to test the validity of these assumptions and to estimate the background levels, as such the current basic study assumes the two signals are separated without background.

A smear is performed on the calculated interactions at the near detector and the flux and correlation matrices for each channel and far detector are then projected to the appropriate far

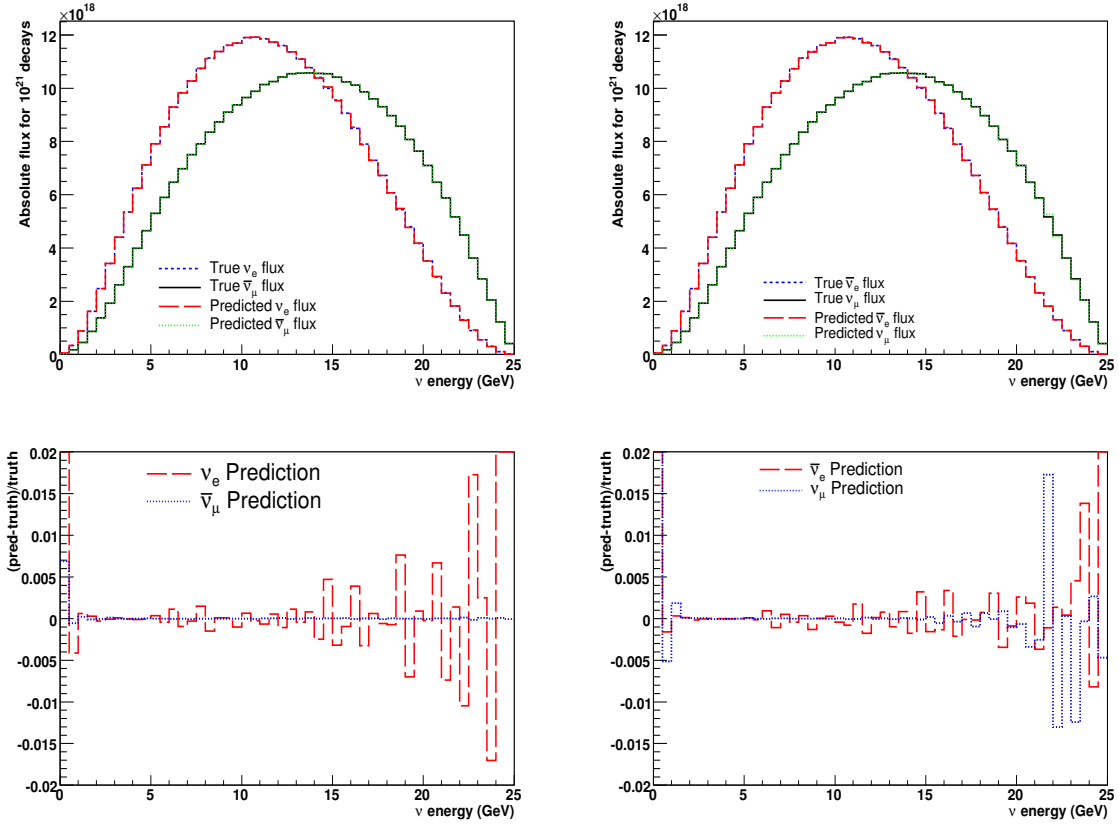


Figure 7.6: Comparison of predicted to true flux through the ND for stored  $\mu^+$  (left) and stored  $\mu^-$  (right). (top) Actual spectra and (bottom) fractional residuals.

detector in bins of 0.5 GeV width. The total integrated interaction spectra expected at a near detector over a data taking run of 5 years allows the flux through the detector to be predicted to a high level of accuracy using the inversion of the response matrices (see Fig. 7.6). Only slight oscillation of the predicted values is visible at higher energies. However, the quality of the prediction is likely to be worse were the technique to be utilised for a limited data-set or the efficiencies or energy resolutions reduced. In the future a more sophisticated unfolding will be developed. The far detector spectra are calculated as in section 7.1 with the non-oscillation predictions from the near detector then being used to perform a fit to this data using the function:

$$\chi^2 = \sum_i \sum_j (N_{i,j} - n_{i,j}) V_{i,j}^{-1} (N_{i,j} - n_{i,j})^T \quad (7.8)$$

where  $i$  is the detector baseline,  $j$  the polarity,  $N$  the predicted spectrum,  $n$  the data spectrum and  $V$  the correlation matrix composed of the projected matrix of the prediction and the expected errors on the far detector measurement. Fig. 7.7 shows the results of fits to a range of  $\theta_{13}$  and  $\delta_{CP}$  values using this technique compared to the same fits performed as described

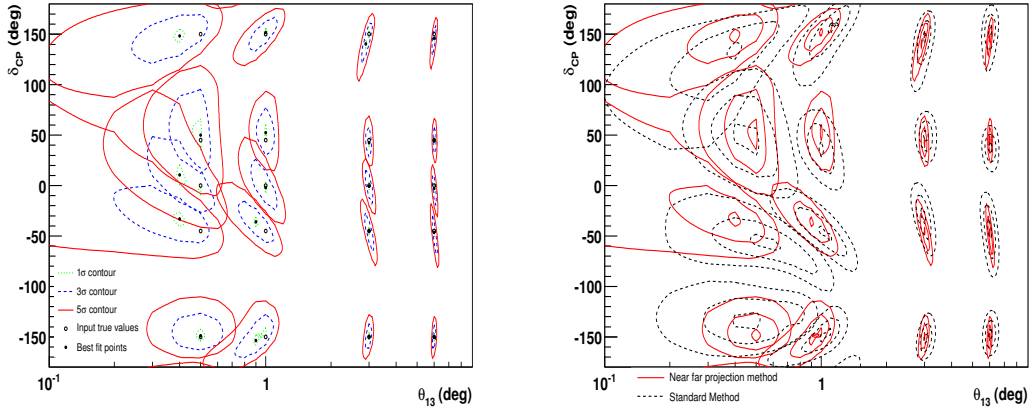


Figure 7.7: Fits to simulated data using the near-far prediction (left) and compared to equivalent fits performed using the standard method (right). All fits assume normal hierarchy.

in section 7.3. As can be seen the resolution of  $\theta_{13}$  is as good or better using the projection technique. Resolution of  $\delta_{CP}$  is generally better for large  $\theta_{13}$  but reduces to a similar level for  $\theta_{13} \leq 1^\circ$ . This tendency is illustrated in Fig. 7.8 for a set of true values of  $\theta_{13} = 1^\circ$  and  $\delta_{CP} = 45^\circ$  where the minimum  $\chi^2$  is projected onto each axis in turn. At the  $1\sigma$  level the

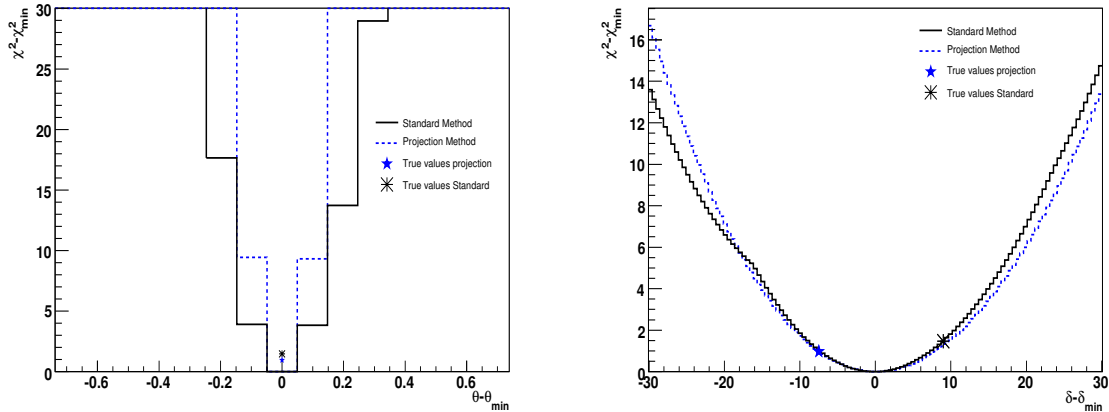


Figure 7.8: Projection of the minimum  $\chi^2$  onto (left) the  $\theta_{13}$  axis and (right) the  $\delta_{CP}$  axis.

fit to  $\theta_{13}$  is very similar for both methods, however, the projection is already better at the  $3\sigma$  level. The projection onto the  $\delta_{CP}$  axis for both methods is very similar, although for this example case the true value is a better fit in the case of the projection method. Fig. 7.9 shows the trend for the measurement of the oscillation parameters for both the standard and projection method with  $1\sigma$  errors garnered from the projection of the minimum  $\chi^2$  onto the appropriate axis. In both cases  $\theta_{13}$  is determined very precisely with the true value being the

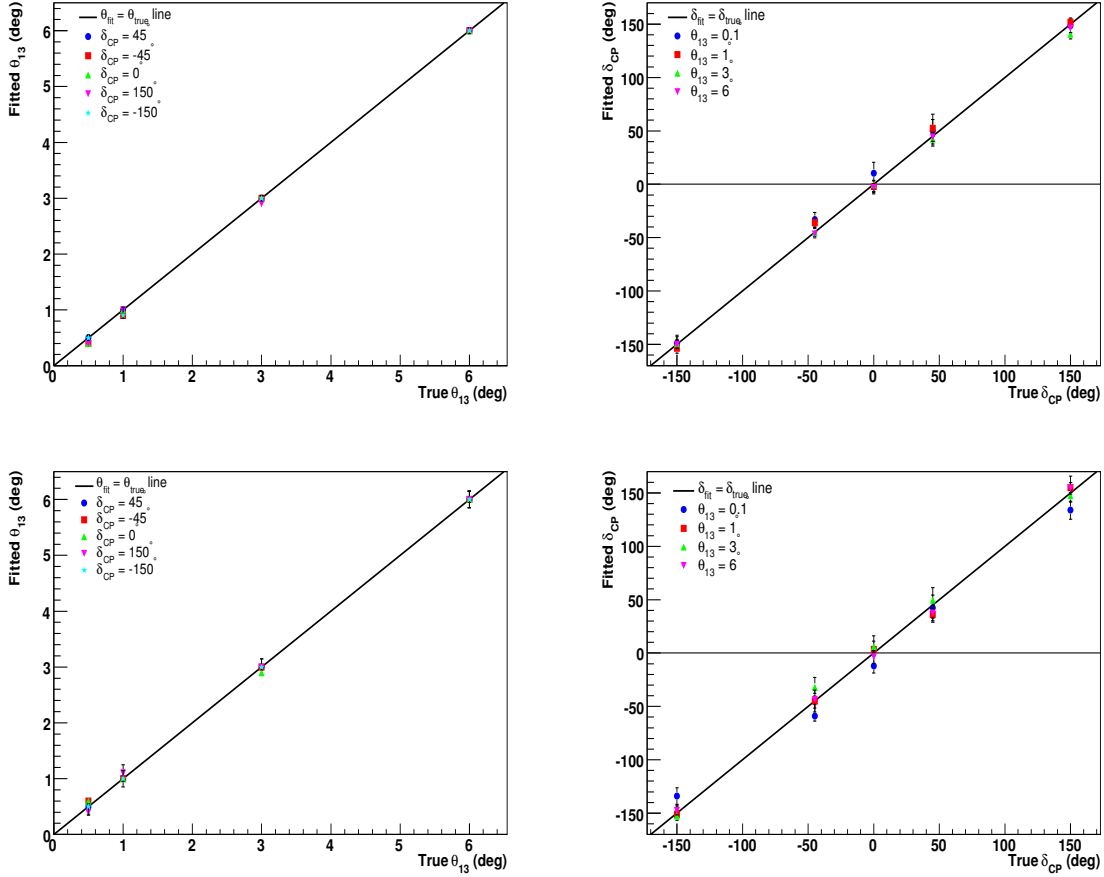


Figure 7.9: *Quality of fit to  $\theta_{13}$  (left) and  $\delta_{CP}$  (right) for a range of values. Using the projection method (top) and the standard method (bottom).*

best fit value in most cases. Determination of  $\delta_{CP}$  is not as precise with the precision of the projection method tending to be somewhat better. Considering the deviation of the the best fit delta value from the true value it can be seen that the mean difference for the standard method is  $\sim 0.9\sigma$  whereas for the projection method it is  $\sim 0.6\sigma$ .

## 7.10 Conclusions

The response of MIND and a parameterisation of the total neutrino and antineutrino cross-sections calculated from the output of the Nuance generator were used to study the sensitivity of the IDS-NF baseline neutrino factory to the measurement of key parameters of the PMNS matrix. The results obtained indicate that such an experiment would remain sensitive to the measurement of  $\theta_{13}$ ,  $\delta_{CP}$  and the true mass hierarchy down to  $\theta_{13}$  values of  $\sim 0.1^\circ$ .

Additionally, a basic method for the projection of the observed near detector spectrum

at a neutrino factory to the far detector sites has been developed. Under the assumption of pure near detector signals it has been shown that this projection can be used to predict the far detector spectrum in the absence of oscillations accurately. While in its current form this method has no clear advantage over the standard theoretical calculation method, with proper development and the use of a high resolution near detector with a sophisticated analysis it has the potential to improve the precision with which the oscillation parameters can be measured.

Either analysis method would allow for the neutrino factory to have the furthest reach in the determination of the remaining parameters of the PMNS matrix.

# Chapter 8

## Conclusions

Neutrino oscillations are now a well established physical phenomenon. As was introduced in chapter 1 the standard mechanism describing the translation from one weak eigenstate to another is well understood and the implication that neutrinos cannot be massless in this paradigm has also been studied extensively. The experiments described in chapter 2 have made measurements of a large part of the parameter space and already give an indication of possible models capable of describing the neutrino and wider lepton sector. However, in order to understand neutrino oscillations fully a new set of experiments are required using high intensity, well understood neutrino sources to study the full parameter space to a high level of precision. The Neutrino Factory facility which was described in detail in chapter 3 and whose detectors form the main focus of this thesis is one such facility which could perform these measurements over a large range of possible values of the smallest mixing angle,  $\theta_{13}$ .

In chapter 4 Active Pixel Sensors were discussed as a possible technology to perform vertex measurements at a detector placed within 1 km of the neutrino factory source. This technology was found to be sensitive to MIP energy particles and to have stable gain and linear response to illumination. The possibility of integration of pre-amplification and digital conversion into individual pixels single out this technology for development as possible tracking and vertexing detectors for future  $e^+e^-$  colliders as well as neutrino factory near detector components.

In chapters 5 and 6 the development of a simulation, digitization, reconstruction and analysis framework for the study and optimisation of the Magnetised Iron Neutrino Detector as a far detector technology was discussed. This detector technology is ideal for the detection of  $\nu_\mu$  ( $\bar{\nu}_\mu$ ) appearance neutrinos indicative of the golden channel oscillation due to the easy scalability to high mass and ease of magnetisation afforded by the iron. Reconstruction algorithms were developed and applied first to the Geant3 simulation which had been used in

the initial studies of this detector technology in the neutrino factory context. Pattern recognition of  $\bar{\nu}_\mu$  deep inelastic scattering events tracked through the simulation was performed for the first time. These algorithms were developed along with an analysis based on track fitting quality and likelihood assessment using the geometric and energy deposit information available for the track. Application of this analysis along with cuts based on the kinematic reconstruction of the neutrino energy allowed for a validation of the conclusions of an earlier fast simulation and analysis.

Introduction of a full interaction spectrum data-set through the use of the Nuance interaction generator allowed study of the effect on the efficiency of low energy interactions like quasi-elastic and resonances. A new simulation of MIND with cuts and data persistency optimised for the study of the golden channel was used to study these interactions using a data-set of several million  $\nu_e$  and  $\nu_\mu$  CC and NC interactions of both polarities. Using a parameterised digitization of the detector scintillators and electronics the reconstruction and analysis algorithms were re-optimised to yield the current state of the art signal efficiency, with an energy threshold at between 2-3 GeV and efficiency plateaus at 70% and 60% for  $\bar{\nu}_\mu$  and  $\nu_\mu$  appearance respectively, and background suppression, at or below  $10^{-4}$  for all channels, for the study of the golden channel with MIND. The level of suppression achievable indicates the possibility to study the remaining parameters of the PMNS matrix down to small values of  $\theta_{13}$ .

In the final chapter, the calculated response of MIND was used in the framework of the IDS-NF baseline neutrino factory design to study the sensitivity of such an experiment to the measurement of the key neutrino oscillation parameters,  $\theta_{13}$ ,  $\delta_{CP}$  and  $sign(\Delta m_{23}^2)$ . Under the assumption that measurement of the absolute flux at the near detector can be performed to an accuracy of 5% and that this measurement coupled with the theoretical calculation of the neutrino spectrum from muon decay could predict the zero oscillation flux the sensitivity to these parameters was quantified across the whole parameter space. The experiments were found to have sensitivity to the measurement of  $\theta_{13}$  down to values  $\sim 0.25^\circ$ , sensitivity to maximal CP-violation down to  $\theta_{13} \sim 1^\circ$  and sensitivity to the determination of the true mass hierarchy for whenever there is sensitivity to  $\theta_{13}$ . Using a basic method for estimation of the far detector zero oscillation flux from a near detector spectral measurement the accuracy with which  $\theta_{13}$  and  $\delta_{CP}$  can be measured has been studied. Results obtained show that the neutrino factory remains the facility with the greatest reach for the measurement of these parameters and that with proper development the projection technique has the potential to increase the level of accuracy with which these parameters can be measured.

# Bibliography

- [1] Boris Kayser. Neutrino Oscillation Phenomenology. In F.J.P. Soler, Colin D. Froggatt, and Franz Muheim, editors, *Neutrinos in particle physics, astrophysics and cosmology*, pages 51–64. CRC Press, 2008.
- [2] Andre de Gouvea, James Jenkins, and Boris Kayser. Neutrino mass hierarchy, vacuum oscillations, and vanishing  $|U_{e3}|$ . *Phys. Rev.*, D71:113009, 2005.
- [3] Beate Bornschein. Absolute neutrino mass measurements. In F.J.P. Soler, Colin D. Froggatt, and Franz Muheim, editors, *Neutrinos in particle physics, astrophysics and cosmology*, pages 261–285. CRC Press, 2008.
- [4] S. Rigolin. Physics reach of beta-beams and nu-factories: The problem of degeneracies. *Nucl. Phys. Proc. Suppl.*, 155:33–37, 2006.
- [5] J. Bahcall. <http://www.sns.ias.edu/jnb/>.
- [6] J. Hosaka et al. Solar neutrino measurements in Super-Kamiokande-I. *Phys. Rev.*, D73:112001, 2006.
- [7] G. L. Fogli, E. Lisi, A. Marrone, D. Montanino, and A. Palazzo. Getting the most from the statistical analysis of solar neutrino oscillations. *Phys. Rev.*, D66:053010, 2002.
- [8] J. Hosaka et al. Three flavor neutrino oscillation analysis of atmospheric neutrinos in Super-Kamiokande. *Phys. Rev.*, D74:032002, 2006.
- [9] S. Abe et al. Precision Measurement of Neutrino Oscillation Parameters with KamLAND. *Phys. Rev. Lett.*, 100:221803, 2008.
- [10] M. H. Ahn et al. Measurement of Neutrino Oscillation by the K2K Experiment. *Phys. Rev.*, D74:072003, 2006.
- [11] The MINOS collaboration. <http://www-numi.fnal.gov/PublicInfo/forscientists.html>.

- [12] A. A. Aguilar-Arevalo et al. A Search for electron neutrino appearance at the  $\Delta m^2 \sim 1\text{eV}^2$  scale. *Phys. Rev. Lett.*, 98:231801, 2007.
- [13] J. C. Gallardo et al. Muon Muon Collider: Feasibility Study. Prepared for 1996 DPF / DPB Summer Study on New Directions for High Energy Physics (Snowmass 96), Snowmass, Colorado, 25 Jun - 12 Jul 1996.
- [14] A. Bandyopadhyay et al. Physics at a future Neutrino Factory and super-beam facility. *Rept. Prog. Phys.*, 72, 2009.
- [15] Giovanni De Lellis, Pasquale Migliozi, and Pietro Santorelli. Charm physics with neutrinos. *Phys. Rept.*, 399:227–320, 2004.
- [16] G. P. Zeller. Low energy neutrino cross sections from K2K, MiniBooNE, SciBooNE, and MINERvA. *J. Phys. Conf. Ser.*, 136:022028, 2008.
- [17] A. Cervera et al. Golden measurements at a neutrino factory. *Nucl. Phys.*, B579:17–55, 2000.
- [18] A. Cervera-Villanueva. Review of large magnetic calorimeters for a neutrino factory. *Nucl. Phys. Proc. Suppl.*, 149:201–202, 2005.
- [19] A. Cervera-Villanueva. MIND performance and prototyping. *AIP Conf. Proc.*, 981:178–180, 2008.
- [20] W. Pauli. Dear radioactive ladies and gentlemen. *Phys. Today*, 31N9:27, 1978.
- [21] C. L. Cowan, F. Reines, F. B. Harrison, H. W. Kruse, and A. D. McGuire. Detection of the free neutrino: A Confirmation. *Science*, 124:103–104, 1956.
- [22] C. S. Wu, E. Ambler, R. W. Hayward, D. D. Hoppes, and R. P. Hudson. Experimental Test of Parity Conservation in Beta Decay. *Phys. Rev.*, 105:1413–1414, 1957.
- [23] M. Goldhaber, L. Grodzins, and A. W. Sunyar. Helicity of Neutrinos. *Phys. Rev.*, 109:1015–1017, 1958.
- [24] K. Zuber. *Neutrino physics*. IOP, 2003.
- [25] C. Amsler et al. Review of particle physics. *Physics Letters B*, 667(1-5):1 – 6, 2008. and 2009 partial update for 2010 edition.
- [26] Ziro Maki, Masami Nakagawa, and Shoichi Sakata. Remarks on the unified model of elementary particles. *Prog. Theor. Phys.*, 28:870–880, 1962.

- [27] B. Pontecorvo. Neutrino experiments and the question of leptonic-charge conservation. *Sov. Phys. JETP*, 26:984–988, 1968.
- [28] L. Wolfenstein. Neutrino oscillations in matter. *Phys. Rev.*, D17:2369–2374, 1978.
- [29] S. P. Mikheyev and A. Yu. Smirnov. Resonant neutrino oscillations in matter. *Prog. Part. Nucl. Phys.*, 23:41–136, 1989.
- [30] H. W. Zaglauer and K. H. Schwarzer. The Mixing Angles in Matter for Three Generations of Neutrinos and the MSW Mechanism. *Z. Phys.*, C40:273, 1988.
- [31] A. De Rujula, M. B. Gavela, and P. Hernandez. Neutrino oscillation physics with a neutrino factory. *Nucl. Phys.*, B547:21–38, 1999.
- [32] J. Angrik et al. KATRIN design report 2004. FZKA-7090.
- [33] Ettore Majorana. Theory of the Symmetry of Electrons and Positrons. *Nuovo Cim.*, 14:171–184, 1937.
- [34] W. H. Furry. On transition probabilities in double beta- disintegration. *Phys. Rev.*, 56:1184–1193, 1939.
- [35] Rabindra N. Mohapatra and Goran Senjanovic. Neutrino mass and spontaneous parity nonconservation. *Phys. Rev. Lett.*, 44:912, 1980.
- [36] Fabrice Piquemal. Double beta decay review. *J. Phys. Conf. Ser.*, 120:052004, 2008.
- [37] J. Burguet-Castell, M. B. Gavela, J. J. Gomez-Cadenas, P. Hernandez, and Olga Mena. On the measurement of leptonic CP violation. *Nucl. Phys.*, B608:301–318, 2001.
- [38] V. Barger, D. Marfatia, and K. Whisnant. Breaking eight-fold degeneracies in neutrino CP violation, mixing, and mass hierarchy. *Phys. Rev.*, D65:073023, 2002.
- [39] Patrick Huber and Walter Winter. Neutrino factories and the 'magic' baseline. *Phys. Rev.*, D68:037301, 2003.
- [40] John N. Bahcall, Aldo M. Serenelli, and Sarbani Basu. 10,000 Standard Solar Models: a Monte Carlo Simulation. *Astrophys. J. Suppl.*, 165:400–431, 2006.
- [41] R. Davis. A review of the Homestake solar neutrino experiment. *Prog. Part. Nucl. Phys.*, 32:13–32, 1994.

- [42] J. N. Abdurashitov et al. Measurement of the solar neutrino capture rate by the Russian-American gallium solar neutrino experiment during one half of the 22-year cycle of solar activity. *J. Exp. Theor. Phys.*, 95:181–193, 2002.
- [43] W. Hampel et al. GALLEX solar neutrino observations: Results for GALLEX IV. *Phys. Lett.*, B447:127–133, 1999.
- [44] Q. R. Ahmad et al. Measurement of the charged current interactions produced by B-8 solar neutrinos at the Sudbury Neutrino Observatory. *Phys. Rev. Lett.*, 87:071301, 2001.
- [45] John N. Bahcall, M. C. Gonzalez-Garcia, and Carlos Peña Garay. Global analysis of solar neutrino oscillations including SNO CC measurement. *JHEP*, 08:014, 2001.
- [46] C. Arpesella et al. Direct Measurement of the Be-7 Solar Neutrino Flux with 192 Days of Borexino Data. *Phys. Rev. Lett.*, 101:091302, 2008.
- [47] W. W. M. Allison et al. Neutrino oscillation effects in Soudan-2 upward-stopping muons. *Phys. Rev.*, D72:052005, 2005.
- [48] M. Ambrosio et al. Measurements of atmospheric muon neutrino oscillations, global analysis of the data collected with MACRO detector. *Eur. Phys. J.*, C36:323–339, 2004.
- [49] M. Apollonio et al. Limits on Neutrino Oscillations from the CHOOZ Experiment. *Phys. Lett.*, B466:415–430, 1999.
- [50] M. G. Catanesi et al. The HARP detector at the CERN PS. *Nucl. Instrum. Meth.*, A571:527–561, 2007.
- [51] Magdalena Posiadala. Status of the NA61 (SHINE) experiment at CERN. internal collaboration note, 2009.
- [52] P. Adamson et al. A Study of Muon Neutrino Disappearance Using the Fermilab Main Injector Neutrino Beam. *Phys. Rev.*, D77:072002, 2008.
- [53] P. Adamson et al. Search for muon-neutrino to electron-neutrino transitions in MINOS. *Phys. Rev. Lett.*, 103:261802, 2009.
- [54] C. Athanassopoulos et al. Evidence for  $\bar{\nu}_\mu \rightarrow \bar{\nu}_e$  Oscillation from the LSND Experiment at the Los Alamos Meson Physics Facility. *Phys. Rev. Lett.*, 77:3082–3085, 1996.

- 
- [55] C. Athanassopoulos et al. Evidence for  $\nu_\mu \rightarrow \nu_e$  Neutrino Oscillations from LSND. *Phys. Rev. Lett.*, 81:1774–1777, 1998.
- [56] A. A. Aguilar-Arevalo et al. Observed Event Excess in the MiniBooNE Search for  $\bar{\nu}_\mu \rightarrow \bar{\nu}_e$  Oscillations, 2010. arXiv:1007.1150.
- [57] Y. Hayato. T2K at J-PARC. *Nucl. Phys. Proc. Suppl.*, 143:269–276, 2005.
- [58] D. S. Ayres et al. NOvA proposal to build a 30-kiloton off-axis detector to study neutrino oscillations in the Fermilab NuMI beamline, 2004. hep-ex/0503053.
- [59] P. Zucchelli. A novel concept for a  $\bar{\nu}_e/\nu_e$  neutrino factory: The beta beam. *Phys. Lett.*, B532:166–172, 2002.
- [60] J. Aysto, D. Forkel-Wirth, M. Lindroos, H. L. Ravn, and P. Van Duppen. A Second Generation Radioactive Nuclear Beam Facility at CERN. CERN-PS-2000-075-OP.
- [61] J. Burguet-Castell, D. Casper, E. Couce, J. J. Gomez-Cadenas, and P. Hernandez. Optimal beta-beam at the CERN-SPS. *Nucl. Phys.*, B725:306–326, 2005.
- [62] C. Rubbia, A. Ferrari, Y. Kadi, and V. Vlachoudis. Beam cooling with ionisation losses. *Nucl. Instrum. Meth.*, A568:475–487, 2006.
- [63] Jose Bernabeu, Catalina Espinoza, Christopher Orme, Sergio Palomares-Ruiz, and Silva Pascoli. A combined beta-beam and electron capture neutrino experiment. *JHEP*, 06:040, 2009.
- [64] D. G. Koshkarev. Proposal for a Decay Ring to Produce Intense Secondary Particle Beams at the SPS. CERN/ISR-DI/74-62, 1974.
- [65] D. Cline and D. Neuffer. A Muon Storage Ring for Neutrino Oscillations Experiments. *AIP Conf. Proc.*, 68:846–847, 1980.
- [66] S. Geer. Neutrino beams from muon storage rings: Characteristics and physics potential. *Phys. Rev.*, D57:6989–6997, 1998.
- [67] J. S. Berg et al. Accelerator design concept for future neutrino facilities. *JINST*, 4:P07001, 2009.
- [68] T. Abe et al. Detectors and flux instrumentation for future neutrino facilities. *JINST*, 4:T05001, 2009.

- [69] Valeri Lebedev and Sergei Nagaitsev. Project X ICD-2 and its upgrades for Neutrino Factory or Muon Collider. *AIP Conf. Proc.*, 1222:274–278, 2010.
- [70] T. Nakadaira et al. T2K target. *AIP Conf. Proc.*, 981:290–292, 2008.
- [71] *The MERIT High-Power Target Experiment at the CERN PS*, 2008. Presented at 11th European Particle Accelerator Conference (EPAC 08), Magazzini del Cotone, Genoa, Italy, 23-27 Jun 2008.
- [72] *Preliminary Experiments on a Fluidised Powder Target*, 2008. EPAC’08, 11th European Particle Accelerator Conference, 23- 27 June 2008, Genoa, Italy.
- [73] *Technical implementation of feasibility study-II design*, 2001. Prepared for 18th International Conference on High-Energy Accelerators (HEACC 2001), Tsukuba, Japan, 26-30 Mar 2001.
- [74] The MICE collaboration. MICE: An International Muon Ionisation Cooling Experiment, Technical Reference Document. MICE-TRD-2005.
- [75] Malcolm Ellis and F. J. P. Soler. Near detector at a neutrino factory. *Nucl. Instrum. Meth.*, A569:127–131, 2006.
- [76] K. S. McFarland. Short-baseline opportunities and challenges at a neutrino factory. *Nucl. Instrum. Meth.*, A451:218–228, 2000.
- [77] D. G. Michael et al. The Magnetized steel and scintillator calorimeters of the MINOS experiment. *Nucl. Instrum. Meth.*, A596:190–228, 2008.
- [78] Alan Bross, Malcolm Ellis, Steve Geer, Olga Mena, and Silvia Pascoli. The low-energy neutrino factory. *AIP Conf. Proc.*, 981:187–189, 2008.
- [79] Thomas Schwetz, M. A. Tortola, and Jose W. F. Valle. Three-flavour neutrino oscillation update. *New J. Phys.*, 10:113011, 2008.
- [80] Davide Meloni, Tommy Ohlsson, Walter Winter, and He Zhang. Non-standard interactions versus non-unitary lepton flavor mixing at a neutrino factory. *JHEP*, 04:041, 2010.
- [81] R Petti et al. A precise measurement of Charm Dimuon production in neutrino interactions from the NOMAD experiment. *PoS*, DIS 2010:170, 2010.
- [82] A. Kayis-Topaksu et al. Leading order analysis of neutrino induced dimuon events in the CHORUS experiment. *Nucl. Phys.*, B798:1–16, 2008.

- [83] G. Barichello et al. Performance of the NOMAD-STAR detector. *Nucl. Instrum. Meth.*, A506:217–237, 2003.
- [84] Jaap Velthuis et al. Status of the UK MAPS Project. *Proceedings of LCW 2005*, 2005. In the Proceedings of 2005 International Linear Collider Workshop (LCWS 2005), Stanford, California, 18-22 Mar 2005.
- [85] Multidimensional Integrated Intelligent Imaging. URL: <http://mi3.shef.ac.uk>.
- [86] B. Pain, Guang Yang, T.J. Cunningham, C. Wrigley, and B. Hancock. An enhanced-performance CMOS imager with a flushed-reset photodiode pixel. *Electron Devices, IEEE Transactions on*, 50(1):48–56, Jan 2003.
- [87] J. Janesick. *Scientific Charge Coupled Devices*. SPIE Press, 2001.
- [88] D. Maneuski. *Pixellated Radiation Detectors for Scientific Applications*. PhD thesis, School of Physics & Astronomy, University of Glasgow, 2009.
- [89] Bedabrata Pain and Bruce R. Hancock. Accurate estimation of conversion gain and quantum efficiency in CMOS imagers. In Morley M. Blouke, Nitin Sampat, and Ricardo J. Motta, editors, *Sensors and Camera Systems for Scientific, Industrial, and Digital Photography Applications IV*, volume 5017, pages 94–103. SPIE, 2003.
- [90] J. Janesick. *Photon Transfer*. SPIE Press, 2007.
- [91] R. Turchetta. RAL HEPAPS4 manual. Available from RAL, 2006.
- [92] L. Eklund et al. First results from the HEPAPS4 active pixel sensor. *Nucl. Instrum. Meth.*, A598:64–66, 2009.
- [93] D. Maneuski, L. Eklund, A. Laing, R. Turchetta, and V. O’Shea. Characterisation of HEPAPS4—A family of CMOS active pixel sensors for charged particle detection. *Nuclear Instruments and Methods in Physics Research Section A: Accelerators, Spectrometers, Detectors and Associated Equipment*, 604(1-2):404 – 407, 2009. PSD8 - Proceedings of the 8th International Conference on Position Sensitive Detectors.
- [94] J. J. Velthuis et al. First results of the ISIS1 beam test. *Nucl. Instrum. Meth.*, A599:161–166, 2009.
- [95] H. Bichsel. Straggling in thin silicon detectors. *Rev. Mod. Phys.*, 60:663–699, 1988.

- [96] Andrew Blue, A. Clark, S. Houston, A. Laing, D. Maneuski, M. Prydderch, R. Turchetta, and V. O'Shea. Optical and electrical characterization of a back-thinned cmos active pixel sensor. *Nuclear Instruments and Methods in Physics Research Section A: Accelerators, Spectrometers, Detectors and Associated Equipment*, 604(1-2):215 – 217, 2009. PSD8 - Proceedings of the 8th International Conference on Position Sensitive Detectors.
- [97] B. Pontecorvo. Mesonium and antimesonium. *Sov. Phys. JETP*, 6:429, 1957.
- [98] B. Pontecorvo. Inverse beta processes and nonconservation of lepton charge. *Sov. Phys. JETP*, 7:172–173, 1958.
- [99] EUROnu: A High Intensity Neutrino Oscillation Facility in Europe. URL: <http://www.euronu.org/>.
- [100] The International Design Study for the Neutrino Factory. URL: <https://www.ids-nf.org/wiki/FrontPage>.
- [101] A. Cervera, F. Dydak, and J. Gomez Cadenas. A large magnetic detector for the neutrino factory. *Nucl. Instrum. Meth.*, A451:123–130, 2000.
- [102] Geant 3.21 CERN Program Library. CERN Long write up W5013. <http://wwwasdoc.web.cern.ch/wwwasdoc/pdfdir/geant.pdf>.
- [103] A. Cervera and A. Laing. Status of MIND. *PoS*, Nufact08:042, 2008.
- [104] A. M. Dziewonski and D. L. Anderson. Preliminary reference earth model. *Phys. Earth Planet. Interiors*, 25:297–356, 1981.
- [105] J. Burguet-Castell, M. B. Gavela, J. J. Gomez-Cadenas, P. Hernandez, and Olga Mena. Superbeams plus neutrino factory: The golden path to leptonic CP violation. *Nucl. Phys.*, B646:301–320, 2002.
- [106] G. Ingelman, A. Edin, and J. Rathsman. LEPTO 6.5 - A Monte Carlo generator for deep inelastic lepton-nucleon scattering. *Computer Physics Communications*, 101:108–134(27), 1997.
- [107] A. Cervera-Villanueva, J. J. Gomez-Cadenas, and J. A. Hernando. 'RecPack' a reconstruction toolkit. *Nucl. Instrum. Meth.*, A534:180–183, 2004.
- [108] D. Emeliyanov, I. Gorbounov, and I. Kisel. Otr/itr-cats: Tracking based on cellular automaton and kalman filter, 2001. HERA-B note 01-137.

- [109] P. Adamson et al. The MINOS calibration detector. *Nucl. Instrum. Meth.*, A556:119–133, 2006.
- [110] G. Bari et al. Analysis of the performance of the MONOLITH prototype. *Nucl. Instrum. Meth.*, A508:170–174, 2003.
- [111] R. Brun and F. Rademakers. ROOT: An object oriented data analysis framework. *Nucl. Instrum. Meth.*, A389:81–86, 1997.
- [112] Andrea Donini, Patrick Huber, Silvia Pascoli, Walter Winter, and Osamu Yasuda. Physics and Performance Evaluation Group. *AIP Conf. Proc.*, 981:43–45, 2008.
- [113] D. Casper. The nuance neutrino physics simulation, and the future. *Nucl. Phys. Proc. Suppl.*, 112:161–170, 2002.
- [114] John Apostolakis and Dennis H. Wright. An overview of the GEANT4 toolkit. *AIP Conf. Proc.*, 896:1–10, 2007.
- [115] Geant4 Physics Reference Manual. <http://cern.ch/geant4/UserDocumentation/UsersGuides/PhysicsReferenceManual/html/>.
- [116] Anna Pla-Dalmau, Alan D. Bross, Victor V. Rykalin, and Brian M. Wood. Extruded plastic scintillator for MINERvA. To appear in the proceedings of 2005 IEEE Nuclear Science Symposium and Medical Imaging Conference, El Conquistador Resort, Puerto Rico, 23-29 Oct 2005.
- [117] A. Blondel, M. Campanelli, and M. Fechner. Energy reconstruction in quasi-elastic events unfolding physics and detector effects. *Nucl. Instrum. Meth.*, A535:665–673, 2004.
- [118] V. Lyubushkin et al. A study of quasi-elastic muon neutrino and antineutrino scattering in the NOMAD experiment. *Eur. Phys. J.*, C63:355–381, 2009.
- [119] A. A. Aguilar-Arevalo et al. First Measurement of the Muon Neutrino Charged Current Quasielastic Double Differential Cross Section. *Phys. Rev.*, D81:092005, 2010.
- [120] A. Rodriguez et al. Measurement of single charged pion production in the charged-current interactions of neutrinos in a 1.3 GeV wide band beam. *Phys. Rev.*, D78:032003, 2008.
- [121] A. Donini, J. J. Gomez Cadenas, and D. Meloni. The  $\tau$ -contamination of the golden muon sample at the Neutrino Factory, 2010. arXiv:1005.2275.

- [122] T. Kafka and V. Paolone. Prospects and status of the MINERvA experiment at FNAL. *Prog. Part. Nucl. Phys.*, 64:181–183, 2010.
- [123] D. G. Michael et al. Observation of muon neutrino disappearance with the minos detectors and the numi neutrino beam. *Phys. Rev. Lett.*, 97:191801, 2006.
- [124] A. Laing and F. J. P. Soler. Flux measurement at a neutrino factory near detector for neutrino oscillations. *AIP Conf. Proc.*, 981:166–168, 2008.
- [125] G. Cowan. *Statistical data analysis*. Oxford University Press, UK: Clarendon, 1998.
- [126] Andrew Laing and F. J. P. Soler. Oscillation probability fits using near detector data at a neutrino factory. *PoS*, NFACT08:129, 2008.

# Appendix A

## Response Matrices for chapter 5 analysis

This appendix presents numerically the response matrices of MIND extracted for signal and backgrounds in chapter 5.

### Signal Efficiency

	0-2.5	2.5-3.5	3.5-4.5	4.5-5.5	5.5-6.5	6.5-7.5	7.5-10	10-15	15-20	20-25	25-30
0-2.5	0	0	0	0	0	0	0	0	0	0	0
2.5-3.5	1.78	1.26	0.01	0	0	0	0	0	0	0	0
3.5-4.5	0.49	5.94	6.54	0.20	0.04	0	0	0	0	0	0
4.5-5.5	0.08	1.71	20.24	16.07	0.68	0.03	0.01	0	0	0	0
5.5-6.5	0.04	0.39	6.04	28.25	20.72	1.59	0.07	0	0	0	0
6.5-7.5	0	0.12	1.18	7.26	31.82	20.23	1.21	0.01	0	0	0
7.5-10	0	0.09	0.70	2.31	11.22	40.36	38.50	1.38	0.01	0.01	0.01
10-15	0	0.06	0.30	0.67	1.18	2.29	26.76	47.64	2.15	0.075	0.032
15-20	0	0	0.14	0.32	0.24	0.35	0.58	19.15	40.25	2.68	0.26
20-25	0	0	0.10	0.07	0.14	0.25	0.17	0.66	24.72	33.40	2.87
25-30	0	0	0	0.12	0.07	0.06	0.12	0.15	1.77	28.15	27.86
overflow	0	0.01	0.04	0.09	0.33	0.40	0.44	0.43	0.62	4.90	37.72

Table A.1: *Signal Efficiency response matrix; All values  $\times 10^{-2}$*

$\bar{\nu}_\mu$  CC background

	0-2.5	2.5-3.5	3.5-4.5	4.5-5.5	5.5-6.5	6.5-7.5	7.5-10	10-15	15-20	20-25	25-30
0-2.5	0	0	0	0	0	0	0	0	0	0	0
2.5-3.5	0	0	0.14	0	0	0	0	0	0	0	0
3.5-4.5	0	0	0.29	0	0	0	0	0	0	0	0
4.5-5.5	0	0	0.43	0.29	0.14	0	0	0	0	0	0
5.5-6.5	0	0	0.14	0.15	0.14	0	0	0	0	0	0
6.5-7.5	0	0	0	0.15	0	0.29	0.06	0	0	0.03	0
7.5-10	0	0	0.14	0.15	0.72	0	0.29	0.03	0.03	0	0
10-15	0	0	0	0.29	0.29	0.15	0.29	0.29	0.03	0.03	0.03
15-20	0	0	0	0.15	0	0	0	0.26	0.20	0.09	0.03
20-25	0	0	0	0	0	0	0.06	0.06	0.03	0.09	0.06
25-30	0	0	0	0	0	0	0	0	0.03	0.06	0.09
overflow	0	0	0	0.15	0	0	0	0.06	0.03	0.14	0.17

Table A.2:  $\bar{\nu}_\mu$  CC background response matrix; All values  $\times 10^{-3}$

NC background

	0-2.5	2.5-3.5	3.5-4.5	4.5-5.5	5.5-6.5	6.5-7.5	7.5-10	10-15	15-20	20-25	25-30
0-2.5	0	0	0	0	0	0	0	0	0	0	0
2.5-3.5	0	0.01	0	0.01	0	0	0	0	0	0	0
3.5-4.5	0	0	0.02	0.01	0.02	0	0	0	0	0	0
4.5-5.5	0.03	0.05	0.02	0.02	0.01	0.01	0	0.01	0.01	0.01	0
5.5-6.5	0	0	0.02	0.02	0.01	0.04	0.01	0.01	0.01	0	0.01
6.5-7.5	0	0.01	0	0	0.02	0	0	0.01	0	0.01	0
7.5-10	0	0.01	0.01	0.01	0	0	0	0.01	0	0	0
10-15	0	0	0	0	0	0	0	0	0.01	0.01	0
15-20	0	0	0	0	0.01	0	0	0	0	0	0
20-25	0	0	0	0	0	0	0	0	0	0	0
25-30	0	0	0	0	0	0	0	0	0	0	0
overflow	0	0	0	0	0	0	0	0	0	0	0

Table A.3: Neutral current background response matrix; All values  $\times 10^{-3}$

$\nu_e$  CC background

	0-2.5	2.5-3.5	3.5-4.5	4.5-5.5	5.5-6.5	6.5-7.5	7.5-10	10-15	15-20	20-25	25-30
0-2.5	0	0	0	0	0	0	0	0	0	0	0
2.5-3.5	0	0	0	0	0	0	0	0	0	0	0
3.5-4.5	0	0	0	0	0	0	0	0	0	0	0
4.5-5.5	0	0	0	0.03	0	0	0	0	0	0	0
5.5-6.5	0	0	0.03	0	0	0	0	0	0	0	0
6.5-7.5	0	0	0.06	0	0	0	0	0	0	0	0
7.5-10	0	0	0	0	0	0	0	0.01	0	0	0
10-15	0	0	0	0	0	0	0	0	0	0	0
15-20	0	0	0	0	0	0	0	0	0.01	0	0
20-25	0	0	0	0	0	0	0	0	0	0	0
25-30	0	0	0	0	0	0	0	0	0	0.01	0.01
overflow	0	0	0	0	0	0	0	0	0	0	0

Table A.4:  $\nu_e$  CC background response matrix; All values  $\times 10^{-3}$

# Appendix B

## Response Matrices for chapter 6 analysis

This appendix presents numerically the response matrices of MIND extracted for all signal and backgrounds for the golden channel oscillation search in chapter 6.

### $\nu_\mu$ appearance

#### Signal Efficiency

	0-2.0	2.0-3.0	3.0-4.0	4.0-5.0	5.0-6.0	6.0-8.0	8.0-10.0	10.0-12.5	12.5-15.0	15.0-20.0	20.0-25.0
0-2.0	211.8	331.0	48.55	13.92	5.73	2.371	0.790	0.377	0.142	0.076	0.039
2.0-3.0	154.4	1379	522.0	118.0	42.03	15.18	4.903	1.916	1.049	0.572	0.156
3.0-4.0	45.17	906.6	1408	554.5	145.6	41.82	13.36	4.334	2.211	0.934	0.429
4.0-5.0	17.93	422.1	1377	1352	544.5	105.4	26.26	8.951	3.288	1.449	0.722
5.0-6.0	7.509	155.6	744.7	1476	1233	318.5	49.26	14.82	4.535	2.307	0.761
6.0-8.0	2.017	70.17	421.2	1469	2729	2010	447.4	71.04	18.31	7.302	3.025
8.0-10.0	0.112	7.406	46.89	230.1	850.6	2371	1823	380.8	56.63	13.65	5.212
10.05-12.5	0	2.134	12.61	37.15	134.9	963.9	2756	2011	416.5	48.96	11.50
12.5-15.0	0	0.126	2.739	11.20	27.05	127.4	886.8	2519	1788	242.5	22.84
15.0-20.0	0	0.126	0.498	2.346	7.930	36.72	173.2	1207	3621	2840	340.5
20.0-25.0	0	0	0.083	0.076	0.088	1.186	11.52	61.27	380.2	2665	2562
overflow	0	0	0	0	0	0.514	0.757	5.685	31.86	477.2	3338

Table B.1:  $\nu_\mu$  appearance detection efficiency. All values  $\times 10^{-4}$

$\bar{\nu}_\mu$  CC background

	0-2.0	2.0-3.0	3.0-4.0	4.0-5.0	5.0-6.0	6.0-8.0	8.0-10.0	10.0-12.5	12.5-15.0	15.0-20.0	20.0-25.0
0-2.0	0	0	0.096	0	0	0.041	0	0	0	0	0
2.0-3.0	0.346	0.546	0	0.083	0	0	0	0	0	0.039	0.020
3.0-4.0	0.173	0.273	0.096	0	0	0.084	0	0.065	0.029	0.077	0.020
4.0-5.0	0.173	0.546	0.192	0.166	0	0.042	0.068	0.065	0	0	0.020
5.0-6.0	0	0.273	0.384	0.083	0.187	0.042	0.034	0	0.029	0.039	0.039
6.0-8.0	0	0.273	0.288	0.249	0.468	0.209	0.068	0.097	0.115	0.096	0.039
8.0-10.0	0	0	0.096	0	0	0.084	0.137	0.129	0.086	0.116	0.020
10.0-12.5	0	0	0	0	0.094	0.042	0.205	0.032	0.086	0.019	0.138
12.5-15.0	0	0	0	0.083	0.094	0	0.102	0	0.058	0.058	0.079
15.0-20.0	0	0	0	0	0	0.084	0.068	0.065	0.029	0.116	0.079
20.0-25.0	0	0	0	0	0	0.042	0	0.032	0.086	0.058	0.059
overflow	0	0	0	0	0	0	0	0	0	0.019	0.098

Table B.2:  $\bar{\nu}_\mu$  CC background. All values  $\times 10^{-4}$ .

$\nu_e$  CC background

	0-2.0	2.0-3.0	3.0-4.0	4.0-5.0	5.0-6.0	6.0-8.0	8.0-10.0	10.0-12.5	12.5-15.0	15.0-20.0	20.0-25.0
0-2.0	0	0	0	0	0	0	0	0	0.020	0.013	0
2.0-3.0	0	0	0	0	0	0	0.023	0.045	0.040	0	0
3.0-4.0	0	0	0	0	0	0	0	0	0	0.013	0.055
4.0-5.0	0	0	0	0	0	0.028	0	0	0	0	0.014
5.0-6.0	0	0	0	0	0	0	0	0	0	0	0.014
6.0-8.0	0	0	0	0	0	0	0	0	0.020	0	0
8.0-10.0	0	0	0	0	0	0	0	0	0	0	0
10.0-12.5	0	0	0	0.054	0	0	0	0	0	0	0
12.5-15.0	0	0	0	0	0	0	0	0	0	0	0
15.0-20.0	0	0	0	0	0	0	0	0.022	0.020	0	0
20.0-25.0	0	0	0	0	0	0	0	0	0	0	0
overflow	0	0	0	0	0	0	0	0	0	0	0

Table B.3:  $\nu_e$  CC background. All values  $\times 10^{-4}$ .

NC background

	0-2.0	2.0-3.0	3.0-4.0	4.0-5.0	5.0-6.0	6.0-8.0	8.0-10.0	10.0-12.5	12.5-15.0	15.0-20.0	20.0-25.0
0-2.0	0	0	0	0	0.035	0	0.026	0.050	0.022	0.015	0
2.0-3.0	0	0	0.034	0.061	0.070	0.016	0.052	0.050	0.034	0.030	0.039
3.0-4.0	0	0	0	0.061	0.070	0	0.052	0.076	0.056	0.068	0.055
4.0-5.0	0	0	0.034	0.030	0.106	0.157	0.210	0.088	0.146	0.106	0.086
5.0-6.0	0	0	0	0.030	0.035	0.031	0.026	0.076	0.067	0.030	0.023
6.0-8.0	0	0	0	0	0	0.094	0.105	0.113	0.067	0.046	0.047
8.0-10.0	0	0	0	0	0.035	0.047	0.026	0.088	0.011	0.015	0.023
10.0-12.5	0	0	0	0	0	0	0.013	0.025	0.034	0.046	0.055
12.5-15.0	0	0	0	0	0	0	0	0	0.034	0.015	0.008
15.0-20.0	0	0	0	0	0	0	0	0.013	0.011	0.030	0.016
20.0-25.0	0	0	0	0	0	0	0	0	0	0	0.008
overflow	0	0	0	0	0	0	0	0	0	0	0

Table B.4: NC background. All values  $\times 10^{-4}$ .

$\bar{\nu}_\mu$  appearance  
Signal Efficiency

	0-2.0	2.0-3.0	3.0-4.0	4.0-5.0	5.0-6.0	6.0-8.0	8.0-10.0	10.0-12.5	12.5-15.0	15.0-20.0	20.0-25.0
0-2.0	169.5	228.4	47.07	9.966	3.558	1.170	0.648	0.485	0.173	0.077	0
2.0-3.0	378.0	1007	392.8	103.1	24.72	7.939	2.594	1.260	0.490	0.270	0.157
3.0-4.0	310.3	1762	1234	435.1	115.1	22.06	4.983	2.197	0.951	0.481	0.216
4.0-5.0	97.66	1271	2188	1306	448.7	79.27	12.66	3.521	1.729	0.828	0.452
5.0-6.0	24.41	419.5	1627	2009	1188	258.6	30.55	8.561	2.825	1.367	0.748
6.0-8.0	6.926	146.9	895.2	2620	3790	2173	386.3	51.72	12.80	4.622	2.715
8.0-10.0	0.346	12.01	87.04	400.3	1451	3242	2012	354.2	48.22	12.81	5.371
10.0-12.5	0.173	3.274	25.27	70.34	224.4	1460	3617	2256	393.9	49.64	15.19
12.5-15.0	0	0.136	5.283	26.99	55.52	199.2	1243	3171	1971	249.2	29.33
15.0-20.0	0	0.136	0.384	2.907	14.79	68.24	273.2	1634	4485	3151	357.7
20.0-25.0	0	0	0	0	0.281	1.713	19.83	95.11	528.3	3212	2766
overflow	0	0	0	0	0	0.209	1.058	7.980	44.73	631.9	3982

Table B.5:  $\bar{\nu}_\mu$  appearance detection efficiency. All values  $\times 10^{-4}$

$\nu_\mu$  CC background

	0-2.0	2.0-3.0	3.0-4.0	4.0-5.0	5.0-6.0	6.0-8.0	8.0-10.0	10.0-12.5	12.5-15.0	15.0-20.0	20.0-25.0
0-2.0	0	0.251	0	0	0	0	0	0	0	0	0
2.0-3.0	0.112	0.251	0	0	0	0	0	0	0	0	0.039
3.0-4.0	0.224	0.126	0	0.076	0	0	0	0	0	0	0.020
4.0-5.0	0	0.628	0.249	0.076	0.176	0.079	0	0	0	0	0
5.0-6.0	0	0	0.166	0.378	0.088	0.040	0.033	0	0.028	0	0
6.0-8.0	0	0.251	0.249	0.605	0.529	0.119	0.329	0.126	0.057	0.095	0.098
8.0-10.0	0	0.126	0	0.151	0.176	0.316	0.099	0.063	0.028	0.057	0.078
10.0-12.5	0	0	0	0.076	0.088	0.277	0.066	0.063	0.142	0.076	0.098
12.5-15.0	0	0	0	0	0.088	0.119	0.197	0.126	0.113	0.057	0.098
15.0-20.0	0	0	0	0	0	0	0.033	0.063	0.085	0.038	0.078
20.0-25.0	0	0	0	0	0	0	0	0.031	0.028	0.057	0.059
overflow	0	0	0	0	0	0	0	0	0.057	0.038	0.078

Table B.6:  $\bar{\nu}_\mu$  CC background. All values  $\times 10^{-4}$ .

$\bar{\nu}_e$  CC background

	0-2.0	2.0-3.0	3.0-4.0	4.0-5.0	5.0-6.0	6.0-8.0	8.0-10.0	10.0-12.5	12.5-15.0	15.0-20.0	20.0-25.0
0-2.0	0	0	0	0	0	0	0.030	0	0	0.017	0.018
2.0-3.0	0	0	0	0	0	0.037	0	0.029	0	0	0.053
3.0-4.0	0	0	0	0	0	0	0	0	0	0	0
4.0-5.0	0	0	0	0	0	0	0	0	0	0.035	0
5.0-6.0	0	0	0	0	0	0	0	0	0.026	0	0.018
6.0-8.0	0	0	0	0	0	0	0	0	0	0	0
8.0-10.0	0	0	0	0	0	0	0	0	0	0.017	0
10.0-12.5	0	0	0	0	0	0.037	0	0	0	0	0
12.5-15.0	0	0	0	0	0	0	0	0	0	0	0
15.0-20.0	0	0	0	0	0	0	0	0	0	0	0
20.0-25.0	0	0	0	0	0	0	0	0	0	0	0
overflow	0	0	0	0	0	0	0	0	0	0	0

Table B.7:  $\bar{\nu}_e$  CC background. All values  $\times 10^{-4}$ .

NC background

	0-2.0	2.0-3.0	3.0-4.0	4.0-5.0	5.0-6.0	6.0-8.0	8.0-10.0	10.0-12.5	12.5-15.0	15.0-20.0	20.0-25.0
0-2.0	0	0	0	0	0.070	0.016	0.013	0.038	0.056	0.023	0.055
2.0-3.0	0	0	0.068	0.030	0.070	0.094	0.026	0.038	0.079	0.061	0.063
3.0-4.0	0	0	0.137	0.091	0.106	0.110	0.092	0.088	0.213	0.129	0.117
4.0-5.0	0	0	0.068	0.122	0.317	0.268	0.275	0.189	0.213	0.236	0.250
5.0-6.0	0	0	0	0.030	0	0.063	0.079	0.101	0.067	0.084	0.055
6.0-8.0	0	0	0	0	0.070	0.094	0.171	0.076	0.180	0.137	0.156
8.0-10.0	0	0	0	0	0	0.016	0.105	0.076	0.101	0.084	0.117
10.0-12.5	0	0	0	0	0	0	0.039	0.06	0.056	0.053	0.055
12.5-15.0	0	0	0	0	0	0	0	0.025	0.011	0.053	0.031
15.0-20.0	0	0	0	0	0	0	0	0	0.011	0.023	0.047
20.0-25.0	0	0	0	0	0	0	0	0	0	0	0.008
overflow	0	0	0	0	0	0	0	0	0	0	0.008

Table B.8: NC background. All values  $\times 10^{-4}$ .